A Study of the Application of Air-Jet Vortex Generators to Intake Ducts

Christoph Küpper, Dipl. -Ing.

Thesis submitted for the degree of

Doctor of Philosophy

in the School of Engineering

City University

London

Centre for Aeronautics

Department of Mechanical Engineering

and Aeronautics

City University

Northampton Square

London EC1V 0HB

April 1999

Table of Contents

List of Tables

Table **Page**

List of Figures

Figure **Page**

Acknowledgements

I would like to thank my supervisor, Dr. F.S. Henry for his support throughout this project and the writing-up of the thesis.

My thanks to DERA Bedford for giving me the opportunity to realise this project and to Prof. H.H. Pearcey who initiated the project with Dr. F.S. Henry.

I am grateful to Mr. Neil Lewington who offered advice and English grammar lessons throughout the Ph.D.. I would like to express many thanks to my dreadlocked office mate Mr. Saif Deen Akanni for his choice of good music during hours of programming.

Of course, not forgetting the girls of the general office Barbara Clarke, Janet Hartley and Rachel O'Flynn for their help and support during the last three and a half years.

Most of all I am eternally indebted to my partner Dr. Gaby Fischer for her persistent support and encouragement throughout the years of my Ph.D.. Without her love and soul massages I would not have had the strength and power to cope.

Declaration

I grant powers of discretion to the University Librarian to allow the thesis to be copied in whole or in part without further reference to the author. This permission covers only single copies made for study purposes, subject to normal conditions of acknowledgement.

Abstract

Many modern combat aircraft have S-bend intake ducts supplying air to the engine compressor. At high Mach number and/or extreme manoeuvre conditions such ducts can produce excessive flow distortions at the engine face due to flow separating at the first bend of the duct. It has been proposed that vortex generators may be usefully employed in such intake ducts to enhance the homogeneity of the pressure distribution at the engine face, and hence, reduce the unsteady loading on the engine. Both vane and air jets have been tested experimentally as vortex generators and each has been found to reduce the flow distortion that would otherwise reach the engine face.

The objective of this thesis was to construct a local numerical model reflecting the physical geometry and conditions of the fully turbulent flow field in the proximity of a vortex generator array. The location of the array is approximately at the first bend downstream in an S-bend intake duct.

In this project, five different model geometries were tested. Two were used for model verification and the remaining three for investigation of the local flow structure in the vicinity of the vortex generators within the duct. Two of the local duct models neglected any curvature effects (referred to as flat plate models). The third duct model, referred to as a sector model took into account the circular nature of the duct's cross section. The flow is assumed to be incompressible and fully turbulent and was solved using the Finite Volume, Navier-Stokes Code CFX 4 (CFDS, AEA Technology, Harwell) on a non-orthogonal, body-fitted, grid using the k-ε turbulence model and standard wall functions.

The behaviour of the longitudinal vortices produced by the vanes and airjets is presented in terms of circulation and peak vorticity decay, peak vorticity paths in cross-stream and streamwise direction, cross-stream vorticity profiles, cross-stream shear stress distribution and streamwise and cross-stream velocity profiles.

Negligible difference in results was observed for the flat plate models with and without the jet inlet tube; neither did we see significant differences between the flat plate model and the sector model, since the airjet momentum was not drastically altered. Comparing the predicted results provided by vanes and air jets reflected major differences in vortex circulation between the two but the enhancement in transverse skin friction was of similar magnitude. Experiments also showed that both types of vortex generator provided like enhancement of the flow field. The optimum pitch and skew angle configuration for the air jets in terms of maximum enhancement of the flow field was predicted with 30° pitch and 75° skew angle.

Nomenclature

English	Definition
A	Area
a	Coefficient in the discretised Navier-Stokes equation
ADI	Alternating-Direction-Implicit
AJVG	Air-Jet Vortex Generator
B_x	Body force in x-direction
b	Coefficient in the discretised Navier-Stokes equation
C	Chord length from domain entry
c_p	Pressure coefficient
CDS	Central Differencing Scheme
CFD	Computational Fluid Dynamics
COFD	Common Flow Down
COFU	Common Flow Up
d	Exact differential
dh	Domain height
D	Intake duct diameter
D_{exit}	Engine face diameter
D_{jet}	Air jet diameter
DNS	Direct Numerical Simulation
FDM	Finite Difference Method
FEM	Finite Element Method
FVM	Finite Volume Method
HDS	Hybrid Differencing Scheme
HUW	Higher-order Upwind Differencing Scheme
h_v	Vane VG height
I, J, K	Notation
J	Jacobi matrix
k	Turbulent kinetic energy
L	Length of the flat plate model

L_d	Downstream length from the VG centre
$l_{jet\ tube}$	Jet inlet tube length
l_m	Prandtl mixing length
l_v	Vane VG length
l_x	Distance from inlet to downstream Vortex Generator location
LES	Large Eddy Simulation
MVG	Micro Vortex Generator
N	Grid block number
n	Number of cells
P	Pressure
PDE	Partial Differential Equation
PISO	Pressure-Implicit with Splitting of Operators
RANS	Reynolds Averaged Navier-Stokes equations method
RNS	Reduced Navier-Stokes
R	Intake duct radius
SIMPLE	Semi-Implicit Method for Pressure Linked Equations
S	Source term
s	Distance along centre line from duct entry plane
t	Time
t_v	Vane VG thickness
UDS	Upwind Differencing Scheme
u, v, w	Fluctuating velocity components x, y, z directions
U, V, W	Mean velocity in components the x, y, z directions
U_0	Free stream velocity component in streamwise direction
U_τ	Streamwise friction velocity $= \sqrt{\frac{\tau_w}{\rho}}$
V	Volume
VG	Vortex Generator
VRAT	Velocity ratio of airjet velocity divided by free stream velocity
VVG	Vane Vortex Generator
V_x	Viscous forces in x-direction
$\vec{v}$	Velocity vector

W	Width of the flat plate model
X, Y, Z	Locations in an orthogonal coordinate system
x, y, z	Orthogonal coordinates
y^+	Dimensionless wall distance $= \frac{U_\tau y}{\nu}$

Greek	Definition
α_{VG}	Spacing angle
β	Volumetric expansion coefficient
γ	Angle in a skewed grid cell
Γ	Diffusion coefficient
Γ_C	Circulation $= \int_C (v dy + w dz) \cong \sum_{i=1}^{n} [\omega_i \, \Delta y_i \, \Delta z_i]$
δ	Streamwise boundary layer thickness
Δ	Finite change in quantity
ε	Dissipation rate
ζ	Skewness
η, ξ, φ	Curvilinear coordinate system
φ	Circumferential angle
θ	Pitch angle with respect to the solid surface
θ_l	Streamwise local angle
κ	Von Karman constant
μ	Dynamic molecular viscosity
ν	Kinematic molecular viscosity
ν_t	Turbulent or eddy viscosity
ρ	Fluid density
τ_w	Streamwise wall shear stress
ϕ	Skew angle with respect to the centre line
ω	Turbulent time scale $\equiv \frac{\varepsilon}{k}$

ω_S	Streamwise vorticity $= \frac{\partial W}{\partial y} - \frac{\partial V}{\partial z}$

Subscripts

0	Solution domain inlet condition
b	Bulk
c	Chord length
D	Diameter of S-bend duct
e	Exit
e	East face of a finite volume
eq	Equivalent, i.e. based on hydraulic diameter of rectangular duct
E	East located finite volume centre
i	Inlet
n	North face of a finite volume
N	North located finite volume centre
P	Centre point of a finite volume
t	Turbulent
VG	Centre of the airjet vortex generator orifice
w	West face of a finite volume
W	West located finite volume centre

Superscript

*	Initial guess of a property
'	Corrected value of a property
–	Mean value

Other	**Definition**
exp	Exponential function
∇	$= div = \frac{\partial}{\partial x} + \frac{\partial}{\partial y} + \frac{\partial}{\partial z}$
∂	Partial differential operator

1 Introduction

1.1 Problem Definition

Many modern aircraft are equipped with S-bend engine intake ducts. These are used to decelerate the air entering the inlet to a desired flow velocity and pressure at the engine face. The static pressure increases to recover the atmospheric pressure as the engine face is approached. Not only the pressure level but also the flow and pressure uniformity in the cross-stream direction is of great importance to ensure high propulsion efficiency. Non-uniform flow conditions at the duct exit will lower the surge limit, increase the likelihood of engine stall and cause unsteady loading on the engine. Surging is associated with reversed flow caused by a sudden drop in delivery pressure. S-shaped inlet ducts are built into both commercial aeroplanes, e. g. Airbus A300, Boeing 727 and Lockhead L-1011, and military aircraft like Northrop B-2, McDonnell Douglas F-18 and Lockheed Martin F-22. These ducts often generate unwanted flow distortions at the subsonic engine face, particularly under conditions of high free stream Mach number and/or extreme manoeuvre conditions. Anderson (1991) described a number of sources of flow field distortion that are ingested by the inlet diffuser or generated within the duct itself.

These include:

- Flow separation at the cowl lip (duct inlet) during manoeuvring flight
- Spillage of the fuselage boundary layer into the inlet diffuser
- Ingestion of aircraft vortices and wakes coming from upstream disturbances
- Secondary flow (i. e. strong cross-stream pressure gradients) and flow separation within the inlet duct itself, usually at the first bend, developed by the ducts centreline curvature, often called "naturally" occurring vortices (Wellborn et al., 1992 and Reichert & Wendt, 1994, among others)

The effect of one or more of the aforementioned flow field phenomena occurring is to increase the total flow field distortion at the engine face and reduce the pressure recovery possibly to a critical limit. In an ideal case, the inlet diffuser would convert all of the kinetic energy from the air to pressure energy at the engine face, i.e. pressure recovery would be 100%. However, energy losses occur because of the

dissipative effect of viscosity. If the energy losses exceed a certain limit the level of pressure at the engine face is too low to ensure a steady loading on the first blade row of the compressor.

Flows in S-bend ducts are characterised by their three-dimensional nature and the development of vortical structures. The whole flow structure is very complex, because of the interaction of different phenomena such as; for example, flow separation and development of shock waves (Dvorak A, 1996). The two main forces which are involved in creating vortex flow structure are volume (body) forces (e.g. centrifugal forces) and surface forces (viscous and pressure forces).

The development of secondary flow in a curved tube is very similar to the flow in the first bend of an S-bend intake duct. Berger, Talbot & Yao (1983) reviewed entry flow in a laminar case for a curved pipe. They showed that if the flow enters the pipe from a large reservoir the central core of the flow behaves inviscidly. The thin boundary layer near the wall develops initially like in a straight pipe. However, just downstream of the entrance two distinct regions are formed: the first region is an inviscid core, where the pressure gradient force is balanced by the centrifugal force which is caused by the curved motion of the bulk fluid; the second region comprises a thin boundary layer where inertia and viscous forces are balanced. The centrifugal force causes the wall static pressure to be higher at the outside than at the inside of the bend (see Figure 1.1). This causes a transverse or azimuthal flow along the wall within the boundary layer from the outside to the inside of the bend. The longitudinal growth of the boundary layer causes a reduction in flow area of the core flow thereby accelerating it. Thus curvature of the bend induces a fast moving core flow directed to the outside of the bend combined with slower moving fluid within the boundary layer along the wall to the inside of the bend. This leads to the development of a pair of counter-rotating helical vortices situated symmetrically with respect to the duct's symmetry plane. A pair of counter-rotating vortices is also observed as a typical flow pattern at the exit of S-bend intake ducts. Bansod & Bradshaw (1972) observed in experiments with S-bend ducts of constant diameter that soon after the end of the first bend the boundary layer on the inside of the bend increased rapidly and local regions of large yaw angles were measured. They understood this phenomenon as an

indication of a pair of counter-rotating vortices. After the inflection plane; i.e. the intersection of the two bends, the wall static pressure gradient reverses as a result of the change of sign in curvature. Thus the boundary layer fluid could be expected to migrate in the opposite direction. However, the circumferential drift of the boundary layer fluid builds up in the first bend and therefore needs a certain time to reverse. The pressure gradient at the inside of the first bend is negligible and therefore the change of curvature does not affect significantly the flow direction in this area. Bansod & Bradshaw (1972) measured a favourable (negative) streamwise pressure gradient in the middle of the second bend which stretches the pair of helical vortices and accelerates the existing longitudinal vortex line towards the exit of the duct.

If the S-bend duct has an exit to inlet diameter ratio greater than one an adverse (positive) axial pressure gradient will occur which will adversely influence the flow structure. Two factors could cause separation of the boundary layer from the surface. One factor is the change of wall static pressures due to curvature between the first and second bend and the second is the increase of pressure through the diffusing geometry. As a result, fluid particles will be slowed down, i.e. they will lose momentum. In terms of energy conservation, the fluid particles consume so much of their kinetic energy due to the large friction forces in the thin boundary layer that at a certain location the adverse pressure is dominant and forces the fluid particles to reverse. In a two-dimensional boundary layer, e.g. on a flat plate without cross-stream pressure gradients, the fluid must leave the surface and a straight separation line perpendicular to the main flow direction would appear. In the case of the S-bend intake duct a three-dimensional boundary layer exists. In these boundary layers the fluid can move along the wall in a direction which is not aligned with the adverse pressure gradient. A separation bubble (Tobak & Peake, 1982) develops, i.e. the pair of counter-rotating vortices lift off the surface and streaklines converging towards the symmetry plane of the lower half of the duct can be observed (Wellborn et al., 1992). As a result, the boundary layer lifts up from the solid surface and the total pressure at the engine face will be reduced.

Several techniques may be employed to suppress or control boundary layer separation. Gad-el-Hak & Bushnell (1991) and Bushnell (1992) recently reviewed methods of separation control, which include active and passive techniques to delay

separation. These methods are divided into two groups; those inducing longitudinal vortices aligned to the main flow, or those modifying the velocity profile near the wall. The latter group includes shaping of the surface geometry to more streamlining curvature in order to reduce the steepness of the pressure rise and generating a viscosity gradient normal to the solid surface. The techniques used to achieve the viscosity gradients are surface heating or cooling, film boiling, cavitation, sublimation, chemical reaction and wall injection of a secondary fluid with lower or higher viscosity. Shear layer thinning by suction or tangential blowing is also often used to prevent boundary layer separation. All these velocity profile shaping methods are active. In terms of S-bend intake ducts no applications of these active methods are known to work satisfactorily with the exception of flow distortion control via active and passive induction of longitudinal vortices. Weng & Guo (1992), however, describe a different approach. They divided the inlet cross section of a diffusing rectangular S-bend duct with a blade-shaped spoiler in order to reduce the strength of "natural" vortices at the engine face. They observed reduction of vorticity at the duct exit, but were only successful at small angles of attack.

It has been proposed (Anderson, 1991 ,AGARD-AR-270, 1991 among others) that passive Vane Vortex Generators (VVGs) may be usefully employed, upstream of the separation region in S-bend intake ducts (see Figure 1.1) to produce effective flow control.

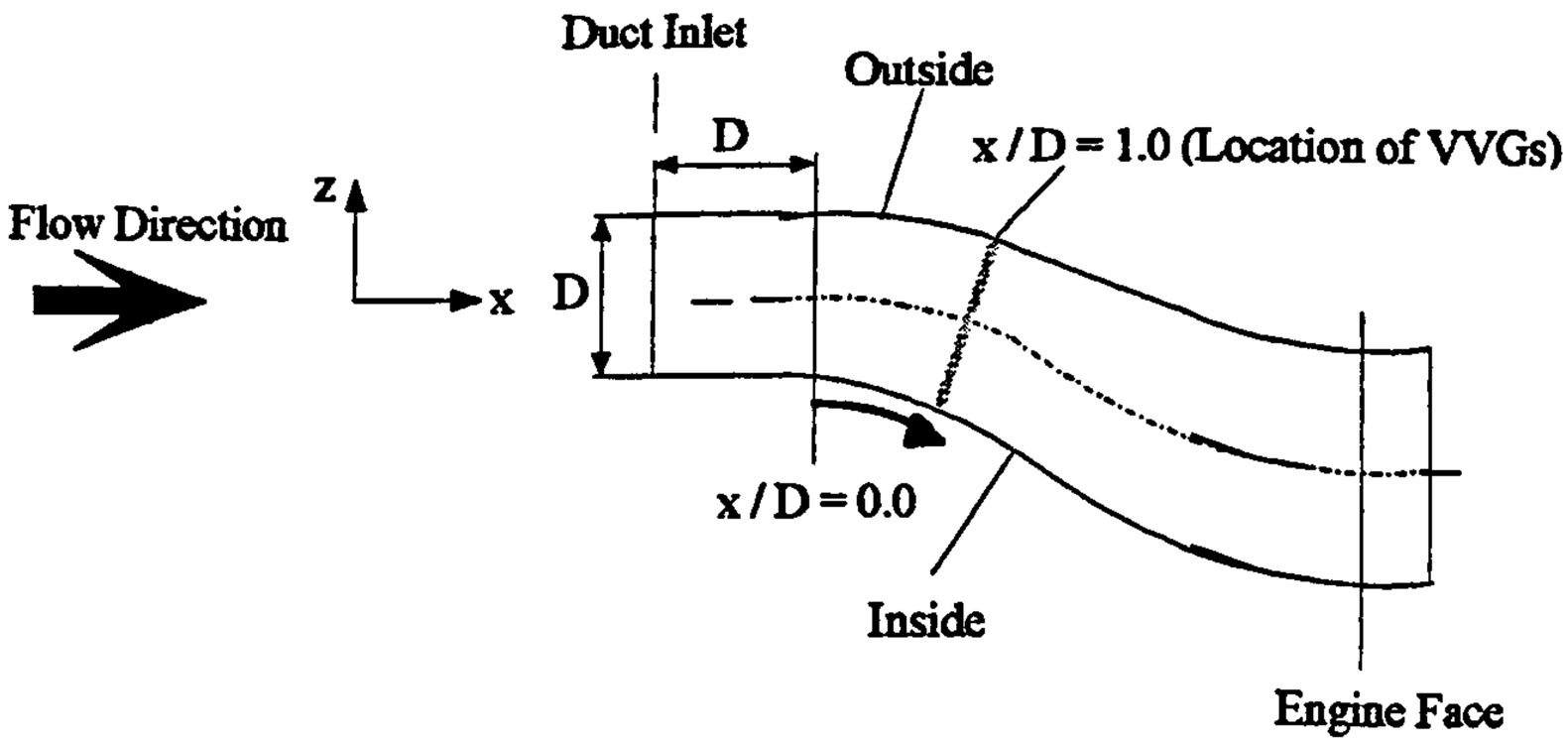

Figure 1.1: S-bend RAE2129 intake duct with location of a vortex generator sector

Anderson & Gibb, 1992, 1993, and Anderson et al., 1993, among others, have shown that VVGs can enhance the homogeneity of the circumferential distribution of total pressure (see Figure 1.2) at the engine face, and hence, reduce the unsteady loading on the engine.

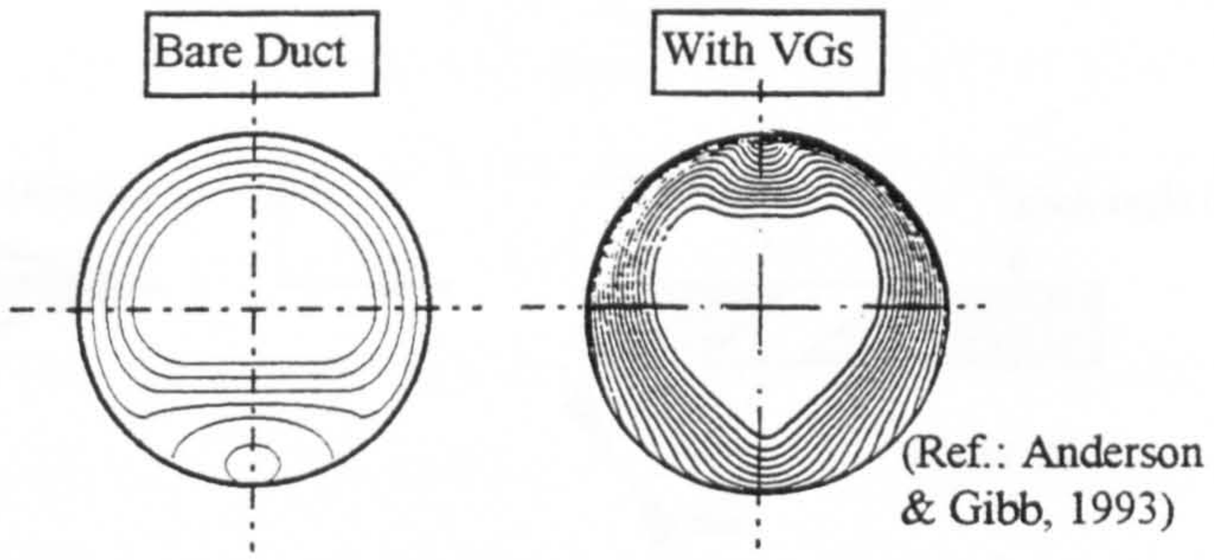

Figure 1.2: Schematic of engine face total pressure contours

Both passive (Vanes) (see Figure 1.3) and active (Air-jet) Vortex Generators (AJVGs) (see Figure 1.4) have been considered. Both generate vortices that are approximately aligned with the mean flow direction.

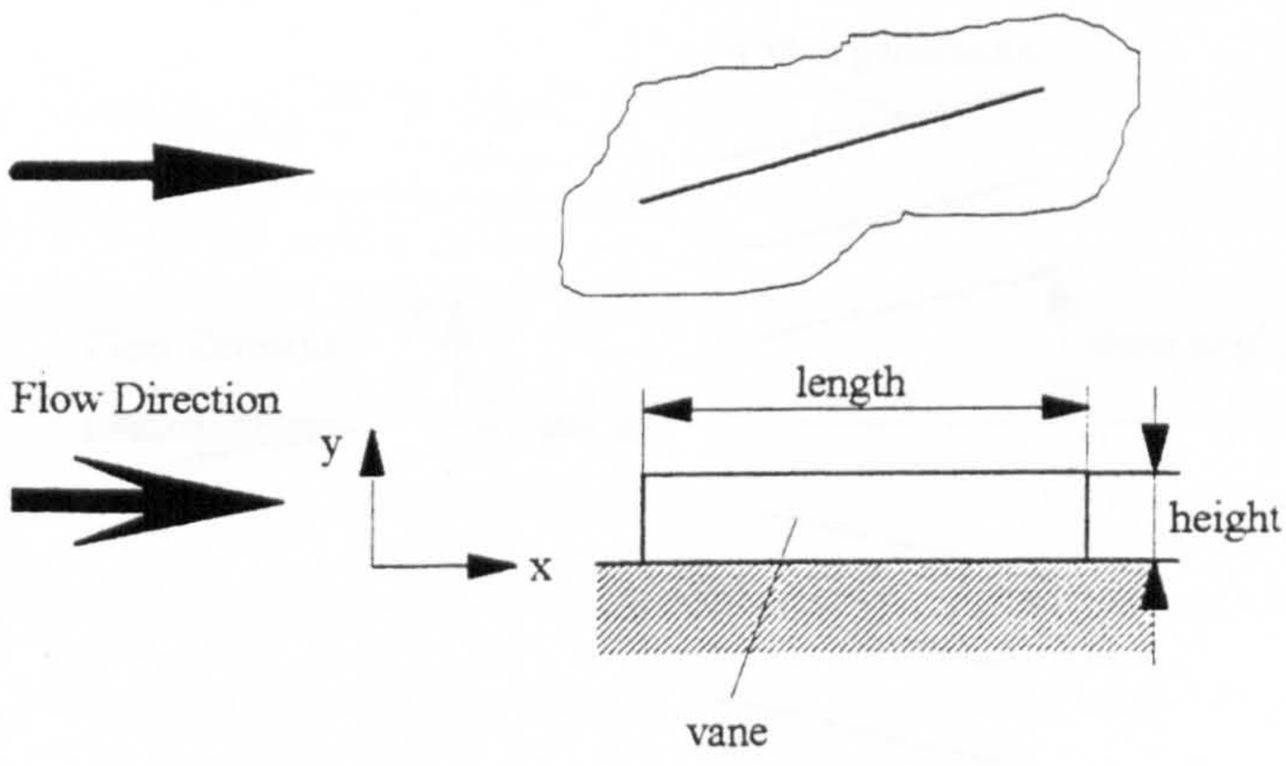

Figure 1.3: Vane vortex generator

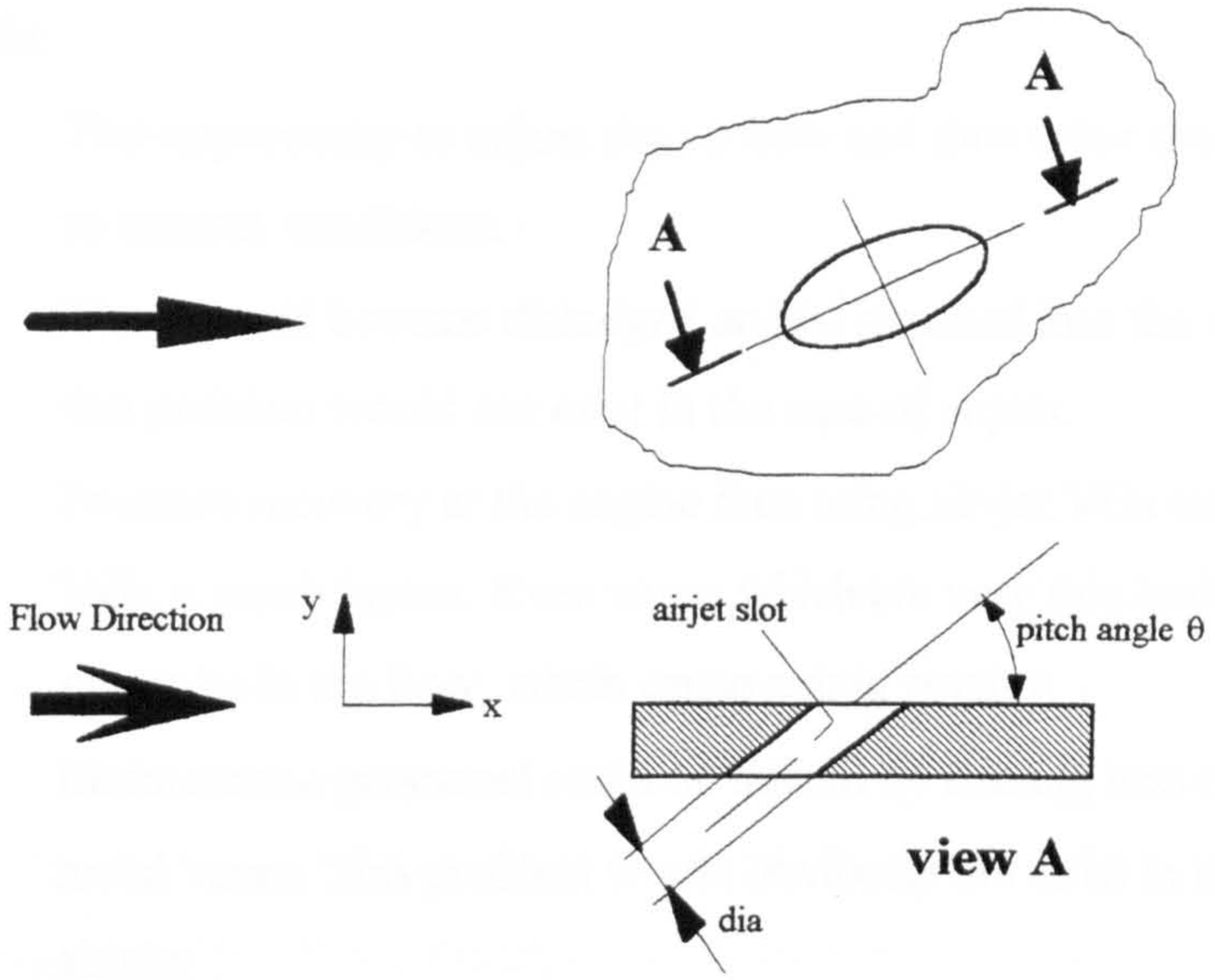

Figure 1.4: Airjet vortex generator

The vanes are fixed on the inner surface of the duct (see Fig. 1.5) whilst the airjets are produced by forcing air through small holes drilled through the duct wall at a pitch angle of θ and a skew angle of ϕ. Both types of generators are positioned just before the first bend (see Figure 1.1).

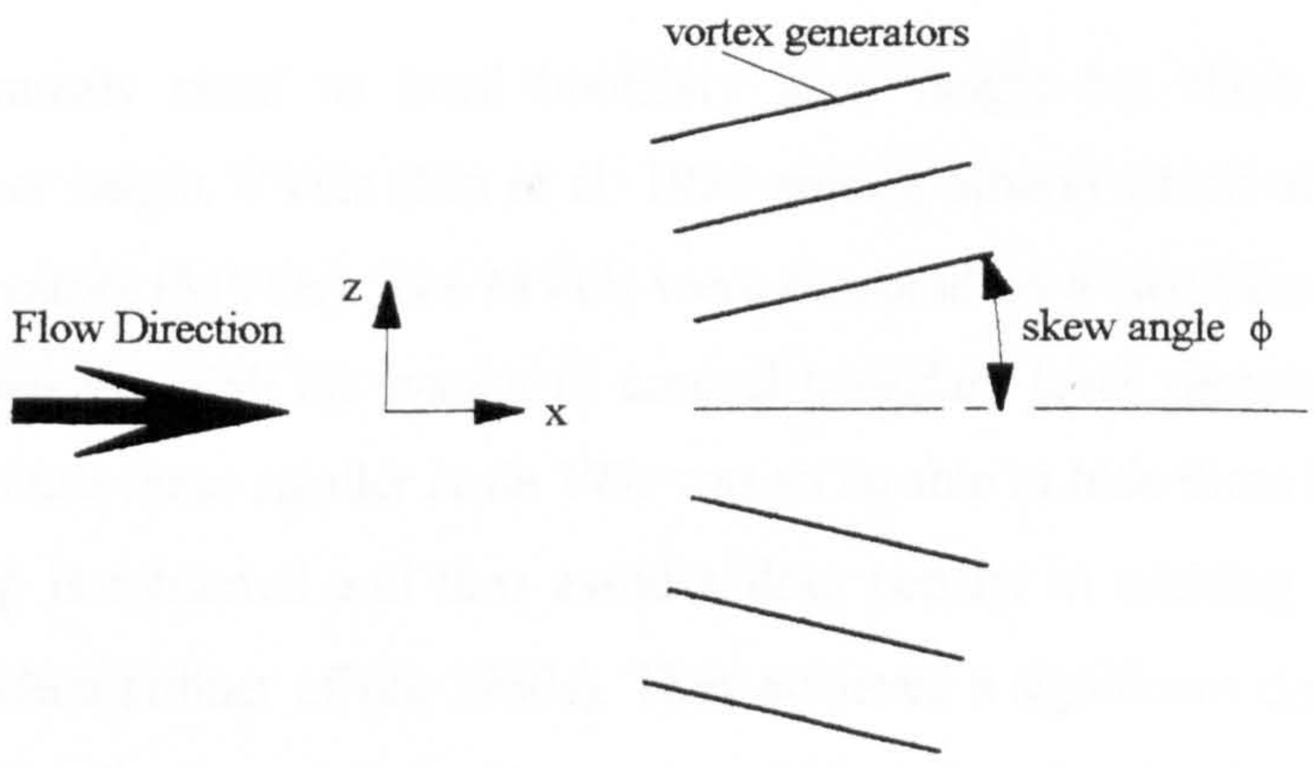

Figure 1.5: Inclined vortex generators to oncoming flow

Airjets may have several advantages over vanes.

These include:

- The opportunity to adjust the jet flow and thus tailor the enhancement to current conditions.
- Vanes could become dislodged and be ingested into the engine. Again, this problem would not exist in the case of airjets.
- Pressure recovery at the engine face using air-jet VGs rather than vane VGs is much higher. Even vanes which are very thin bodies are obstacles in the flow, which cause a drag penalty.
- Maintenance personnel could be injured by coming into contact with metal vanes. This problem would obviously not exist in the case of airjets.

There are also disadvantages for AJVGs when compared to VVGs which are:

- Dust particles could block the orifice.
- Additional costs for piping to feed the AJVGs.
- Increasing weight of the S-bend duct through installed air feeding system.

VVGs are mostly sized to local boundary layer height but there are also sub-boundary-layer height VVGs (Lin et al. 1994 among others) which are called Micro Vortex Generators (MVGs). The MVGs were mounted on a two-dimensional single-flap, three element, high lift system to control boundary layer separation. The main motivation to use these smaller scale VGs was to be able to hide them inside the wing when the flap is retracted and thus avoid a drag penalty in cruising (as on the De Havilland Trident airliner of the 1960s). They achieved a significant downstream shift of the separation line associated with an appreciably reduced wake drag.

Pearcey (1961) describes the principle of boundary layer control by VGs as the induced mixing between the external or core stream and the boundary layer region. The mixing process can be described as fluid particles with high momentum moving in the streamwise direction along helical paths to mix with the lower momentum boundary-layer flow. This is a continuous process that inhibits the natural boundary

layer growth and, therefore, delays separation. The sources for the natural growth of the boundary layer thickness are friction at the solid surface, streamwise and transverse adverse pressure gradients and low energy secondary flow.

The two basic configurations of VGs are:

1) Co-rotating vortices:

The VGs are mounted at the same angle of attack with respect to the oncoming flow direction. Therefore the shed vortices rotate in the same direction.

Anderson (1991) described co-rotating VGs as very competitive in reducing flow separation because of their downstream effectiveness, i.e. the vortices persist inside the affected boundary layer. The induced vortices remain close to the wall and act against the often strong developed secondary flow due to the centreline curvature in S-bend ducts.

2) Counter-rotating or contra-rotating vortices:

These VGs are grouped in pairs inclined in opposite directions to the flow. In this configuration the vortices of each individual pair rotate with opposite direction.

Anderson (1991) considered them effective if they are placed slightly upstream of the region of separation. They were used successfully in F/A-18 inlet ducts. However, a disadvantage of this type of generator compared with the co-rotating type, is that the vortices tend to lift off the duct surface if the VGs are spaced improperly. As a result, higher loss in pressure recovery and larger total pressure distortion at the compressor face can result.

1.2 Goal and Specific Key Objectives

The goal is to investigate numerically the effectiveness of vane vortex generators (VVGs) versus airjet vortex generators (AJVGs) in a particular subsonic incompressible flow pertinent to inlet aerodynamics. The primary objective is to investigate in detail the way in which longitudinal vortices produced by AJVGs and VVGs mix the main high momentum flow with the low momentum flow in the boundary layer in S-bend intake ducts. This will be accomplished by studying the flow in the region local to the vortex generators (VGs). A secondary objective is to produce input data for the Reduced Navier-Stokes code (RNS3D).

We have successfully used the Finite Volume Navier-Stokes code, CFX 4, at City University, in numerical experiments of flow control (see Henry & Pearcey, 1994 and Akanni & Henry, 1995). Because of this experience, we have chosen to exploit the code's capabilities, where we address the following questions:

- What is the difference in vortex structure of the induced longitudinal vortices produced by a VVG and a AJVG?

- What is the optimum configuration for the AJVGs, in terms of pitch and skew angles for co- and counter-rotating vortex systems?

- What effect does modelling the AJVG inlet tube have on the resulting combined air-jet vortex system?

Key issues are:

- The design of a local numerical model which reasonably reflects the physical geometry and conditions of the flow field in the vicinity of the VGs.

- An increase in the understanding of how longitudinal vortices produced by VVGs and AJVGs interact with the boundary-layer flow.

- The production of input data for RNS3D which describes the effect of AJVGs in terms of vortex strength and cross-stream location.

1.3 Methods

Experimental studies of VVGs, employed in S-bend intake ducts have been reported in AGARD-AR-270 (1991) and Gibb & Anderson (1995). Numerical studies were performed using the Reduced Navier-Stokes (RNS3D) code of Anderson (1991) to model the effect of VVGs. However, while wind-tunnel experiments of AJVGs in S-bend intake ducts have been performed by Gibb & Anderson (1995) and Senseney et al. (1996), no comparable AJVG computations were performed by these authors. The elemental vortex flow approximations used in RNS3D did not enable the modelling of the complex vortical flow which develops as the airjets enter the boundary layer. We counter this weakness by developing a model that locally provides the complex flow mechanisms of the interacting air-jet/boundary layer combination. This first set of computations is called a local flat plate model.

There has been extensive experimental work on VVGs mounted on a flat plate, e.g. Westphal et al. (1987), Pauley & Eaton (1988) and ESDU (1994, 1995). Computational investigations of VVGs fixed on a flat plate have been reported by Liandrat et al. (1987). Johnston & Nishi (1990), Compton & Johnston (1992), Selby et al. (1992) and Pearcey et al. (1993) studied experimentally induced longitudinal vortices (via AJVGs) into the boundary layer over a flat plate. Computational studies of AJVGs installed on a flat plate were performed by Zhang (1993a, 1993b), Henry & Pearcey (1994) and Akamni & Henry (1995). To date, no known comparable CFD work on AJVGs within an S-bend intake duct has been performed.

The physical geometry of a typical S-bend intake duct with VGs is shown in Figure 1.6. In our second set computations of the local flow in a sector, as we show below in View AA in Figure 1.6, we have set the spacing angle α_{VG} equal to 15°. This is called a local sector model.

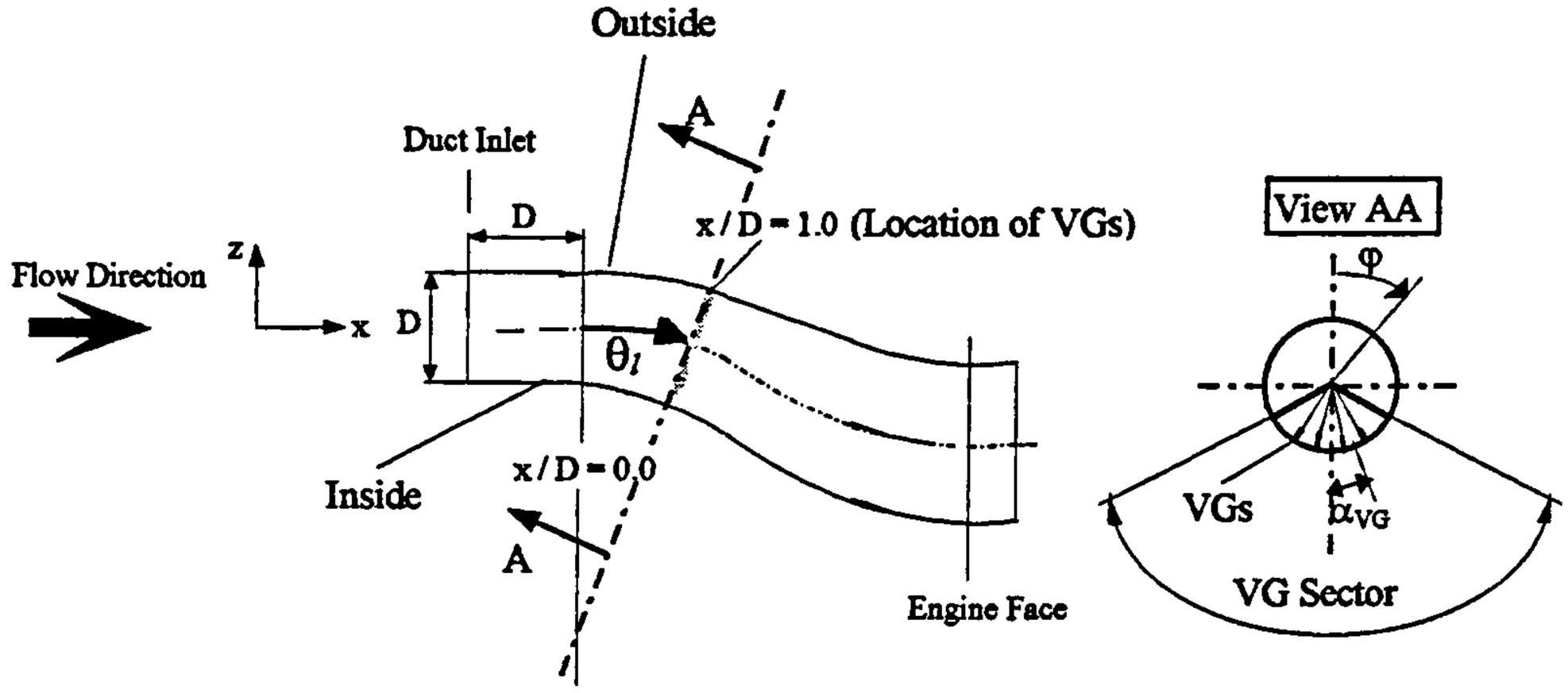

Figure 1.6: S-bend intake duct with detail view AA of the spacing angle α_{VG}, the circumferential angle φ and the local angle θ_l

Knowing from experiments (Gibb & Anderson, 1995) that AJVGs reduce more significantly the flow field distortion than VVGs, it was considered necessary to clarify how AJVGs and VVGs interact with the boundary layer. Our project has, as one of the three issues defined in the previous section, the generation of data to answer these questions in a form which can be fed into RNS3D. Using this data as local initial information, the whole S-bend intake duct can be computed by employing the reduced Navier-Stokes code RNS3D from Anderson. The data will take the form of the initial strengths and positions of the vortices. The data will be generated by solving the full Navier-Stokes equations in a small region surrounding the VGs. The two local models to be used are shown in the following Figure 1.7.

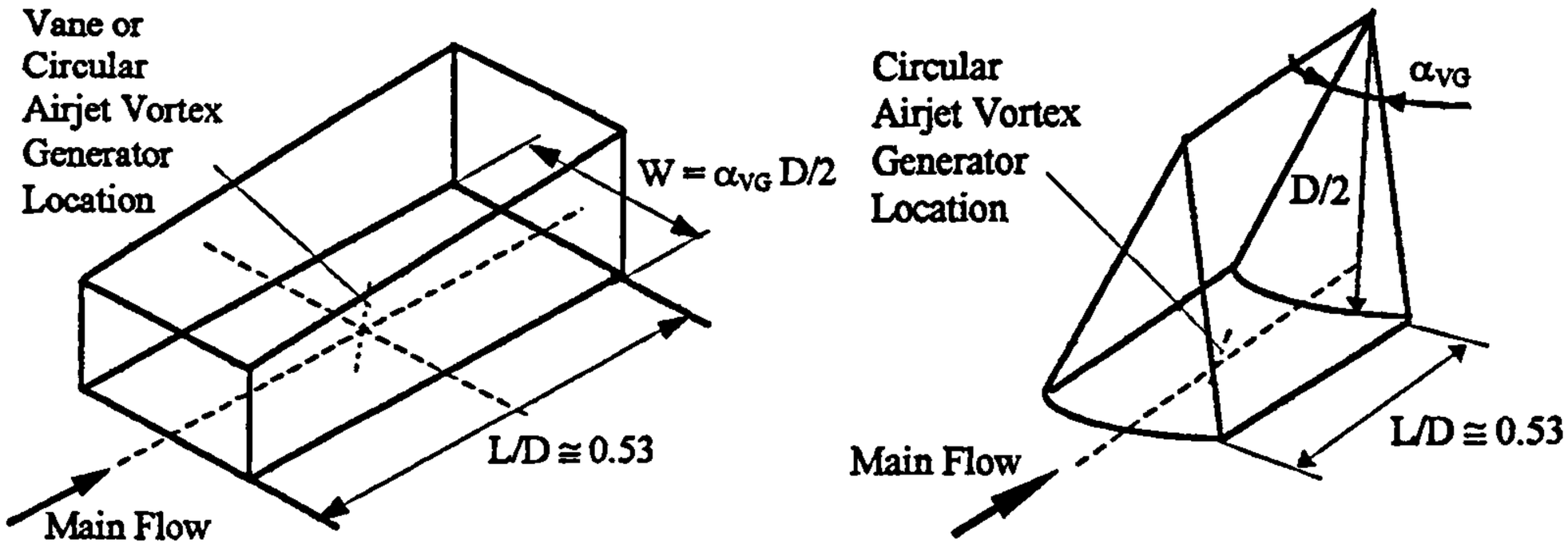

Figure 1.7: Local sector model and flat plate model

The equations were solved with the Finite Volume Method, using the code CFX 4 (formerly Flow3d, AEA Technology, Harwell), on a block-structured, body-fitted grid. CFX 4 has been used successfully for the analysis of three-dimensional fully turbulent flow (e.g. Henry & Pearcey, 1994, Akanni & Henry, 1995). The two-equation k-ε turbulence model, based on the eddy viscosity principle, and standard wall functions was employed. The alternative to wall function would be solving close to the wall to a distance of y^+=0.5 (see Anderson, 1991). The number of grid cells across the boundary layer would then reach $O(2\times10^5)$ because of the steep gradients of turbulent quantities in the viscous sublayer. Being restricted to the computational capacity of $O(3\times10^5)$ the wall function approach offers a significant advantage. Their weakness, nevertheless, is that the wall function approach fails when the flow is hugely separated. However, we know that AJVGs typically reattach separated flow so that we might expect the use of wall functions to be valid with this method of flow control.

The eddy viscosity approximation in contrast to Reynolds stress closure does not take into consideration the transport of Reynolds stresses and assumes isotropic turbulence distribution. However, it has been shown previously in experiments (reviewed in Bradshaw, Cebeci & Whitelaw, 1981: p. 218) that the benefits of using the second moment closures are small. The main problem of employing Reynolds stress models is the necessity of modelling the pressure strain term (see, for example, Speziale 1991) which has to be calibrated for each individual flow situation.

2 Literature Review and State of the Art

2.1 Introduction

As mentioned in Chapter 1, aircraft with S-bend intake ducts often have substantial propulsion efficiency losses due to flow separation. The latter usually occurs between the first and second bend in the inlet duct itself. Many researchers have proved experimentally (see Section 2.2.1) and numerically (see Section 2.2.2) that due to the centre line curvature associated with S-bend intake ducts, secondary motion occurs in the form of a double helix, i.e. a pair of longitudinal counter-rotating vortices. If the pair of counter-rotating vortices is strong enough developed then large regions of streamwise flow separation occur. Both effects were observed as unwanted flow field distortion at the engine face. One of the most promising techniques to minimise engine face distortion is the installing of VVGs or AJVGs upstream of the boundary layer separation region. Table 1.1 and table 1.2 gives an overview of significant literature which is discussed in detail in the following Sections.

Separation control mechanism does not only apply to intake ducts, it also applies to many other flows. *Gad-el-Hak and Bushnell (1991)* presented an excellent review of all available and applied methods of separation control. They examined the historical background of the most important research and discussed the physics of separation in great detail. They suggested expanding the studies of flow separation control beyond the already established methods of blowing/suction and standard VVGs. In particular they suggested for future research:

- AJVGs with steady and pulsed injection
- Converting typical two-dimensional problems into three dimensions
- Enhancing the near wall region with high momentum air; introducing weak upstream shocks for turbulence amplification and spanwise swept shocks to adjust momentum deficit
- Introducing devices, e.g. miniaturised VVGs, to reinforce downstream longitudinal vortices
- Embedding lifting surfaces which produce useful downwash areas to force momentum towards the wall

PAGE NUMBERING AS ORIGINAL

Table 1.1: S-bend intake ducts

Experimental Studies

Date, Author	Application, Inlet condition	Results ($dc_p/dx \equiv$ maximum pressure gradient)
1972, Bansod & Bradshaw 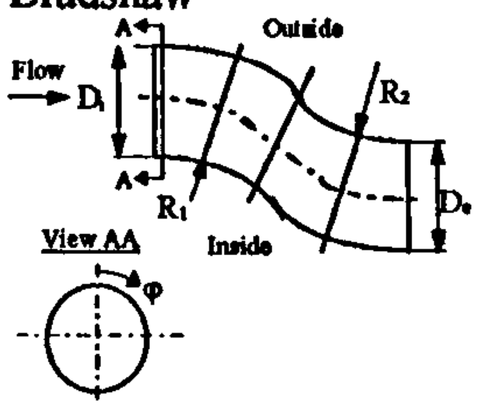	Circular duct, D=150mm Short intake (R/D=2.25, two 45° bends) Tristar intake (R_1/D=3.5, R_2/D=2.25) Optimum intake(R_1/D=2.25, R_2/D=3.5) U_0=45m/s, $Re_D=0.5\times10^6$ δ_0/D=0.05	Axial sinusoidal static pressure and skin friction distribution along the inside (φ=180°) and outside (φ=0°) of the duct. **Short intake:** φ=0°: $dc_p/dx \cong -0.58$; φ=180°: $dc_p/dx \cong 0.81$, (x=s/D) **Tristar intake:** φ=0°: $dc_p/dx \cong -0.42$; φ=180°: $dc_p/dx \cong 0.43$ **Optimum intake:** φ=0°: $dc_p/dx \cong -0.47$; φ=180°: $dc_p/dx \cong 0.76$ Zig-zag axial skin friction development after the mid point of the first bend at φ=90°. Boundary layer (b.l.) thickened rapidly towards the duct's centre line along the inside (φ=180°) beyond two diameters downstream. A pair of longitudinal contra-rotating vortices starts developing at the inflection plane placed symmetrically. No separation occurred.
1982, Guo & Seddon 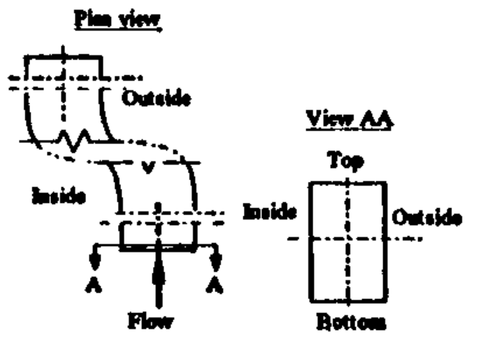	Rectangular duct, const. D_h A=150mm×60mm D_{eq} 85.7mm R=228mm, two 35° bends U_0=40m/s $Re_{eq1}=2.7\times10^5$ $Re_{eq2}=2.1\times10^5$ Duct incidence (0° to 30°) Duct yaw (0° to 10°)	Axial sinusoidal static pressure distribution along the inside and outside of the duct. **Re_{eq1}:** Outside: $dc_p/dx \cong -0.32$; Inside: $dc_p/dx \cong 0.31$, ($x=s/D_{eq}$) **Re_{eq2}:** Outside: $dc_p/dx \cong -0.15$; Inside: $dc_p/dx \cong 0.14$ At 0° incidence: After the first bend a weak pair of contra-rotating vortices occurred. After the second bend the pair of vortices remains weak but changed it rotation sense. Between 10° and 30°incidence: A single vortex is generated in the first bend and a S-like double vortex pattern at the exit of the duct. The average total pressure coefficient at the exit of the duct decreased by 42% at 30° incidence compared to the value at 0° incidence. Flow separation occurred from 20° incidence onwards along the bottom wall after the first bend. Neither the change of Re_{eq}, i.e. from high to low mass flow rate nor the change of yaw angle changed significantly the secondary flow structure in the duct.

1983, Guo & Seddon 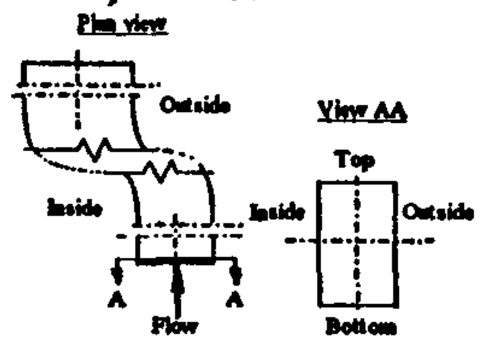 	Rectangular to circular duct A_e/A_i=1.338 A_i=(127×100)mm^2 D_{eqi}=111.9mm, D_e=150mm Offset=177.6mm U_0=40m/s Re_{eqi}=2.7×10^5 Duct incidence (0° to 30°) Offset reduction by 16%	Axial sinusoidal static pressure distribution along the outside. Gradually increasing static pressure along the inside of the duct. Outside: $dc_p/dx \cong -0.42$; Inside: $dc_p/dx \cong 0.54$, ($x=s/D_{eqi}$) At 0° incidence: (see Guo & Seddon, 1982). Between 10° and 30°incidence: A single strong vortex developed after the first bend and kept the rotation sense downstream towards the exit plane where a concentrically rotating vortex was observed. The average total pressure coefficient at the exit of the duct decreased by 58% at 30° incidence compared to the value at 0° incidence. Flow separation occupied 25% of the whole cross section area after the first bend at 30° incidence. The offset reduction did not significantly effect the flow structure.
1984, Taylor et al. (see duct sketch of Bansod & Bradshaw, 1972)	Circular duct. D=48mm, R=336mm, two 22.5° bends U_b=16.4m/s, Re_D=48,000 δ_0/D=0.02 to 0.01	Axial static pressure distribution (see Bansod & Bradshaw, 1972). φ=0°: $dc_p/dx \cong -0.3$; φ=180°: $dc_p/dx \cong 0.16$, ($x=s/D$) No flow separation occurred. Pressure driven secondary flow was observed in the first half of the duct. Along the second bend the secondary flow attenuated at the pipe wall and reversed in the core flow.
1987, Vakili et al. (see duct sketch of Bansod & Bradshaw, 1972)	Circular S-bend diffuser A_e/A_i=1.51 D_i=165.1mm, D_e=203.2mm Two 30° bends, R=825.5mm M=0.6, Re_{Di}=9.91×10^5 $\delta_0/D = 0.01_i$	Axial sinusoidal static pressure distribution along the outside (φ=0°) of the duct. Continuously increasing static pressure, except in the area of separation, along the inside (φ=180°) and at φ=90°. φ=10°: $dc_p/dx \cong -0.24$; φ=90°: $dc_p/dx \cong 0.14$; φ=170°: $dc_p/dx \cong 0.23$, ($x=s/D_i$) Flow separation occurred between the first and the second bend along the inside located by using surface oil patterns and measuring constant axial static pressure distribution. A weak pair of contra-rotating vortices were determined at the first bend and displaced by the area of separation towards the outside of the duct. Downstream of the area of separation the pair of contra-rotating vortices was twice as strong as the one before the separation area.
1992, Wellborn et al. (see duct sketch of Bansod & Bradshaw, 1972)	Circular S-bend diffuser A_e/A_i=1.52 D_i=204.2mm, D_e=251.4mm Two 30° bends, R=1021mm M=0.6, Re_{Di}=2.6×10^6 $\delta_0/D_i = 0.035_i$	Axial static pressure distribution (see Vakili et al., 1987) φ=10°: $dc_p/dx \cong -0.39$; φ=90°: $dc_p/dx \cong 0.17$; φ=170°: $dc_p/dx \cong 0.32$, ($x=s/D_i$) Circumferential static pressure distribution (φ=0° to 180°) is approximately linearly decreasing at the first bend and increasing at the second bend. Flow separated between the first and the second bend. Streaklines of fluorescent oil on the duct surface showed two spiral nodes placed symmetrically on the centre line of the duct along the inside at φ=180°. Development of the pair of contra-rotating (see Vakili et al., 1987). Total pressure contours at the first bend showed only slightly varied boundary layer thickness with circumferential position. Towards the exit plane the boundary layer thickened to approximately the duct radius at a circumferential position between 90° and 270°. As a result the core flow was shifted to the upper half of the duct.

1993, Whitelaw & Yu (see duct sketch of Bansod & Bradshaw, 1972)	Circular S-bend diffuser A_e/A_i=1.4 D_i=48mm, D_e=56.8mm Offset=170.4mm, U_b=1.37m/s, Re_D=40,000 Case 1: $\delta_0/D_i = 0.5$ Case 2: $\delta_0/D_i = 0.2$	Axial static pressure distribution (see Vakili et al., 1987) **Case 1:** φ=0°: $dc_p/dx \cong -0.17$; φ=90°: $dc_p/dx \cong 0.12$; φ=180°: $dc_p/dx \cong 0.22$, (x=s/D_i) **Case 2:** φ=0°: $dc_p/dx \cong -0.22$; φ=90°: $dc_p/dx \cong 0.11$; φ=180°: $dc_p/dx \cong 0.21$ Flow separation was in an incipient state because a low magnitude of negative streamwise ($\approx 0.02U_b$) velocity was measured. The area of separation started just upstream of the inflection plane and extended close to the exit of the S-bend. **Case 1:** 1/3 of the duct length was effected by separation. The pair of contra-rotating vortices occupied 1/3 of the lower half of the duct. **Case 2:** 1/2 of the duct length was effected by separation. The pair of contra-rotating vortices occupied almost the whole lower half of the duct.

Numerical Studies			
Date, Author	**Application, Inlet condition**	**Numerical Method**	**Results**
1978, Eisemann et al.	Circular duct + const. D M=0.1, $Re_D=1\times10^5$	Forward marching integration procedure Eddy viscosity turbulence model Standard wall function	Typical pair of contra-rotating vortices. Flow separation near the end of the first bend. (Not coincident with experiments). Problem: Pressure model was not capable to determine the highly three-dimensional flow near the end of the first bend.
1986, Kunik	Circular S-bend diffuser (the same inlet condition and geometry than Vakili et al., 1987)	Spatial marching procedure, PEPSIG Algebraic mixing length turbulence model Solved to the wall	Quantitatively correct prediction of the flow structure. Flow separation predicted further downstream than the measured location. Problem: "flare" approximation used to march through the separated flow region caused the shift of separation.
1991, AGARD-AR-270 (see duct sketch of Bansod & Bradshaw, 1972)	Circular S-bend diffuser RAE2129, A_e/A_i=1.4 D_i=128.8mm, D_e=152.4mm Case 1: M=0.794 $Re_{De}=1.848\times10^6$ Case 2: M=0.412 $Re_{De}=1.158\times10^6$ $\delta_0/D_i = 0.06$	Code 1: Navier-Stokes approach + k-ε turbulence model + wall function Code 2: Euler approach Code 3: Navier-Stokes approach with thin layer approximation + Baldwin & Lomax turbulence model + solved to the wall	Case 1: None of the three codes predicted the flow structure correctly. Case 2: The static pressure distribution was predicted correctly at the engine face from Code 3 and along the S-bend from Code 1. Problem: Flow prediction depends very much on boundary conditions available from experimental data.

1992, Smith et al.	Circular S-bend diffuser (the same inlet condition and geometry than Vakili et al., 1987)	Navier-Stokes approach, PARC3D Baldwin & Lomax turbulence model Solved to the wall	Good agreement with experimental total pressure contours up to the second bend. Region of flow separation occurred approximately $0.5D_i$ downstream of the experimentally determined location. At duct exit region of inviscid core flow was twice as large as the experiment showed. <u>Problem:</u> Grid density in cross-flow direction was too coarse. Turbulence model was too simple.
1993, Anderson et al.	Circular S-bend diffuser (see Case 1 and Case 2 in AGARD-AR-270, 1991) + Case 3: M=0.2 $Re_{D_e}=0.594\times10^6$ $\delta_0/D_i = 0.005$	Code 1 Navier-Stokes approach, PARC3D (see Smith et al., 1992 but with improved turbulence model) Code 2 Reduced-Navier Stokes approach (RNS3D) Spatial marching integration method + Eddy viscosity turbulence model + Solved to the wall	<u>Code 1 and 2:</u> Pressure recovery distribution agreed with experimental data. Flow separation, i.e. region of vortex lift off, was predicted further downstream and less strong than experimental data and occurred already at Ma=0.2 (at Ma=0.3 in experiment). Code 2 reflected flow distortion at the duct exit closer to experimental data than Code 1.
1997, May	Circular S-bend diffuser (the same geometry than AGARD-AR-270, 1991) Case 1: High mass flow rate Case 2: Low mass flow rate M=0.21 $Re_{D_e}=8.6\times10^5$	Navier-Stokes code, SAUNA 8 turbulence models 1) Baldwin & Lomax, 2) k-ε, 3) RNG k-ε, 4)Non-linear k-ε, 5) k-ω, 6) k-ω + shear stress modification, 7) Non-linear k-ω, 8) Non-linear k-ω + shear stress modification 2), 3) + 4) with wall function Other models solved to the wall	<u>Case 1:</u> Regions of separation was predicted in the sequence of 8) > 7) > 6), 5) > 1) > 2), 3), 4). Turbulence model 8) predicted closest to experimental data. Turbulence models 2), 3) and 4) did not predict any separation. All turbulence models, except 2), 3) and 4), predicted location of separation futher downstream compared to experimental data. <u>Case 2:</u> All turbulence models failed to predict any secondary flow.

Table 1.2: Vortex generator studies			
VVG Experimental Studies			
Date, Author	**Application, Inlet condition**	**Vortex Generator**	**Results**
1948, Taylor	Diffuser	VVGs	Boundary layer control
1961, Pearcey	Aerofoils + wings	VVGs	Prevent shock induced boundary layer (b.l.) separation
1968, Brown et al.	Rectangular to semiannular intake duct, M=2.65	Wing VGs	Flow uniformity at the engine face
1991, AGARD AR 270	Intake ducts for high speed vehicles	VVGs	Boundary layer control
1995, Gibb & Anderson	S-bend intake duct M2129 (see Table 1.1, AGARD, 1991), M=0.2 to 0.8	VVGs	Reduced engine face flow distortion + improved pressure recovery
1996, Wendt & Reichert	S-bend intake duct (see Wellborn et al., 1992)	Tapered fin VGs	Influence of ingested vortices onto the flow field at the engine face could be controlled via VGs
1996, Reichert & Wendt	Non diffusing (see Vakili et al., 1984) + diffusing S-bend intake ducts (see Vakili et al., 1987), inlet condition see Wellborn et al., 1992	Wishbone VGs	• Main reason for flow field distortion at the engine face is not b.l. separation but secondary flow produced by streamline curvature. • VGs redirected the flow ⇒ reduced flow field distortion + improved pressure recovery
1997, Foster et al.	Rectangular to semiannular intake duct td118 (similar to Brown et al., 1968), M=0.784, $Re_{eqi}=3.2\times10^6$ $\delta_0/D_{eqi}=0.008$	Tapered fin VGs	• Reduced flow field distortion at the engine face • No improved pressure recovery
1987, Westphal et al.	Flat plate, $U_0=27$m/s $\delta_{VG}=13$mm, $\delta_{VG}/C=0.014$	Half delta VG single	Flattened vortex close to the solid plate
1988, Pauley & Eaton	Flat plate, $U_0=16$m/s $\delta_{VG}=13$mm, $\delta_{VG}/C=0.025$	Half delta VGs Co- and counter rotating pairs	COFD, COFU, secondary vorticity on the upwash side but no roll up, 15-25% of the main vortex strength

1991, Littell & Eaton	Rotational tab om a flat wind tunnel floor, U_0=13m/s δ_{VG}=15mm, δ_{VG}/C=0.028	Half delta VGs	• Unsteady flow behind VGs, • minor.roll up of secondary vortex • Convection speed 90% of main flow • Formation + relaxation = actuation + convection time of the induced vortices
1993, Wendt et al. (Ext. from Pauley & Eaton)	Flat wind tunnel floor, U_0=70m/s, $Re_C=3\times10^6$ δ_{VG}=10mm, δ_{VG}/C=0.016	Rectangular wing Vgs Array of counter rotating VGs	• Large spacing ⇒ less interaction with boundary layer • Small spacing ⇒ merging to one strong vortex and strong interaction with boundary layer
1994, Wendt & Hingst	Flat wind tunnel floor, U_0=70m/s, $Re_C=13\times10^6$ δ_{VG}=833mm, δ_{VG}/C=0.28	Wishbone VG single	One strong counter-rotating pair with only one streamwise velocity deficit for both vortex cores coincident with the tip of the VG
1994/1995, ESDU	Aerofoils + diffusers	Wing VGs or VVGs	Control shock induced flow separation

VVGs Numerical Studies

Date, Author	Application, Inlet condition	Vortex Generator	Numerical Method	Results
1955, Jones	Flat plate	Wing type VG Array of counter-rotating VGs	Analytical approach	Determined numerically the vortex trajectory
1991, Anderson	S-bend intake duct (see Vakili et al., 1987)	VVG system	3D RNS (Reduced Navier-Stokes code) Eddy viscosity turb. model Solved to the wall	Separation of the b.l. and suppression of b.l. with induced vortices
1992, Anderson et al.	S-bend intake duct Boeing 727-100/TAY651-54 M=0.1 to 0.6 $Re_D=12.71\times10^6$ δ /D=0.005	VVG system	RNS3D Eddy viscosity turb. model Solved to the wall	• Difference between inflow and external aerodyn. is dimensionality, not reenergising the b. l. but constructing vorticity patterns, VVG performance influenced by: • Throat Mach number • separation = f(D_{Duct} in the first bend)
1992, Anderson & Gibb	S-bend intake duct RAE2129 (see Table 1.1, AGARD-AR-270, 1991)	VVG system	RNS3D Eddy viscosity turb. model Solved to the wall	Optimum VVG configuration

1993, Anderson & Gibb	S-bend intake duct M2129 (see Table 1.1, AGARD-AR-270, 1991))	VVG system	RNS3D Eddy viscosity turb. model Solved to the wall	• VVG height=f(Re), • Defined a correlation to calculate VVG height
1987, Liandrat et al.	Flat plate U_0=30m/s	VVGs single + pair	• Parabolized Navier-Stokes Equat. • Implemented algebraic diffusion model to integrate the Reynolds stress equation Solved to the wall	Due to the algebraic diffusion model it became possible to predict the VG pair interaction with the b. l.

AJVGs Experimental Studies			
Date, Author	**Application, Inlet condition**	**Vortex Generator**	**Results**
1952/1960, Wallis	Aerofoil, $Re_C=4\times10^6$	Circular AJVG D_{jet}=0.71mm, D_{jet}/C=0.075	Delay of boundary layer separation
1961, Pearcey	Aerofoils + wings M=1.0 to 1.4	Circular AJVGs Co-rotating array	• Improved pressure recovery • Prevent shock-induced separation
1995, Gibb & Anderson	S-bend intake duct M2129 (see Table 1.1, AGARD-AR-270, 1991)	Circular AJVGs D_{jet}=1mm, x/D_i=1 (see Figure 1.1)	Co-rotating vortices most successful in reducing engine face distortion
1996, Senseney et al.	Rectangular S-bend diffuser $A_i=(25.4\times16.79)mm^2$, Offset/$D_{eqe}$=0.81 A_e/A_i=1.5, D_{eqe}=28.82mm M=0.6, $Re_{eqe}=3.46\times10^7$ δ_0=2.7mm , δ_0/D_{eqi}=0.12	Circular AJVGs D_{jet}=0.6mm D_{jet}/C=0.005	Co-rotating vortices most successful in delaying b.l. separation
1990, Johnston & Nishi	Flat plate U_0=15m/s δ_{VG}=15mm	Circular AJVGs Co- and counter-rotating arrays D_{jet}=6.35mm, D_{jet}/C=0.021	Counter-rotating in downwash configuration showed most delay of b.l. separation

1992, Compton & Johnston	Flat plate U_0=15m/s, δ_{VG}=14mm	Circular AJVG, single D_{jet}=6.35mm, D_{jet}/C=0.012	Strong dependency of the vorticity peak to the skew angle
1992, Selby et al.	25° ramp mounted on a wind tunnel floor U_0=40m/s, δ_{VG}=33mm	Circular AJVGs Co- and counter-rotating arrays	• Altering the pitch angle to ensure the momentum transfer is closer to the wall • Co-rotating vortices provided best pressure recovery + b.l. delay results
1993, Pearcey et al.	Full-span half aerofoil transonic wind tunnel M=1.0 to 1.65	Rectangular AJVGs Co-rotating array C=305mm, x/C=0.35	Suppression of b.l. separation + improved pressure recovery

AJVGs Numerical Studies				
Date, Author	**Application, Inlet condition**	**Vortex Generator**	**Numerical Method**	**Results**
1993a, Zhang	Flat plate (see Compton & Johnston, 1992)	• Circular AJVGs • single • co- and counter-rotating D_{jet}=6.35mm	• K-ε turbulence model + wall function • Reynolds stress model + wall function	• Contra rotating vortices stronger in terms of b.l. separation delay
1993b, Zhang	Flat plate U_0=13.5m/s δ_0^*=1.81mm	• Circular + rectangular AJVGs • Array • co- and counter-rotating D_{jet}=10mm, $A_{rect.jet}$=31.7mm^2 x/D_{jet}=5	• K-ε turbulence model + wall function • Reynolds stress model + wall function	• Results see Zhang 1993b • No difference between circular and rectangular jets
1994, Henry & Pearcey	Flat plate Re=5×10^6 δ_{VG}=3.4mm	• Rectangular AJVG • single with various aspect ratios A_{jet}=125mm^2, x/C=0.2, C=0.5m	• K-ε turbulence model + wall function	• Significant boundary layer thinning, i.e. b.l. separation delay
1995, Akanni & Henry	Flat plate Re=2.37×10^6 δ_{VG}=3.9mm	• Rectangular AJVG • single with various aspect ratios A_{jet}=627mm^2, x/C=0.2, C=0.5m	• K-ε turbulence model + wall function	• Results see Henry & Pearcy (1994) • Improved visualisation of vortex development

2.2 S-bend Intake Ducts

2.2.1 Experimental Studies

Bansod and Bradshaw (1972) examined three different circular S-bend ducts and a straight pipe, all of the same constant diameter of D = 150mm. The first duct is a "short intake" which comprised two 45° bends. The ratio of the centreline radius of curvature to the duct diameter (R/D) was equal to 2.25. The second duct was an approximation to the dorsal intake of the Lockheed Tri-Star aircraft. It consisted of an upstream bend with a ratio of R/D = 3.5 followed by a 45° bend with a ratio of R/D = 2.25. In the case of the third duct they exchanged the upstream bend (R/D = 3.5) with the downstream bend (R/D = 2.25) of the Tri-Star intake and called it "Optimum intake". The straight pipe had the same centre-line length as the "short intake". The free stream velocity was measured to be 45m/s so that a Reynolds number, based on the duct diameter was 0.5×10^6.

Measurements were taken of the axial static pressure distribution along the duct wall of the three ducts, at two circumferential angles, $\varphi = 0°$ and $\varphi = 180°$ (see Figure 2.1). They referenced their static pressure coefficient with the static pressure at the duct entry plane. At both circumferential angles the axial variation of the static pressure coefficient c_p between the maximum values showed a sinusoidal character (see Figure 2.2).

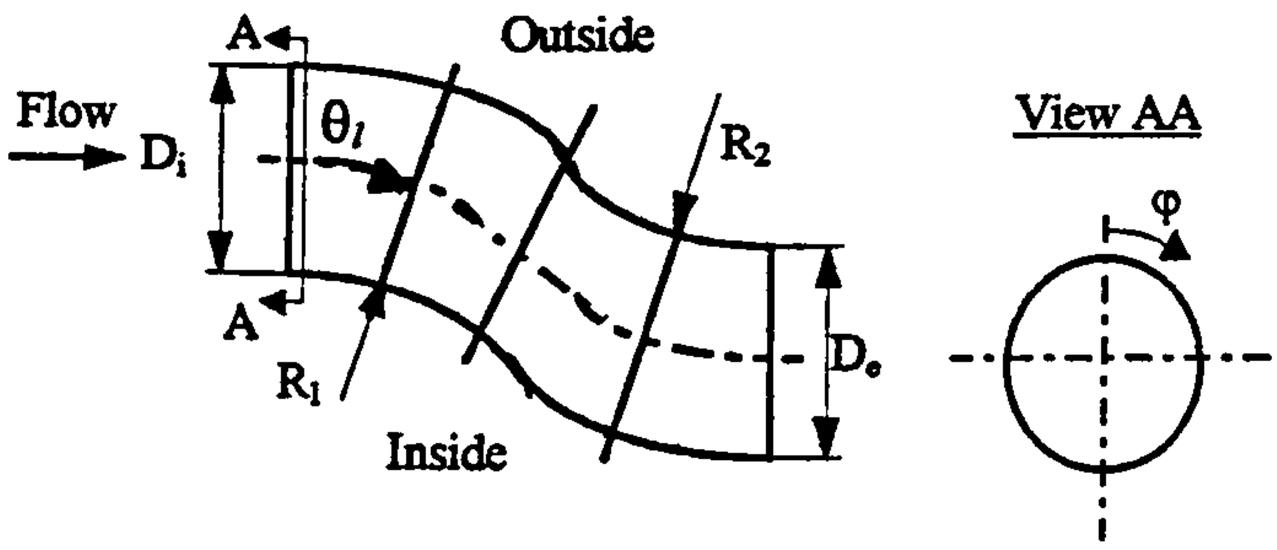

Figure 2.1: Sketch of a S-bend duct configuration

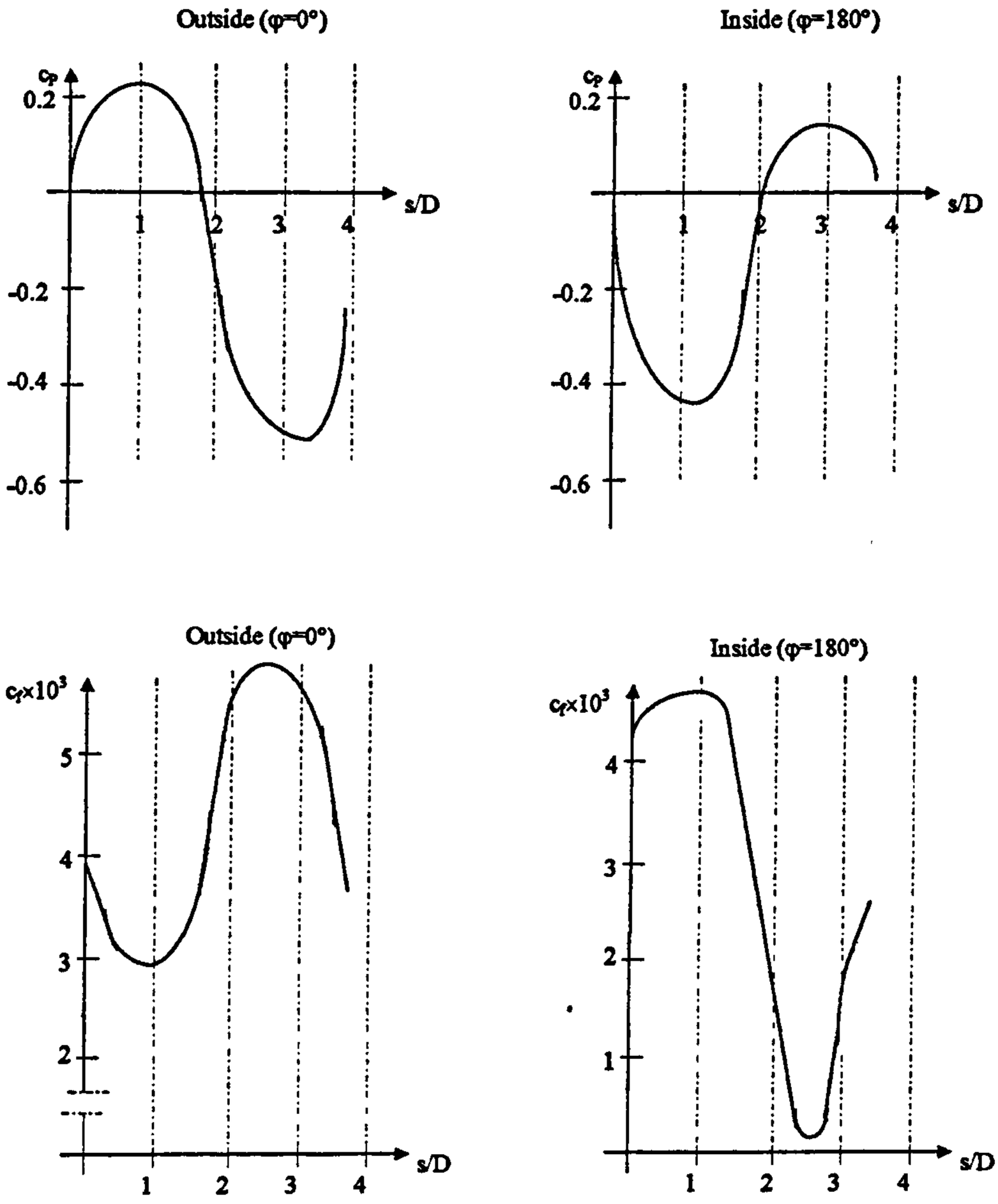

Figure 2.2: Sketch of simusoidal distribution of axial static pressure and streamwise skin friction of a S-bend duct with constant diameter

However, on the outside of the ducts ($\varphi = 0°$) an initial increase of static pressure to a positive maximum of approximately $c_p = 0.233$ was followed by a decrease to a minimum of approximately $c_p = -0.6$. In contrast, on the inside of the ducts ($\varphi = 180°$) the static pressure decreased rapidly to a minimum of approximately $c_p = -0.467$ followed by an increase to a maximum of $c_p = 0.167$. The difference in pressure distribution between the two sides of the duct is caused by the duct curvature, i.e. centrifugal forces induced the flow to move towards the outer wall of the duct. The fact that two bends were joined at an angle of 180° between their centreline curvature

resulted in a sinusoidal axial pressure profile. The static pressure amplitudes were stretched in the axial direction depending on the length of the duct.

The development of skin friction in the axial direction was determined experimentally at three circumferential angles, i.e. $\varphi = 0°$, $\varphi = 90°$ and $\varphi = 180°$. Again a sinusoidal axial distribution of the skin friction coefficient was detected at the inside ($\varphi = 180°$) and outside ($\varphi = 0°$) of the ducts (see Figure 2.2). The duct entrance skin friction coefficients were approximately $c_f = 4.0\times10^{-3}$. However, the sequence of maxima to minima were opposite to the static pressure distribution, with similar development for all three ducts. The fluid experienced an acceleration in the first bend on the inside ($\varphi = 180°$) thus the skin friction increased to a maximum which was approximately $c_f = 4.6\times10^{-3}$ in the case of the "optimum intake", followed by a steep decrease starting from the mid point of the first bend to a minimum of $c_f = 0.3\times10^{-3}$ in the case of the "short intake" close to the entrance of the second bend. Further, downstream in the second bend the skin friction rose again to a maximum of $c_f = 3.0\times10^{-3}$ in terms of the "optimum duct". The final acceleration towards the exit of the ducts was caused by a favourable longitudinal pressure gradient from the middle of the second bend. On the outside ($\varphi = 0°$) of the ducts the fluid was decelerated up to the mid point of the first bend, accelerated up to the entrance of the second bend and decelerated towards the exit. The minimum in the first bend was approximately $c_f = 2.6\times10^{-3}$ ("Tristar intake"), the maximum at the exit of the first bend was approximately $c_f = 5.6\times10^{-3}$ ("short intake") and the minimum at the exit of the duct was measured to be $c_f = 0.83\times10^{-3}$ ("optimum duct"). A zig-zag axial skin friction development after the mid point of the first bend at a circumferential angle of $\varphi = 90°$ was observed. The average level of skin friction was $c_f = 3.5\times10^{-3}$ and was compared to the skin friction of the straight pipe. This skin friction development might be explained as the combination of a small region of separation near $\varphi = 180°$ between the first and second bend, and the re-energising process of the boundary layer fluid by the pair of contra-rotating vortices. Therefore an alternating procedure of thickening and thinning of the three dimensional boundary layer occurred instead of a continuous increase of boundary layer thickness as in the straight pipe flow.

The circumferential variation of skin friction over the range of $0° \leq \varphi \leq 180°$ was measured only for the "short intake" at five axial locations, i.e. at the inlet, the mid point of the first bend, the inflection plane, the mid point of the second bend and the exit plane. At the inlet a circumferential averaged value of skin friction was measured to be approximately $c_f = 3.9\times10^{-3}$. At the mid point of the first bend, i.e. one diameter downstream, skin friction was found to change from $c_f = 3.0\times10^{-3}$ at $\varphi = 0°$ to a maximum of $c_f = 4.85\times10^{-3}$ at $\varphi = 120°$. At the inflection plane, i.e. two diameter downstream, skin friction decreased from $c_f = 4.13\times10^{-3}$ at $\varphi = 0°$ to $c_f = 2.17\times10^{-3}$ at $\varphi = 180°$. The maximum change, i.e. decrease of skin friction was observed at the mid point of the second bend, i.e. three diameter downstream, of $\Delta c_f = -4.5\times10^{-3}$ from $c_f = 5.3\times10^{-3}$ at $\varphi = 0°$ to $c_f = 0.8\times10^{-3}$ at $\varphi = 180°$. At the exit plane the circumferential skin friction variation was minor between $c_f = 3.55\times10^{-3}$ at $\varphi = 0°$ and $c_f = 3.85\times10^{-3}$ at $\varphi = 165°$. Between $\varphi = 165°$ and $\varphi = 180°$ the skin friction decreased rapidly to approximately $c_f = 3.0\times10^{-3}$. This phenomenon might be explained by the presence of a thick boundary layer ($\delta \cong 0.5D$) generated by the pair of counter-rotating longitudinal vortices.

At the mid-point of the second bend and at the exit of the ducts (at $\varphi = 180°$) the radial variation of total pressure loss was measured for the three ducts. At both locations the total pressure loss decreased to approximately zero towards the duct centre line. The difference between the two downstream locations is that at the duct exit the boundary layer has reached a thickness of the radius of the duct whereas at the mid point of the second bend the boundary layer thickness has reached only approximately 60% of the duct radius.

In all three ducts the boundary layer thickness was of similar magnitude as the straight pipe value between the inlet and approximately two diameters downstream. Further downstream along the inside of the ducts (at $\varphi = 180°$) the boundary layer thickened rapidly towards the exit to a maximum of 50% of the duct diameter.

Even though the pressure loss contours at the exit plane showed the lowest value for the "short intake", the magnitudes for all three duct geometries showed similar results in terms of displacement of the boundary layers in the lower half of the ducts towards the centreline.

Circumferential components of velocity were measured at the inflection plane, the mid point of the second bend and the exit plane. The equipment used did not allow the measurement of the radial velocity components in the thin boundary layer. Bansod & Bradshaw (1972) observed that the pair of longitudinal contra-rotating vortices starts developing at the inflection plane placed symmetrically. Towards the exit the helical vortex circulation becomes stronger but also slightly unsymmetrical.

Bansod & Bradshaw (1972) concluded that the shorter an S-bend intake duct is the more is the likelihood of avoiding boundary layer separation. The boundary layer at the outside ($\varphi = 0°$) of the duct is thinned caused by the centrifugal forces thus separation might not occur. Simultaneously the pair of contra-rotating vortices which they called "built-in vortex generators" could provide an appropriate mixing of the low momentum flow within the boundary layer with the high momentum fluid outside the boundary layer. They suggested to install real VGs towards the end of the first bend to support the naturally occurring vortices in order to prevent possible boundary layer separation between the first and the second bend.

Guo and Seddon (1982) investigated an S-shaped rectangular duct of 150mm×60mm (see Figure 2.3). Two bends with a radius of curvature of R = 228mm are joined with opposite centre line curvature. The tangential angle between the centre lines of the two ducts was 35°. Between the two bends and at the end of the second bend a straight duct of 100mm length was fixed. A cowl lip was mounted upstream of the first bend as an inlet part. The cowl lip had a NACA1-series profile. A free stream velocity of 40m/s entered the duct. Two mass flow rates were investigated, i.e. a high flow rate with an equivalent Reynolds number of $Re = 2.7\times10^5$, and a low flow rate with the corresponding Reynolds number of $Re = 2.1\times10^5$ based on the hydraulic diameter.

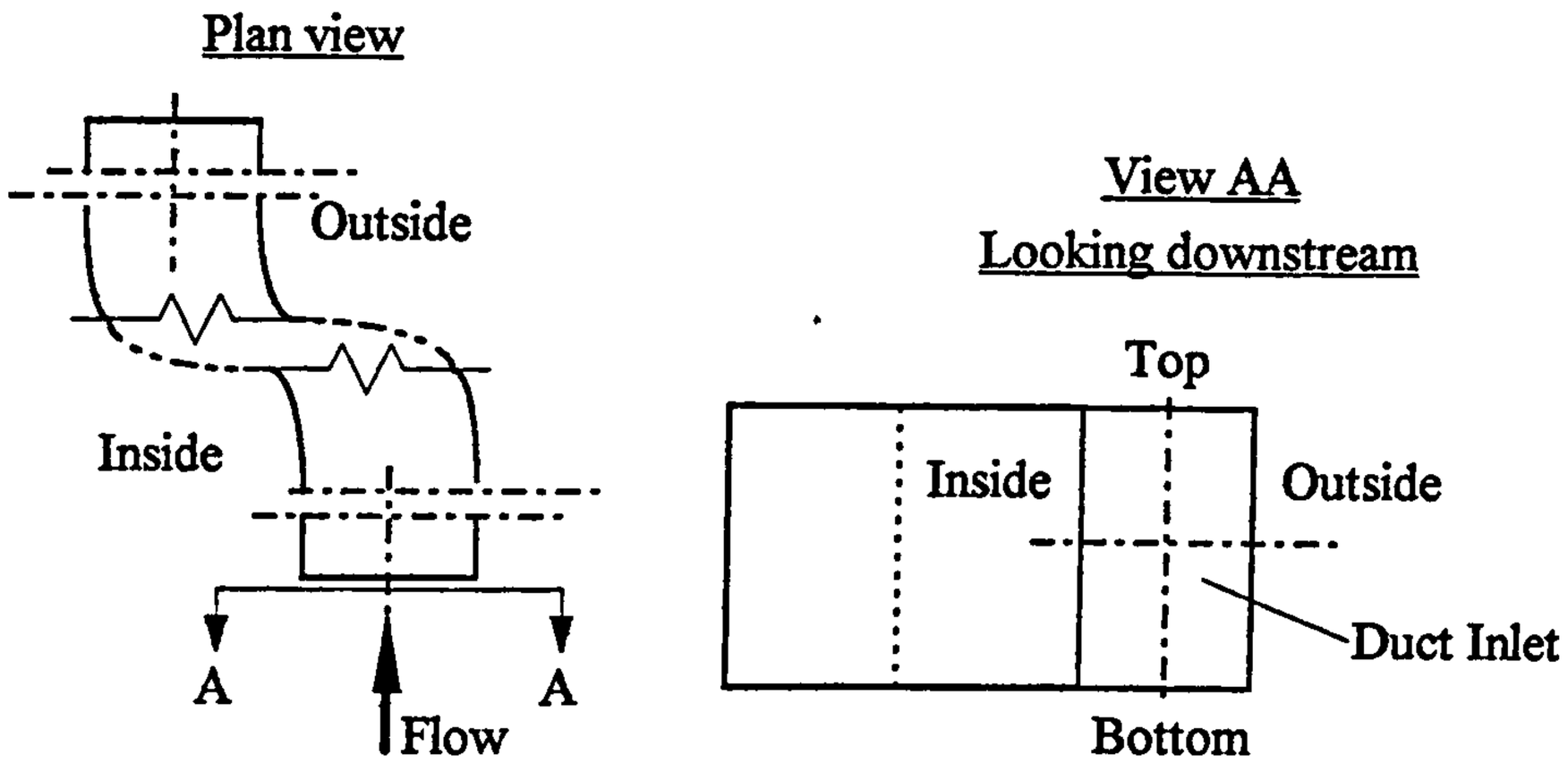

Figure 2.3: Definition of the four sides of the duct

They measured secondary motion after both the first and the second bends at 0° to 30° incidence and 0° to 10° yaw. Guo & Seddon (1982) described the secondary motion pattern as swirl. At 0° incidence after the first bend nearly all cross flow velocity vectors were directed towards the outside wall. Close to the outside of the duct the fluid was directed towards the bottom in the lower half and towards the top in the upper half of the duct. These phenomena could be understood as the beginning of the pair of contra-rotating vortices, typical for singly-curved bends. After the second bend the flow had changed completely to the opposite direction, i.e. from the outside to the inside towards the ducts offset. Even though the characteristic of the pair of contra-rotating vortices became more obvious it was still weak. They concluded that the thicker boundary layer in the second bend caused the more prominent secondary flow structure. With increasing incidence the cross velocity vector pattern after the first bend changed from symmetry between upper and lower half of the duct to a dominant vortex in the lower half of the duct. The dominant vortex, which Guo & Seddon defined as high swirl, had a clockwise rotation sense, looking downstream, with maximum velocity vectors close to the bottom wall towards the inside of the duct. After the second bend an S-like double vortex pattern was observed (see Figure 2.4).

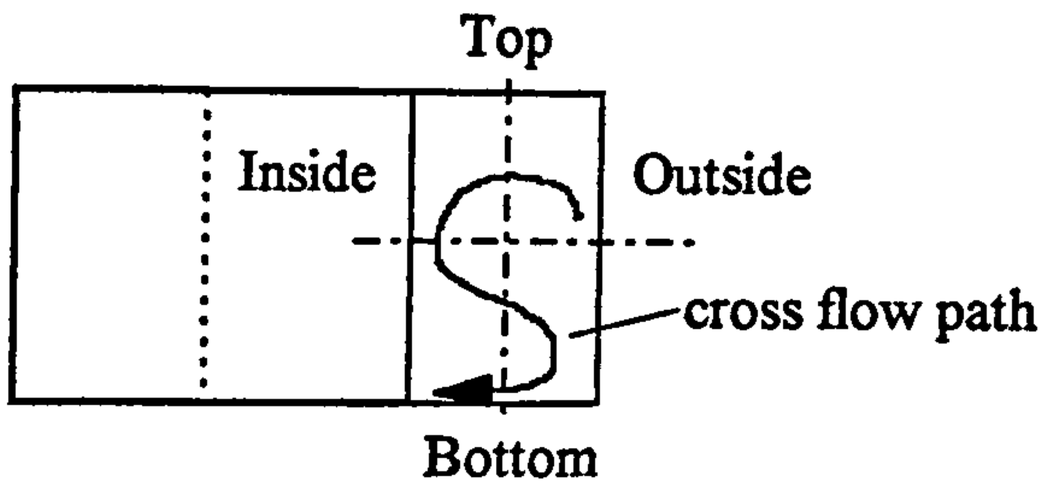

Figure 2.4: S-like double vortex pattern

That phenomenon might be described as follows. The flow in the upper half of the duct moved from the outside to the inside wall. Approaching the symmetry plane between the upper and lower half of the duct from the upper half, the fluid developed an anti-clockwise rotation sense towards the inner wall (looking downstream). Just below the symmetry plane the flow was driven by the anti-clockwise vortex towards the outer wall and changes the rotation sense at the outer wall back towards the inner wall. Flow separation occurred at 20° incidence and above along the bottom wall of the duct after the first bend.

The axial static pressure development along the inside and outside walls showed a similar sinusoidal distribution than that which Bansod & Bradshaw (1972) measured in their circular S-bend ducts. Guo & Seddon (1982) calibrated the static pressure coefficient c_p with the free stream static pressure. At high mass flow rate and 0° incidence, Guo & Seddon (1982) measured a negative streamwise pressure gradient of $\Delta c_p \cong -0.8$ along the outside wall. Along the inside wall the static pressure increased by approximately $\Delta c_p \cong 0.6$. These results are similar to those of Bansod & Bradshaw (1972) who determined experimentally $\Delta c_{p,outside} \cong -0.833$ and $\Delta c_{p,inside} \cong 0.634$. The static pressure distribution along the top and bottom wall are very similar and minor, and decreased by approximately $\Delta c_p \cong -0.1$. However, at high incidence the static pressure distribution along the top wall had a large negative difference of approximately $\Delta c_p \cong -1.4$. Along the bottom wall a large positive static pressure difference of circa $\Delta c_p \cong 1.1$ drove the fluid to separate. The axial static pressure

distributions did not change significantly on the outside and inside of the duct compared to the data at 0° incidence.

The average total pressure coefficient determined at the exit of the second bend, i.e. the level of distortion of total pressure, was strongly dependent on the angle of incidence. Associated with the S-like double vortex at 30° incidence, the average total pressure coefficient decreased by approximately 42% compared to the value at 0° incidence.

Measurements of turbulent fluctuating velocities (u, v, w) showed a strong dependence on the angle of incidence at the two axial locations, Station 1 and Station 2, i.e. after the first and second bend, respectively. As soon as separation appeared the level of turbulence increased rapidly close to the area of separation. At 0° incidence at Station 1 they determined a turbulence level of 4% close to the wall. In contrast, at 30° incidence, the turbulence level increased to 23.1% in the vicinity of separation at the wall. No significant difference in magnitude could be observed between the fluctuating velocity components.

Neither the change of mass flow rate nor a change of yaw angle to 10° influenced the results significantly in terms of secondary flow structure.

Guo and Seddon (1983) examined experimentally a diffusing S-bend intake duct with varying cross-section from rectangular to circular. The diffuser area ratio was 1.338 with an exit diameter of 150mm and a rectangular inlet of 127×100mm (see Figure 2.5).

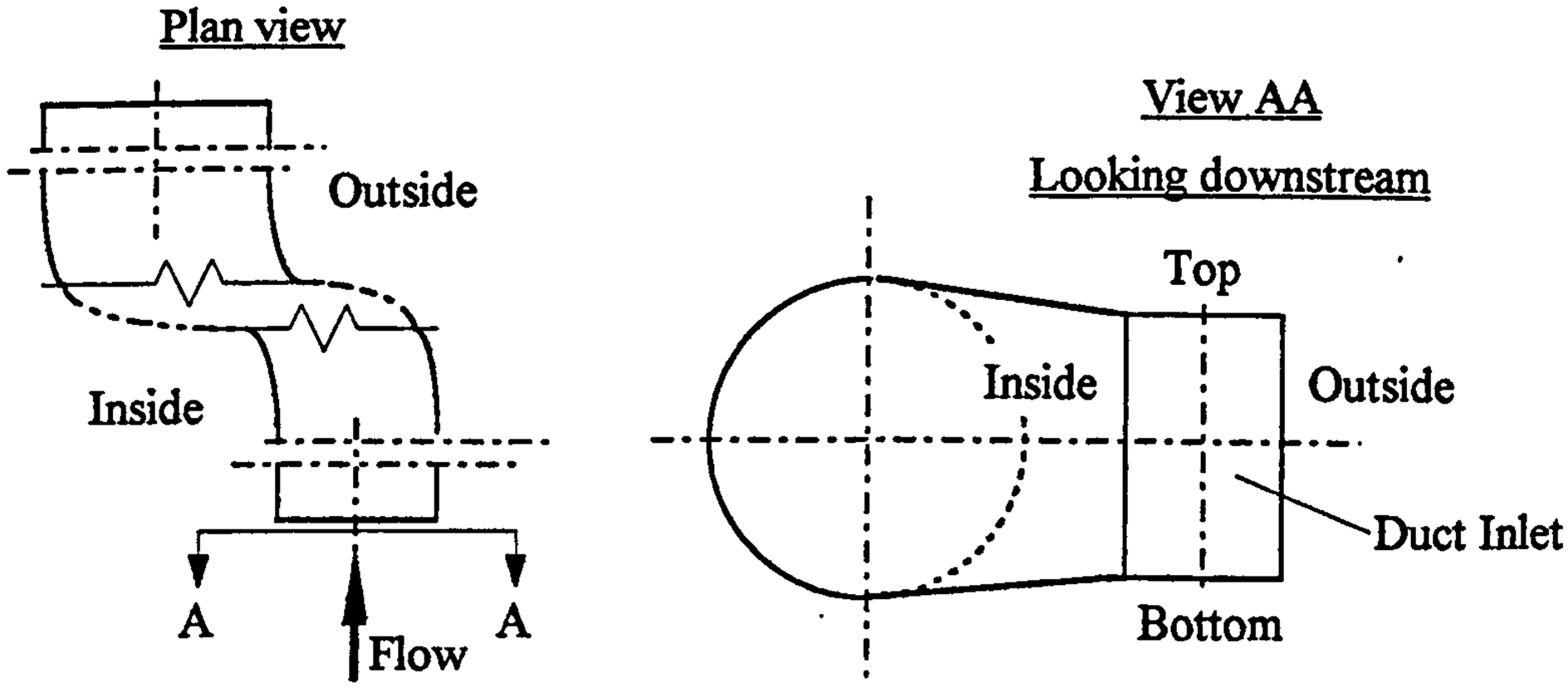

Figure 2.5: Definition of the four sides of the rectangular to circular duct

The diffuser offset was equal to 177.6mm and the main five components were an inlet lip, first bend, mid straight part, second bend and rear straight part. The total length of the diffuser from the throat to the exit was designed to be 663.4 mm. The experiments were examined at high mass flow rate condition (see Guo & Seddon, 1982). They measured cross flow velocities after both the first and the second bend, i.e. Station 1 and Station 2, at 10° to 30° incidence.

The axial static wall pressure distribution shows a sinusoidal distribution on the outside wall, as Bansod & Bradshaw (1972) and Guo & Seddon (1982) detected, but not along the inside wall. At 0° incidence the static pressure rises gradually by approximately $\Delta c_p \cong 1.1$ ($\Delta c_p \cong 0.6$, Guo & Seddon, 1982) along the inside wall. The positive pressure gradient starts from the first bend to the end of the second bend because of the streamwise increase of cross section area. The negative pressure difference along the outside wall was measured to be $\Delta c_p \cong -0.4$, in contrast to a $\Delta c_p \cong -0.8$ of the rectangular non-diffusing duct (see Guo & Seddon, 1982). The pressure along the inside in the second bend was, as expected, larger than the pressure along the outside in the second bend. The downstream change of pressure magnitudes is a result of change in centrifugal force direction, i.e. change of curvature from convex to concave along the inside wall. The downstream development of static pressure along the top and bottom walls is identical and increases gradually by approximately $\Delta c_p \cong 0.54$ compared to a decrease of $\Delta c_p \cong -0.1$ in the case of the rectangular S-bend (Guo & Seddon, 1982). However, at high incidence (30°) similar static pressure characteristics were observed as in the rectangular duct (Guo & Seddon, 1982). The pressure development along the top wall shows a large negative difference of $\Delta c_p \cong -1.17$ similar to $\Delta c_p \cong -1.4$ of the rectangular duct. Along the bottom wall a pressure difference of $\Delta c_p \cong 1.18$ with positive direction caused separation as in the case of the rectangular duct ($\Delta c_p \cong 1.1$). This pressure gradient starts approximately at the mid point of the first bend, i.e. between this location and just downstream of the lip an area of more or less constant pressure occurred. The stagnation of pressure indicates a region of flow separation. No significant difference in terms of axial static pressure distribution along the inside and outside walls with high incidence compared to 0° incidence could be observed coincident with the data for the rectangular duct.

The average total pressure coefficient c_{pav} was measured at the exit of the duct and was found to be highly dependent on the angle of incidence as it was observed for the rectangular duct. From approximately $c_{pav} = 0.87$ at 10° incidence the coefficient decreased rapidly to $c_{pav} = 0.37$ at 30° incidence, i.e. in total by about 58% compared to 42% in the rectangular case (i.e. from $c_{pav} = 0.84$ to $c_{pav} = 0.5$). The huge area of flow separation at Station 1 at 30° incidence, which occupied 25% of the whole cross section area, was the main cause for the drop in total pressure. If the offset was reduced by approximately 16% no significant effect on mean total pressure was observed

Secondary motion was measured at Station 1 and 2 at low and high incidence. At 0° the same flow pattern as in the rectangular duct was measured, i.e. a weak pair of contra-rotating vortices at Station 1 and Station 2, but with opposite direction. With increasing angle of incidence the symmetrical pair of vortices disappeared and one single strong vortex developed. At Station 1 a separation bubble occurred at the inside of the duct which drove the flow around the bubble and a strong clockwise (looking downstream) rotating vortex was generated. The separation originated at the inside of the bottom lip and migrated quickly towards the inside of the first bend. This phenomenon was also observed for the rectangular duct. The flow behaves completely differently downstream after the first bend compared to the rectangular duct. The residue of the separated flow kept the clockwise rotation sense and developed downstream a single strong vortex, rotating fairly concentrically at the exit plane. In the case of the rectangular duct an S-like vortex was observed. Guo & Seddon (1983) concluded in general that the production of secondary motion, which they called "swirl" in an S-bend intake duct depends on an interplay of five factors. 1) the pressure gradient associated with bends, 2) the pressure gradients caused by an angle of incidence, 3) inertia of the flow, 4) influence of flow separation, 5) geometry of the duct cross-sections.

Taylor et al. (1984) investigated a circular S-bend duct with constant diameter of 48mm. Two 22.5° bends with a mean radius of curvature of R = 336mm were mounted together. This water tunnel experiment was examined at a Reynolds number of 790 as a laminar case, and at Re = 48,000 as turbulent flow. The bulk velocities

were 16.4m/s (turbulent) and 1.00m/s (laminar). Upstream and downstream of the S-bend a front and a rear straight pipe was fixed. The front pipe had a length of 0.21m and the rear pipe a length of 1.82m. The boundary layer at the inlet of the first bend varied between 10% and 20% of the diameter for turbulent flow and was measured to be 25% of the duct diameter in the laminar case.

In turbulent flow the axial wall static pressure distribution shows the familiar sinusoidal distribution along the inside ($\varphi = 0°$, see Figure 2.1) and the outside ($\varphi = 180°$) wall. The pressure coefficient was calibrated with the reference pressure at the inlet of the S-bend. The negative pressure difference along the outside wall was approximately $\Delta c_p \cong -0.4$ and the positive difference $\Delta c_p \cong 0.2$ along the inside wall. Bansod & Bradshaw (1972) determined experimentally $\Delta c_{p,outside} \cong -0.833$ and $\Delta c_{p,inside} \cong 0.634$.

Taylor et al. (1984) measured a maximum of pressure driven secondary flow of $0.12U_b$ (U_b = bulk velocity) in the first half of the S-bend in turbulent flow. Along the second bend the already established secondary flow decreased near the pipe wall and reversed in the core flow region. No flow separation was observed. In laminar flow, the magnitude of secondary flow was observed to be more significant in the thicker boundary layer.

Vakili et al. (1987) examined a circular S-bend diffuser with a ratio of exit to inlet area of $A_e/A_i = 1.51$. The inlet diameter was $D_i = 165.1$mm whereas the exit diameter was measured to be $D_e = 203.2$mm. The mean radius of the two 30° bends was R = 825.5mm. A straight front pipe of constant diameter D_i was fixed upstream of the bend with a length of $4.75D_i$. The S-bend was extended with a straight pipe of diameter D_e and a length of $9D_e$ to minimise the occurrence of end effects. Turbulent flow entered the duct with a free stream Mach number of 0.6, with the boundary layer measured to be 10% of the duct inlet diameter at the entrance of the first bend.

Surface oil patterns were used to locate the regions of possible flow separation. The separation started at $\theta_l \cong 22°$ (see Figure 2.1) and extended to an angle of $\theta_l \cong 44°$. The static pressure distribution in the axial direction supports the findings of flow separation. Between $x/D_i \cong 1.64$ and $x/D_i \cong 3.0$ the pressure along the inside wall ($\varphi = 170°$) and at $\varphi = 90°$ did not change significantly. As expected, the static pressure

described the typical sinusoidal distribution along the outside ($\varphi = 10°$) as seen in all the other references mentioned before, with an initial continuous rise up to the second bend. The change in static pressure along the outside wall was measured to be $\Delta c_{p,outside} \cong -0.23$. No sign of separation could be observed because the centrifugal forces were thinning the boundary layer enough to withstand the adverse pressure gradient towards the second bend. At the other two locations the changes of the continuously increasing static pressure, except in the area of separation, were detected to be $\Delta c_p \cong 0.46$ at $\varphi = 90°$ and $\Delta c_{p,inside} \cong 0.68$ at $\varphi = 170°$. For comparison, Bansod & Bradshaw (1972) determined experimentally $\Delta c_{p,outside} \cong -0.833$ and $\Delta c_{p,inside} \cong 0.634$. Taylor et al. (1984) measured in their water tunnel experiment $\Delta c_{p,outside} \cong -0.4$ and $\Delta c_{p,inside} \cong 0.2$. The pressure changes along the insides were very similar to those of Bansod & Bradshaw (1972). However, the changes in static pressure along the outside wall were different. The reason is that the pressure increased initially more in the case of Vakili et al., caused by the larger mean radius of curvature, of R = 825.5mm of the 30° bend compared to 337.5mm ("short intake") and 525mm ("Tristar intake") in Bansod & Bradshaw (1972).

Total pressure contours were determined at six axial locations. Up to the mid point of the first bend the flow seems to be axissymmetric. Further downstream at $\theta_l = 30°$ (see Figure 2.1) the development of secondary motion and the flow separation on the inside of the duct becomes obvious in form of an overall thicker boundary layer. It was shown that the potential core moved to the outside of the duct due to the effect of streamline curvature. At $\theta_l = 45°$ and $\theta_l = 60°$ the area of low total pressure flow was increasing rapidly and covered more than the lower half of the exit plane.

Vector plots of transverse velocities showed the typical pair of contra-rotating but weakly developed vortices over an axial distance of $0° \leq \theta_l \leq 15°$ (see Figure 2.1). At the inflection plane ($\theta_l = 30°$) the separation bubble on the inside of the duct became distinct, displacing the flow towards the outside. Further downstream behind the separation bubble at $\theta_l = 45°$ and at $\theta_l = 60°$ the pair of contra-rotating vortices was re-established and approximately twice as strong as the one before the separation bubble.

Wellborn et al. (1992) examined a circular diffusing S-bend with a ratio of exit cross section area to inlet area of $A_e/A_i = 1.52$, very similar to Vakili et al. (1987). The two 30° bends were joined with mean radii of R = 1021mm. Upstream and downstream of the S-bend duct straight pipes of 762mm length with the appropriate diameter were installed. The duct inlet diameter is D_i = 204.2mm and the exit diameter is D_e = 251.4mm. The inlet centre line Mach number of 0.6 was determined at a location of $0.5D_i$ upstream of the S-bend entrance. They determined a Reynolds number of 2.6×10^6, based on the centreline velocity and the inlet diameter D_i.

Streaklines of fluorescent oil on the duct surface were used to visualise the flow characteristics. Firstly they concluded that the flow was symmetric, i.e. the flow in one half of the duct between $\varphi = 0°$ and $\varphi = 180°$ is equal to the other half between $\varphi = 180°$ and $\varphi = 360°$. Secondly they observed the two typical spiral nodes, caused through separation of the three dimensional boundary layer. The symmetry line of the spiral nodes is coincident with the symmetry line of the duct at $\varphi = 180°$. The flow started separating at the upstream saddle point at $x/D_i \cong 2.02$ and reattached to the surface at the downstream saddle point at $x/D_i \cong 4.13$. Thirdly secondary motion in the form of boundary cross flow was observed. In the first bend the streaklines were driven towards the inside of the duct ($\varphi = 180°$) caused by the transverse pressure gradient developed through curvature. In the second bend at a circumferential angle position of $\varphi = 90°$ the streaklines diverged, i.e. the upper streaklines converged towards the outside of the duct ($\varphi = 0°$) while the lower lines converged towards the inside of the duct ($\varphi = 180°$).

Four planes of transverse velocity vectors supported the existence of secondary motion. At the first plane at $x/D_i = 0.96$ the magnitude of secondary motion was very low. The second plane was at $x/D_i = 2.97$ and was located within the region of separation. The transverse velocity plot indicated the boundary of the separation bubble which deflected the vectors towards the centre line. At a location of $x/D_i = 4.01$ the core flow returned to the streamwise direction while re-establishing the pair of contra-rotating vortices. At the exit of the duct ($x/D_i = 5.73$) the pair of contra-rotating vortices is strongly developed and convected low momentum fluid of the boundary layer towards the centre of the duct. As a result the core flow is shifted to the upper half of the duct.

The total pressure planes were at the same downstream locations as the transverse velocity vector plots. They reflected the flow situation described above using the transverse velocity plots. At the first plane ($x/D_i = 0.96$) the boundary layer varied only slightly in thickness with circumferential position. The thickness was greatest at the outside ($\varphi = 0°$) and least at the inside ($\varphi = 180°$). The difference was caused by the streamwise pressure gradient which decelerates the fluid at the outside and accelerated the fluid along the inside. The second ($x/D_i = 2.97$), third ($x/D_i = 4.01$) and exit plane ($x/D_i = 5.73$) showed a region of low total pressure which increased to a maximum at the exit plane. The region of low total pressure or low streamwise velocity was caused by reversed flow and convection of low momentum fluid from the boundary layer towards the centre of the duct.

The axial surface static pressure distribution showed the same characteristics as Vakili et al (1987) described. Along the outside ($\varphi = 10°$) the typical sinusoidal pressure distribution occurred with a value of $\Delta c_{p,outside} \cong -0.21$, whereas a continuous increase of pressure, disturbed by the separation bubble, appeared along the inside ($\varphi = 170°$) and at a circumferential position of $\varphi = 90°$. The pressure rose along the inside, was held at the saddle point of separation, kept constant in the first half of the separation area (between $x/D_i \cong 2.02$ and $x/D_i \cong 3.10$) and started rising again close to the saddle point of reattachment. Along the inside the pressure rose by approximately $\Delta c_{p,inside} \cong 0.71$ and at $\varphi = 90°$ by $\Delta c_p \cong 0.45$. For comparison Vakili et al. (1987) measured a change of static pressure of $\Delta c_{p,outside} \cong -0.23$, $\Delta c_{p,inside} \cong 0.68$ and at $\varphi = 90°$ of $\Delta c_p \cong 0.46$.

The circumferential static pressure distribution ($10° \leq \varphi \leq 170°$) was experimentally determined at four planes, i.e. Station 1 at $x/D_i \cong -0.5$, Station 2 at $x/D_i \cong 0.96$, Station 3 at $x/D_i \cong 2.97$ and Station 4 at $x/D_i \cong 4.01$. The data at the first plane could be taken as a reference plane thus $c_p = 0.0$. At Station 2 and 3 the pressure coefficient did not change significantly between $10° \leq \varphi \leq 30°$ and between $150° \leq \varphi \leq 170°$. At Station 2 from $\varphi = 30°$ to $150°$ the coefficient of static pressure decreased approximately linearly by $\Delta c_p \cong -0.3$. In contrast, at Station 3 which is located at the beginning of the second bend the pressure rose between $30° \leq \varphi \leq 100°$ linearly by $\Delta c_p \cong 0.1$. At Station 4 the distribution of circumferential pressure increased

approximately linearly between $10° \leq \varphi \leq 120°$ by $\Delta c_p \cong 0.18$. At Station 3 and 4 the static pressure experienced a very slight drop towards the circumferential position of $\varphi = 170°$. Wellborn et al. (1992) suggested this drop indicated the extent of the separation bubble in the circumferential direction.

Whitelaw and Yu (1993) examined a scaled down version of the circular S-shaped diffusing duct RAE2129. The ratio of exit to inlet area is $A_e/A_i = 1.4$, where the inlet diameter was equal to $D_i = 48$mm and the exit diameter $D_e = 56.8$mm. The offset between the centre lines of the two bends was equal to 51.1mm and the total length was measured to be 170.4mm. The inlet bulk velocity was $U_b = 1.37$ m/s and the Reynolds number based on the inlet diameter was equal to 40,000. They investigated the flow structure with two different inflow conditions. The first condition consisted of a fully developed pipe flow ($\delta_0 = 0.5D_i$), whereas the second condition described an entry flow with $\delta_0 = 0.2D_i$.

The axial static pressure distribution exhibited sinusoidal development along the outside ($\varphi = 0°$) and continuously increase along the inside ($\varphi = 180°$) as measured by Vakili et al. (1987) ($\Delta c_{p,outside} \cong -0.23$, $\Delta c_{p,inside} \cong 0.68$) and Wellborn et al. (1992) ($\Delta c_{p,outside} \cong -0.21$, $\Delta c_{p,inside} \cong 0.71$). The change in static pressure was measured to be $\Delta c_{p,outside} \cong -0.22$ for the case of fully developed pipe flow and $\Delta c_{p,outside} \cong -0.27$ for the case of $\delta_0 = 0.2D_i$. Along the inside ($\varphi = 180°$) wall of the duct the static pressure increased monotonically with $\Delta c_{p,inside} \cong 0.71$ for $\delta_0 = 0.5D_i$, and $\Delta c_{p,inside} \cong 0.66$ for entry flow conditions ($\delta_0 = 0.2D_i$). It was shown that no significant difference in terms of static pressure distribution could be measured between the two different inlet conditions. Whitelaw & Yu (1993) suggested that the insensitivity of their measuring equipment was responsible for the lack of difference. They expected a difference in static pressure distribution because they detected a larger region of separation in the case of the thinner inlet boundary layer.

From measurements of the streamwise mean velocity they concluded that the maximum negative streamwise velocity did not exceed $-0.02U_b$ and thus the separation bubble was about to occur. The saddle point of separation was measured to be along the inside wall ($\varphi = 180°$) of the first bend, just upstream of the inflection plane. The saddle point of reattachment was detected to be close to the exit of the S-

bend. At inlet condition $\delta_0 = 0.2D_i$ the separation bubble length was approximately half of the duct length and the thickness reached a maximum of $0.15D_i$. In the case of the fully developed pipe flow the region of separation was approximately one third of the duct length with a maximum thickness of $0.1D_i$. Whitelaw & Yu (1993) argued that the larger region of incipient separation in the case of the thinner boundary layer ($\delta_0 = 0.2D_i$) was responsible for the large pair of contra-rotating vortices at the exit. The pair of vortices occupied almost the lower half of the duct with a maximum secondary velocity of $0.2U_b$. In the case of the thicker inlet boundary layer ($\delta_0 = 0.5D_i$) only a third of the lower half of the duct was occupied by the pair of contra-rotating vortices. The maximum secondary velocity in this case was measured to be $0.15U_b$. The typical distortion of the exit face caused by the pair of contra-rotating vortices could be observed, i.e. the boundary layer was thickened along the inside of the duct by pushing the core up towards the outside of the duct. The shear stress also reached a maximum of $\overline{uv}/U_b^2 \cong -0.008$ at the exit plane at inlet condition $\delta_0 = 0.2D_i$.

2.2.2 Numerical Studies

Eisemann et al. (1978) developed a method for computing compressible three-dimensional turbulent subsonic flow in curved ducts, e.g. circular S-bend with constant diameter. The flow was calculated at a Reynolds number of 1×10^5 based on the duct diamter and an inlet Mach number of 0.1.

Their main aim was to approximate the governing equations for viscous flow into a formulation which can be solved by a forward marching integration procedure in the direction of the primary flow. The turbulent flow model was based on the eddy-viscosity concept where the eddy-viscosity distribution was described using Prandtl's mixing-length hypothesis. The pressure development was approximated by a quasi-two-dimensional inviscid formulation.

The predictions were successful in terms of describing the typical pair of counter-rotating vortices in the first bend. However, the method predicted separation near the end of the first bend which does not happen in a duct with constant diameter. They

suggested that the quasi-two-dimensional inviscid pressure model was not capable of determining the highly three-dimensional flow in that region.

Kunik (1986) developed a computer analysis, called PEPSIG, to compute compressible three-dimensional subsonic viscous flow through curved ducts by a spatial marching procedure. He applied his numerical method to the S-bend diffuser geometry investigated experimentally by Vakili et al. (1985, 1987). He approximated the Navier-Stokes equations with the assumption that the flow was primarily in the direction of the centre line with transverse secondary flow and employed an algebraic mixing length turbulence model.

Compared with the experimental results from Vakili et al. (1985) with identical inlet conditions the numerical approach predicted quantitatively (and correctly) the flow structure in the duct. However, the region of separation was predicted further downstream than the measured location. Kunik suggested that the "flare" approximation caused the different downstream location. This approximation was used to allow the numerical approach to march through the separation area. Together with the prediction of a slightly lower magnitude of total pressure, the prediction of transverse velocities also showed a weaker pair of contra-rotating vortices at the duct exit.

In *AGARD-AR-270 (1991)* three different numerical approaches were used to predict the flow in the circular S-bend diffuser RAE2129. The duct had a ratio of exit cross-section area to inlet cross-section area of $A_e/A_i = 1.4$. The exit diameter was $D_e = 152.4$mm and the inlet diameter was $D_i = 128.8$mm. Two inlet conditions were tested: In Case 1 (high mass flow) the Mach number to the S-bend was equal to 0.794 and the Reynolds number equal to 1.848×10^6, based on the inlet diameter D_i. In Case 2 (low mass flow) the Mach number was equal to 0.412 and the Reynolds number equal to 1.158×10^6.

The first code RANSAC was a three-dimensional, cell centred Finite Volume approach with implicit pressure correction for the Reynolds averaged Navier-Stokes equations (RANS). Turbulence was modelled using the standard k-ε model with a wall function near the solid surface. The second code, FLU3M, was an Euler

approach with a flow solver based on the explicit central difference scheme proposed by Jameson. The third code IKARUS, solved the three-dimensional Navier-Stokes equations by using an explicit Finite Volume method with the Runge-Kutta-type time integration. This method used the thin-layer approximation and the Baldwin-Lomax turbulence model.

A comparison between experiment and numerical compressible prediction was very difficult for Case 1, because the flow from the intake lip along a constant diameter part into the S-bend was influenced by shock waves. Thus the flow changed between supersonic and subsonic conditions along the duct.

However the RANSAC code modelled only the S-bend without the intake lip. As a result the shock on the cowl was missed thus the inlet flow conditions, i.e. the static wall pressures, into the S-bend were different from the real situation.

The flow in the whole duct device, i.e. including the inlet cowl lip, was predicted by the two codes FLU3M and IKARUS.

The Euler code predicted the static wall pressure drop downstream of the shock on the cowl lip to be less than that measured in experiments. That was qualitatively correct because the inviscid Euler solution did not predict any separation as a result of the shock on the cowl lip. The code IKARUS predicted the static wall pressure distribution on the cowl in perfect agreement with the experiment. However, no shocks were predicted and so the flow remained supersonic in the constant area duct upstream of the S-bend. The region of separation was much smaller than in the experiment and the total pressure loss at the engine face was underestimated.

In Case 2 (low mass flow) the flow situation was simpler because the flow was completely subsonic.

As in Case 1 the Euler code, FLU3M, predicted higher static pressure along the duct because of the missing displacement effects of the boundary layer and the neglect of the separation bubble. The Navier-Stokes code IKARUS underpredicted the static pressure minimum on the intake lip and along into the S-bend up to a location of $x/D_i \cong 1.5$. Thus the boundary layer thickness was predicted to be larger than that of the experimental data. But at the engine face, agreement between the experimental and predicted viscous flow thickness was achieved. In the S-bend RANSAC predicted the static pressure distribution closely compared with experimental data.

The conclusion of the AGARD team was that flow with strong secondary motions was sensitive to the onset flow. Thus it seemed to be important that the boundary conditions were defined from available experimental data.

Smith et al. (1992) predicted the flow inside a circular S-bend diffuser, which had the geometry and inlet conditions as in the experiment from Vakili et al. (1987). Their computer program PARC3D solved the full three-dimensional RANS equations in strong conservative form by using the Beam and Warming approximate factorisation algorithm. The algebraic stress model from Baldwin and Lomax was used to model the turbulent flow.

The numerical solution predicted the saddle point of separation approximately $0.5D_i$ downstream of the experimentally determined location.

Comparing the experimental data with the numerical total pressure contours there was good agreement up to the mid point of the second bend. Further downstream the secondary flow developed much more rapidly in the experimental case than that of the predictions. At the exit of the duct the numerical approach predicted a region of inviscid core flow which was approximately twice as large as the experiment showed.

Smith et al. (1992) suggested that the boundary layer flow was not appropriately solved thus the pair of contra-rotating vortices had less strength than those of the experiments. They believed that higher grid solution in the cross-flow direction could improve the results and/or a more appropriate turbulence model, like the two equation k-ε turbulence model with a low Reynolds number model near the wall.

Smith et al. (1992) concluded that in PNS (Parabolized Navier-Stokes) solvers the inflow boundary conditions have to be very accurate for the particular flow situation, i.e. they should be provided either by a Full Navier Stokes solver or experimental data.

Anderson et al. (1993) investigated numerically the circular S-bend diffuser M2129 with the same geometry as the RAE2129 examined by the AGARD-AR-270 (1991). A straight pipe with the duct inlet diameter and a length of one diameter was fixed upstream of the S-bend inlet. They compared the results of a three-dimensional implicit Full Navier-Stokes (FNS) code with the solutions of a three-dimensional Reduced Navier Stokes (RNS) analysis. Both predictions were compared with

experimental data supplied by the AGARD-AR-270 (1991). Three different inlet conditions were investigated with the boundary layer thickness one diameter upstream of the first bend corresponding to $0.12D_i$. The first two throat conditions were identical to Case 1 and Case 2 described in AGARD-AR-270 (1991). Case 3 was defined with a inlet Mach number of 0.2 and the corresponding Reynolds of 0.594×10^6 based on the duct inlet diameter.

The RNS code, RNS3D, solved viscous subsonic flows by a spatial marching integration procedure using the velocity-decomposition approach of Briley & McDonald (1984). The eddy-viscosity formulation was used as the turbulence model. The "flare" approximation (see Kunik, 1986) was employed to compute the flow through the region of flow separation.

The FNS analysis, PARC3D (see also Smith et al., 1992), solved the Reynolds averaged Navier-Stokes equations (RANS) in strong conservation form. Turbulence was modelled by using the algebraic eddy viscosity model from the Baldwin-Lomax model which Anderson et al. (1993) improved for the region of reversed flow. In this region the inner fluid layer was replaced with the outer layer model up to the solid surface. Outside the separation bubble the conventional Baldwin-Lomax model was used.

Both numerical analyses predicted pressure recovery distributions which coincided with experimental data, i.e. decreasing pressure recovery with increasing inlet Mach numbers. In terms of flow distortion at the engine face only RNS3D reflected the experimental results correctly whereas PARC3D overpredicted the magnitude of distortion.

Flow separation, i.e. the region where the pair of contra-rotating vortices lifted off the solid surface, was predicted by both codes consistently but much further downstream and less strong than experimental data showed. Both numerical approaches indicated also separation from $M = 0.2$ whereas experimental oil flow visualisation showed that the vortex lift off appeared from a Mach number of 0.3. Anderson et al. (1993) suggested that the mixing length turbulence model was unable to predict the correct location.

The most significant difference between the FNS and RNS solutions appeared in the axial skin friction distribution along the inside of the duct at Case 1 ($M = 0.794$) and

Case 2 (M = 0.412) upstream of the region of separation, i.e. in the first bend of the duct. RNS3D predicted much higher values of skin friction than PARC3D. No experimental data was available for comparison. In all three cases an almost constant distribution of minimum skin friction occurred in the region of separation. Anderson et al. (1993) concluded that the significant difference in skin friction prediction was caused by the turbulence models. On one hand the low skin friction flow with an adverse pressure gradient was not modelled accurately, and on the other hand the flow behaviour near the wall, analysed as vortex lift off, was not described in an appropriate way.

May (1997) applied the SAUNA CFD system to the geometry of the M2129 S-bend intake diffuser which had the same measurements as the RAE2129 investigated by AGARD-AR-270 (1991). The purpose was to test eight different turbulence models against experimental data:

- the zero equation Baldwin-Lomax (BL) model
- the two equation standard k-ε model
- the RNG k-ε model } plus standard wall functions
- the non-linear (cubic) k-ε model (NL k-ε model)
- the two equation standard k-ω model
- the k-ω model with shear stress transport modification (SST k-ω model)
- the non-linear k-ω model (NL k-ω model)
- the non-linear k-ω model with shear stress transport modification (NL SST k-ω model)

Two different mass flow rates were used, i.e. high mass flow rate (mfr1) and low mass flow rate (mfr2). In both cases the free stream Mach number was equal to 0.21 and the corresponding Reynolds number, based on the maximum diameter, was equal to 8.6×10^5.

At high mass flow rate condition (mfr1), downstream just after the first bend along the inside of the duct, the NL SST k-ω turbulence model provided the closest prediction in terms of reversed flow compared to the experimental data. This turbulence model included the effects of streamwise curvature. In the following

sequence the turbulence models predicted less separation: NL k-ω > k-ω > BL > k-ε. The k-ε model did not predict any region of separation.

Comparing the total pressure distributions at the engine face the BL model predicted the closest results to the experimental data. The k-ε model underpredicted and the k-ω models overpredicted the pair of contra-rotating vortices. Thus the location of the separation bubble was predicted too far downstream compared to the experimental data.

In terms of the low mass flow (mfr2) all turbulent models failed to predict any secondary flow, even though an area of constant axial static pressure was predicted, which is usually evidence of separation. All models overpredicted the total pressure recovery map compared to the experimental data, i.e. the secondary flow effects were underpredicted. As a result May (1997) suggested to introduce second moment closures especially in the case of low mass flow rate.

May (1997) concluded for the case of the high mass flow rate that the main reason for the failure of predicting the secondary flow of the k-ε turbulence models are the employed wall functions. He suggested to use instead of the wall functions an integration through the viscous sublayer in order to capture the effect of the vortex lift off. The k-ω turbulence models which integrated through the viscous sublayer showed an appropriate amount of secondary flow.

In general, all numerical approaches failed to reasonably predict the measured magnitude and streamwise location of the region of flow separation.

2.3 Vane Vortex Generators (VVGs)

2.3.1 Experimental Studies

VVGs were introduced to control the behaviour of the boundary layer in diffusers by *Taylor (1948)*. Further investigation into the application of VVGs was performed by *Pearcey (1961)*. His work covered boundary layer control for aerofoils and wings to prevent shock-induced separation. The influence of wing geometry was studied experimentally. For the first time different shapes and arrangements of VVGs were investigated. *Brown et al. (1968)* achieved uniformity of flow properties in a subsonic inlet intake duct diffuser with small, low-aspect-ratio wings (see Figure 2.6), designed for a Lockheed aircraft. The geometry of the intake duct diffuser was characterised by a rectangular inlet with a smooth transition to a semicircular cross-plane at the engine face (see Figure 2.7). Brown et al. (1968) tested several VG configurations, e.g. VGs on the ramp surface and on the cowl surface and a second row downstream of the first. The first VGs were located at approximately 1/3 of the total length (l_x in Figure 2.7) of the duct. The free stream conditions were adjusted to a Mach number of 2.65.

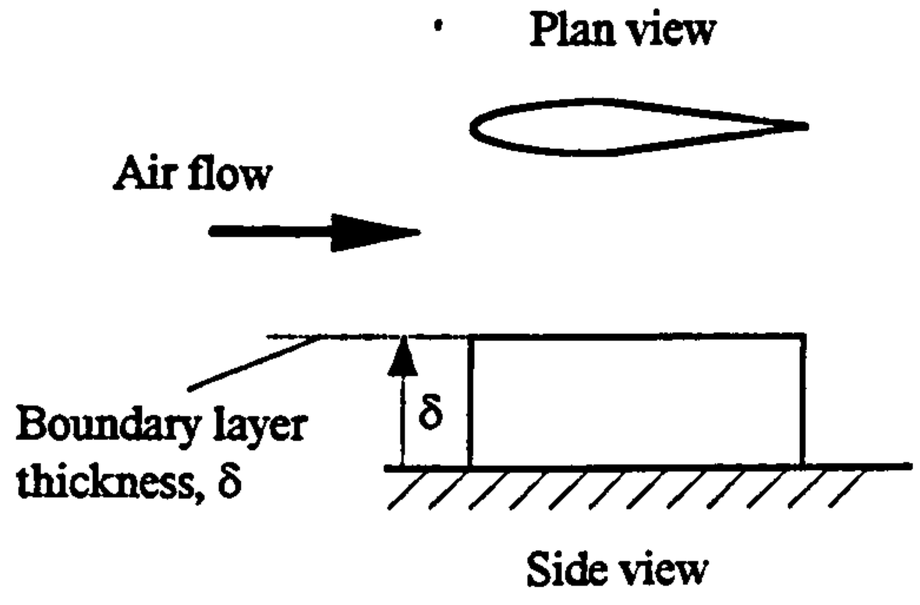

Figure 2.6: Wing VG geometry

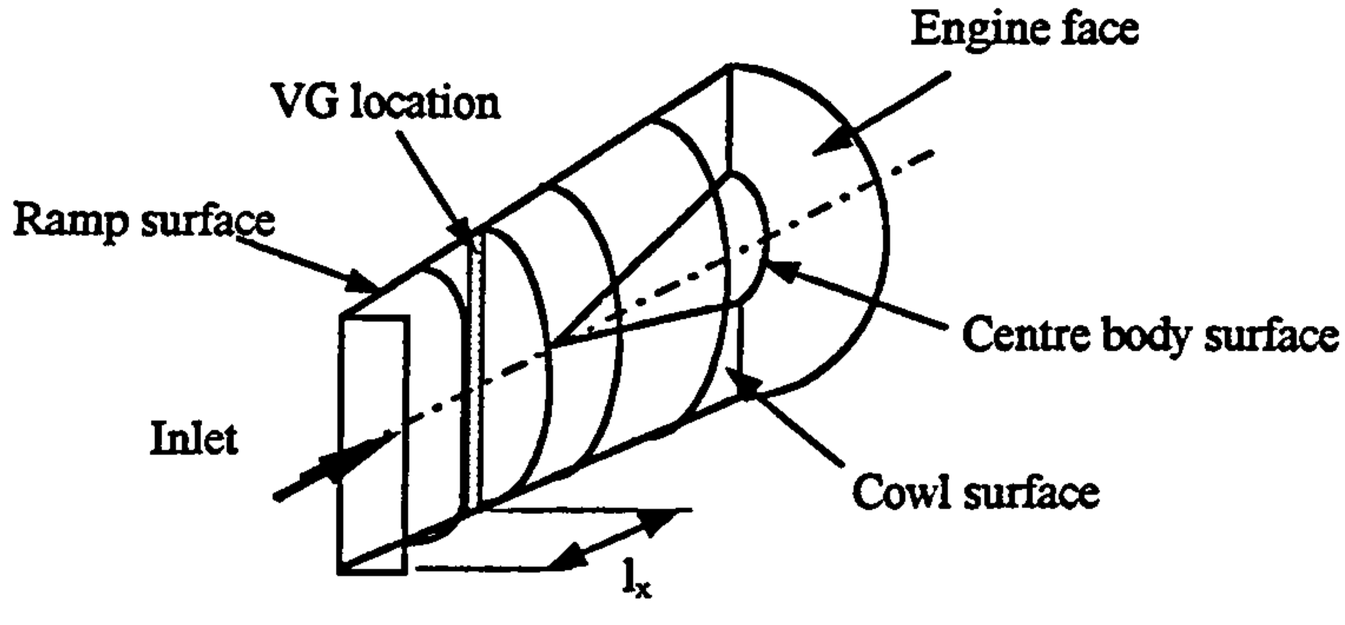

Figure 2.7: Sketch of half of the intake duct geometry

The region with the main adverse pressure gradient occurred on the centre body of the diffuser. He concluded that high pressure recovery and flow uniformity at the engine face was achieved, even though, for practical reasons, the diffuser had to be shortened. He also concluded that the design and arrangement of VGs were entirely responsible for successful boundary layer control. However, inappropriate design of the VG arrays resulted in significant losses in the diffuser performance.

More recent air intake duct investigations are reported in AGARD-AR-270 (1991) where several intake ducts geometries for high speed vehicles were tested. Their suggestion agreed with previous findings from Brown et al. (1968) that VVGs may be usefully employed to control boundary layer separation. *Gibb and Anderson (1995)* designed a model of the RAE2129 S-bend intake duct, which was one of the ducts considered in the AGARD-AR-270 (1991) (see Section 2.2.2). They fitted the model duct M2129 with rectangular VVGs at a location as shown in Figure 1.1. The degree of flow distortion on the engine face and the total pressure recovery were used to judge performance. Tests with different skew angles were carried out for a Mach number range from 0.2 to 0.8. Gibb & Anderson (1995) concluded that VVGs provided excellent improvements in reducing the engine face distortion and increasing total pressure recovery. A significant reduction of unsteadiness in loading of the engine was therefore achieved, providing less vibration, and a wider stable flow range and a larger flight envelope.

Wendt and Reichert (1996) investigated non-uniform conditions at the inlet caused by the ingestion of trailing vortices. The duct geometry is identical to the experimental set up of Wellborn et al. (1992) (see Section 2.2.1). A strong connection is believed

to exist between the location of the ingested vortex entry to the S-bend inlet duct and the development of the flow field at the engine face. They ingested longitudinal vortices at three different cross-stream locations (see Figure 2.8). The vortices were generated using a pinwheel.

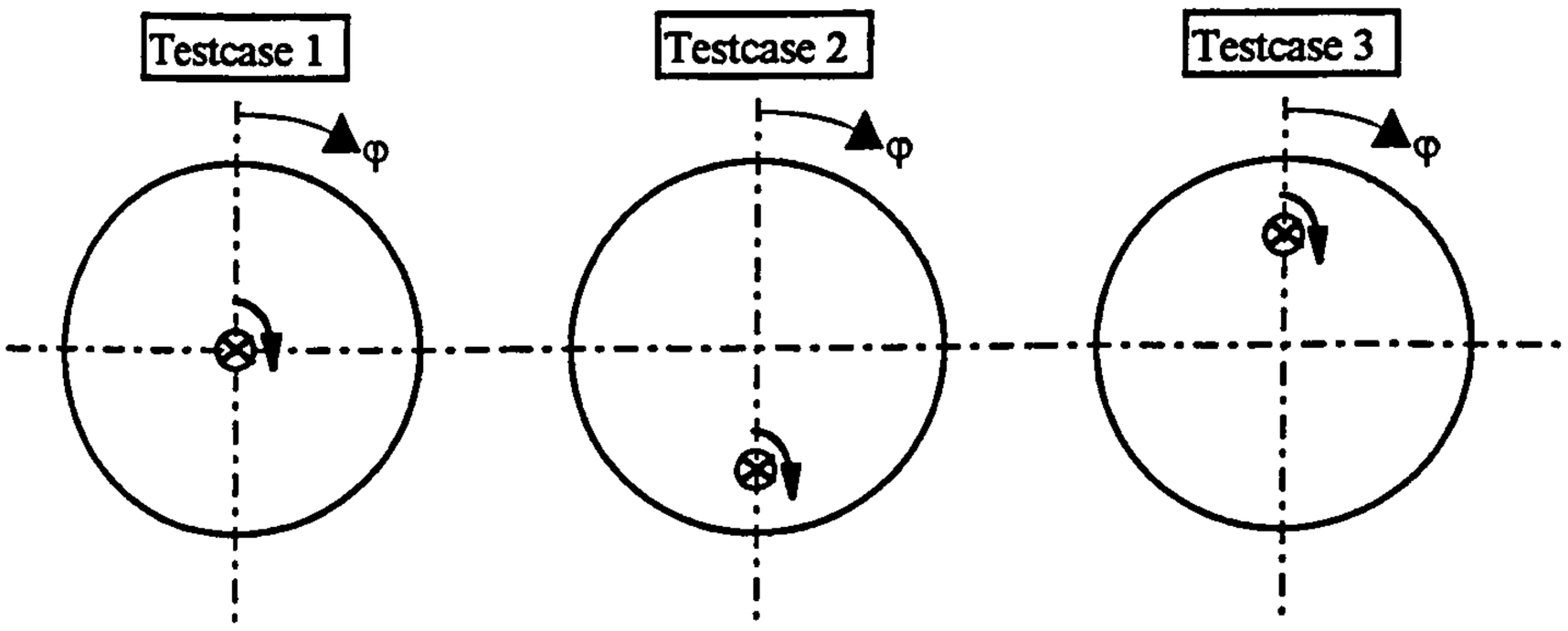

Figure 2.8: Positions of the ingested vortex at the entrance face of the duct looking downstream

In the first case the centre of the ingested vortex coincided with the centreline of the inlet cross plane. In the second case, the vortex was located near the duct surface where strong secondary flows caused boundary layer separation. In the third case the vortex was located opposite the location of the second case. Both a bare S-duct and an S-duct inlet with VGs were tested. The duct inflow was fully turbulent with an inlet Mach number of 0.6 and a Reynolds number, based on the inlet diameter, of 2.6×10^6. The boundary layer thickness at the inlet was approximately 4% of the duct inlet diameter. Two pairs of tapered-fin VGs (see Figure 2.9), with a blade height of the order of the flow field boundary layer thickness were mounted symmetrically on the inside of the duct at $\varphi=180°$ (see Figure 2.8) just before the first bend, i.e. near the origin of separation in the bare duct.

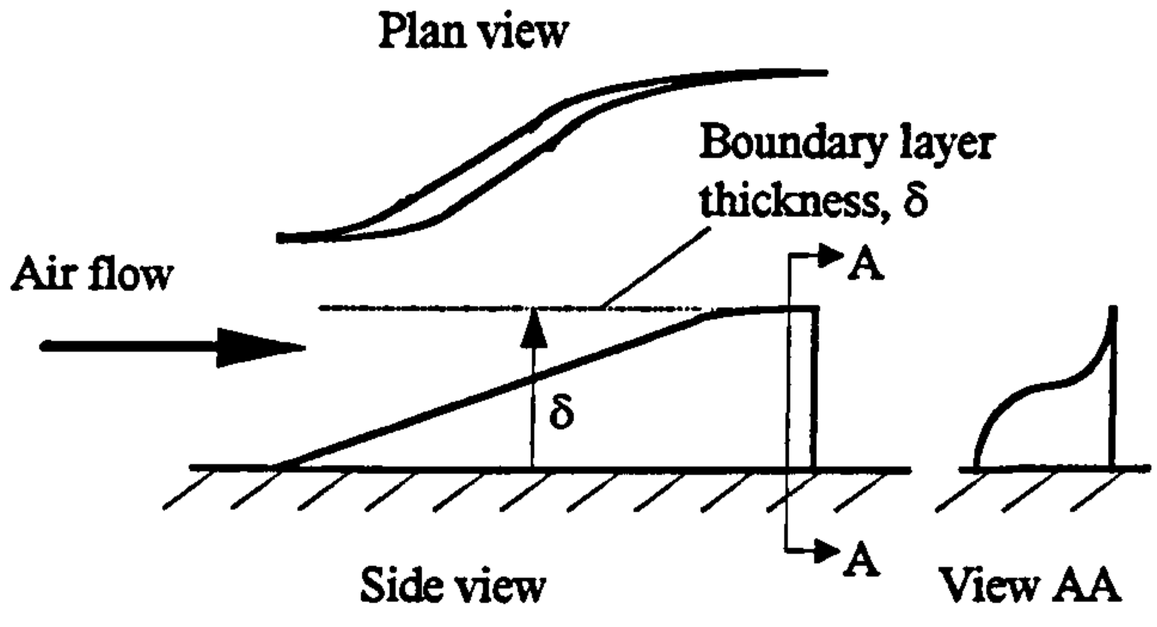

Figure 2.9: Tapered-fin VG geometry

In all three cases conclusions were drawn from transverse velocity, total pressure at inlet and exit cross-plane and duct surface flow visualisation. The oil flow visualisation pattern showed clearly that in all three cases flow separation was prevented by employing an array of VGs. Compared to the flow without the ingested vortex in Case 1, little effect was observed on the inlet and exit cross-plane total pressure contours or on the near-surface flow behaviour. In Case 2 the total pressure profiles and the surface flow features differed significantly from the ingestion free duct. The symmetrical spiral nodes, which are typical separation streaklines for three dimensional boundary layers lost their mirror image and a smaller concentrated region of vortical flow occurred on the surface, centred on the inside of the duct at $\varphi = 180°$. Also in Case 2, the ingested vortex produced a strong transverse flow at the duct exit plane. Shed vortices produced by the VG array in Case 2 were enhanced by the convective influence of the ingested vortex. In Case 3 no significant difference of the measured quantities with and without ingested vortex were observed.

Reichert and Wendt (1996) reached the conclusion that strong similarities exist between the flow field of non-diffusing and diffusing S-ducts at the engine face. In both cases at identical inflow conditions, a pair of naturally occurring vortices dominate the flow field, but no boundary layer separation exists in the non-diffusing S-duct. In the case of the non-diffusing S-duct they referred to the experiment of Vakili et al. (1984) who used the same inflow conditions and the same inlet diameter as Vakili et al. (1987) (see Section 2.2.1). In the case of the diffusing duct Reichert & Wendt (1996) used for their experiment the inflow conditions and the duct geometry of the set up of Wellborn et al. (1992).

Reichert & Wendt (1996) suggested flow field distortion at the engine face is not a result of the boundary layer separation but is dependent on the secondary flow produced by streamline curvature. Their objectives were to improve the total pressure recovery and the circumferential pressure distribution at the exit of the curved duct by employing wishbone (see Figure 2.10) and tapered-fin type VGs.

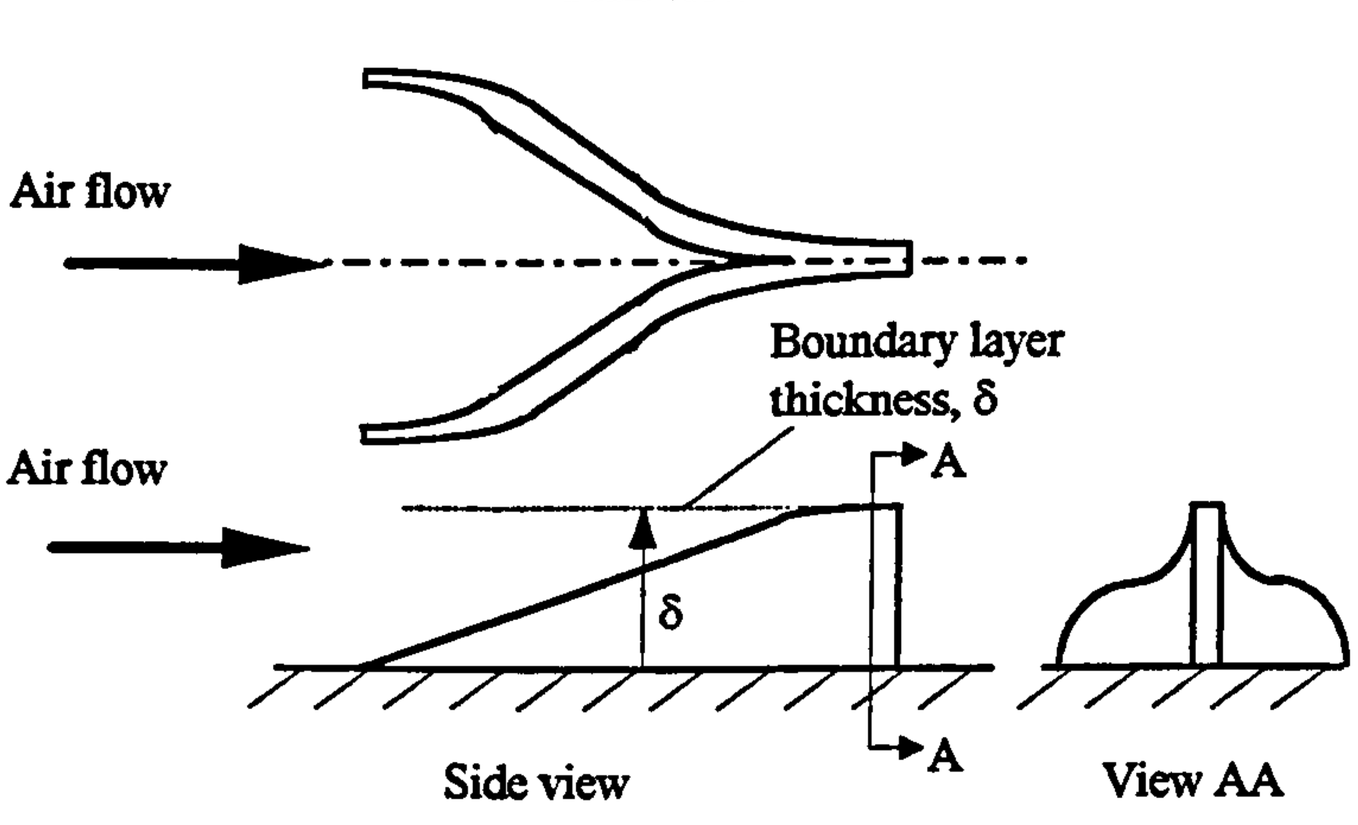

Figure 2.10: Wishbone VG geometry

They varied the number, orientation, size, lateral spacing and axial location of the VGs. Comparing the two types of VGs and the bare duct, both VGs reduced the radial distortion and improved total pressure recovery but the tapered-fin VGs showed, in general, better performance than the wishbone VG. The tapered-fin VGs influenced the secondary motion development by shifting the flow in the boundary layer away from the inside of the first bend to suppress the naturally existing pair of vortices. Reichert & Wendt concluded that redirecting the flow using VGs seems to be much more effective in terms of improving the distortion and the total pressure recovery than re-energising the boundary layer.

Foster et al. (1997) explored the ability of VGs (tapered-fin types) to reduce the circumferential total pressure distortion and enhance the total pressure recovery in a Rectangular-to-Semiannular Diffuser (see Figure 2.7); i.e., a similar inlet duct geometry to that examined by Brown et al. (1968). This type of diffuser is used as the subsonic section of a bifurcated supersonic inlet. The location of the rectangular

portion in the bifurcated inlet is immediately downstream of the normal shock, whilst the semiannular end of the diffuser is placed immediately upstream of the compressor front face. The inlet flow Mach number is 0.8 and decreases to 0.4 at the engine face. On the cowl surface two pairs of co-rotating tapered-fin VGs were mounted. Two additional co-rotating pairs were fixed on the ramp surface at either side of the centrebody. The locations of the VGs were determined from previous oil-flow visualisation with a distance $l_x = 0.45D_{exit}$ downstream of the inlet face (see Figure 2.7). Improvements in the circumferential pressure distribution were observed but the VG configuration did not enhance the total pressure recovery significantly.

Between the research of Taylor (1948), Pearcey (1961) and Brown et al. (1968) and the most recent from Reichert & Wendt (1996) and Foster (1997), numerous studies have been done on investigating the physical phenomena of longitudinal vortices produced by VGs on flat plate models. *Westphal et al. (1987)* analysed in detail, the development of a weak single longitudinal vortex interacting with a fully turbulent boundary layer in an adverse pressure gradient. The vortex was induced by a half delta wing VG (see Figure 2.11) mounted on the flat wall of a boundary layer wind tunnel at an skew angle of 12°.

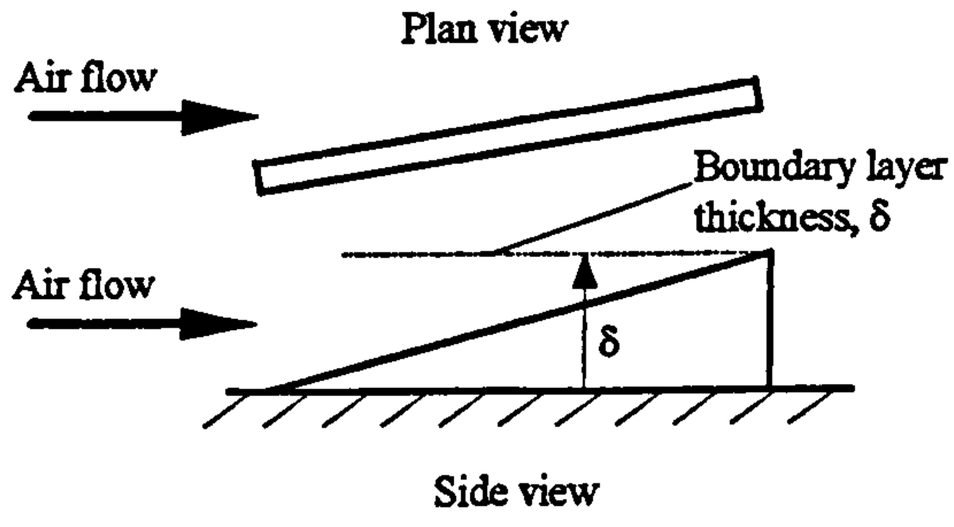

Figure 2.11: Half delta wing VG geometry

They observed the vortex core growing significantly in the streamwise direction. This is known as "vortex breakdown" and it was generated through the effect of the strong adverse pressure gradient on the longitudinal vortex at the location of the leading-edge of the VGs. If the distance from the vortex centre to the solid tunnel wall coincides with the radius of the vortex, then the shape of vorticity and therefore the

shape of the vortex itself became flattened or elliptical. The flattening effect is caused by the adverse pressure gradient which increases the rate of vortex core growth and therefore stronger distortion of the core shape occurs.

Pauley and Eaton (1988) extended the work of Westphal et al. (1987) to study the development of longitudinal vortex pairs in a turbulent boundary layer. They conducted experiments with co- and counter-rotating vortices generated with half delta wing VGs. They divided the counter-rotating vortices into "common flow down" and "common flow up" types to differentiate between the direction of the secondary motion toward or away from the wall, respectively. As suggested by Westphal et al. (1987), Pauley & Eaton adopted the location and value of maximum vorticity to describe the strength and movement of the vortices.

They found, from vorticity contour plots, that a region of opposite vorticity exists below the vortex, similar to findings by Shabaka et al. (1985). Their explanation for this secondary vorticity is based on the interaction of the secondary flow and the no-slip condition at the wall. The location of the opposite vorticity is on the up-wash side of the primary vortex. Even when the secondary vorticity was growing downstream, Pauley & Eaton never observed an obvious rollup of a second vortex. The streamwise velocity contour plots clearly showed a velocity deficit in the area of the vortex centre. Further downstream when the velocity returned to the usual boundary layer profile a slight increase of the main vorticity was observed and defined as "a mean stretching" of the vortex. They pointed out that the peak vorticity decay describes the diffusion speed of vorticity. Integrating the vorticity of the primary vortex is indicative of the vortex strength decay rate. Defining positive and negative vorticity enabled primary and secondary induced vorticity to be differentiated. The magnitude of secondary vorticity strength was found to be 15 - 25% of the amount of circulation in the main vortex. Overall the vorticity for skew angles less than 25° was found to be weak.

Pauley & Eaton (1988) tested different VG spacings at various downstream locations. An important difference between the two counter-rotating configurations was that the Common Flow Down (COFD) pair moved apart during downstream development and produced a constantly widening region of boundary layer thinning. The Common Flow Up (COFU) vortices have a strong interaction with each other but experience

only a minor influence from their image vortices and viscous flow near the wall. However, in the COFU case, the vortices were forced together where vortex interaction convected them away from the surface. The COFD vortices remain close to the wall where the influence of the viscous flow is considerable. As a result an elliptical shape of the vortices occurred. The peak vorticity rapidly decayed in the COFU case as the vorticity spreads in the vertical direction as a result of the lifting up effect. The lifting up effect reduced the magnitude of opposite sign vorticity found in the COFD case. The effects of VG spacing influenced the development of the vortices for the COFU and COFD cases differently. In the COFD case the thickness of the boundary layer between the vortex pair increased with increasing distance. The level of interaction in the COFU case was considerable if they were closely spaced but when fixed far apart the vortices decayed before they could interact. A single pair of co-rotating vortices lost identity and formed a single vortex if the spacing was not more than two VG heights. The mechanism of spreading vorticity was observed to be similar to the COFD. Based on these results, they found two spacing arrangements, one for the COFD and a second for the co-rotating case where the decay of vorticity was similar. For an isolated vortex, vorticity with opposite sign compared to the primary vortex exists on the up-wash side. The most important influence of secondary motion is thickening or thinning of the boundary layer depending on the VG configurations.

Littell and Eaton (1991) focused on the unsteady flow field behind a rapidly movable (in pitch) half delta wing VG, which was only partially embedded in the turbulent boundary layer. The single VG was fixed on a rotational tab, driven by a Printed Circuit Motor, located on the wind tunnel floor. Unsteadiness was caused through a rapid change of the skew angle in a range from 0° to -18°. The flow was measured at four downstream locations with a crosswire anemometer. They observed that the main longitudinal vortex was formed instantaneously when the vane was skewed from 0° to -18°. A second vortex was evident even though the strength was minimal compared to the main vortex. No influence from the secondary vortex on the primary vortex was observed. The substantial velocity deficit in the core of the primary vortex was substituted with an accelerated core during the relaxation. They determined that the downstream convection speed of the main vortex was over 90% of the free stream

velocity. The total time of unsteady behaviour, i.e. formation and relaxation of the vortex, appeared to be the sum of the actuation time of the VG plus the convection time downstream of the VG chord.

Wendt et al. (1993) extended the experimental work of Pauley & Eaton (1988) to an array of four counter-rotating rectangular wing VGs (see Figure 2.6), fixed on a flat vertical splitter plate in a subsonic wind tunnel (COFU configuration). The VGs were equally spaced at a skew-angle of ±10°. They observed vorticity with opposite sign to the main longitudinal vortex system at the wall and underneath the main vortex due to the viscous interaction of the substantial spanwise cross flow of the vortex and the wall. This vorticity appears to be concentrated in the upwash region of the main vortex and increased in the streamwise direction, but no helical movement of the vorticity was observed. The position of the vortex core was identical with the peak vorticity in the spanwise and vertical directions. To investigate the spacing dependency, the characteristics of the vortical flow structure were analysed at two downstream cross planes. Their results indicated a strong influence of the VG spacing:

- Large spacing generated widely spaced streamwise vortices (COFU pairs) which moved downstream away from the wall and therefore the interaction with the boundary layer became less effective. The only mechanism for dissipation was the wall non-slip conditions.
- Small spacing forced the vortices to move downstream near the wall in tight arrays interacting strongly with each other. The result was a rapid decay of the individual strengths but merging to one single longitudinal vortex provided substantial interaction with the boundary layer.

Wendt and Hingst (1994) investigated the influence of a wishbone VG (see Figure 2.10) on the flow structure of a fully turbulent boundary layer (see Reichert & Wendt, 1996). They mounted a single vortex generator on the flat wind tunnel wall with a test Mach number of 0.2. A strong counter-rotating pair of vortices were observed at two downstream spanwise locations. They determined the vorticity strength and the decay by comparing the peak vortictiy at each cross-plane. The strength of the longitudinal vortex pair and the rotation sense caused the pair to rapidly convect from the surface.

Unlike the other vortex pair systems only one streamwise velocity deficit occurred enclosing both vortex cores coincident with the Wishbone VG tip location.

The *ESDU (1994,1995)* memorandum is probably the most detailed compendium of work on solid VGs, of various wing and vane type geometries, for the control of shock-induced flow separation. Research covers a single VG to an array of generators in all configurations discussed previously. The physics of longitudinal development of induced vortices is described and practical correlations are presented in detail.

2.3.2 Numerical Studies

Jones (1955) was one of the first who used an analytical approach to calculate the paths of trailing vortices from a system of counter-rotating VVGs on a flat plate. He compared his results with water tunnel experiments. He emphasised the advantage of determining the vortex trajectory numerically instead of setting up lengthy experimental programmes. He confirmed the experimentally observed results that trailing vortices initially approach the surface of the flat plate down to a certain distance from the surface and then start to convect away. According to his calculations, the distance to the plane surface was greater than the experimentally determined values. In agreement with experiments he concluded that the projection of the vortex paths on a plane perpendicular to the stream do not depend on the vortex strength.

More recently Anderson (1991) predicted boundary layer separation in a bare S-bend intake duct with the geometry and inlet conditions used by Vakili et al. (1987) (see Section 2.2.1). He employed a reduced Navier-Stokes (3D RNS), initial value, space marching, code. The turbulence model was based on the eddy viscosity formulation employing Prandtl's mixing length model. To model the VGs in the RNS code (Kunik, 1986) a stream function-vorticity formulation was introduced for the governing equations. The shed vortices were modelled as a source term into the vorticity equation. Results showed significant delay of boundary layer separation and a more uniform circumferential pressure distribution at the engine face.

Anderson et al. (1992) demonstrated, with an updated version of the code (RNS3D), that it can be used to design a VVG system for the inlet duct of the Boeing 727-100 aircraft series. He pointed out that the major difference between external

aerodynamics and inflow problems is the dimensionality of the flow field. In terms of inlet ducts the flow field is always three dimensional rather than two-dimensional as it can be in the case of some external flows. The longitudinal vortices are not used to energise the local boundary layer, but to construct a vorticity pattern which interacts with the aerodynamic characteristics of the inlet diffuser. The goal is to achieve a low engine face flow distortion over the flight envelope. They showed that engine face distortion is a complex function of vortex strength, VVG scale, VVG arrangement and secondary flow field structure. They defined three categories of variables which influence a VVG performance: (1) the inflow conditions defined by Reynolds number and the magnitude of the incoming mass flow; (2) the aerodynamic characteristics, i.e. separation is dependent on the duct diameter in the first bend of the S-bend duct; (3) the design of the VVGs themselves, their arrangement, geometry and location in the duct.

Anderson and Gibb (1992) presented a numerical study using the reduced Navier-Stokes code (RNS3D) to define the optimum VVG configuration for the RAE2129 inlet S-duct. The test conditions and the geometry are identical to those applied in AGARD-AR-270 (1991). A model of the RAE2129 inlet S-duct, the M2129 (see Anderson et al., 1993, see Section 2.2.2), was further examined by *Anderson and Gibb (1993)*. Additional to the findings of 1992 it was observed that the scale of the VVGs (ratio of vane height to boundary layer thickness) varied substantially between wind tunnel test and flight conditions. The reason was the difference in magnitude of the Reynolds number, which was seven times larger at flight conditions than in the wind tunnel test. As a result, the boundary layer thickness was significantly thinner at flight conditions than in the wind tunnel test requiring the height of the VG to be adjusted for each condition. To manage the flow field distortion at the engine face in the most efficient way, an optimum VVG configuration was determined which depended on the axial centreline distance from the inlet, the skew angle, the number of co-rotating VVGs and the blade height. Only within a very narrow range of VG configurations, close to the optimum installation at flight and wind tunnel test conditions, were the scaling of the VVGs similar. A preliminary correlation to scale the VG blade height for wind tunnel test conditions was suggested. The VG blade

height was scaled to the undisturbed boundary layer thickness at the circumferential position of approximately φ=180° (see Figure 2.1).

Liandrat et al. (1987) investigated numerically the longitudinal vortex interaction with the boundary layer on a simple flat plate. They based their numerical simulation on experiments of Shabaka et al. (1985). Diffusion in the longitudinal direction was neglected and the Navier-Stokes equations parabolised along the main flow direction. Employing a forward marching scheme they calculated the interactive effects of the streamwise vortices on the turbulent boundary layer. The results obtained with a turbulence model based on the Boussinesq hypothesis provided acceptable predictions for the single vortex but poor results for a pair of vortices. However, when they implemented a simple algebraic diffusion model to integrate the Reynolds stress transport equations in the streamwise direction, they achieved much better results for the vortex pair effects. Previously *Raj and Iversen (1978)* suggested that the capability of a turbulence model has a significant influence on the merging process of the vortices.

2.4 Air-Jet Vortex Generators (AJVGs)

2.4.1 Experimental Studies

Wallis (1952, 1960) was the first to employ AJVGs to delay separation of a turbulent boundary layer by introducing longitudinal vortices. He installed circular AJVGs on a simple aerofoil to issue a cross flow velocity component into the main flow and achieved persistent vorticity to delay boundary layer separation. Wallis appreciated the great advantage of controlling the flow with negligible drag penalty compared to VVGs. Further investigation into the application of co-rotating arrays of circular AJVGs and Slot Blowing was performed by *Pearcey (1961)*. His work covered boundary layer control for aerofoils and wings to prevent shock-induced separation.

More recently *Gibb and Anderson (1995)* designed a model of the RAE2129 S-bend intake duct. The inflow conditions and the geometry is identical to the RAE2129 S-bend investigated in AGARD-AR-270 (1991). They fitted the M2129 duct with an array of ten co-rotating circular AJVGs of 1mm diameter at a streamwise location as shown in Figure 1.1. The degree of distortion on the engine face and the total pressure recovery were used to judge performance. Tests with different pitch and

skew angle combinations were carried out over a Mach number range of 0.2 to 0.8. The AJVGs were fed from a common annular plenum chamber which was created through a second inner wall. Control of the jet velocity was achieved by altering conditions in the plenum chamber. Gibb & Anderson (1995) concluded from their experiments that AJVGs provided excellent improvement in reducing the engine face distortion and enhancing total pressure recovery. Therefore a significant reduction of unsteadiness in loading the engine was achieved providing less vibration, a wider stable flow range, and larger flight envelope.

Senseney et al. (1996) examined turbulence and distortion levels for a Short Highly Offset Diffuser with a rectangular S-bend shape. This kind of diffuser is used in the Boeing 727, Lockheed L-1011, the Northrop B-2, McDonnell Douglas F-18 and Lockheed Martin F-22. Experiments were performed on a subscale diffuser with an inlet Mach number of 0.6 and an inlet boundary layer thickness of 2.7mm. The inlet plane dimension was 24.4mm×16.79mm and the exit plane had the size of 25.4mm×25.4mm thus an exit to inlet area ratio is equal to 1.5. The centreline offset was defined to be an indirect measure of duct curvature and was determined to be $\Delta y/D_{eq} = 0.81$ ($D_{eq} = 28.82$mm, is the equivalent diameter of the duct exit). The length of the duct was equal to $2.07D_{eq}$. The AJVG were located just downstream of the first bend on the lower surface of the duct. The jets were arranged in a co-rotating array of three circular AJVGs, of 0.6 mm diameter. The jets were skewed of 45° with respect to the mean flow and pitched of 25° relative to the lower surface tangent. With a blowing mass flow rate of 0.48% of the main flow they achieved an increase of the static pressure coefficient of about 50% at the exit plane. The recovery of the total averaged engine face pressure increased by about 1.3%, as well as improving the isentropic efficiency of the diffuser. Less flow reversal was observed in the region of separation thus decreased boundary layer thickness at the engine face, especially close to the centreline. A similar improvement was observed for the level of turbulent distortion at the diffuser exit.

Apart from Wallis (1952, 1960) and Pearcey (1961) and the recent application to S-bend intake ducts from Gibb & Anderson (1995) and Senseney et al. (1996) there are only a few publications about AJVG applications. *Johnston and Nishi (1990)* focused their research on a simple flat plate geometry. They explored the effectiveness of

AJVGs in controlling turbulent boundary layer separation in a region with large stall. A possible application for this work is jet engine compressors where the AJVGs are activated via valves if required. The jets, each of 6.35mm diameter, were located at seven downstream positions on a smooth flat wall of a low speed wind tunnel. At each location an array of six equally spaced AJVGs in the cross-stream direction were pitched at 45°. They defined various configurations of co-rotating and counter-rotating vortices with skew angles of ±90°. An alternative arrangement was defined with a skew angle of 180° of the AJVGs to main the flow direction, i.e. pointing directly upstream. The ratio of jet speed to free stream speed was varied between 0 and 1. Their conclusion was that skewed jets were effective in contrast to jets aligned to the main flow. The counter-rotating configuration COFD (see Section 2.3.1, Pauley & Eaton) achieved the best results in terms of reducing the large stalled regions with a velocity ratio of 0.8 and moved the detachment location downstream. In the COFU configuration the change of velocity ratio did not significantly affect the detachment location.

Compton and Johnston (1992) conducted an experimental study on the behaviour of a single pitched and skewed AJVG issuing into a two-dimensional turbulent boundary layer. The diameter of the jet was 6.35mm and issued from an orifice in a flat rectangular surface in a wind tunnel. They fixed the pitch angle to 45°, varied the skew angle between 90° and 45° and tested velocity ratios of jet speed to free stream velocity from 0.7 to 1.3. At four streamwise locations measured data was used to plot three different graphs, i.e. velocity vector plots, streamwise mean velocity ratio contours (local velocity / free stream velocity) and vorticity contours. Analysing the data they found the maximum secondary velocity was about 7% of the free stream velocity. Therefore the vortex was defined as being weak compared to the strength of vortices generated by equivalently sized VVGs. However, the structure and the velocity deficit contours of the vortex was seen to be quite similar. The decay rate of maximum vorticity did not coincide with the exponential shape of that for VVGs. The AJVG showed different positions of peak vorticity and core location of the vortex, equal to the vortical flow structure of subscale solid VGs. A substantial dependence of peak vorticity levels according to the range of skew angles and velocity ratios was observed.

Selby et al. (1992) used AJVGs to control separation of fully turbulent flow in a low speed wind tunnel. The separation model was a two-dimensional 25° ramp mounted on the wind tunnel floor with an array of 10 equally spaced AJVGs. The investigation focused on varying jet diameter, skew and pitch angle, AJVG speeds and streamwise orifice location. They measured the pressure distribution to evaluate the pressure coefficient c_p. Improvements in the VG performance, in terms of pressure recovery and reattachment line location, were achieved as the following conditions were varied. (1) Increasing the jet exit velocity by either decreasing the jet orifice diameter or increasing the volume flow rate through the air jets. (2) Altering the pitch angle to ensure the momentum transfer is closer to the wall. (3) Variation of the jet skew angle to increase the strength of the dominant vortex in the pair. (4) Adjusting the upstream location of the jets. (5) Changing the air jet array configuration to produce co- as opposed to counter-rotating vortices. (6) Employing an array of co-rotating air jets as opposed to slot blowing.

Pearcey et al. (1993) employed inclined AJVGs to suppress shock-induced separation. Their model was a full-span half aerofoil mounted on the tunnel wall of a transonic wind tunnel. Nine rectangular jets were equally spaced across the span of the model with a range of skew angles between 45° to 90° and a range of pitch angles between 30° to 45°. The AJVGs were located at 35% of the cord length from the leading edge and 5% chord upstream from the point where the shock first occurred. The arrays were aligned in a co-rotating sense forcing the vortices as close as possible to the surface in the streamwise direction. The main aim of the study was to compare the downstream pressure recovery caused by the longitudinal vortex system produced by the jets to well established results for VVGs. Comparable improvements in performance, in terms of suppression of flow separation, were recorded for both vane and air jet VGs.

2.4.2 Numerical Studies

Zhang (1993a) conducted a numerical study of a single vortex and co- and contra-rotating longitudinal vortices produced by pitched and skewed circular Jets, in a fully turbulent boundary layer on a flat plate. The AJVGs were circular orifices with a diameter of 6.35mm. He predicted the vortical flow structure using the Finite Volume

code CFDS-FLOW3D with both a k-ε turbulence model with linear-logarithmic wall function and a Reynolds Stress Model. He altered the pitch and skew angle, the velocity ratio of the jet to the free stream speed and the spacing. Results were validated with experimental data based on vorticity plots at streamwise cross plane locations. In the case of the single vortex, Zhang (1993a) found close agreement with experiments in terms of a region of opposite secondary vorticity to the primary vortex. In his opinion, the interaction between vorticity areas with opposite sign is the mechanism which generates the main vortex. From skew angles of 60° to 90°, no change of effectiveness was observed. He suggested that high jet velocity ratios do not have a significant influence on the formation of the vortex, but the vortex should stay within the boundary layer. Contra-rotating vortices were observed to be stronger than co-rotating vortices in terms of suppressing boundary layer separation, even if contra-rotating vortices tend to lift up from the surface and lose effectiveness in terms of separation control. The circulation level of the co-rotating jet arrangements on cross-planes was independent of the jet spacing as the individual vortices diffuse faster than do the vortices in the alternative configuration. If the AJVG spacing was increased in the contra-rotating case the strength of cross plane vorticity decreased. However, the individual vortex strength was independent of spacing.

Zhang (1993b) compared rectangular and circular AJVG performance issuing into a fully turbulent flow on a flat plate in terms of vorticity contours and velocity plots on downstream cross planes. He employed the same numerical code and turbulence models as in his previous study to investigate co- and contra-rotating jet configurations. The AJVG spacing for the co- and contra-rotating study was fixed, the jet orifice diameter was equal to 10 mm with pitch and skew angles constant at 30° and 90° respectively. As previously mentioned by Zhang (1993a), the contra-rotating vortices produced stronger circulation than in the co-rotating case. However, the disadvantage of premature convection of the vortices from the surface, compared to the co-rotating arrays, remains an issue. Even if the k-ε turbulence model overpredicted vorticity strength, in general there was good agreement with both k-ε and Reynolds Stress Models for the contra-rotating configuration. Zhang could find no significant difference in terms of predicting vorticity contours by employing a rectangular or a circular jet arrangement. He simulated a 6.35mm diameter circular jet

orifice and a 3.56mm×8.9mm rectangular jet. Employing pitch and skew angles of 45° and 90° for the co-rotating AJVG arrangement.

Henry and Pearcey (1994) presented a numerical study of an array of rectangular AJVGs with different aspect ratios issuing into the fully turbulent boundary on a flat plate. They used the Finite Volume Navier-Stokes code CFDS-FLOW3D with standard k-ε turbulence model and wall functions. Various combinations of pitch and skew angles were used between 60° and 90° for the skew angle and 15° and 90° for the pitch angle. The optimum skew angle in terms of enhancing the transverse skin friction was found to be at 60° coinciding with previous experimental data of Pearcey et al. (1993) and numerical findings of Zhang (1993). Probably the best results in terms of skin friction and therefore thinning of the turbulent boundary layer was determined at a pitch angle of 30°. Little effect was observed in changing the aspect ratio as long as the mass flow rate remained constant. Henry & Pearcey (1994) also considered the case of a turbulent boundary layer in an adverse pressure gradient. A considerable increase of skin friction near the original point of separation was achieved, i.e. an appreciable thinning of the boundary layer, and thus a delay of boundary layer separation.

Akanni and Henry (1995) continued the work of Henry & Pearcey (1994) obtaining more detailed results in terms of development mechanism of longitudinal vortices produced by a single rectangular air jet, issuing into a fully turbulent flow over a flat plate. The numerical model is taken from Henry & Pearcey (1994) but a more sophisticated post processing tool was employed. Use of an improved flow visualisation package resulted in the discovery of a possible second streamwise vortex accompanying the main longitudinal vortex. However, the second vortex dissipated rapidly after formation. It was seen to be ingested by the main vortex, i. e. close to the air jet orifice, and only the one vortex travelled downstream.

There are no known results of numerical applications of AJVGs in S-bend intake ducts.

2.5 Summary and Outstanding Problems

From experiments discussed in Section 2.2.1 (see also Table 1.1), the flow structure inside an S-bend intake duct is reasonably well understood. In the case of a circular S-bend (see Figure 2.1) the flow starts as a two-dimensional entry flow but develops a three-dimensional character downstream in the form of the typical pair of counter or contra-rotating vortices (see Figure 2.12).

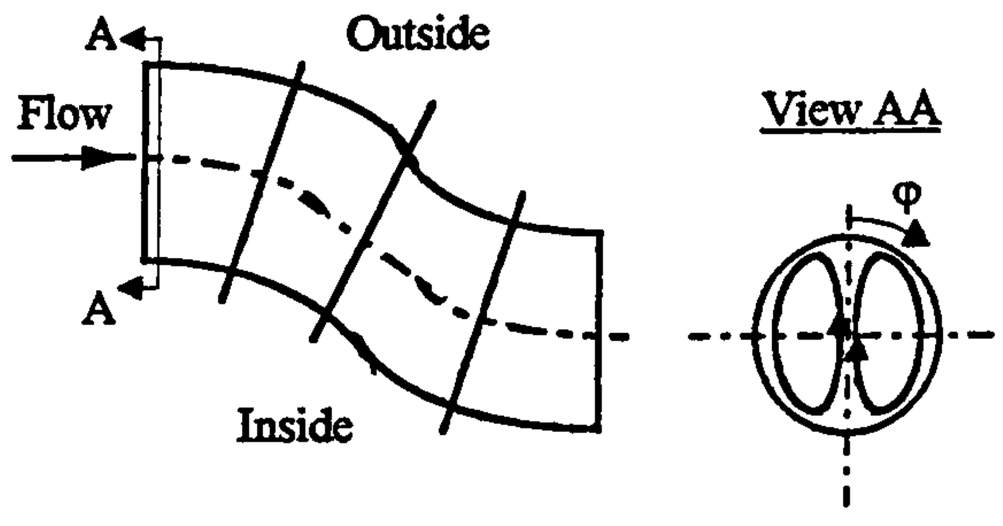

Figure 2.12: S-bend duct with the typical pair of longitudinal counter-rotating vortices

This pattern of vortices is caused by a combination of slowly moving circumferential boundary flow from the outside ($\varphi = 0°$) to the inside ($\varphi = 180°$) of the duct with the fast moving inviscid core flow in streamwise direction.

The further development of the flow depends on the geometry of the circular duct, i.e. whether the duct has a constant diameter or whether it is a diffusing duct with gradually increasing cross section area. In the case of a diffusing S-bend the combination of curvature and increasing diameter causes an axial adverse, i.e. positive, pressure gradient along the inside of the duct combined with the changing circumferential pressure field at each axial station. The growing three-dimensional boundary layer is slowed down and at a certain streamwise location departs from the surface at a saddle point of separation. A three-dimensional separation pattern (see Figure 2.13) with this saddle point of separation and additional points of separation and a node of reattachment are formed between the first and the second bend along the inside of the duct.

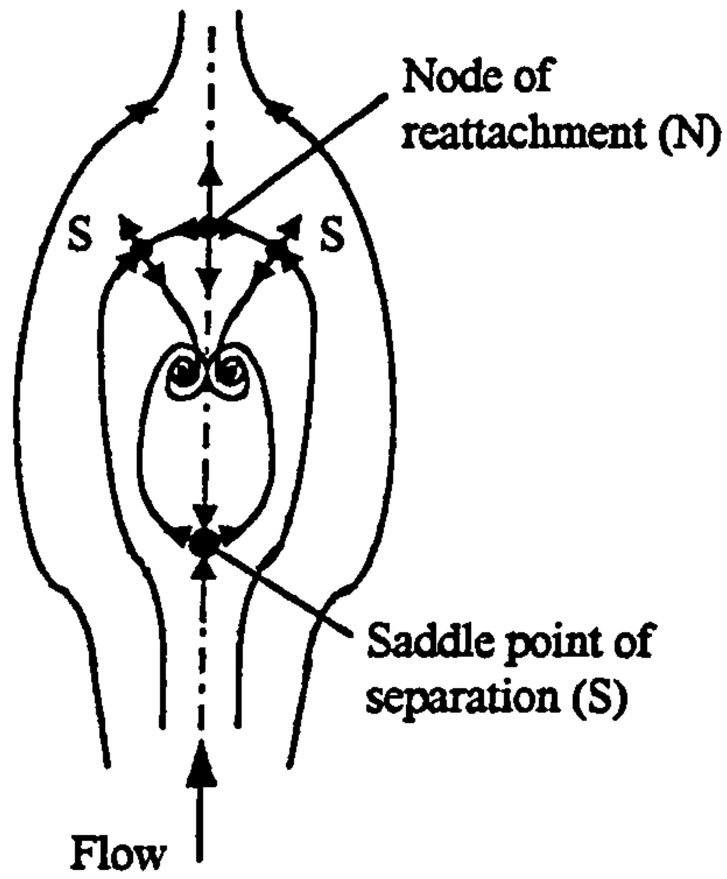

Figure 2.13: Three-dimensional separation pattern with spiral nodes of separation

The pattern of oil streaklines proved the presence of these spiral nodes and hence 3D separation (see e.g. Wendt & Reichert, 1996). Along the separation region the transverse flow is mainly directed towards the outside of the duct. The axial static pressure along the outside of the duct has a sinusoidal distribution. The skin friction distribution also shows a sinusoidal development but with the opposite sense to that of the static pressure.

The flow in S-bend ducts with constant diameters also has a pair of contra-rotating vortices, but without any sign of flow separation of the surface. It is observed that the secondary flow was established in the first bend and strengthened after the inflection plane towards the exit of the duct (see Bansod & Bradshaw, 1972). As in the diffusing duct, the axial static pressure and the skin friction develop along the inside and the outside of the duct in a sinusoidal form.

The secondary flow characteristics change depending on the duct cross-section geometry, i.e. circular, rectangular or rectangular to circular. The main difference between the secondary flow pattern of a circular and a rectangular duct is that in the case of the rectangular duct the secondary flow changes to the opposite direction between the first and the second bend. In contrast, the pair of contra-rotating vortices in the circular duct keeps the same flow orientation throughout the duct.

Another factor which influences the secondary flow pattern in rectangular ducts is the angle of incidence, if the angle is greater than 10°. With increasing angle of incidence, to a maximum of 30°, the pair of contra-rotating vortices disappear and a single

strong vortex occurs after the first bend in the lower half of a rectangular duct (see Figure 2.4). In this duct, with constant cross-section area, a single vortex is generated in the first bend and develops further downstream towards the exit into an S-like double vortex pattern. Flow separation appears along the bottom wall after the first bend at 20° incidence and above. A further change of secondary flow occurs in an S-shaped diffuser with a rectangular inlet and a circular exit at high angles of incidence. In this case also a strong clockwise rotating single vortex appears at the first bend. However, further downstream towards the exit the rotation sense is kept and a fairly concentric strong single vortex is observed at the engine face.

Guo & Seddon (1983) suggested that the characteristic of the secondary flow is depending on five interactive factors. 1) the pressure gradient associated with S-bends, 2) the pressure gradient initiated by angle of incidence, 3) the inertia of the flow defined by inflow conditions, 4) the appearance of flow separation, and 5) the cross-section geometry of the duct.

Numerous numerical studies, discussed in Section 2.2.2 (see also Table 1.1) were attempted to reflect the complex flow situation inside of S-bend ducts. The general flow characteristics predicted were fairly close to the experimental data. However, concentrating on circular ducts, the main difficulty is to predict the interaction between the inviscid core flow and the viscous boundary layer flow, especially after the first bend.

Eisemann et al. (1978) predicted flow separation in the case of an S-duct with constant diameter even though it is known from experiments that separation does not occur in such a geometry. Presumably, Eisemann et al. predicted the pressure field defective Kunik (1986) used an RNS code and predicted a region of separation in a diffusing S-bend but it was located further downstream compared with experimental data. As a result of the downstream shifted location of separation, the pair of contra-rotating vortices was weaker than that of the experiment. Thus the flow distortion at the engine face was underpredicted and the pressure recovery overpredicted.

Studies in AGARD-AR-270 (1991) and Smith et al. (1992) used RANS codes and predicted the axial location of the region of separation in diffusing S-bends incorrectly. Anderson et al. (1993) compared a slightly modified version of the RANS

code from Smith et al. (1992) with the reduced Navier-Stokes code (RNS3D). Again both codes calculated the region of separation to be further downstream than found in experiments. Additionally, flow separation occurred at lower inflow conditions (i.e. from M = 0.2) than experiments showed (at M = 0.3).

May (1997) compared eight different turbulence models in terms of secondary flow prediction in a diffusing S-bend. Three k-ε, four k-ω turbulence models and the zero equation Baldwin-Lomax model were tested. He used two different inflow conditions, i.e. a high and a low mass flow rate. All k-ε turbulence models failed to predict any separation wall functions employed. The non-linear k-ω model which integrated through the viscous sublayer (that is without wall function) showed the best results compared to experiments at high mass flow rates, even though the separation area was again predicted too far downstream. The Baldwin-Lomax model predicted the lowest strength of separation. At low mass flow rates no turbulence model was capable to capture the vortex lift off phenomenon.

The above S-bend predictions indicate that all numerical approaches failed to describe correctly the measured magnitude and streamwise location of the region of flow separation due to attempts to artificially negotiate the separation zone(s).

The most promising technique to reduce the flow distortion and to increase the pressure recovery at the engine face is the instalment of an array of Vortex Generators (VGs) just upstream of the saddle point of separation on the inside of the duct (see Figure 1.6). The two main groups of VGs are the passive Vane VGs and the active Air jet VGs (AJVGs) and were discussed in Sections 2.3 and 2.4 (see also Table 1.2). Many experimental and numerical studies of different geometries of VVGs have been examined to test the effectiveness of VVGs in ducts and in simplified flat plate models. Only a few experimental investigations and no numerical predictions are known in terms of AJVGs in S-ducts. In simplified flat plate models the secondary flow structure caused by AJVGs was experimentally investigated by only a few researchers and even fewer numerical predictions are known.

VGs in S-bends are employed to produce longitudinal vortices which either destroy the pair of contra-rotating vortices or support them. Inhibiting the secondary flow

caused by centre line curvature can be achieved by introducing a vortex pattern which redirects the flow. This method was used by Anderson et al. (1992) who employed the RNS3D code to investigate numerically the benefit of VVGs in an S-bend diffuser. Their reduced Navier-Stokes code modelled the VVGs as a stream function-vorticity formulation. Thus the vicinity of the VVGs could not be investigated appropriately but only the influence of the generated vortices onto the main flow. They used the redirecting approach and achieved improvement in terms of flow distortion and pressure recovery at the engine face. They concluded that the engine face distortion is a complex function of vortex strength, VVG scale and arrangement, and the existing secondary flow structure caused by the geometry of the duct and the inflow conditions.

It is not perfectly clear yet which approach is the most effective in terms of a minimum of flow distortion and a maximum of pressure recovery. However, most of the known research employed the approach of redirecting the flow.

Gibb & Anderson (1995) designed their VG array experiment based on the redirecting theory by generating two sets of co-rotating vortices with opposite rotation sense symmetrically with respect to the symmetry line. They examined VVGs and AJVGs and achieved both an appreciable reduction of flow distortion and an increase of pressure recovery.

Reichert & Wendt (1996) suggested also the redirecting approach and argued that the flow field distortion is not depending mainly on the occurrence of flow separation and thus re-energising the boundary layer was not the correct technique. Their conclusion may be supported by the fact that in S-bend ducts with constant diameter boundary layer separation did not occur but the flow field distortion at the engine face is of a similar magnitude than that of a diffusing duct.

In numerous flat plate model experiments, discussed in Section 2.3.1 (see also Table 1.2), the development of longitudinal vortices produced by VVGs in interaction with a turbulent boundary layer were investigated. VG scale, VG geometry or VG configuration all influence the results. The combination of all three factors, the application (inflow or outflow) and the free stream conditions define the optimum VG configuration for each particular case.

Pauley & Eaton (1988) examined in detail the behaviour of co- and counter-rotating pairs of vortices generated by different configurations of VVGs. Their main conclusion was that the correct spacing of VVGs is very important because this detail decides whether an interaction between the single VVGs takes place in terms of thinning or thickening the boundary layer height. In any case, AJVGs offer the advantage of not causing additional drag. They need to be skewed to produce effective secondary flow instead of being aligned to the main flow (see experiments of Johnston & Nishi, 1990). Zhang (1993a) and Henry & Pearcey (1994) found in their numerical studies using a full Navier-Stokes code, that skew angles above 60° do not change appreciably the development of secondary flow. Both employed the k-ε model and their results were in good agreement with experiments. They suggested also that the pitch angle should not exceed 30° if the produced vortices are to remain in the boundary layer region while they are travelling in a streamwise direction. Henry & Pearcey (1994) concluded that the aspect ratio of the air jet orifice does not alter the effect as long as the mass flow rate is being kept constant.

In general, little research has been undertaken in terms of employing AJVGs in S-bend ducts as discussed in Section 2.4. Previous investigations with VVGs suggest that redirecting the flow in diffusing S-bend intake ducts is the most adequate technique to reduce the flow field distortion and increase the pressure recovery at the engine face. The lack of any studies of AJVGs in S-bends and the difficulty in computing viscous flow in S-bend ducts generates the need for a local model which describes the complex vortical flow structure in the vicinity of the jet orifice. The approximations used in the reduced Navier-Stokes code (RNS3D) preclude it from computing the local flow. Our local model can be used to produce the optimum configuration as input data to RNS3D.

3 Numerical Models and Methods used

3.1 Introduction

The term Computational Fluid Dynamics (CFD) describes the study of fluid flow by solving numerically the partial differential equations governing the flow. In a defined solution domain the governing equations describe the flow field as a continuum and therefore at any time or location quantities like the velocity and pressure are determinable. Before the equations can be solved numerically the original set of equations have to be approximated to discrete points which represent, all together, the solution domain as a closed control unit in the form of a numerical grid. It can be shown that the resulting algebraic equations describe exactly the flow field if the distance between the discrete points reaches the limit of zero. Employing a numerical method, like the Finite Volume Method (used in this project), algebraic equations link the dependent variables at adjacent grid nodes. Since the governing equations are non-linear, an iterative computational procedure is used. The sequence to set up a fluid flow problem is shown in the following flow chart:

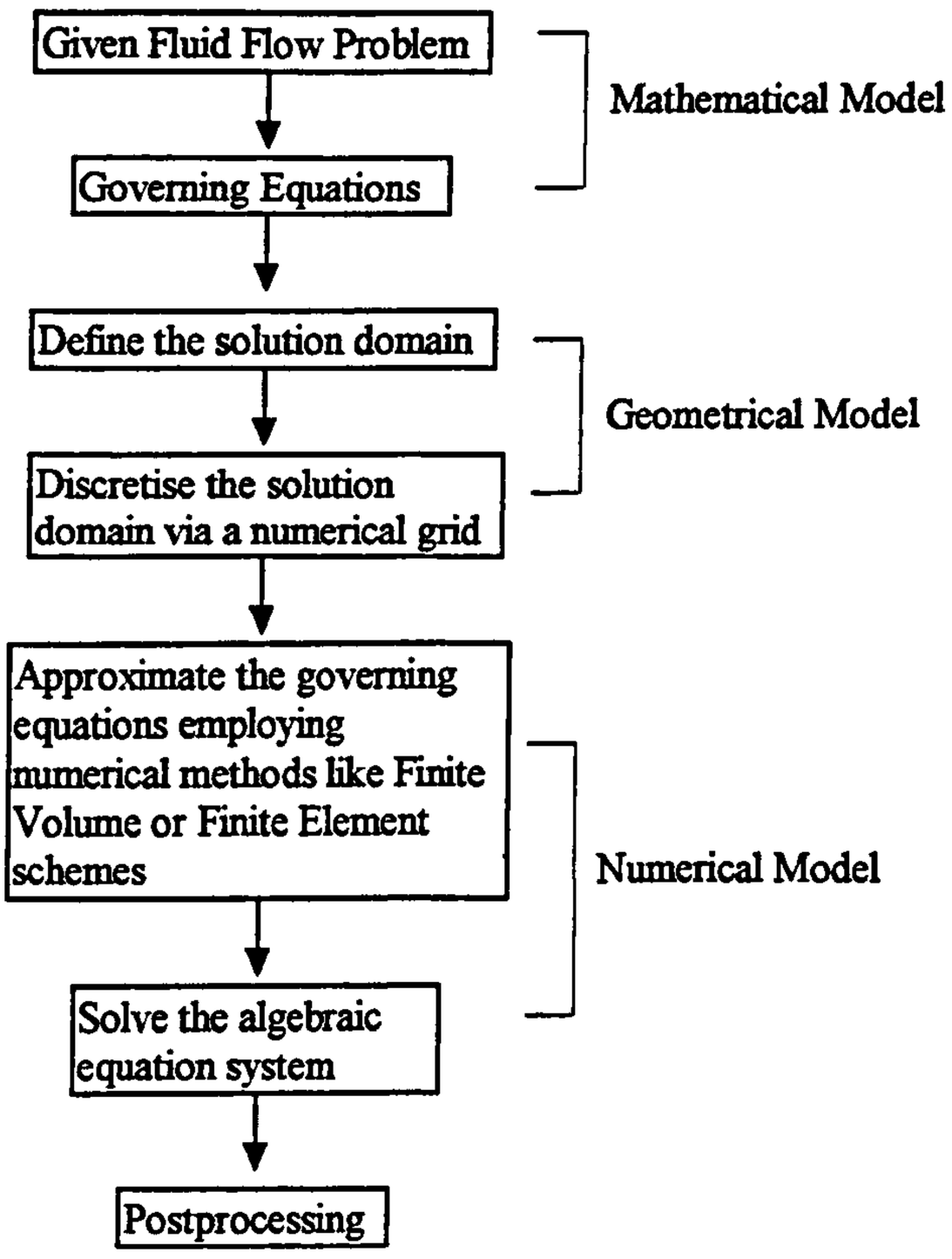

Figure 3.1: Flow chart of the sequence of CFD

Numerous CFD vendors exist supplying both Finite Difference Method (FDM) based software and Finite Element Method (FEM) CFD codes. These commercial suppliers deliver multi purpose codes which address a wide range of fluid flow simulations. Most solve the governing equations in generalised, body fitted coordinates with pre- and post-processing modules for grid generation and data analysis, respectively, in the same software package. The customer may therefore tackle the problem from grid generation to the final graphs, preparation in one package. However, if more complex geometries have to be discretised or visualised, additional processing software is also commercially available. One very powerful grid generation package with structured and unstructured capabilities is ICEM CFD. Specialist packages for post-processing of CFD results include the software products, PATRAN, FEMVIEW, UNIRAS, AVS and ENSIGHT.

Examples of CFD programs based on FDM are, CFX 4, FLUENT, PHOENIX, STAR-CD, FLOW-3D and CFD-ACE. FEM based codes includes FIDAP, FLOTRAN, N3S and NISA/3D-FLUID. A recent comparison of several commercial CFD codes has been reported by Freitas (1995) for certain benchmark flows. However, clear conclusions could not be made because not all participants calculated the complete set of flows.

CFX 4 is the code used in this project and will be described in detail in a later section. CFX 4 was chosen because the Department of Mechanical Engineering and Aeronautics of City University has many man-years experience in the use and application of this code, and it has been shown to give reasonable results in a variety of similar applications (see Henry & Pearcey, 1994 and Akanni & Henry, 1995).

3.2 Governing Equations

There are two different methods used to formulate the fundamental equations. The physical principles which apply are conservation of mass, momentum and energy. The first approach considers a finite volume fixed in space with the fluid flowing through this control volume. This approach is called the "Euler System" and yields "conservative equations". The second approach, the "Lagrange system" considers a finite mass moving with the main flow. In this case equations in "nonconservative form" are obtained.

The following governing equations were generated using the first approach and hence have the form of a partial differential equation with conservative character.

The continuity equation in conservative form yields:

$$\boxed{\frac{\partial \rho}{\partial t} + \nabla \cdot (\rho \vec{v}) = 0} \quad (3.1)$$

where, $\rho \equiv$ fluid density

$\vec{v} \equiv$ velocity vector

Introducing a general variable ϕ (= u, v, w) and a general diffusion coefficient Γ the general differential momentum equation is:

$$\boxed{\frac{\partial(\rho\phi)}{\partial t} + \nabla(\rho \vec{v}\, \phi) = \nabla(\Gamma\, \nabla\phi) + S_\phi} \quad (3.2)$$

The source term S_ϕ in x-direction, for example, may be written as:

$$S_x = -\frac{\partial p}{\partial x} + B_x + V_x$$

where, $B_x \equiv$ body forces

$V_x \equiv$ additional viscous forces

The full derivation of equation (3.2) is given in Appendix A.

3.3 Grid Generation Techniques

3.3.1 Introduction

After the solution domain has been defined for a given fluid flow problem, it is necessary to create a computational grid before any CFD codes, i.e. FDM or FEM software can be employed. Before the gridding process of the solution domain can start, the spatial coordinates of all solid surfaces, inlet, outlets, symmetry, periodic and other geometrical boundary features applying to the problem have to be defined.

To allow more flexibility in terms of a wider range of problems with complex geometries, modern CFD codes use body-fitted grids. As this definition implies, certain grid surfaces are coincident with the boundaries of the solution domain. Figure 3.2 demonstrates that each grid surface from the physical, non-orthogonal and curvilinear coordinate system (ξ, η, φ) can be considered to be a surface of constant value of the computational domain.

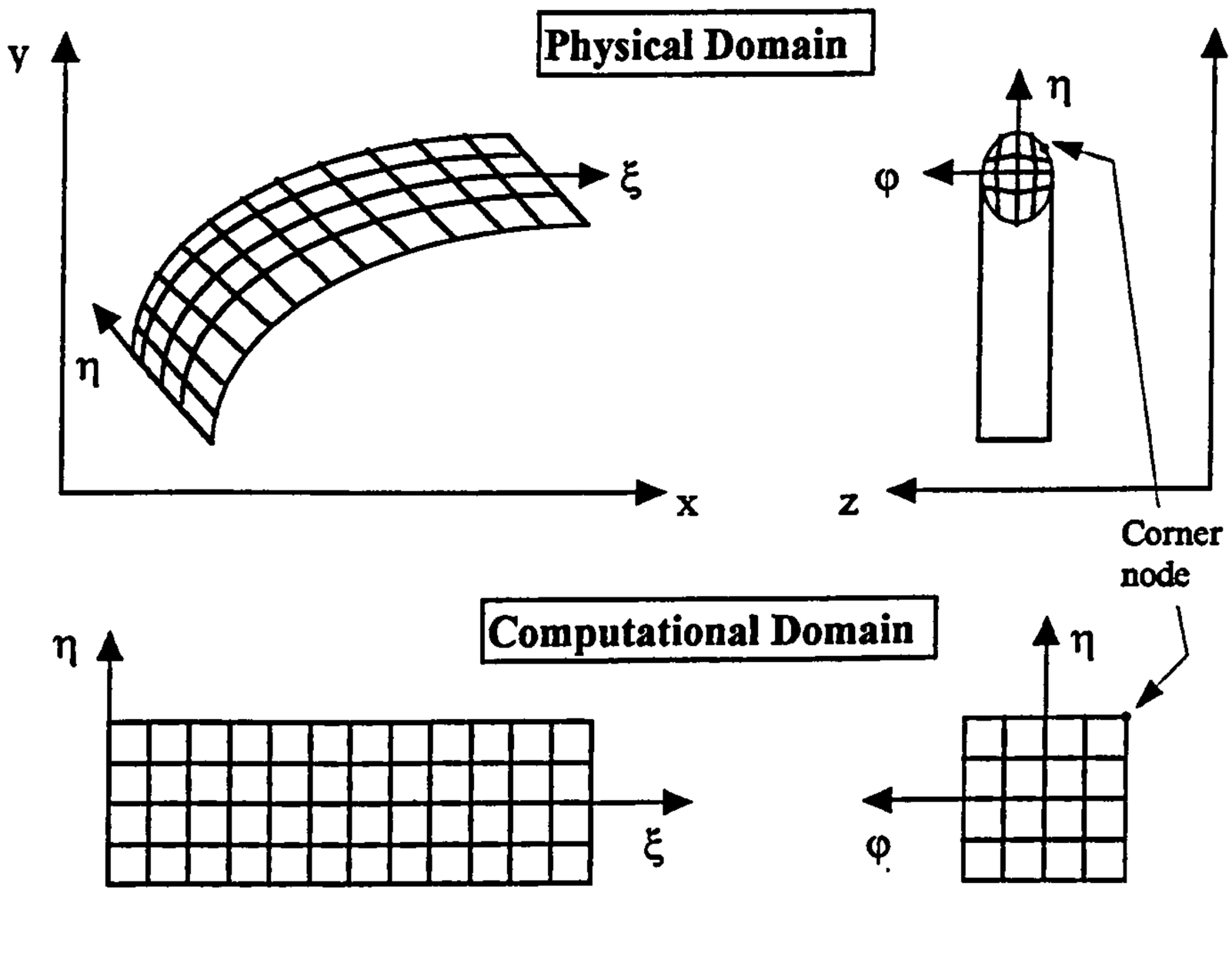

Figure 3.2: Single-block grid

The price for the flexibility of body-fitted grids is an increase in complexities of the governing equations. A so called metric tensor defines the transformation from a rectangular Cartesian computational space to the general, non-orthogonal physical

coordinate system. The transformation is shown using a two-dimensional example of the governing equations. The basic equations in Cartesian coordinates for a two-dimensional incompressible flow are:

Continuity

$$\boxed{\frac{\partial u}{\partial x}+\frac{\partial v}{\partial y}=0} \tag{3.3}$$

x-momentum

$$\boxed{\rho\frac{\partial}{\partial x}uu+\rho\frac{\partial}{\partial y}vu=-\frac{\partial p}{\partial x}+\frac{\partial}{\partial x}\mu\frac{\partial u}{\partial x}+\frac{\partial}{\partial y}\mu\frac{\partial u}{\partial y}+S_x} \tag{3.4}$$

where $S_x=\frac{\partial}{\partial x}\mu\frac{\partial u}{\partial x}+\frac{\partial}{\partial y}\mu\frac{\partial v}{\partial x}$

y-momentum

$$\boxed{\rho\frac{\partial}{\partial x}uv+\rho\frac{\partial}{\partial y}vv=-\frac{\partial p}{\partial y}+\frac{\partial}{\partial x}\mu\frac{\partial v}{\partial x}+\frac{\partial}{\partial y}\mu\frac{\partial v}{\partial y}+S_y} \tag{3.5}$$

where $S_y=\frac{\partial}{\partial x}\mu\frac{\partial u}{\partial y}+\frac{\partial}{\partial y}\mu\frac{\partial v}{\partial y}$

The coordinate transformation to the computational space will be as:

$$x=x(\xi,\eta),\ y=y(\xi,\eta) \tag{3.6}$$

Therefore the exact differentials for the general parameter ϕ are:

$$\frac{\partial\phi}{\partial x}=\frac{\partial\xi}{\partial x}\frac{\partial\phi}{\partial\xi}+\frac{\partial\eta}{\partial x}\frac{\partial\phi}{\partial\eta} \tag{3.7}$$

$$\frac{\partial\phi}{\partial y}=\frac{\partial\xi}{\partial y}\frac{\partial\phi}{\partial\xi}+\frac{\partial\eta}{\partial y}\frac{\partial\phi}{\partial\eta} \tag{3.8}$$

Using the expressions below:

$$\boxed{\frac{\partial \xi}{\partial x}=\frac{1}{J}\frac{\partial y}{\partial \eta}},\quad \boxed{\frac{\partial \xi}{\partial y}=-\frac{1}{J}\frac{\partial x}{\partial \eta}},\quad \boxed{\frac{\partial \eta}{\partial x}=-\frac{1}{J}\frac{\partial y}{\partial \xi}},\quad \boxed{\frac{\partial \eta}{\partial y}=\frac{1}{J}\frac{\partial x}{\partial \xi}} \tag{3.9}$$

where the Jacobi matrix is defined as:

$$J\equiv\frac{\partial(x,y)}{\partial(\xi,\eta)}=\begin{vmatrix}\frac{\partial x}{\partial \xi} & \frac{\partial x}{\partial \eta}\\ \frac{\partial y}{\partial \xi} & \frac{\partial y}{\partial \eta}\end{vmatrix}=\frac{\partial x}{\partial \xi}\frac{\partial y}{\partial \eta}-\frac{\partial x}{\partial \eta}\frac{\partial y}{\partial \xi}$$

Equations (3.7) and (3.8) can be rearranged to:

$$\frac{\partial \phi}{\partial x}=\frac{1}{J}\left[\frac{\partial}{\partial \xi}\left(\frac{\partial y}{\partial \eta}\phi\right)-\frac{\partial}{\partial \eta}\left(\frac{\partial y}{\partial \xi}\phi\right)\right] \tag{3.10}$$

$$\frac{\partial \phi}{\partial y}=\frac{1}{J}\left[\frac{\partial}{\partial \eta}\left(\frac{\partial x}{\partial \xi}\phi\right)-\frac{\partial}{\partial \xi}\left(\frac{\partial x}{\partial \eta}\phi\right)\right] \tag{3.11}$$

Employing equations (3.10) and (3.11) the continuity equation can be expressed in general coordinates as:

$$\boxed{\frac{\partial}{\partial \xi}G_1+\frac{\partial}{\partial \eta}G_2=0} \tag{3.12}$$

where

$$G_1=\frac{\partial y}{\partial \eta}u-\frac{\partial x}{\partial \eta}v,\qquad G_2=\frac{\partial x}{\partial \xi}v-\frac{\partial y}{\partial \xi}u \tag{3.13}$$

Following similar arguments the momentum equations in the general coordinate system yield:

$$\rho\frac{\partial}{\partial\xi}(G_1 u)+\rho\frac{\partial}{\partial\eta}(G_2 u)=-\frac{\partial}{\partial\xi}\left(\frac{\partial y}{\partial\eta}p\right)+\frac{\partial}{\partial\eta}\left(\frac{\partial y}{\partial\xi}p\right)$$
$$+\frac{\partial}{\partial\xi}\left[\frac{1}{J}\mu\left(\alpha\frac{\partial u}{\partial\xi}-\beta\frac{\partial u}{\partial\eta}\right)\right]+\frac{\partial}{\partial\eta}\left[\frac{1}{J}\mu\left(\gamma\frac{\partial u}{\partial\eta}-\beta\frac{\partial u}{\partial\xi}\right)\right]+JS_x \qquad (3.14)$$

$$\rho\frac{\partial}{\partial\xi}(G_1 v)+\rho\frac{\partial}{\partial\eta}(G_2 v)=-\frac{\partial}{\partial\eta}\left(\frac{\partial x}{\partial\xi}p\right)+\frac{\partial}{\partial\xi}\left(\frac{\partial x}{\partial\eta}p\right)$$
$$+\frac{\partial}{\partial\xi}\left[\frac{1}{J}\mu\left(\alpha\frac{\partial v}{\partial\xi}-\beta\frac{\partial v}{\partial\eta}\right)\right]+\frac{\partial}{\partial\eta}\left[\frac{1}{J}\mu\left(\gamma\frac{\partial v}{\partial\eta}-\beta\frac{\partial v}{\partial\xi}\right)\right]+JS_y \qquad (3.15)$$

where

$$\alpha=\left(\frac{\partial x}{\partial\eta}\right)^2+\left(\frac{\partial y}{\partial\eta}\right)^2,\qquad \beta=\frac{\partial x\partial x}{\partial\xi\partial\eta}+\frac{\partial y\partial y}{\partial\xi\partial\eta},\qquad \gamma=\left(\frac{\partial x}{\partial\xi}\right)^2+\left(\frac{\partial y}{\partial\xi}\right)^2$$

3.3.2 Grid Topologies

There are essentially three different types of numerical grids:

- Single block or fully structured grids
- Multi-block or block-structured grids
- Unstructured grids

Single-Block Grids

The simplest version of a numerical grid is the single-block grid which is shown in Figure 3.2. This type of grid is traditionally employed in FDM where the physical curved domain is transformed into the rectangular computational solution domain, i.e. into a hexahedron shape. But even if the geometry is relatively simple like the elliptic cross section, shown in Figure 3.2, it can be seen that the corner grid cells are substantially distorted in physical space to the extent that two of their sides are very nearly at 180° to each other. As a result of this, it can be shown that the accuracy of the solution, particularly the shear stress near the wall will be degraded.

Multi-block Grids

This type of mesh structure could be seen as a further development of the single-block grid. If the geometry of the solution domain is complex it becomes necessary to divide the domain into several subdomains which are called grid blocks. Each block is a hexahedral in computational space, and as the individual blocks have simpler boundary geometries the grid generation becomes easier in the individual blocks. Referring to Figure 3.3, where a single-block grid was employed to discretise an elliptic shape, the great disadvantage of this approach was the significantly distorted corner cells. Using the multi-block approach, the improvement of the grid structure and thus the accuracy of the flow field solution, is apparent (see Figure 3.3). Specifically there are no distorted corner cells in the multi-block grid.

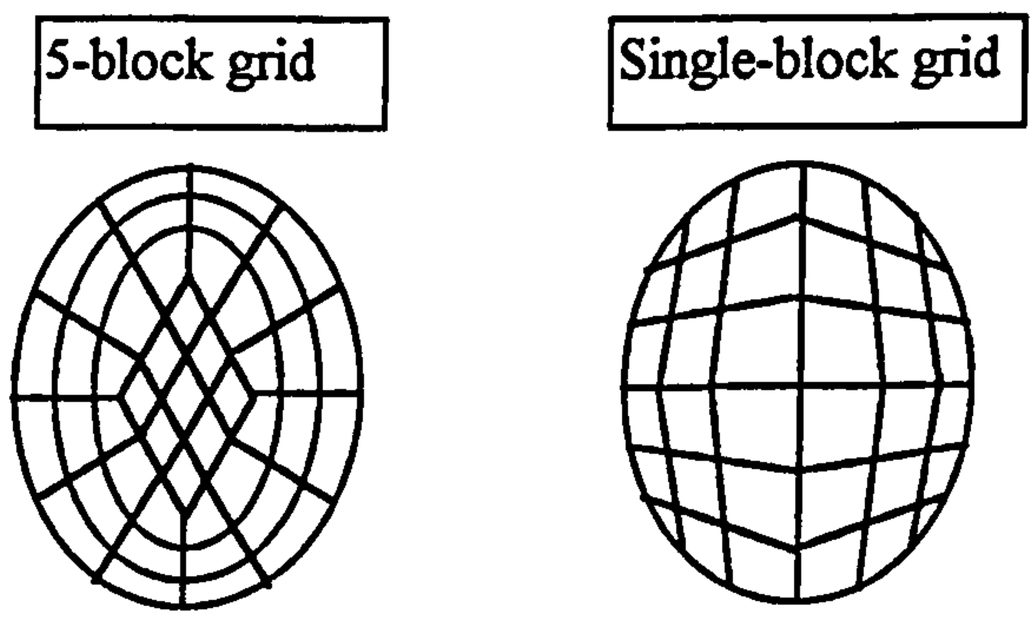

Figure 3.3: Example of a multi-block and a single-block grid for the same shape

Multi-block grids are very powerful because they provide a high variety of mesh shapes.

Unstructured Grids

These grids were traditionally employed in FEM methods. They allow a range of cell shapes. Any combinations of triangular, rectangular and curved-sided cells, may be used. The main feature, in addition to the arbitrary cell shape, is that the number of cells surrounding any one node in the grid is not constant throughout the grid, unlike a multi-block structured grid. But there are two negative aspects. First a local

coordinate system is required for each grid element. Secondly, information has to be stored which define the neighbours of each individual element. As a result, computer storage requirements are substantially more than in the case of the multi-block grid method. However, there are applications where the high flexibility of arbitrary cell shapes is necessary.

3.3.3 Generation Methods

There are, in principal, two main methods of grid generation, one is based on algebraic expressions, and in the other method, partial differential equations are solved.

Algebraic Method

The main task is, like in any other grid generation method, to map the physical domain (x, y) onto the computational domain (ξ, η). The way to solve this problem, in general, may be divided into two steps (see Schoenung, 1990: pp. 77-99). First, the physical domain boundary (x, y) is mapped onto the computational domain boundary (ξ, η). Secondly an information transfer from the boundary to the interior points is achieved by employing an interpolation scheme.

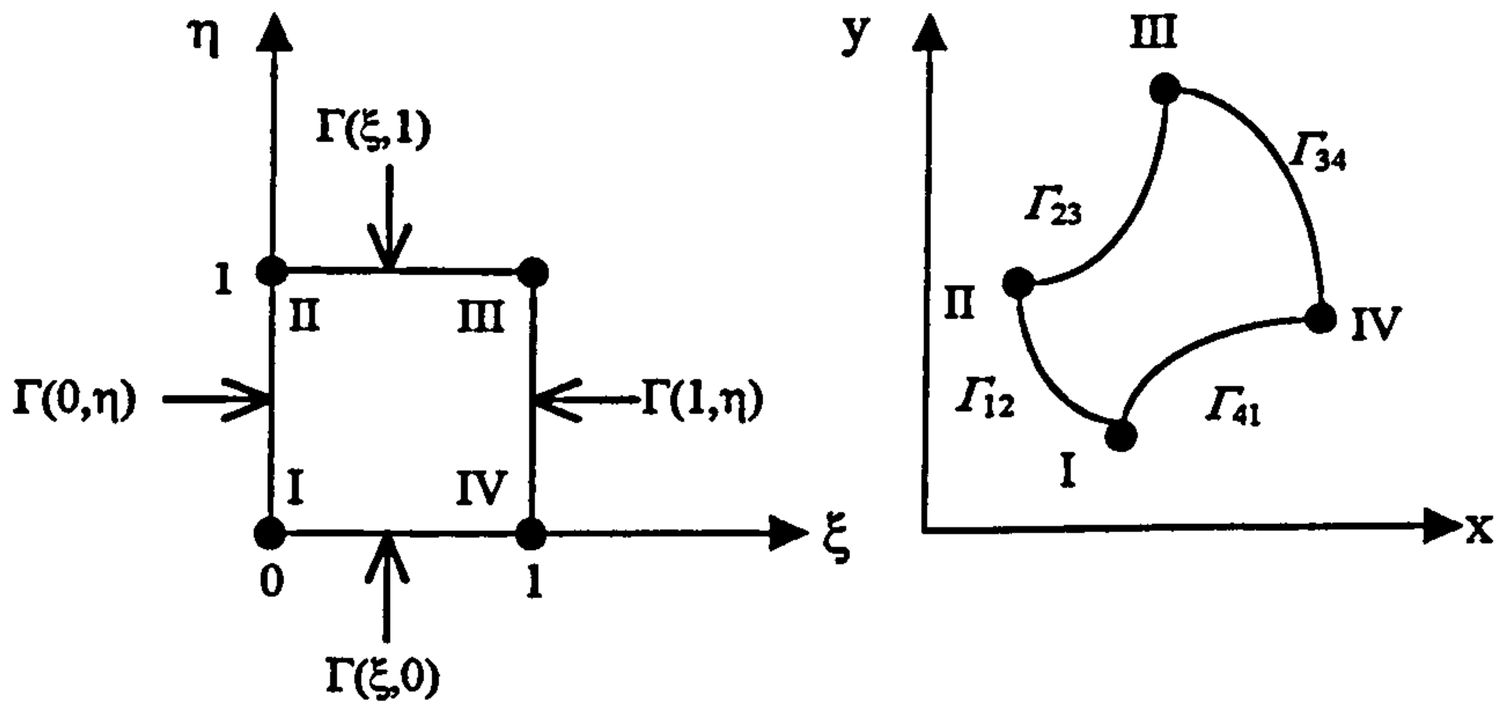

Figure 3.4: Boundary transformation

Therefore a function F is needed to map the physical boundary (x, y) onto the computational boundary (ξ, η) (see Figure 3.4) as:

$$\Gamma_{12} \rightarrow \Gamma(0,\eta)$$
$$\Gamma_{23} \rightarrow \Gamma(\xi,1)$$
$$\Gamma_{34} \rightarrow \Gamma(1,\eta)$$
$$\Gamma_{41} \rightarrow \Gamma(\xi,0)$$

This function F can be determined with a parameterisation of the boundaries (Γ_{12}, Γ_{23}, Γ_{34}, Γ_{41}) via their arc length (L_{12}, L_{23}, L_{34}, L_{41}) which are calculated from the given Cartesian coordinates (x, y) of the physical points I to IV, so that:

$$\Gamma_{12} = \begin{pmatrix} x(l) \\ y(l) \end{pmatrix} \quad \text{where } 0 \le l \le L_{12}$$

Through normalising with the arc length L ($\xi = l/L$ and $\eta = l/L$) the required parameterisation of the boundaries is derived as:

$$F = \begin{bmatrix} x(0,\eta) \\ y(0,\eta) \end{bmatrix} \qquad \Gamma_{12} \rightarrow \Gamma(0,\eta)$$

Using similar arguments, the mapping functions for all boundaries can be found; i.e.,

$$F = F(\xi,\eta) = \begin{bmatrix} x(\xi,\eta) \\ y(\xi,\eta) \end{bmatrix}$$

For more simple boundaries it is often possible to find analytical expressions for the mapping function F.

The second step is to find an appropriate interpolation scheme which ensures monotonic information transfer from the boundaries to the interior of the computational solution domain. This process is termed 'blending'. The transfinite interpolation method of Gordon & Hall (1973) is the most popular blending scheme for two dimensions. Eriksson (1982) extended this method to three dimensions. The scheme of Gordon & Hall (1973) uses two interpolation functions, one for each Cartesian coordinate direction (ξ, η). These two functions have to fulfil two conditions. First, the start and end point have to be coincident with the boundaries of the Cartesian coordinate system, i.e. the value of these two points have to be 0 or 1. Secondly, the interpolation functions have to have a monotonic variation between the start and the end point. A first order polynomial matches these two conditions and

hence is an appropriate interpolation function. Higher-order polynomials may be used if more conditions like orthogonality have to be satisfied, e.g.

- Lagrange-technique
- Hermite technique
- Splines
- Exponential functions

Finally, the two interpolation functions for the two Cartesian directions have to be connected with the boundary mapping functions F to ensure a monotonic information transfer into the interior of the solution domain. The "Boolean sum method" is the preferred scheme and it allows a multi-directional interpolation from the entire boundary into the solution domain. For a detailed description of the algebraic grid generation method see Thompson et al. (1985: pp. 279-326). The main advantage of the algebraic method is that it does not consume much time and is thus a proper interactive generation scheme. A disadvantage is that grid overlapping often occurs, but this can be avoided by constraint curves.

Partial Differential Method

In general, partial differential equations (PDE) of second order are employed to generate grids but biharmonic fourth-order equations are also used. According to the type of equations used, the PDE method, is classified into elliptic, hyperbolic and parabolic grid generation methods. One suggestion of the two-dimensional hyperbolic scheme is from Steger & Chaussee (1980) and for the three-dimensional case from Bridgeman et al. (1982). A combination of parabolic and hyperbolic grid generation method is examined by Nakamura & Suzuki (1987). A mixture of elliptic and hyperbolic methods is the hybrid scheme described by Spardling et al. (1991). However, the most common method is the elliptic grid generation scheme which is described briefly below.

Elliptic grid generation

Either Laplace- or Poisson-equations are solved in the elliptic generation scheme. Due to the smoothing character of Laplace operators this method tends to produce smooth grid distributions. This scheme is based on the fact that the Laplace equation describes

a body-fitted mesh which coincides with the streamlines and potential lines of a two-dimensional irrotational flow. Both the potential and the stream function are solved via the Laplace equation. In practice the inverse Laplace equations have to be solved because the boundary coordinates are known in the Cartesian (ξ, η) coordinate system, i.e. $x(\xi, \eta)$ and $y(\xi, \eta)$. For the two-dimensional case the inverse Laplace equations are:

$$\alpha\frac{\partial^2 x}{\partial \xi^2} - 2\beta\frac{\partial^2 x}{\partial \xi \partial \eta} + \gamma\frac{\partial^2 x}{\partial \eta^2} = 0 \qquad \alpha\frac{\partial^2 y}{\partial \xi^2} - 2\beta\frac{\partial^2 y}{\partial \xi \partial \eta} + \gamma\frac{\partial^2 y}{\partial \eta^2} = 0$$

where

$$\alpha = \left(\frac{\partial x}{\partial \eta}\right)^2 + \left(\frac{\partial y}{\partial \eta}\right)^2, \qquad \beta = \frac{\partial x}{\partial \xi}\frac{\partial x}{\partial \eta} + \frac{\partial y}{\partial \xi}\frac{\partial y}{\partial \eta}, \qquad \gamma = \left(\frac{\partial x}{\partial \xi}\right)^2 + \left(\frac{\partial y}{\partial \xi}\right)^2$$

For a solution of the Laplace equations to exist, the Jacobi matrix must be not equal zero in any point in the solution domain so that mesh overlapping is avoided.

$$J = \begin{vmatrix} \frac{\partial x}{\partial \xi} & \frac{\partial x}{\partial \eta} \\ \frac{\partial y}{\partial \xi} & \frac{\partial y}{\partial \eta} \end{vmatrix} \neq 0$$

If there is an additional requirement of orthogonality, then the solution of the Laplace equations have to have the form of the Cauchy-Riemann-equations for any interior point and the boundaries. As a result the coefficient β becomes zero and the original Laplace equations for a two-dimensional case will be simplified to:

$$\frac{\partial x}{\partial \xi} = a\frac{\partial y}{\partial \eta} \qquad \frac{\partial x}{\partial \eta} = -\frac{1}{a}\frac{\partial y}{\partial \xi}$$

where

$$a = \left(\frac{\alpha}{\gamma}\right)^{-1/2} = \text{constant}$$

The orthogonality condition is only possible for the two dimensional case (Sorenson, 1980) and requires mixed boundary conditions, i.e. Dirichlet- and Neumann (gradient) boundary conditions. This may result in the grid points on the boundary being shifted and an unwanted corner node distribution generated. If only Dirichlet boundary conditions are applied the boundary nodes are fixed but orthogonality is not guaranteed. One way to improve and control the grid distribution is to add source terms to the right hand side of the Laplace equation e.g.:

$$\frac{\partial^2 \xi}{\partial x^2}+\frac{\partial^2 \xi}{\partial y^2}=P(\xi,\eta), \qquad \frac{\partial^2 \eta}{\partial x^2}+\frac{\partial^2 \eta}{\partial y^2}=Q(\xi,\eta)$$

In analogy to the original Laplace equations, the source terms have to be inverted and solved with the appropriate boundary conditions. Mesh overlapping is avoided if the Jacobi matrix is not equal to zero, but there is no explicit control of orthogonality and thus the Dirichlet boundary condition is applied in most cases. Shieh (1984) extended Sorenson's method (1980) to three dimensions via three source terms. Warsi (1986) introduced a differential method, based on Gauss' equations, to smooth the surface grid in the three-dimensional case.

The Poisson equations describe heat transfer and therefore the source terms are analogous to heat sinks and sources. The grid lines could be interpreted as isothermals and so the heat source terms tend to move the grid lines away from the source whereas the sink terms attract the grid lines towards the sink.

There are also fourth order PDE schemes which solve biharmonic equations and thus require boundary conditions on all boundaries, i.e. Dirichlet- and Neumann conditions. As a result there is more control of the grid generation process. Sparis (1985) developed the biharmonic method for a two-dimensional case.

Adaptive Gridding

In flows where locally high gradients occur, like shocks or flames, the fluid quantities change abruptly and the adaptive gridding method is of great advantage. This grid technique redistributes the grid density during the numerical calculation process depending on the local flow field. Therefore the grid distribution will be "adapted" to

the results of the governing equations. There are essentially two different approaches to adaptive meshing. These are the global and the local refinement techniques. Both grid generation methods (algebraic and PDE schemes) described before can be incorporated into adaptive gridding because all that is required is the recomputing of the grid metrics in the flow solver at each adaption cycle.

• Global refinement

In the global refinement method the total number of grid points are constant so that a shift of nodes towards regions of high gradients results in the grid becoming coarser in the rest of the solution domain. The new grid will have the same number of grid points but with a different local node concentration.

Most of the mesh-redistribution methods are based on the variational principle, e.g. Warsi & Thompson (1990). Kim & Thompson (1990) suggested a modification to the source terms (see Elliptic grid generation) in the elliptic mesh generation method so that a grid clustering is produced in areas of high solution gradient or truncation error. Minimisation functionals are often employed to construct, simultaneously both the various solution-based criteria; e.g. truncation error or gradients, and grid quality criteria; e.g. orthogonality or grid smoothness.

• Local refinement

This approach changes the local grid concentration, where high gradients occur, via additional grid points and does not shift points from the rest of the solution domain to the regions of high flow gradients. Therefore no regions of coarser grid distribution will be generated in contrast to the global refinement approach.

Berger & Jameson (1984) and Quirk (1994) suggested a block structured grid refinement where regular shaped regions are uniformly refined. In contrast Davis & Dannehoffer (1991) and Aftosmis (1993) refined the grid only where it was necessary and treated the total final grid as unstructured data.

The implementation procedure is much easier in the case of Berger & Jameson (1984) and Quirk (1994) structured grid approach than in Davis & Dannehoffer (1991) and Aftosmis (1993) unstructured grid method. The grid enrichment is more advanced in Davis & Dannehoffer (1991) and Aftosmis (1993) suggestion than in Berger & Jameson (1984) and Quirk (1994) approach. Recently Dannehoffer (1991) combined both approaches.

3.4 Discretisation Methods of the Navier-Stokes Equations

3.4.1 Introduction

A CFD study is similar to an experimental investigation in that, in both cases, flow quantities are determined at discrete points within the domain of interest. However, the great advantage of the numerical approach is the high degree of flexibility. If the grid is sufficiently fine, so that all flow phenomena are properly captured, any quantity at any location in the flow field may be determined. The Navier-Stokes equations are valid over laminar, transitional, turbulent and sonic range flows. If an analytical solution of the Navier-Stokes equations could be found, it would be applicable to a class of flows. However, employing the CFD technique, a particular flow configuration has to be considered. As in the experimental case, a single solution for one defined flow configuration will be achieved.

There are several numerical methods to discretise the equations, i.e. to transform the Navier-Stokes equations from their original partial differential form into an algebraic form. The two main discretisation methods are described below. These are:

- Finite Volume Method (FVM)
- Finite Element Method (FEM)

The preferred approach in aeronautical applications is the FVM method, which is described briefly in the following section. The FEM method was originally developed for stress analysis in structural systems and is still used. The use of unstructured grids allowed mesh clustering of very high density at zones of particular interest. However, today this advantage has disappeared because more generalised gridding techniques have been developed for the FVM method.

Throughout this research project the CFD code CFX 4 (AEA Technology) was used. This code employs the Finite Volume Method for the discretisation of the Navier-Stokes equations and this method will be described briefly below.

3.4.2 Finite Volume Method

The solution domain is divided into a number of non-overlapping control volumes with a node point placed at the centre of each control volume (see Figure 3.5).

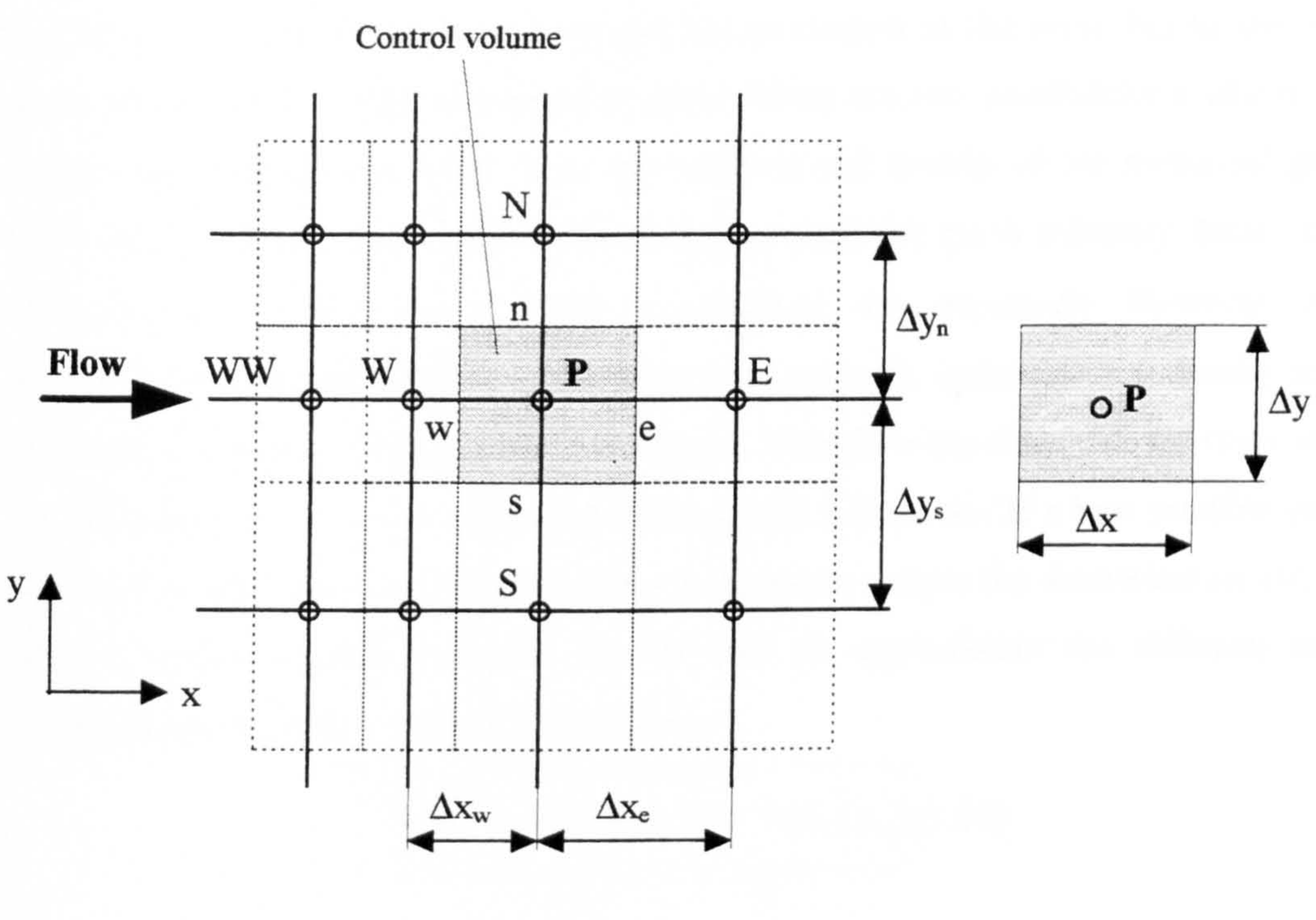

Figure 3.5: Control volume in a non-staggered grid with compass notation

The momentum equations are integrated over each control volume. The required integrals are evaluated and the variation of the general parameter ϕ (= u, v, w) over a cell has to be assumed. A linear variation is usually chosen.

The result of this procedure is a set of three non-linear and coupled algebraic equations for each control volume. Each set contains four unknowns; one for each of the three velocity components and one for the pressure. A fourth equation, for the pressure, is derived from the continuity equation. The derivation of these equations will be discussed in detail in a later section (Pressure-Velocity Correction Method).

The control-volume formulation satisfies the integral conservation of mass, momentum and energy over any group of control volumes and therefore over the whole solution domain. The conservation characteristic is independent of the number of grid points and thus, even a coarse grid solution provides exact integral balances.

The accuracy of a numerical solution depends on minimising two main errors. The first is the round-off error and the second the discretisation or truncation error. The round-off error is the difference between the numerical solution and the exact discretised solution. The discretisation error is the exact discretised result subtracted from the analytical solution. The round-off error is a function of the computer architecture and hence the code developer has no control of this error, but he/she can exert some control on the discretisation error. There are two possibilities available to reduce the discretisation error. First the structure and density of the numerical grid may be considered. If the grid in all directions could be made infinitely dense, the variation of the parameter ϕ could be described very accurately. However, the computer capacity is finite, thus a compromise between optimum grid density and available computing resource has to be found. Therefore the discretisation error can be minimised only to a certain extent through grid refinement. If a best possible grid has been found, there is a second avenue available to reduce the discretisation error. That is, more accurate formulas can be used to approximate the diffusion and advection terms in the momentum equations.

$$\boxed{\frac{\partial(\rho\phi)}{\partial t}+\nabla(\rho\vec{v}\,\phi)=\nabla(\Gamma\,\nabla\phi)+S_\phi} \quad (3.16)$$

Advection terms — Diffusion terms

Unfortunately the choice of the advection scheme affects not only accuracy but also influences convergence. The modeller has often to reach a compromise between achievable accuracy and a stable solution.

In the Finite Volume code, CFX 4, employed for this project, the primitive variables are defined at the centre of the control volume. The governing equations are integrated over each control volume, i.e. over all control faces.

$$\boxed{\int\frac{\partial(\rho\phi)}{\partial t}dV+\int\nabla(\rho\vec{v}\,\phi)\cdot n\,dA-\int\nabla(\Gamma\,\nabla\phi)\cdot n\,dA=\int S_\phi n dV} \quad (3.17)$$

In a two-dimensional case the set of equations are:

$$\boxed{\iint \nabla(\rho \vec{v}\ \phi)dxdy = \iint \nabla(\Gamma\ \nabla\phi)dxdy + \iint S_\phi dxdy - \iint \frac{\partial(\rho\phi)}{\partial t}dxdy} \quad (3.18)$$

Advection terms — Diffusion terms

In the following section (Advection Term Modelling) various approximation methods for the advection terms are described. All of these schemes are called differencing methods even if they are not derived from Finite Difference approaches.

In a simplified one-dimensional (1-D) case with constant Δx, it can be shown that approximating the governing equations using Finite Differencing results in the same algebraic equation than employing the Finite Volume approach. In the case of a 1-D, steady flow, the momentum equation may be simplified to;

$$\boxed{\frac{\partial(u\phi)}{\partial x} - \frac{\partial}{\partial x}\Gamma\frac{\partial\phi}{\partial x} = 0} \quad (3.19)$$

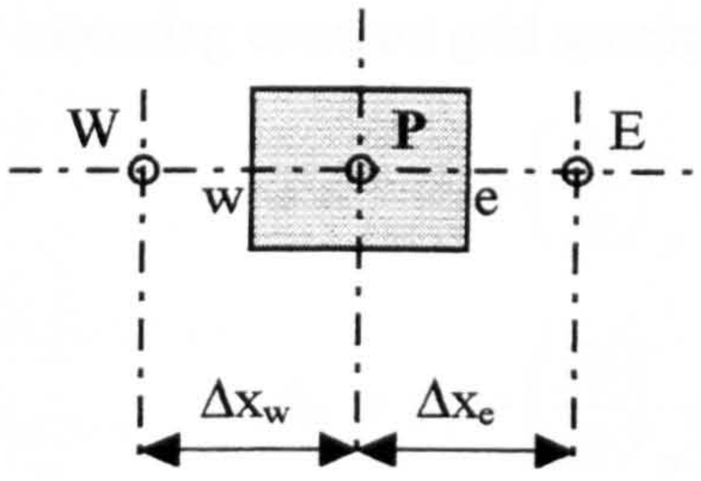

Figure 3.6: Control volume with compass notation

In the Finite Volume approach the first derivative (see Equation 3.19) can be approximated; i.e.,

$$\boxed{\int_w^e \frac{\partial\phi}{\partial x}dx = \phi_e - \phi_w} \quad (3.20)$$

Using simple averaging of the parameter ϕ on the east and on the west face (see Figure 3.6); i.e.,

$$\phi_e = \frac{1}{2}(\phi_P + \phi_E), \qquad \phi_w = \frac{1}{2}(\phi_P + \phi_W)$$

Equation (3.20) becomes

$$\phi_e - \phi_w = \frac{1}{2}(\phi_E - \phi_W) \quad (3.21)$$

The second derivative (see Equation 3.19) can be approximated as; i.e.,

$$\int_w^e \frac{\partial}{\partial x}\Gamma\frac{\partial \phi}{\partial x}dx = \Gamma\left(\left.\frac{\partial \phi}{\partial x}\right|_e - \left.\frac{\partial \phi}{\partial x}\right|_w\right)$$
$$= \Gamma\left(\frac{\phi_E - \phi_P}{\Delta x} - \frac{\phi_P - \phi_W}{\Delta x}\right) \quad (3.22)$$

Substituting the approximations for the first and the second derivative into the one-dimensional momentum (Equation 3.19) and dividing by Δx, it can be written,

$$\boxed{u\frac{(\phi_E - \phi_W)}{2\Delta x} - \Gamma\frac{\phi_E - 2\phi_P + \phi_W}{\Delta x^2} = 0} \quad (3.23)$$

Equation (3.23) can also determined by Finite Differencing. Specifically, the first derivative of the parameter ϕ (see Equation 3.19) at the east node (see Figure 3.6) and at the west node, for example, can be expressed in terms of a Taylor series, assuming constant grid spacing (Δx = constant).

$$\phi_E = \phi_P + \left(\frac{\partial \phi}{\partial x}\right)_P \Delta x + \left(\frac{\partial^2 \phi}{\partial x^2}\right)_P \frac{\Delta x^2}{2} + \left(\frac{\partial^3 \phi}{\partial x^3}\right)_P \frac{\Delta x^3}{6} + \ldots \quad (3.24)$$

$$\phi_W = \phi_P - \left(\frac{\partial \phi}{\partial x}\right)_P \Delta x + \left(\frac{\partial^2 \phi}{\partial x^2}\right)_P \frac{\Delta x^2}{2} - \left(\frac{\partial^3 \phi}{\partial x^3}\right)_P \frac{\Delta x^3}{6} + \ldots \quad (3.25)$$

Subtracting Equation (3.24) from Equation (3.25) and rearranging, the finite-difference approximation of second-order accuracy is constructed. The remaining term on the right side constitute the truncation error (see Equation 3.26); i.e.,

$$\phi_E - \phi_W = 2\left(\frac{\partial \phi}{\partial x}\right)_P \Delta x + 2\left(\frac{\partial^3 \phi}{\partial x^3}\right)_P \frac{\Delta x^3}{6} + \ldots$$

$$\boxed{\left(\frac{\partial \phi}{\partial x}\right)_P = \frac{\phi_E - \phi_W}{2\Delta x} - \underbrace{\left(\frac{\partial^3 \phi}{\partial x^3}\right)_P \frac{\Delta x^2}{6} + \ldots}_{\text{Truncation error}}} \quad (3.26)$$

$$\boxed{\left(\frac{\partial \phi}{\partial x}\right)_P = \frac{\phi_E - \phi_W}{2\Delta x} + O(\Delta x)^2} \quad (3.27)$$

The second derivative of the parameter ϕ (see Equation 3.19) can be obtained by summing the Taylor series expansions equation (3.24) and (3.25); i.e.,

$$\phi_E + \phi_W = 2\phi_P + \left(\frac{\partial^2 \phi}{\partial x^2}\right)_P \Delta x^2 + \left(\frac{\partial^4 \phi}{\partial x^4}\right)_P \frac{\Delta x^4}{12} + \ldots$$

$$\left(\frac{\partial^2 \phi}{\partial x^2}\right)_P = \frac{\phi_E - 2\phi_P + \phi_W}{\Delta x^2} \underbrace{- \left(\frac{\partial^4 \phi}{\partial x^4}\right)_P \frac{\Delta x^2}{12} + \ldots}_{\text{Truncation error}} \quad (3.28)$$

$$\boxed{\left(\frac{\partial^2 \phi}{\partial x^2}\right)_P = \frac{\phi_E - 2\phi_P + \phi_W}{\Delta x^2} + O\left(\Delta x^2\right)} \quad (3.29)$$

Approximating the 1-D governing equations (3.19) using the Taylor series expressions (Equations 3.27 and 3.28) for the first and second derivatives yields;

$$\boxed{u\frac{(\phi_E - \phi_W)}{2\Delta x} - \Gamma \frac{\phi_E - 2\phi_P + \phi_W}{\Delta x^2} = 0} \quad (3.30)$$

Comparing the algebraic equation (3.30), derived using central differencing via Taylor series expansion, and employing the Finite Volume approach (see Equation 3.23), yield the same approximation for the first and second derivatives of equation (3.19). Both approximations are second order accurate; i.e., the truncation or discretisation error is of second-order in Δx.

We showed for a simplified one-dimensional case, that the Finite Volume approach yields exactly the same algebraic approximations as Finite Differencing. The two-dimensional governing equations (3.18) may then be approximated as follows overleaf. The diffusion terms may be discretised as:

$$\begin{aligned}
\iint \nabla(\Gamma\nabla\phi)dxdy &= \iint\left[\frac{\partial}{\partial x}\left(\Gamma\frac{\partial\phi}{\partial x}\right)+\frac{\partial}{\partial y}\left(\Gamma\frac{\partial\phi}{\partial y}\right)\right]dxdy \\
&= \int\left[\Gamma\frac{\partial\phi}{\partial x}\right]_w^e dy+\int\left[\Gamma\frac{\partial\phi}{\partial y}\right]_s^n dx \\
&= \left[\Gamma\frac{\partial\phi}{\partial x}\right]_e dy-\left[\Gamma\frac{\partial\phi}{\partial x}\right]_w dy \\
&\quad+\left[\Gamma\frac{\partial\phi}{\partial y}\right]_n dx-\left[\Gamma\frac{\partial\phi}{\partial y}\right]_s dx \\
&= \frac{\Gamma}{\Delta x_e}(\phi_E-\phi_P)\Delta y-\frac{\Gamma}{\Delta x_w}(\phi_P-\phi_W)\Delta y \\
&\quad+\frac{\Gamma}{\Delta y_n}(\phi_N-\phi_P)\Delta x-\frac{\Gamma}{\Delta y_s}(\phi_P-\phi_S)\Delta x
\end{aligned} \tag{3.31}$$

The advection terms from equation (3.18) are discretised, using central differencing, for example, more advanced discretisation schemes are discussed later (see Section Advection Term Modelling).

$$\begin{aligned}
\iint \nabla(\rho\vec{v}\,\phi)dxdy &= \iint\left[\frac{\partial(\rho u\phi)}{\partial x}+\frac{\partial(\rho v\phi)}{\partial y}\right]dxdy \\
&= \int[\rho u\phi]_w^e dy+\int[\rho v\phi]_s^n dx \\
&= (\rho u_e\phi_e-\rho u_w\phi_w)\Delta y+(\rho v_n\phi_n-\rho v_s\phi_s)\Delta x \\
&= \rho u_e\frac{(\phi_E+\phi_P)}{2}\Delta y-\rho u_w\frac{(\phi_W+\phi_P)}{2}\Delta y \\
&\quad+\rho v_n\frac{(\phi_N+\phi_P)}{2}\Delta x-\rho v_s\frac{(\phi_S+\phi_P)}{2}\Delta x
\end{aligned} \tag{3.32}$$

Substituting the diffusion and advection terms in equation (3.18) by the discretised algebraic expressions gives,

$$\begin{aligned}
&\phi_P\left(\frac{1}{2}\rho u_e\Delta y+D_e\Delta y-\frac{1}{2}\rho u_w\Delta y+D_w\Delta y+\frac{1}{2}\rho v_n\Delta x+D_n\Delta x-\frac{1}{2}\rho v_s\Delta x+D_s\Delta x\right) \\
&=\phi_E\left(-\frac{1}{2}\rho u_e\Delta y+D_e\Delta y\right)+\phi_W\left(\frac{1}{2}\rho u_w\Delta y+D_w\Delta y\right) \\
&\quad+\phi_N\left(-\frac{1}{2}\rho v_n\Delta x+D_n\Delta x\right)+\phi_S\left(\frac{1}{2}\rho v_s\Delta x+D_s\Delta x\right)+b
\end{aligned}$$

where

$$D_e = \frac{\Gamma}{\Delta x_e}, \quad D_w = \frac{\Gamma}{\Delta x_w}, \quad D_n = \frac{\Gamma}{\Delta y_n}, \quad D_s = \frac{\Gamma}{\Delta y_s}$$

The discretised equation in two dimensions can be written as:

$$\boxed{a_P \phi_P = a_E \phi_E + a_W \phi_W + a_N \phi_N + a_S \phi_S + b} \quad (3.33)$$

where

$$a_E = \left(D_e - \frac{1}{2}\rho u_e\right)\Delta y, \qquad a_W = \left(D_w + \frac{1}{2}\rho u_w\right)\Delta y, \qquad a_N = \left(D_n - \frac{1}{2}\rho v_n\right)\Delta x$$

$$a_S = \left(D_s + \frac{1}{2}\rho v_s\right)\Delta x$$

and it can be shown, by invoking continuity, that

$$a_P = a_E + a_W + a_N + a_S$$

The coefficient b of equation (3.33) is the discrete version of the source term S_ϕ; i.e.,

$$b = S_\phi \Delta x \Delta y$$

$$S_u = -\frac{\partial p}{\partial x} + B_x + V_x - \frac{\partial(\rho\phi)}{\partial t}$$

$$S_v = -\frac{\partial p}{\partial y} + B_y + V_y - \frac{\partial(\rho\phi)}{\partial t}$$

The source term can be linearised following Patankar's suggestion (Patankar, 1980: pp. 35-36) as $S_\phi = S_C + S_P \phi_P$ and a_P is substituted by $a_P - S_P$.

The quantity S_P has to be negative, and its inclusion in a_P enhances the diagonal dominance of the solution matrix.

The resulting set of algebraic equations (3.33) are solved using iterative methods. The calculation process is stopped when some preset convergence criterion has been reached. No CFD codes employ point solvers, e.g. Gaussian Elimination, due to slow convergence. Many CFD codes employ block iterative solvers to enhance the convergence, for example, line-by-line Gauss-Seidel, ADI (Alternating-direction-implicit technique) or Stone's method. For stability reasons transient flows are usually

solved using implicit methods such as the Backward Euler scheme. The two-step Crank-Nicolsen scheme is also used.

Advection Term Modelling

In the following, various advection models will be discussed. These are generally known as Differencing schemes even though they are derived using the Finite Volume technique. However, it was shown in the previous section that the FVM approach and the Finite Differencing scheme can yield identical algebraic approximations of the governing equations, under certain circumstances. Therefore it is valid to call these approximations Differencing schemes.

Central differencing (CDS)

The central differencing method is probably the most obvious scheme to discretise the advection terms because the value of ϕ_w at the west cell face (see Figure 3.5) is approximated from the mean value of the surrounding central node variables, ϕ_W and ϕ_P; i.e.,

$$\boxed{\phi_w = \frac{1}{2}(\phi_W + \phi_P)} \quad (3.34)$$

This scheme is second-order accurate but it is not stable if $Re_C > 2$. The cell Reynolds number Re_C is defined as:

$$\boxed{\mathrm{Re}_c = \frac{u\Delta x}{\upsilon} \propto \frac{Convection}{Diffusion}} \quad \text{with: } \upsilon = \frac{\mu}{\rho}$$

Upwind differencing (UDS)

The quantity ϕ_w on the west cell face (see Figure 3.5) is set equal to either ϕ_W or ϕ_P, depending on the local flow direction; i.e.,

$$\boxed{\phi_w = \begin{cases} \phi_W, & \text{if } u_w > 0 \\ \phi_P, & \text{if } u_w < 0 \end{cases}} \quad (3.35)$$

The upwind method is first-order accurate and is the simplest in a series of other upwind schemes. This scheme is unconditionally stable but it can introduce significant artificial viscosity which tends to "smear" the solution. This method was first

introduced by Courant et al. (1952) and reintroduced by Gentry et al. (1966) and Runchal & Wolfstein (1969).

In CFX 4 seven different advection schemes are available. The Hybrid unconditionally stable method (Spalding, 1972) is employed by default. This scheme operates between second-order central differencing and first-order upwind differencing depending on the cell Reynolds number; i.e.,

Hybrid differencing (HDS):

If $|Re_C| \geq 2$ $\Rightarrow$ Convection is dominant and diffusion is ignored

$\Rightarrow$ Upwind differencing (UDS)

If $|Re_C| < 2$ $\Rightarrow$ Convection and diffusion are of equal importance

$\Rightarrow$ Central differencing (CDS)

Higher order upwind differencing (HUW)

The second upwind scheme is the HUW method which extrapolates to the face from two nodal points further upstream from the west cell face (see Figure 3.5). It was found to be fairly robust (see CFX 4 Manual, 1995).

$$\phi_w = \begin{cases} \frac{3}{2}\phi_W + \frac{1}{2}\phi_{WW}, & \text{if } u_w > 0 \\ \frac{3}{2}\phi_P + \frac{1}{2}\phi_E, & \text{if } u_w < 0 \end{cases} \quad (3.36)$$

Quadratic upwind differencing (QUICK)

This approximation method from Leonard (1979) is third-order accurate.

$$\phi_w = \begin{cases} \frac{3}{8}\phi_P + \frac{3}{4}\phi_W - \frac{1}{8}\phi_{WW}, & \text{if } u_w > 0 \\ \frac{3}{8}\phi_W + \frac{3}{4}\phi_P - \frac{1}{8}\phi_E, & \text{if } u_w < 0 \end{cases} \quad (3.37)$$

Through the additional interpolation from the nodal point, i.e. ϕ_P, downstream located from the west cell face (see Figure 3.5), the method tends to be slightly unstable.

CCCT

In fully turbulent flow higher-order upwind schemes, especially the third-order Quick-method, tend to overshoot, and the results obtain a non-physical character such as a negative turbulent kinetic energy. To prevent this effect the CCCT-scheme is approximated as follows:

$$\phi_w = \begin{cases} \left(\frac{3}{8}-\alpha\right)\phi_P + \left(\frac{3}{4}+2\alpha\right)\phi_W - \left(\frac{1}{8}+\alpha\right)\phi_{WW}, \text{ if } u_w > 0 \\ \left(\frac{3}{8}-\alpha\right)\phi_W + \left(\frac{3}{4}+2\alpha\right)\phi_P - \left(\frac{1}{8}+\alpha\right)\phi_E, \text{ if } u_w < 0 \end{cases} \quad (3.38)$$

The factor α is a function of the curvature of the quantity ϕ. For more details see Alderton & Wilkes (1988).

CONDIF

Another suggestion from Alderton & Wilkes (1988) is the CONDIF-method which is a combination of a modified CDS and upwind differencing. Employing CDS they try to achieve a dominant diagonal solution matrix and to avoid non-physical overshoots by employing the upwind-scheme.

Pressure-Velocity Correction Methods

The Navier-Stokes equations do not contain an explicit equation for pressure. Continuity is, in general, not satisfied and therefore the pressure and velocities are not correctly determined. One strategy was the development of the Poisson equation from the governing equations. However, the solution of this particular equation caused major problems. The main reason is the requirement of the Neumann boundary condition, i.e. pressure gradients normal to the boundary have to be set. It was observed that mass conservation was quite difficult to achieve (Roache, 1972: pp. 180-185) resulting in a drift in the solution process. This was not a major concern while computers were less powerful and most calculations were two-dimensional. For two-dimensional problems the pressure could be eliminated using the so called 'stream-function vorticity' formulation of the governing equations (see Runchal & Wolfstein, 1969). However, the procedure cannot be extended to three-dimensional problems. Patankar & Spalding (1972) introduced the pressure correction scheme

SIMPLE (Semi-Implicit Method for Pressure Linked Equations). This scheme solved the pressure solution problem and has become the basis for most Finite Volume solution procedures.

In the pressure correction procedure an initial guess for the pressure field, (e.g. p* is set to zero) has to be given. As a result approximate values of the velocity components (u*, v*, w*) will be achieved. These will not, in general satisfy the continuity equation. Therefore correction velocity components (u', v', w') have to be calculated.

For example, the discretised equations in a one dimensional steady flow case (see Figure 3.6) may be written as;

$$a_P^u u_P^* = a_E^u u_E^* + a_W^u u_W^* + \frac{1}{\rho}\left(p_e^* - p_w^*\right) \quad (3.39)$$

The corrections also satisfy the above correlation; i.e.,

$$a_P^u u_P^{'} = a_E^u u_E^{'} + a_W^u u_W^{'} + \frac{1}{\rho}\left(p_e^{'} - p_w^{'}\right) \quad (3.40)$$

The correction velocity components are approximated by dropping the neighbour coefficient terms ($a_E^u u_E^{'} + a_W^u u_W^{'}$), because they are unknown. In one dimension, the velocity correction becomes,

$$\boxed{u_P^{'} = \frac{1}{\rho a_P^u}\left(p_e^{'} - p_w^{'}\right)} \quad (3.41)$$

Integrating the continuity equation in the one-dimensional case yields;

$$\boxed{u_e - u_w = 0} \quad (3.42)$$

Substituting the velocities on the west and east face with the correlations,

$$\boxed{u_e = u_e^* + u_e^{'}}, \quad \boxed{u_w = u_w^* + u_w^{'}} \quad (3.43)$$

where,

$$u_e^{'} = \frac{1}{\rho a_e^u}\left(p_E^{'} - p_P^{'}\right), \frac{1}{a_e^u} = \frac{1}{2}\left(\frac{1}{a_P^u} + \frac{1}{a_E^u}\right)$$

$$u_w^{'} = \frac{1}{\rho a_w^u}\left(p_P^{'} - p_W^{'}\right), \frac{1}{a_w^u} = \frac{1}{2}\left(\frac{1}{a_P^u} + \frac{1}{a_W^u}\right)$$

and rearranging the continuity equation (3.42) the pressure correction equation is derived and the first corrected value for p' can be determined; i.e.,

$$\boxed{a_p^p p_p^{'} = a_E^p p_E^{'} + a_W^p p_W^{'} + b^p} \quad (3.44)$$

where, $a_E^p = \frac{1}{\rho a_E^u}$, $a_W^p = \frac{1}{\rho a_W^u}$, $b^p = u_e^* - u_w^*$, $a_p^p = a_E^p + a_W^p$

With the first corrected pressure value p' the first corrected values for the velocity component u' using equation (3.41) and similar arguments for v' and w' can be calculated. The quantity u will be updated by using equation (3.43) and similar arguments for v and w, and p via equation (3.45).

$$\boxed{p_e = p_e^* + p_e^{'}} \quad \boxed{p_w = p_w^* + p_w^{'}} \quad (3.45)$$

If continuity is not satisfied, i.e. the solution is not converged, set u* = u, v* = v, w* = w and p* = p and the correction procedure has to be restarted.

The SIMPLE solution procedure may be outlined as follows:

1.) Guess initial pressure field (p*)

2.) Calculate approximate values of the velocity component u* (see Equation 3.39), and v* and w*. These will not, in general, satisfy the continuity equation.

3) Substituting the velocities in the continuity equation (3.42) with the correlations, $\boxed{u = u^* + u^{'}}$, $\boxed{v = v^* + v^{'}}$, $\boxed{w = w^* + w^{'}}$ to achieve the pressure correction equation similar to equation (3.44).

4) Calculate the corrected value for p' (see Equation 3.44).

5) Calculate the corrected values for the velocity component u' using equation (3.41) and similar equations for v' and w'..

6) Update the quantities u, v, w and p.

7) If the solution is not converged, set u* = u, v* = v, w* = w and p* = p and return to step 2).

Checkerboarding

The main disadvantage of SIMPLE was that the original version required staggered grids to prevent the numerical instability known as "checkerboarding", i.e. a highly nonuniform pressure and velocity field. Considering the one-dimensional grid below,

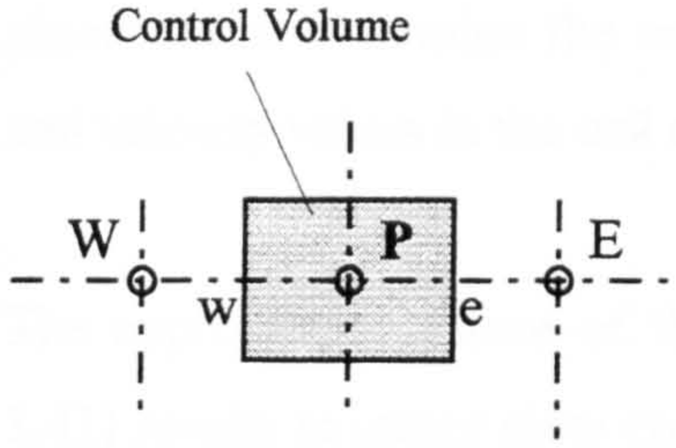

Figure 3.7: One-dimensional grid

The approximation (Equation 3.46) for the pressure means the momentum equation for point P does not contain the pressure at point P; i.e.,

$$\int_w^e \frac{\partial p}{\partial x} dx = p_w - p_e \approx \frac{p_W + p_P}{2} - \frac{p_P + p_E}{2} = \frac{p_W - p_E}{2} \quad (3.46)$$

The result is that a highly non-uniform pressure field would appear uniform in the momentum equation.

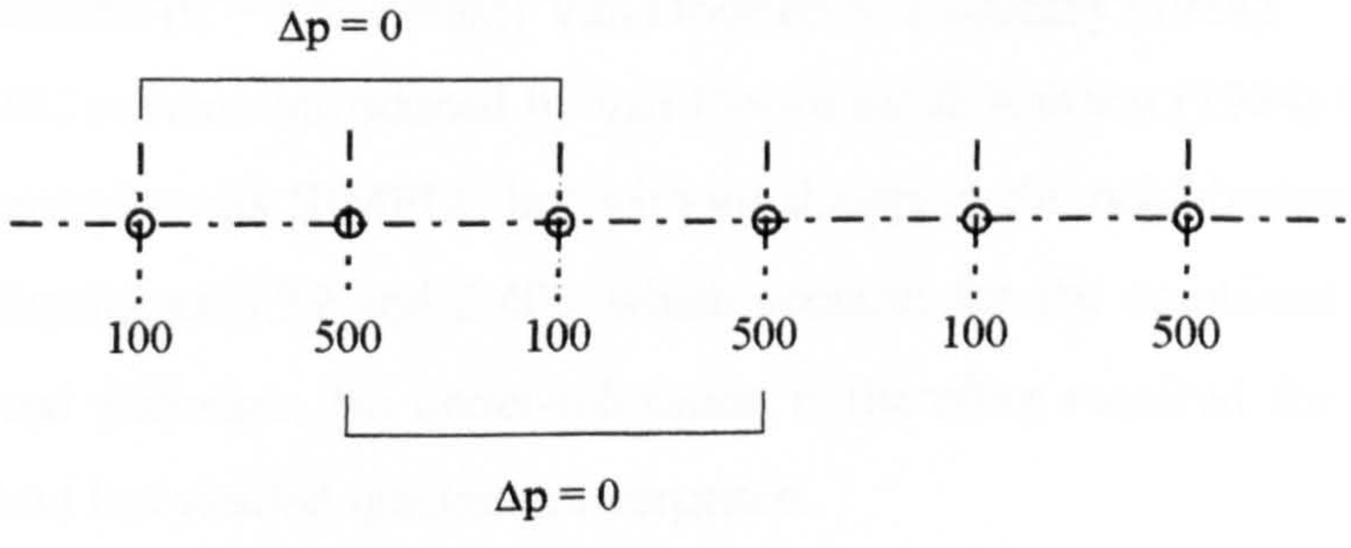

Figure 3.8: Checkerboarding effect on a non-staggered grid

If u_e^* and u_w^* (see Equation 3.43) are calculated by using simple averaging, the numerical instability known as 'checkerboarding' (see Figure 3.8) occurs. Spalding (1972) avoided this problem by introducing staggered grids. In three-dimensional

complex flow situations it becomes difficult to discretise the solution domain with a Cartesian grid structure. Therefore, most multi purpose CFD codes use a body-fitted grid. As a result of the curved grid structure, the use of staggered grids becomes difficult. In order to use the standard primitive variable algorithms like SIMPLE, SIMPLEC and PISO with a non-staggered grid, Rhie & Chow (1983) developed an algorithm to determine the velocity components on the cell faces from the pressure and velocity values in the cell centre.

The approximate nature of the pressure-correction velocity formula (see Equation 3.41) results in rather slow convergence. To avoid divergence u*, v*, w* and p* are underrelaxed, i.e. the dicretised momentum equation (3.33) becomes,

$$\boxed{a_P\phi_P = (1-\alpha)\phi_P + \alpha\left(\sum a_{nb}\phi_{nb} + b\right)} \quad (3.47)$$

where, $0<\alpha<1$

and

$$\boxed{p = p^* + \beta p'} \quad (3.48)$$

where, $0<\beta<1$

This further stabilizes convergence.

Various improvements on the original SIMPLE method have been developed, e.g. SIMPLEST Spalding (1980), SIMPLER (R=Revised) Patankar (1981) and SIMPLEC scheme (C = Consistent) Van Doormool & Raithby (1984).

The SIMPLEC scheme introduced by van Doormaal & Raithby (1984) has the same correction procedure as SIMPLE but without dropping the neighbouring coefficient terms (see Equations 3.39 and 3.40), which account for the combined influence of convection and diffusion. No under-relaxation is therefore required for the pressure and the method has yielded quicker convergence.

The final pressure-correction scheme to be mentioned is the PISO (Pressure-Implicit with Splitting of Operators), which was introduced in 1985 by Issa. The first step is identical to the SIMPLE method but a second pressure correction equation is introduced. This second pressure correction equation accounts for the velocity correction at the neighbouring cells. The method is similar to the SIMPLER scheme.

3.4.3 Numerical Implementation of the Boundary Conditions

Boundaries of the solution domain are described as either inlets, outlets, pressure boundaries, symmetry planes, periodic planes or solid walls. In general, two types of boundary conditions may be defined; (1) the Dirichlet condition, which is a specification of the dependent variables (u, v, w, p) along the boundary, (2) the Neumann condition, which specifies the derivatives (e.g. $\partial u/\partial x$) of the dependent variables.

Solution Domain Inlet Boundary

At an inlet, profiles of the variables are described. For example, the streamwise velocity profile U in y-direction may be given by Prandtl's 1/7-th power law (see Section 3.7). Often the cross stream velocities V and W are set to zero.

The turbulent main flow inlet kinetic energy may be defined using the experimental finding that, the ratio of the Reynolds stress to kinetic energy is constant over most of the boundary layer (see Section 3.7).

Assuming a state of local equilibrium for non-buoyant shear layers, the production is equal to the dissipation rate of turbulence thus the dissipation rate may be defined as shown in Section 3.7.

Outlet Boundary

Mass flow boundaries are defined on the outlet. Neumann boundary conditions are imposed on any kind of transported variables, like velocity, turbulent kinetic energy and dissipation. If the flow is fully developed a zero streamwise gradient condition ($\partial\phi/\partial x = 0$) is valid.

Pressure Boundary

In the case of incompressible flow the pressure is set to a constant value, e.g. the pressure is set to zero.

Symmetry Boundary

The velocity normal to a symmetry plane is equal to zero. The gradients of all other quantities normal to the symmetry plane are equal to zero.

Periodic Boundary

Periodicity ensures that all variables have identical values at both sides of the solution domain. This condition cannot be applied to the pressure in the main-flow direction.

Solid Wall

The non-slip boundary condition is valid for the velocity in laminar and turbulent flow. In turbulent flow wall functions (see Chapter 3.5) are employed to determine velocity parallel to the wall.

3.5 Turbulence Modelling

Introduction

Turbulence is probably the most difficult flow phenomenon to describe because of its chaotic structure which is neither constant in time nor space. As a result, it requires sophisticated techniques to achieve predicted and experimental data.

Hinze (1959: pp. 1-3) defined turbulence as an irregular fluid motion in which all quantities vary in time and space randomly so that these parameters could be statistically averaged. Taylor and von Karman differentiated between "wall turbulence" and "free turbulence" by defining turbulence due to friction at fixed walls or by the flow of fluid layers with different velocities. In real viscous fluids a conversion from kinetic energy into heat will take place, i.e. dissipative effects are active and the motion will decay if there is no continuous source of energy. Viscosity could change turbulent flow to a state of homogeneity so that the turbulence has quantitatively the same structure in all parts of the fluid field. A perfect disorder in terms of no preference for any direction of the statistical features is known as "isotropic turbulence". No average shear stress can occur and, consequently, no gradient of the mean velocity. Otherwise the flow condition is called "shear flow turbulence" or "nonisotropic or anisotropic turbulence".

Rodi (1980: pp. 9-10) described turbulence as an eddying motion, mainly at high Reynolds numbers with a wide spectrum of eddy or vortex sizes with various fluctuation frequencies. The main character of the flow is rotation and the vorticity vectors of the vortex elements are aligned and highly unsteady. He differentiates between large and small eddies which have low and high frequency fluctuations, respectively. In the case of large eddies the size is of the same magnitude as the flow domain. In contrast very small eddies are determined by viscous forces and the spectrum between the smallest and the largest eddies grow with increasing Reynolds number. The large eddies transport most of the momentum and heat. The turbulent correlations $\overline{u_i u_j}$ and $\overline{u_i \varphi}$, which are of a similar scale as the mean flow, have to be approximated with a turbulence model. The large eddies extract kinetic energy from the mean flow to support the large vortical motion. The large vortices stretch each other into smaller ones and so on until the viscous forces dissipate the final eddies because their energy is too low. This process is known as the "energy cascade". The

larger the Reynolds number the smaller the effect of viscosity and the smaller the dissipative eddies compared to the largest eddy motions. If buoyancy is a flow characteristic, potential energy from the mean flow will be exchanged with turbulent kinetic energy in both directions. The large scale eddies determine the interaction and are therefore dependent on the boundary conditions. If the small eddies are isotropic and the large scale motions are not, this condition is defined as being "local isotropy". This occurs when the Reynolds number is high enough so that the spectrum between the largest and the smallest eddies is large.

One of the pioneers to approach a theoretical turbulence correlation was Boussinesq, in 1877. He interpreted turbulence as an increase of viscosity and defined the well known "Eddy Viscosity Concept". A more advanced model, called the "Mixing-Length Hypothesis", was developed by Prandtl in 1925. This was the first approach describing the distribution of the eddy viscosity. Prandtl also introduced, in 1942, the "Free-Shear-Layer Turbulence Model" which was popular because of its simplicity and the fact that it predicts reasonable results for fully developed flows. All the mathematical approaches mentioned above were unable to describe the transport of turbulence and relied instead on empirical constants. In the seventies when computers of sufficient power were available for the first time, more advanced turbulence models were developed. Two different concepts to determine the transport of turbulence were introduced. The first "One-Equation Model" was based on the eddy-viscosity concept whilst the second was introduced by Bradshaw et al. (1967). The concept of Bradshaw et al. (1967) is not based on the eddy-viscosity model, but solves a transport equation for the Reynolds stresses by converting the exact turbulent kinetic energy equation. Both employed empirical functions to describe the length scale of turbulent vortical flow structures. As a further step to predicting turbulence more accurately the "Two-Equation Models" were developed to calculate the distribution of the length scale in addition to the turbulent kinetic energy. The isotropic and nonisotropic k-ε turbulence models are, for example, well known Two Equation Models. In order to deal with more complex and turbulence driven flows the "Turbulent Stress Models" or "Second Order Closure Schemes" were developed. Transport equations for the individual Reynolds stresses $\overline{u_i u_j}$ were derived. The region near a solid surface is characterised by the viscous sublayer. Across this layer

the mean velocity and turbulence properties experience substantial gradients. While it is possible to employ closures to solve up to the wall, it was found that the mean velocity and the turbulent properties could be described adequately for certain flows with "Wall Functions", based on the well established Log layer velocity profile.

There are two extreme methods to tackle turbulent flow numerically; (1) the Direct Numerical Simulation (DNS) is probably the most accurate and sensitive way to predict turbulent flow structure. (2) the Reynolds averaged Navier-Stokes equations method (RANS), which requires the use of turbulence models for the fluctuating quantities.

The problem is that DNS is still restricted to very simple flow problems and relatively low Reynolds numbers because the unsteady Navier-Stokes equation have to be solved for every particular perturbation in the flow. This means huge hardware facilities are required. One fairly recent application is to use DNS as a numerical experiment to achieve preliminary results for a simplified flow model and to feed this data into alternative turbulence calculation methods which are more capable of tackling bigger problems but with less accuracy.

All the constants in RANS approximations are derived empirically from experiments. Therefore, the constants only apply to experiments for which they have been validated.

Large Eddy Simulation (LES) is a method coupling the two mentioned above. The large energy transferring scales or eddies are simulated directly as in DNS but the subgrid small scales which are not so important in terms of turbulent energy transfer are predicted via turbulence models. The following flow chart (see Figures 3.9), shows the available solution techniques, along with the relative cost of employing each technique.

The remaining approaches are all based on the RANS-equations.

- One point closures: These are methods based directly on modelling the Reynolds stress $\overline{\rho u_i u_j}$ in the RANS-equations. A wide variety of such methods exists (e.g. Laurence, 1997).
- Integral methods: The RANS equations have to be integrated over one or more of the independent variables. As a result more terms will be produced and need to be modelled.

• Correlations: One example is the correlation for the friction factor as a function of Reynolds numbers and relative roughness. Others are available in handbooks.

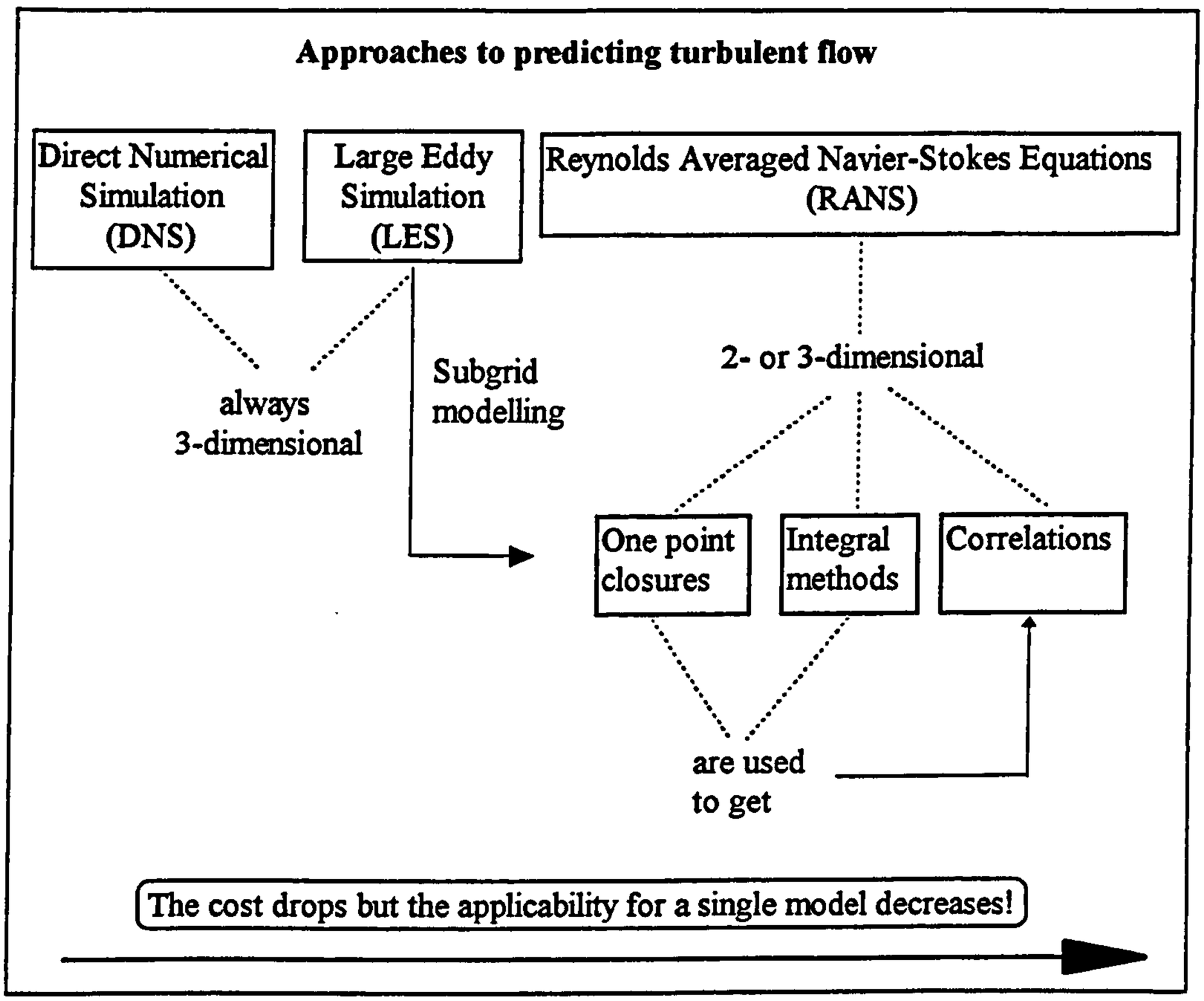

Figure 3.9: Turbulent flow approaches

Two-Equation Models

In terms of large eddies the characteristic length scale is L. This length scale is involved in the energy transfer processes as the turbulent kinetic energy k. If, for example, large eddies were generated by a grid and are convected in the streamwise direction their size at any downstream position would depend on their initial magnitude. Another quantity, the dissipation ε, influences the characteristic length scale L of large eddies by destroying low energy containing small eddies and therefore the average eddy size will become relatively larger. The opposite result to that of dissipation produces the vortex stretching phenomenon, i.e. the eddy size will be reduced through the energy cascade.

One has to find a solution method which combines all turbulent energy transferring processes. The transport equation for the characteristic length L, in addition to the turbulent kinetic k-equation, seems to be the right tool to express the energy balance. These two transport equations define the two equation turbulence model and account for the velocity and the length scale distribution. Even in relatively complex flow structures like recirculation or shear flows the two equation model delivers promising results. It is the simplest method to approach a solution if empirical constants do not represent a satisfying distribution of the length scale L.

Length scale equation

In the length scale equation the dependent variable does not necessarily have to be the length scale L itself. A combination of any kind of the two scales, $\boxed{Z = k^m L^n}$ the turbulent kinetic energy k and the length scale L represent a sufficient base. The kinetic energy distribution is determined by the k-equation (see Rodi, 1980: pp. 26-29). The following equations have been proposed:

- $\varepsilon \propto \frac{k^{3/2}}{L}$ from Chou (1945), Davidov (1961), Jones & Launder (1972)
- kL Rotta (1968) proposed an equation for kL
- $\frac{k^{1/2}}{L}$ Kolmogorov (1968) suggested an equation for the frequency

- $\frac{k}{L^2}$ Saffman (1970) and Spalding (1971) proposed an equation for the turbulence vorticity
- $\omega \equiv \frac{\varepsilon}{k}$ Wilcox (1988) suggested to model the reciprocal turbulent time scale

Some of the length scale equations were derived at first exactly by using the Navier-Stokes equations and afterwards simplified with model assumptions. In contrast there were others who determined them heuristically. A general result (Rodi, 1980: pp. 26-29) for non-buoyant flows is:

$$\boxed{\frac{\partial Z}{\partial t} + U_i \frac{\partial Z}{\partial x_i} = \frac{\partial}{\partial x_i}\left(\frac{\sqrt{kL}}{\sigma_z}\frac{\partial Z}{\partial x_i}\right) + c_{z1}\frac{Z}{k}P - c_{z2}Z\frac{\sqrt{k}}{L} + S} \quad (3.49)$$

rate of change ↑ convection ↑ diffusion ↑ production ↑ destruction ↑

where: σ_z, c_{z1}, and c_{z2} ≡ empirical constants
P ≡ production of kinetic energy
S ≡ secondary source term which differs according to the choice of Z and is mainly important near walls

Except for the source term, S, the main difference between the k-equation and the Z-equation above rests with the diffusion term. Rodi (1980: pp. 26-29) emphasised that no important difference in free flows could be observed with several Z-equations except near the wall. In this region it was observed that for a gradient assumption for diffusion the single constant $Z = \varepsilon$ provided the best results. The ε-equation does not need a secondary source term, S, near the wall and that was the main reason to choose the ε-equation instead of any other length scale equations.

The k-ε Model

At high Reynolds numbers the turbulence is locally isotropic and the rate of dissipation ε is equal to the molecular kinematic viscosity multiplied by the fluctuating vorticity $\overline{\left(\partial u_i / \partial x_j\right)^2}$ (see Rodi, 1980: pp. 26-29). Tennekes & Lumley (1972: pp. 59-64) showed an exact derivation of the transport equation for the fluctuating vorticity and thus the dissipation from the Navier-Stokes equations. In order to solve the

derived transport equation for the dissipation ε the complicated correlations were substituted with model assumptions. There are terms representing the rate of change, convection, diffusion and generation of vorticity as a result of vortex stretching. This vortex stretching is also connected with the energy cascade and therefore with viscous destruction of vorticity. In the case of a locally non isotropic turbulence, more terms occur. The diffusion, generation and destruction terms have to be modelled.

The result of implementing models for the terms described above in equation (3.49) results in the dissipation equation (3.51). Together with the modelled k-equation and the Kolmogorov-Prandtl expression (see Equation 3.52) it forms the so-called "k-ε turbulence model". Substituting the last term (the length scale correlation) of the modelled turbulent kinetic energy transport equation with the dissipation ε, yields:

$$\frac{\partial k}{\partial t}+U_i\frac{\partial k}{\partial x_i}=\frac{\partial}{\partial x_i}\left(\frac{\nu_t}{\sigma_k}\frac{\partial k}{\partial x_i}\right)-\nu_t\left(\frac{\partial U_i}{\partial x_j}+\frac{\partial U_j}{\partial x_i}\right)\frac{\partial U_i}{\partial x_j}-\beta g_i\frac{\nu_t}{\sigma_k}\frac{\partial \phi}{\partial x_i}-\varepsilon \quad (3.50)$$

P G

$$\frac{\partial \varepsilon}{\partial t}+U_i\frac{\partial \varepsilon}{\partial x_i}=\frac{\partial}{\partial x_i}\left(\frac{\nu_t}{\sigma_\varepsilon}\frac{\partial \varepsilon}{\partial x_i}\right)+c_{1\varepsilon}\frac{\varepsilon}{k}(P+G)\left(1+c_{3\varepsilon}R_f\right)-c_{2\varepsilon}\frac{\varepsilon^2}{k} \quad (3.51)$$

rate of change — convection — diffusion — generation and destruction

An expression for the eddy or turbulent viscosity ν_t can be derived from the Kolmogorov-Prandtl expression (see Equation 3.52) and from the model for dissipation ε (see Equation 3.53) in the modelled k-equation. In both expressions the length scale L is involved. In the k-ε model, epsilon, ε, is a function of the distribution of the length scale L. Therefore the length scale L is eliminated from the final expression for the eddy viscosity.

The derivation of the eddy viscosity ν_t equation is as follows:

$$\boxed{\nu_t = c_\mu' \sqrt{k} L} \ (3.52) \quad \Rightarrow \quad \boxed{L = \frac{\nu_t}{c_\mu' \sqrt{k}}} \quad \Big)$$

$$\Big\} \Rightarrow \boxed{\nu_t = c_D c_\mu' \frac{k^2}{\varepsilon}} \Rightarrow \boxed{\nu_t = c_\mu \frac{k^2}{\varepsilon}} \ (3.54)$$

$$\boxed{\varepsilon = c_D \frac{k^{3/2}}{L}} \ (3.53) \quad \Rightarrow \quad \boxed{L = c_D \frac{k^{3/2}}{\varepsilon}} \quad \Big)$$

The accepted set of empirical constants for the k-ε model are:

c_μ	$c_{1\varepsilon}$	$c_{2\varepsilon}$	σ_k	σ_ε
0.09	1.44	1.92	1.0	1.3

Table 3.1 (see Launder & Spalding, 1974)

The empirical constant $c_{3\varepsilon}$, and the flux Richardson number R_f (see Equation 3.51) in buoyant situations are discussed in Rodi (1980: pp. 28-32).

Wall Functions

The region close to a solid surface, e.g. the wall, requires special attention if the flow is fully turbulent with the no-slip boundary conditions. The fully turbulent boundary layer over a smooth flat plate can be divided into an inner and an outer region (see e.g. Anderson et al., 1984: p. 357). The inner region of the boundary layer includes three zones. The first and coincident zone to the wall is the "viscous sublayer" where the magnitude of the viscous forces is greater than the turbulent fluctuations. Therefore, this layer is also often called the "laminar sublayer" due to the laminarisation effect of the mean flow by strong viscous forces but it is quite disorganised over short bursts. The second layer is the "buffer zone" where the influence of the molecular viscosity decreases as the border of the "fully turbulent log-law zone" is approached. The turbulent fluctuations dominate the flow characteristics in the "fully turbulent log-law zone" which represents the connection region between the inner and the outer regions of the boundary layer. To achieve this correspondence the first computational grid point has to be located in the "fully turbulent log-law zone". The valid range of the law of the wall varies depending on the applications. Also, different researchers have found slightly different values, i.e.,

- $30 \leq y^+ \leq 100$ for pipe flow (Rodi, 1980: pp. 44-45)
- $30 \leq y^+ \leq 200$ for a flat plate (Anderson et al., 1984: p. 357)
- $30 \leq y^+ \leq 150$ for a flat plate in LES (Piomelli, 1997)

Piomelli (1997) mentioned a new feature of the flow structure in the viscous sublayer, using DNS data from a turbulent channel flow. He found that, in the viscous sublayer, where most of the shear stress is produced, no interaction with the outer layers occurred and the flow structures regenerate themselves.

Rodi (1980: pp. 44-45) suggested for hydraulic, i.e. pipe flows:

$$\boxed{\frac{U_{res}}{U_\tau} = \frac{1}{\kappa}\ln(y^+E) \text{ with } y^+ = \frac{yU_\tau}{\nu} \text{ and } U_\tau = \sqrt{\frac{\tau_W}{\rho}}} \quad (3.55)$$

with: E = roughness parameter ($E = 9$ for hydraulically smooth walls)

U_{res} = resultant velocity parallel to the wall

In the y+-region (log layer) the Reynolds stresses $\overline{u_i u_j}$ are nearly constant and convection and diffusion of the stresses are insignificant so that the flow structure is in local equilibrium. If the production and dissipation of turbulence is in balance, no buoyancy effects occur and the Reynolds shear stress is approximately equal to the wall shear stress Rodi derived:

$$\boxed{\frac{k}{U_\tau^2} = \frac{1}{\sqrt{C_\mu}}} \quad (3.56) \quad \Rightarrow \quad C_\mu = \frac{U_\tau^4}{k^2} = \frac{\tau_W^2}{\rho^2 k^2}$$

Equation (3.56) is used as a boundary condition for k in one- and two-equation models and with the local equilibrium condition $\varepsilon = P = U_\tau^2 \frac{\partial U}{\partial y}$ the boundary condition for ε yields:

$$\boxed{\varepsilon = \frac{U_\tau^3}{\kappa y}} \quad (3.57)$$

with: $\frac{\partial U}{\partial y} = \frac{U_\tau}{\kappa y}$ (see Schlichting, 1979: pp. 587-588)

A commonly used correlation is for example,

$$\boxed{\frac{\rho U C_\mu^{1/4} \sqrt{k}}{\tau_w} = \frac{1}{\kappa} \ln E y^*} \quad (3.58)$$

with: $y^* = \rho y \sqrt{k} / \mu$

$E = C_\mu^{1/4} \exp(\kappa B)$

$\kappa = 0.41$

$B \cong 5.5$

which has proved to be very successful in flows close to separation where the shear stress approaches zero.

The boundary condition for ε may be written as:

$$\boxed{\varepsilon = \frac{C_\mu^{3/4} k^{3/2}}{\kappa y}} \quad (3.59)$$

3.6 CFX 4: Code Overview

CFX 4 is a multi-purpose flow modelling package for the prediction of laminar and turbulent flow, and heat transfer. The current Version 4 uses multi-block structured grids with body-fitted coordinates. The CFD package consists of the following modules:

- Pre-processing Modules, or Geometry and Grid Generators
- Interactive Frontend
- Frontend Module
- Solution Module
- Post-processing, or Graphics, Modules

The Geometry and Grid Generator Modules may be used to define the geometrical solution domain and the numerical grid. The topological and grid coordinate details are stored internally in a translated form readable by the Frontend.

The Frontend converts the input data into a form which provides efficient computation. The flow problem defining input data can be set up by using the Command Language file (more detail given on page 116). The Interactive Frontend may be used to construct automatically, via a series of displays, the input data file.

The Solution Module solves the discretised flow problem by using the FVM (see Section 3.4.2), prints the solution and dumps the solution to disk files.

The Graphics Modules produces the main graphic data and provides a number of post-processing options.

Figure 3.10 shows a detailed overview of the CFX 4 solver options.

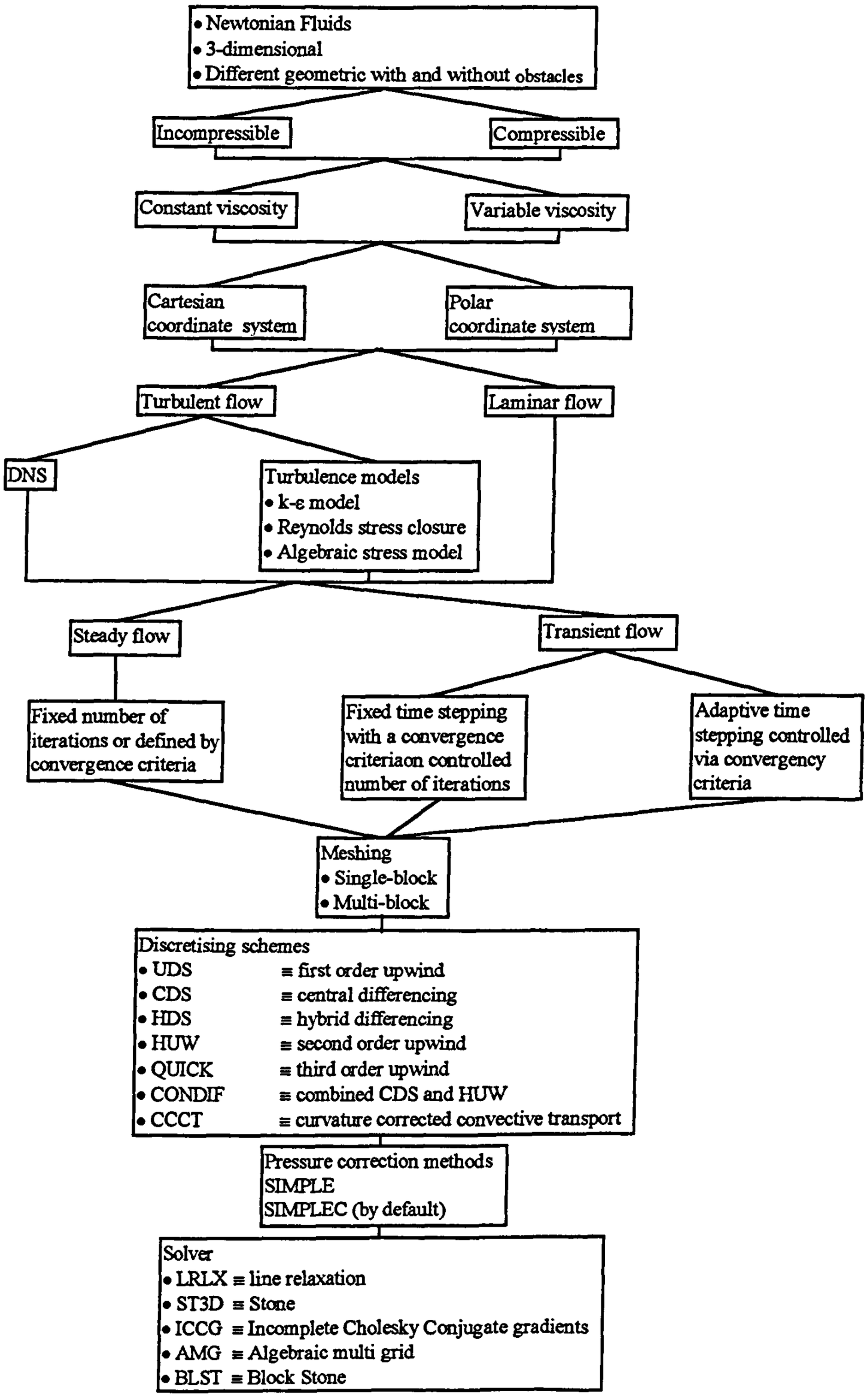

Figure 3.10: CFX 4 flow chart

Command Language File

The Command Language File is a data file containing a set of commands and keywords to define the fluid flow problem. The general structure consists of eight major commands and each of them have subcommands and keywords, some of which are optional.

The VG models used seven major commands, which are:

>>CFXF3D

>>MODEL TOPOLOGY

>>MODEL DATA

>>SOLVER DATA

>>CREATE GRID

>>MODEL BOUNDARY CONDITIONS

>>STOP

The eighth command >>OUTPUT OPTIONS is optional.

Each major command has a certain set of subcommands except the last one, which is >>STOP.

Associated with the first command, >>CFXF3D, are the following subcommands.

>>SET LIMITS

The total work space and the maximum number of blocks, patches and inter block boundaries have to be defined if default are not sufficient.

>>OPTIONS

The grid type and the flow condition are defined.

>>USER FORTRAN

Under this subcommand the used User Fortran routines are declared

The second command, >>MODEL TOPOLOGY, includes the following subcommands.

>>CREATE BLOCK

In case of a multi-block grid, the grid blocks with a certain amount of grid nodes in all three dimensions are defined.

>>CREATE PATCH

This subcommand has four keywords. First the block number is defined, then the patch number, patch type (see Figure 3.11) and orientation of this patch. A patch, as used here, is the general term used for a block face. CFX 4 uses patches to define conditions at the block boundaries.

Figure 3.11 shows all the patch types used in this project

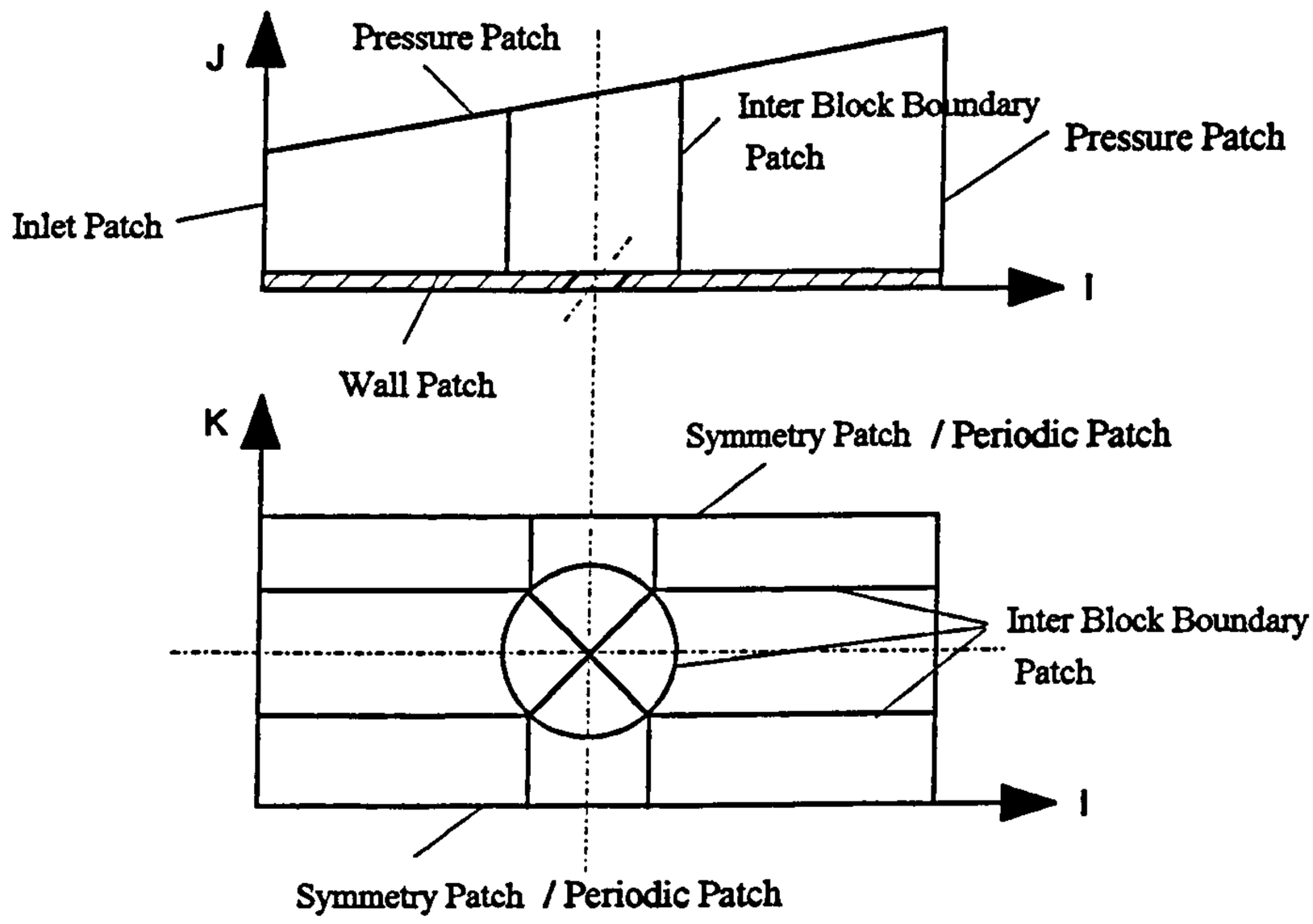

Fig. 3.11: Scheme of patch definition

The patch numbering system is used to define the particular face on a block. The face number is defined as follows (see Figure 3.12); i.e.,

1≡High I, 2≡High J, 3≡High K, 4≡Low I, 5≡Low J, 6≡Low K

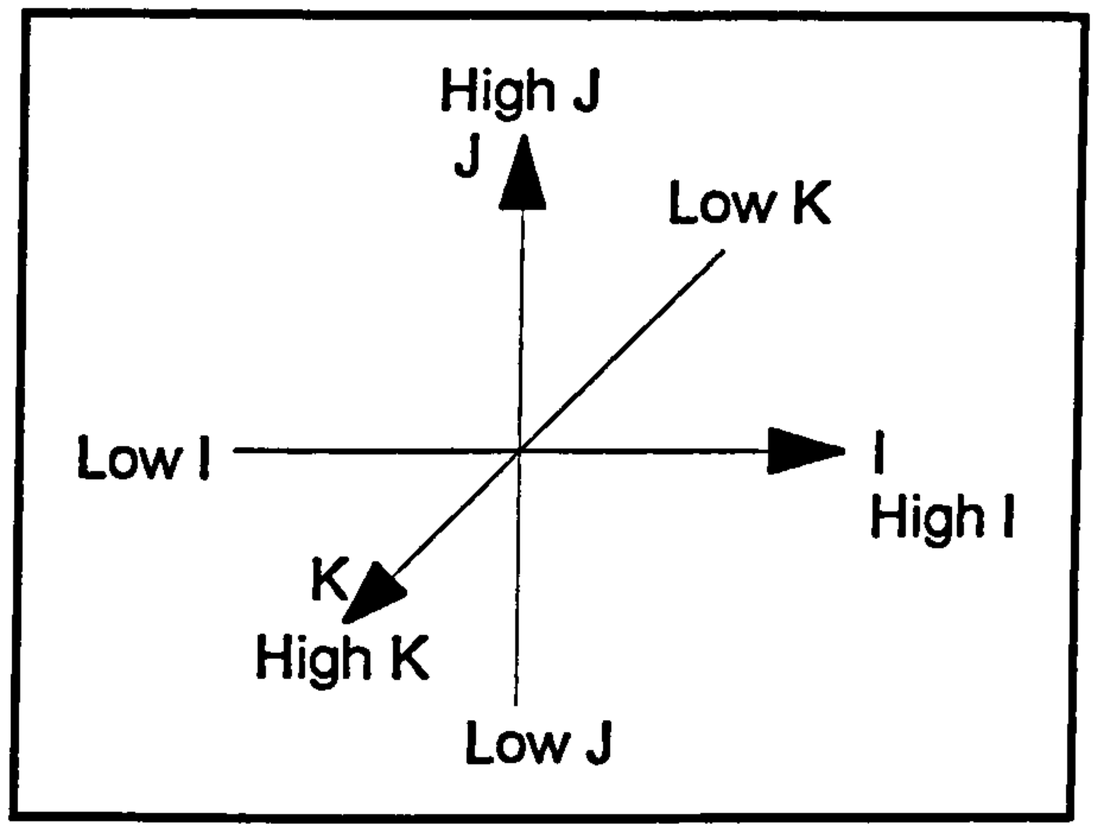

Fig. 3.12: Coordinate system and notation for computational space

>>GLUE PATCHES

Joins inter block boundaries and transfers grid orientation from one block to another. The patch numbering system is the same as mentioned before.

The third command, >>MODEL DATA, includes five subcommands.

>>TITLE

Definition of the fluid flow problem title.

>>PHYSICAL PROPERTIES

>>FLUID PARAMETERS

Definition of the fluid parameters.

>>DIFFERENCING SCHEME

Several differencing schemes are available (see Figure 3.10).

The fourth command, >>SOLVER DATA, uses only one subcommand.

>>PROGRAM CONTROL

The monitoring point in the solution domain is set at which the field values are printed into the output file for each iteration. The sum of the absolute residuals of each cell for the equation being considered will be written into the output file for each iteration. The maximum number of iterations and the mass source tolerance is defined. If this tolerance is reached before the defined number of iterations are made, the calculation stops.

The fifth command, >>CREATE GRID, has two subcommands.

>>INPUT GRID

By default a formatted grid file is read in.

The sixth command, >>MODEL BOUNDARY CONDITIONS, uses one subcommand.

>>SET VARIABLE

Here all boundaries are set to applying to the problem.

The seventh command, >>STOP finishes the command language file.

Fortran Routines

All user Fortran routines are put in one file. For example, USRGRD, USRBCS and USRTRN. The subroutine USRGRD is used to define the grid to be evaluated by CFX 4. USRGRD was used to call the grid generation codes. Any boundary conditions too complex to be defined in the command file are defined in USRBCS. The routine may be used to define the flow characteristics such as the main and jet inlets. USRTRN can be employed to dump flow field information such as velocities, vorticity and wall shear stresses.

3.7 Local Models

3.7.1 Introduction

In this project five different model geometries (see Figures 3.14, 3.18 and 3.19) were designed to investigate the local flow structure in the vicinity of a vortex generator.

As discussed in Chapter 2, the boundary layer in the entrance region of the S-bend duct is two-dimensional but it becomes three-dimensional immediately downstream of the first bend. As a result of both curvature and increasing diameter of the duct an axial adverse static pressure gradient develops. The sector model inlet boundary conditions are purely two dimensional, i.e. no cross flow is imposed. Also the model does not consider the axial pressure gradient imposed by the geometry of the duct. The question arises as to whether the model represents an appropriate approximation of the flow situation in the duct at the location of the air jet; i.e. one diameter downstream of the first bend. To justify the model assumptions, available experimental data from publications will be discussed.

Experimental results are presented in AGARD-AR-270 (1991) for the RAE2129 inlet duct with the geometry of D_i = 128.8 mm, D_e = 152.4 mm, A_e/A_i = 1.4, and an offset/length of 0.45. This S-bend diffuser is exactly the same size and shape as the one from which our numerical sector model is taken. Therefore we can say that our model approximates a region of the diffuser used in these experiments. The test conditions were a throat Mach number of M_i = 0.794 and a corresponding Reynolds number of $Re_i = 1.848\times10^6$. The flow conditions were similar to those of the numerical model, i.e. an inlet Mach number of M = 0.74 and a corresponding Reynolds number of $Re = 3.81\times10^6$. Under these conditions the static wall pressure along the inside of the duct shows a linear increase over the length of the local sector model of only 5% (see Figure 3.3.5 in AGARD-AR-270, 1991). This value is therefore negligibly small and might be in the range of experimental errors. Therefore it does not seem necessary to include this axial gradient in our numerical procedure. Also, the inclusion of another variable factor would complicate our model case further.

However, Whitelaw & Yu (1993) investigated a scaled-down model of RAE 2129 (D_i= 48mm, D_e = 56.8mm, A_e/A_i = 1.4, offset/length = 0.3). The running experimental conditions were at $Re_i = 4\times10^4$ and an inlet bulk mean velocity of U_b = 1.37m/s.

They measured the flow properties for two different inflow conditions. The second condition, i.e. inlet boundary layer thickness $\delta_0 = 0.2D_i$, is comparable to our condition ($\delta_0 = 0.03D$). They observed a pair of contra-rotating vortices of low strength. Separation was only observed further downstream, i.e. outside the range of our local model. They measured a maximum secondary velocity of approximately $0.125U_b$ over the whole cross-section plane. However, over the 15° sector of our model which is located symmetrically to a centre line at a circumferential angle of φ = 172.5° (see Figure 1.6: p. 28) a maximum secondary velocity of approximately $0.025U_b$ was reported. Over the same area the streamwise turbulence levels vary only by $\Delta\sqrt{\overline{u}^2}/U_b = 0.08$. Even smaller is the variation of the shear stress cross-correlation ($\overline{uv}/U_b^2 = -0.001$ to 0.0) in the lower half of the duct, i.e. 90° ≤ φ ≤ 180°.

Bansod & Bradshaw (1972) investigated among other ducts a short intake duct with constant diameter of D = 150mm, but without any straight inlet or outlet extension. The ratio of the centreline radius of curvature to the duct diameter (R/D) was equal to 2.25. The free stream velocity at the duct entry was U_0 = 45m/s, and the Reynolds number based on the diameter was R_i=0.5×10^6. They measured a circumferential variation of the skin friction coefficient over the whole range from φ = 0° to 180° at a streamwise position of approximately one diameter downstream of the first bend. Over the width of our sector model, i.e. from φ = 165° to 180°, the circumferential variation of c_f was measured to be approximately 6% of the circumferential c_f average at the inlet of the duct. The axial change of the skin friction factor c_f is negligible over the model length. The variation in upstream-to-downstream axial wall static pressure [which in AGARD-AR-270 (1991) had been shown to be 5%], is 11% along the inside of the duct at a circumferential angle φ = 180°.

Wellborn et al (1992) looked at an S-bend intake duct with a geometry of two 30° bends, an inlet diameter D_i of 204.2mm, an exit diameter D_e of 251.4mm, and a ratio of the exit and inlet cross section areas A_e/A_i of 1.52. The measurements were conducted at an inlet centreline Mach number of 0.6, and a Reynolds number based on the inlet centreline velocity and duct inlet diameter of 2.6×10^6.

The circumferential variation of surface static pressure at approximately one diameter downstream of the first bend ($x/D_i = 0.96$) is approximately 10% over 15° from φ = 155° to 170° (no measurements were available between φ = 170° and 180°). Knowing from Bansod & Bradshaw's (1972) experimental data that the pressure gradient decreases further from φ = 170° to 180° with the minimum pressure at φ = 180°, we might conclude that the circumferential pressure gradient between φ = 165° and 180° will be less than the measured change of 10%. The total pressure contours plane at $x/D_i = 0.96$ showed that no convection of boundary layer fluid away from the surface could be observed. This suggests that no boundary layer separation occurred and the secondary motion was very weak at this location.

The above mentioned points also apply to flat plate conditions. In addition, however, the flat plate model is a further simplification insofar as no curvature is considered. To prove a potential difference between the two local models elaborate comparisons have been performed (see Chapter 7).

According to the arguments discussed above, based on experimental data (AGARD-AR-270 1991, Whitelaw & Yu 1993, Bansod & Bradshaw 1972, Wellborn et al 1992), we believe that the approximations of the local models are appropriate to investigate the local flow situation in an S-bend intake duct. The experimentally detected secondary motions at the location of investigation are minor. Therefore their inclusion in the numerical procedure would not be of great benefit in terms of our objectives, i.e. to provide local data on initial strengths and positions of vortices produced by vortex generators which could be fed into RNS3D.

3.7.2 Verification Models

The numerical results of the first two models were validated against experimental data due to Bray (1999) thus the numerical models should reflect the experimental geometry and conditions. In the experiment a single AJVG was installed on a rotational plug located on the wind tunnel floor, with the following dimensions (see Figure 3.13):

- Length of the wind tunnel floor: $L = 1.9m$
- Downstream length: $L_d = 1.1m$

- Width of the wind tunnel floor: $W = 0.62m$
- Airjet orifice diameter: $D_{jet} = 0.012m$
- Pitch angle: $\theta = 30°$
- Skew angle: $\phi = 60°$
- Free stream velocity: $U_0 = 20m/s$
- Jet velocity: $U_{jet} = 2*U_0$

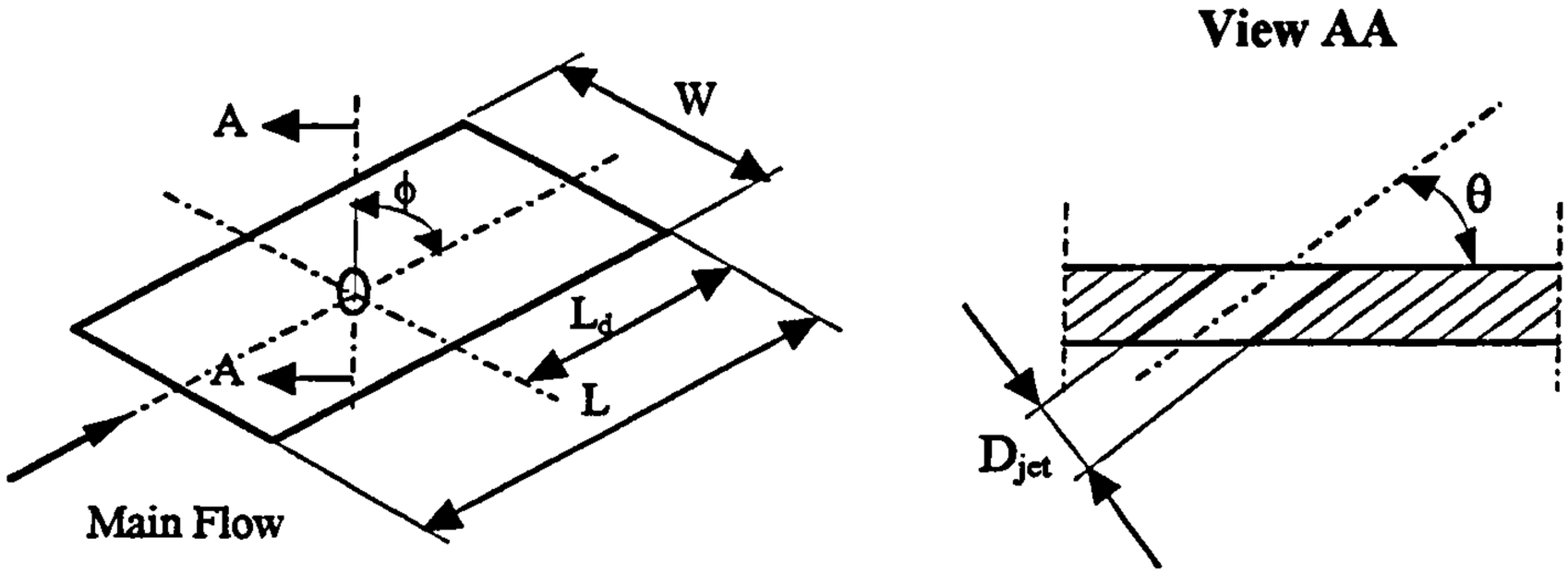

Figure 3.13: Experimental model dimensions

The undisturbed boundary layer thickness δ_{VG} at the centre of the air jet orifice was measured to be 41.5mm.

The two local verification models (see Figure 3.14) comprise an incompressible, turbulent, boundary layer over a flat plate into which a pitched and skewed airjet is issuing. In the case of local model V1 the jet inlet tube is modelled whereas in model V2 a jet velocity vector is defined at the jet orifice.

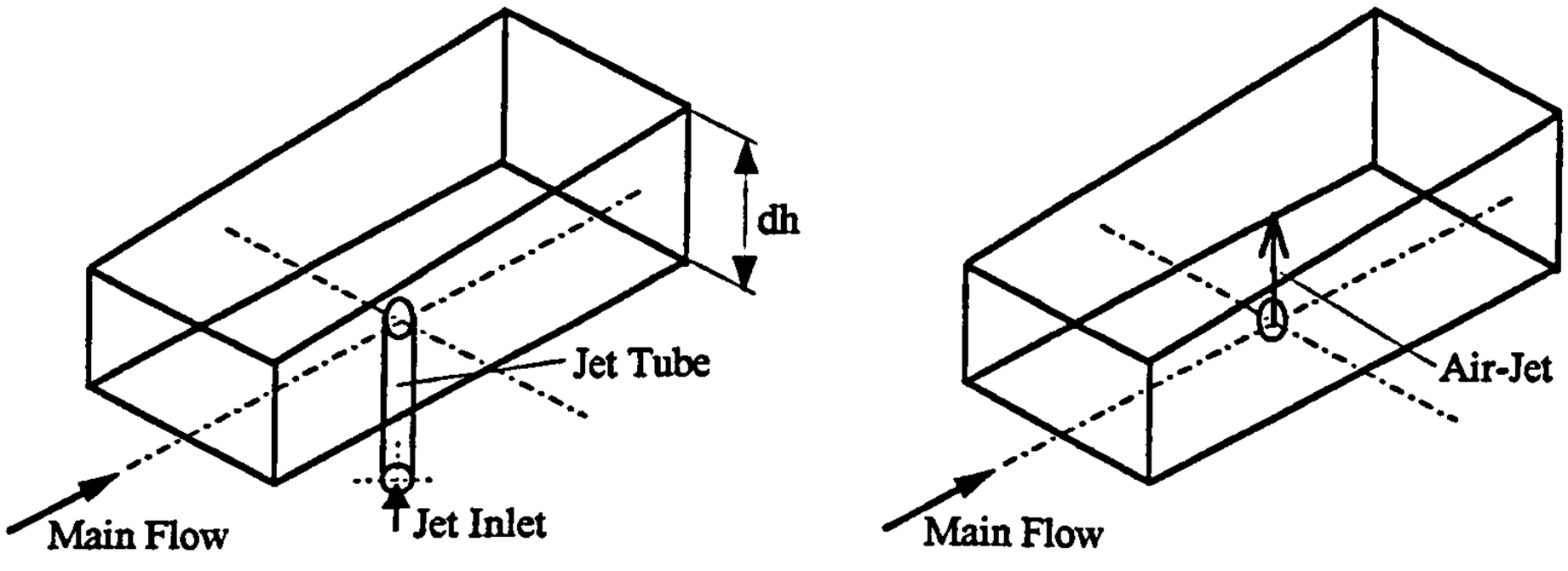

Figure 3.14: Flat plate model V1 with and model V2 without a jet inlet tube

The numerical model details are equivalent to the experimental dimensions except:

- Length of the flat plate: $L = 4*W = 2.48m$
- Downstream length: $L_d = 1.24m$
- Solution domain height: $dh = 5\,\delta$ (undisturbed local boundary layer height see Equation 3.60)
- Jet inlet tube length: $l_{jet\ tube} = 3*D_{jet} = 0.036m$

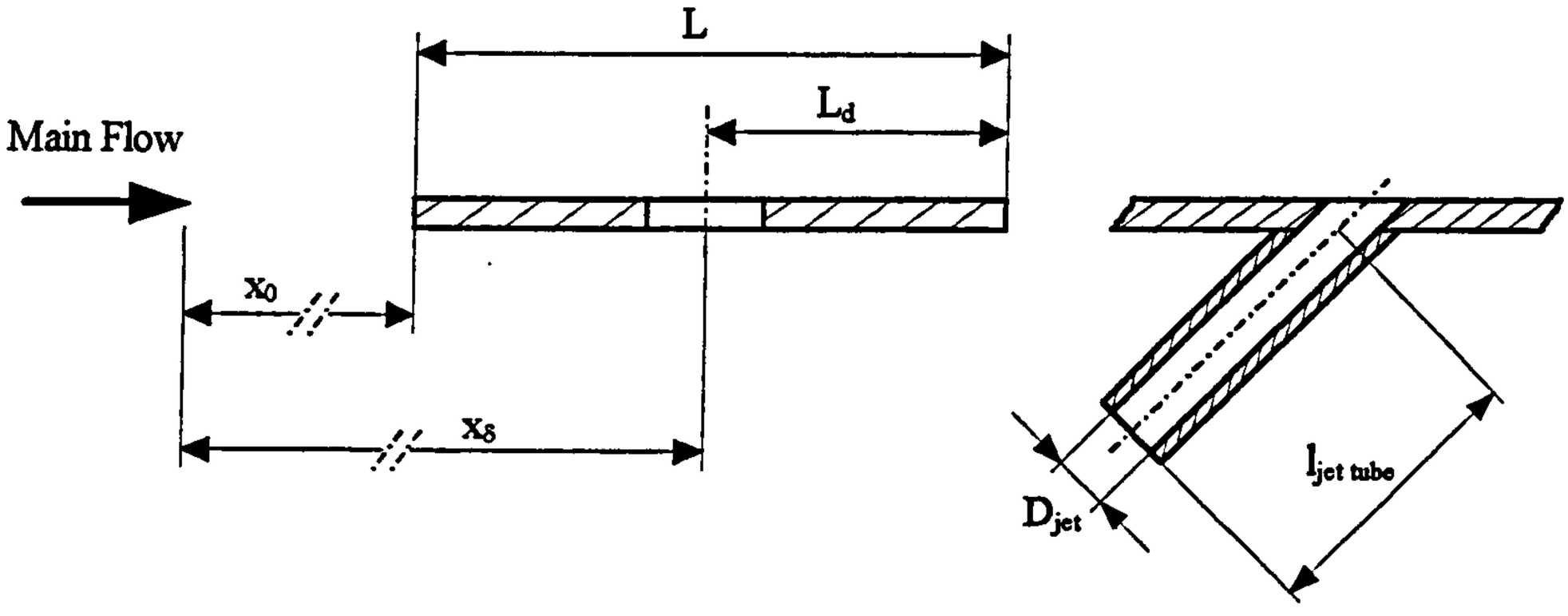

Figure 3.15: Local model set up

To match the undisturbed boundary layer thickness of $\delta = 41.5mm$ at the centre of the airjet orifice, the virtual inlet (see Figure 3.15) was set to $x_0 = x_\delta = 2.207m$. The theoretical boundary layer height was calculated by using the correlation (see Schlichting, 1979: p. 638)

$$\delta = 0.37 \cdot x_0 \cdot \left(\frac{U_0 \cdot x_0}{\upsilon}\right)^{-0.2} \qquad (3.60)$$

with the kinematic viscosity: $\upsilon = \frac{\mu}{\rho}$

where, $\rho = 1.21\ \frac{Kg}{m^3}$

$\mu = 1.81 \times 10^{-5}\ \frac{Kg}{s\,m}$ at T=20°C and p=1 atm

From experiments documented in the literature (see Schlichting, 1979: p. 639), fully turbulent flow conditions in the case of a flat plate (boundary layer) are established, if the Reynolds number is larger than 5×10^5.

The Reynolds number is defined as:

$$\boxed{\mathrm{Re} = \frac{U_0 \cdot \rho \cdot x_0}{\mu}} \quad (3.61)$$

According to equation (3.61) and $x_0 = x_{01} = 0.967m$ and $U_0 = 20m/s$ the inlet Reynolds-number was $\boxed{\mathrm{Re} = 1.3 \times 10^6}$. As $\mathrm{Re} > 5 \times 10^5$ the boundary layer flow was fully turbulent.

3.7.3 Duct Models

The main objective of this project is to design a local numerical model which describes as realistically as possible the physical geometry and conditions of the flow field in the vicinity of the VGs within the S-bend intake duct. Figure 3.16 shows the S-bend intake duct geometry, together with the location of the VG arrays which are two diameters downstream of the duct inlet. The approximations used in the local models are justified according to experimental measurements and are described in section 3.7.1. The spacing angle α_{VG} defines the circumferential distribution of VGs and the circumferential angle φ indicates the local circumferential position on the duct.

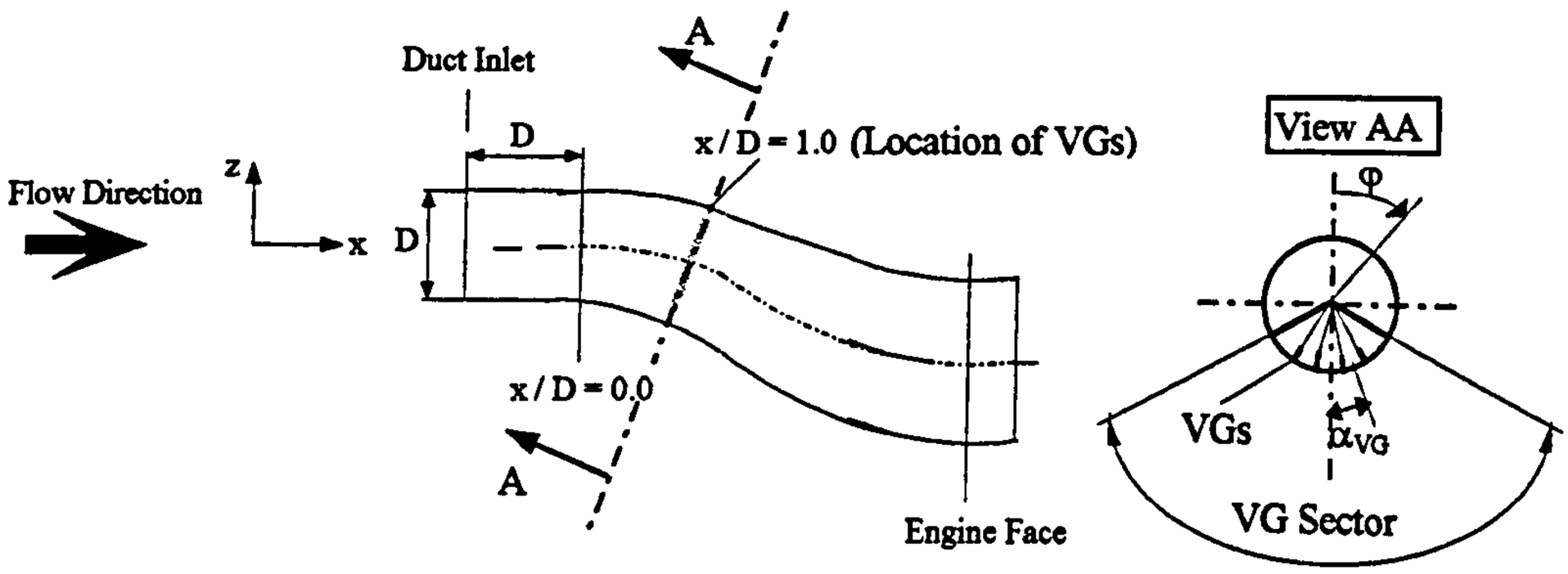

Figure 3.16: S-bend M2129 intake duct with VG location

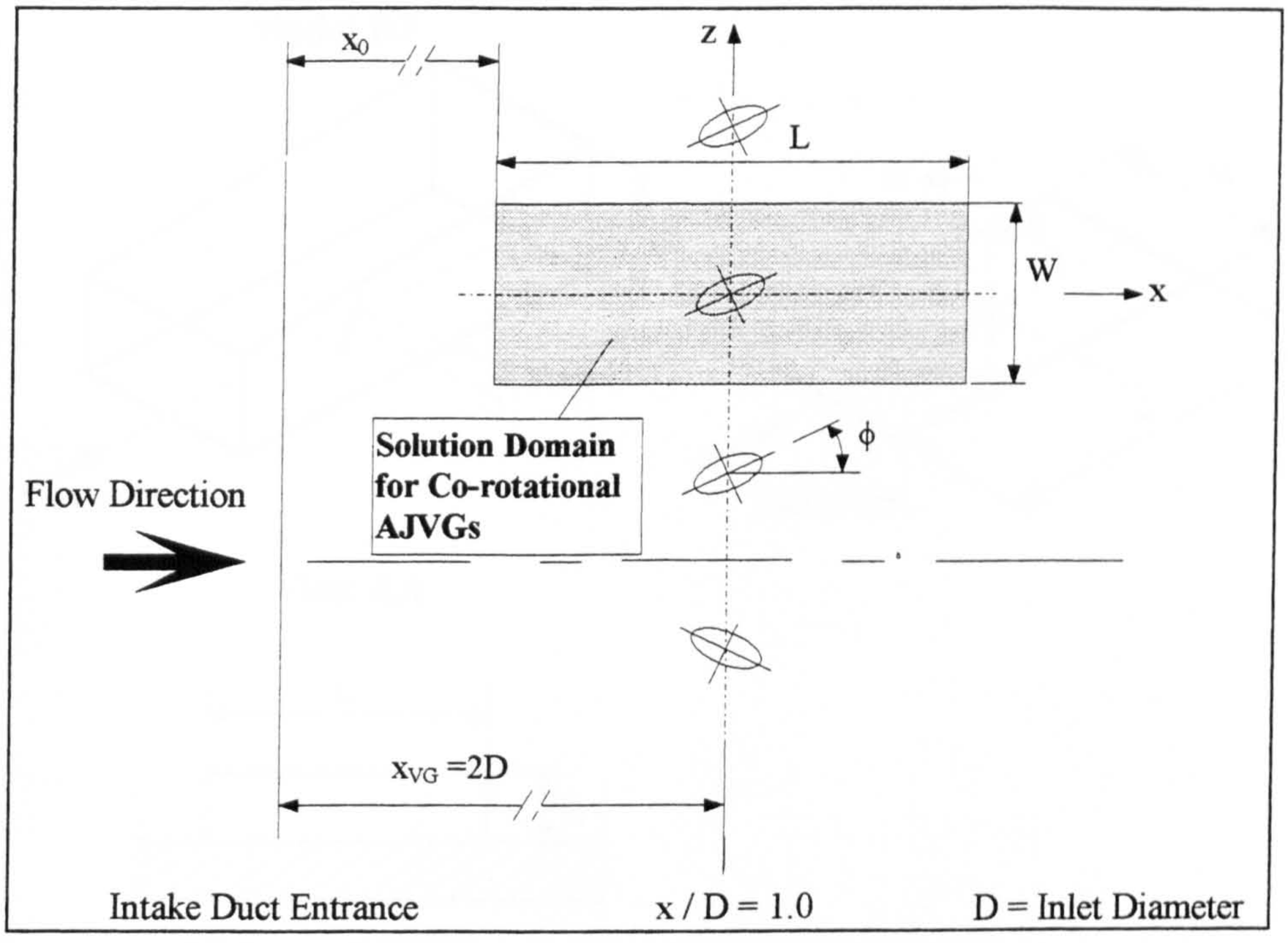

Figure 3.17: VG array with solution domain size

A plan view of the solution domain extent of the numerical local model of one VG is shown in Figure 3.17. Three local models were created in order to examine the interaction of the viscous boundary layer with the longitudinal vortices produced by the VGs. Model D1 described the vicinity of the AJVG and is similar to the flat plate verification model V2 (see Figure 3.14). Model D2 described the vicinity of the VVG with the flat plate model and is shown in Figure 3.18. Model D3 described the vicinity of the AJVG in the form of the sector model (see Figure 3.19).

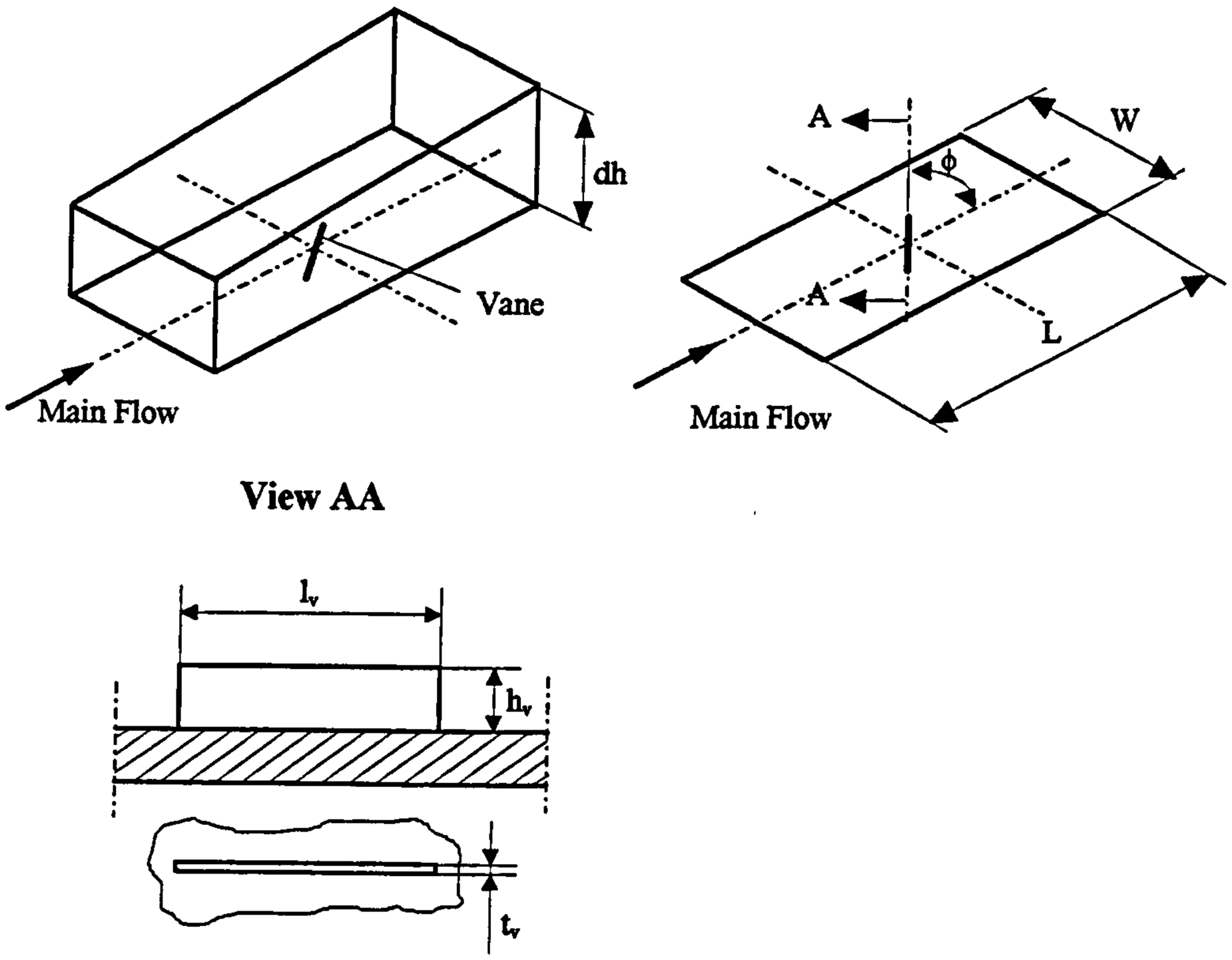

Figure 3.18: Local vane VG flat plate model

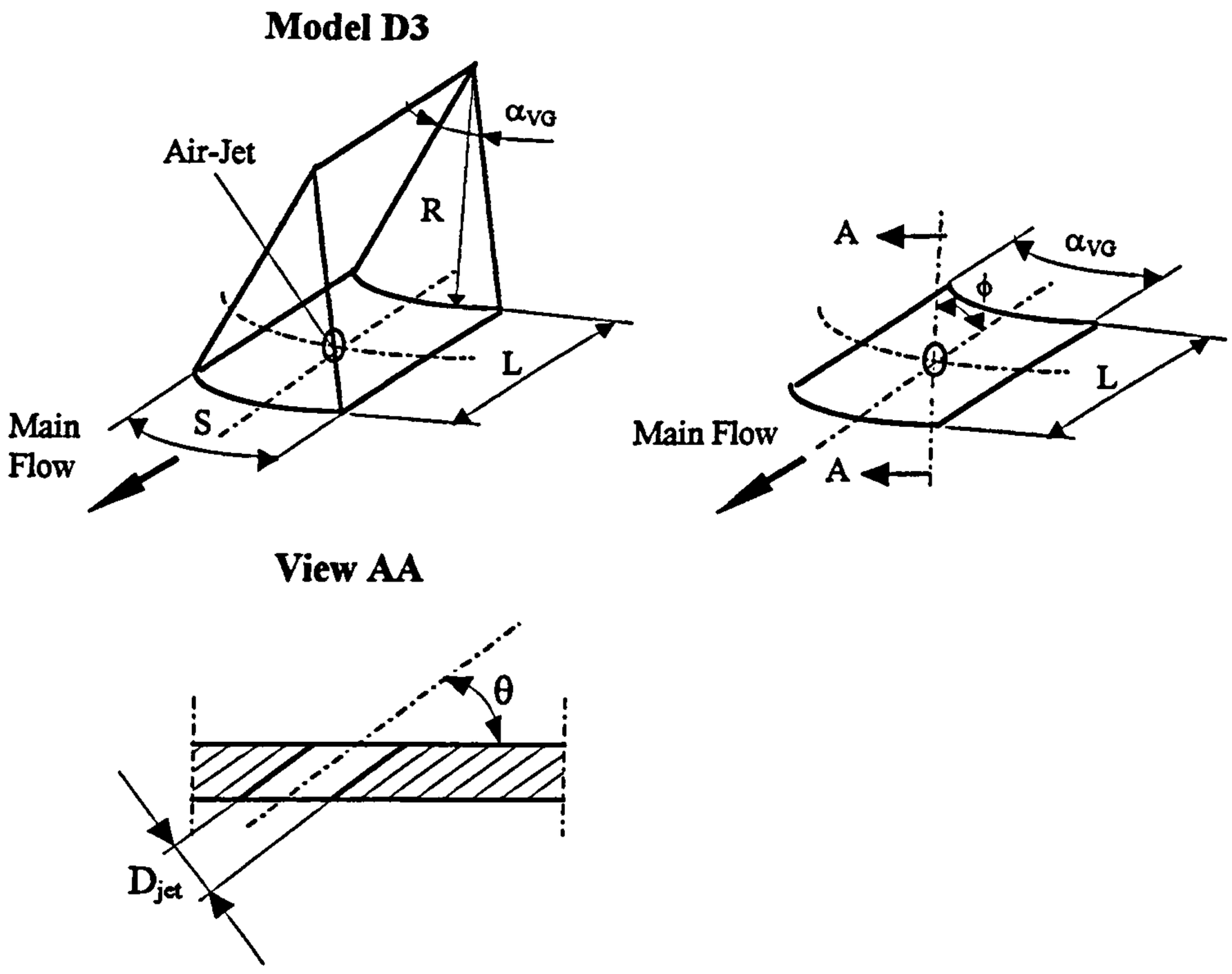

Figure 3.19: Local airjet VG sector model

The details of the three local models used to investigate the flow field at the streamwise position x/D = 1.0 (see Figure 3.16) within the duct, are as follows:

	Model D1 Flat Plate Model with AJVG	**Model D2** Flat Plate Model with VVG	**Model D3** Sector Model with AJVG
Solution domain length	L = 0.0676m	L = 0.0676m	L = 0.0676m
Sector angle			$\alpha_{VG.}$ = 15°
Solution domain width	W = S	W = S	S = α_{VG} R = 0.0169m
Solution domain height	dh = 5 δ (undisturbed local boundary layer height, see Equation 3.60)	dh = 5 δ (undisturbed local boundary layer height, see Equation 3.60)	R = D/2 = 0.0644m
Pitch angles	θ = 45° (see Figure 3.19)		θ = 30°, 45° (see Figure 3.19)
Skew angles	ϕ = 45° (see Figure 3.19)	ϕ = 16° (see Figure 3.18)	ϕ = 30°, 45°, 60°, 75° (see Figure 3.19)
Free stream velocity	U_0 = 254m/s	U_0 = 254m/s	U_0 = 254m/s
Airjet orifice diameter	D_{jet} = 0.001m		D_{jet} = 0.001m
Jet velocity	$U_{jet} = U_0$		$U_{jet} = U_0$
Vane length		l_v = 0.017407m	
Vane height		h_v = 0.004508m	
Vane thickness		t_v = 0.000432m	
Distance between duct entrance and solution domain entrance	x_0 = 0.2238m	x_0 = 0.2238m	x_0 = 0.2238m
Inlet boundary layer height	δ = 0.004m (see Equation 3.60)	δ = 0.004m (see Equation 3.60)	δ = 0.004m (see Equation 3.60)
Inlet Reynolds number	Re = 3.81×10^6 (see Equation 3.61)	Re = 3.81×10^6 see Equation 3.61)	Re = 3.81×10^6 (see Equation 3.61)

Table 3.2

The boundary conditions of the solution domain are:

Inlet boundary conditions

1) Velocity component U

The streamwise velocity profile U in the y-direction was defined in accordance with Prandtl´s 1/7-th power law (see Schlichting, 1979: p. 237).

$$\boxed{U = U_0 \cdot \left(\frac{y}{\delta}\right)^{1/7}} \quad (3.62)$$

2) Turbulent kinetic energy k

At the inlet to the main flow the turbulent kinetic energy was defined using the experimental ratio of the Reynolds stress to kinetic energy being constant over most of the boundary layer, see Figure 3.20 (see Hinze, 1959: p. 492).

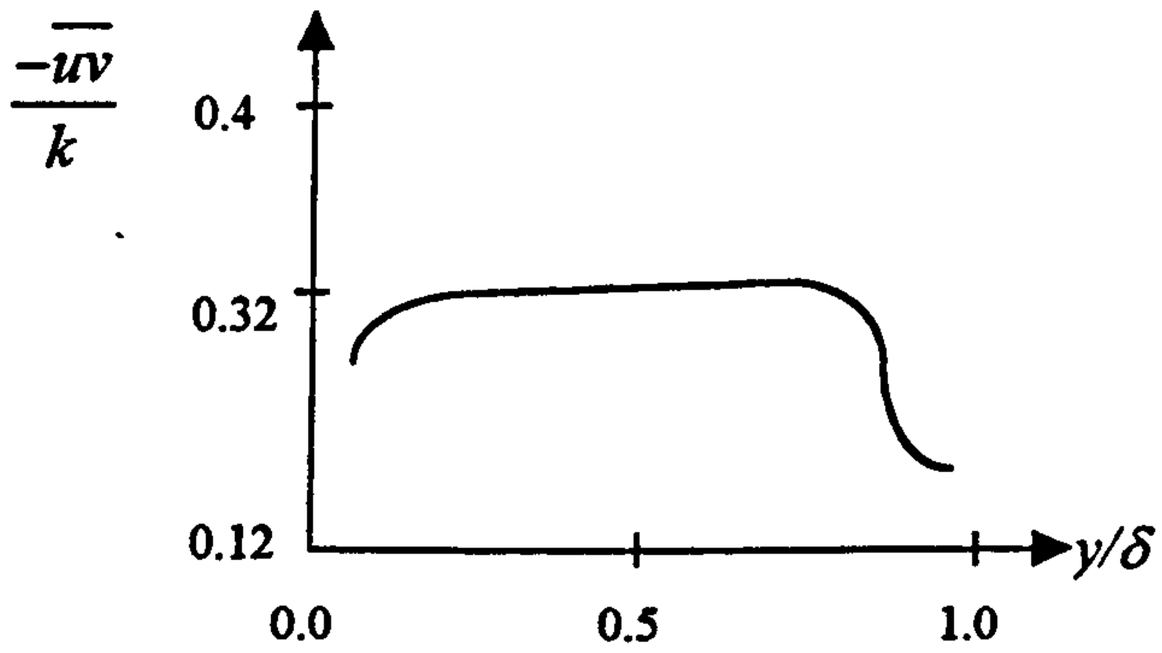

Fig. 3.20: Ratio between turbulent shear stress and turbulent kinetic energy across a boundary layer

According to Hinze (1959: p. 492) the turbulent kinetic energy at the inlet may be approximated as;

$$\boxed{k = \frac{-\overline{uv}}{0.32}} \quad (3.63)$$

The Reynolds stress was estimated using the eddy viscosity model, i. e.,

$$\boxed{\overline{uv} = -l^2 \cdot \left|\frac{\partial U}{\partial y}\right| \frac{\partial U}{\partial y}} \quad (3.64)$$

In wall boundary layers a ramp function of the mixing-length distribution (see Rodi, 1980: p. 17), was found to work satisfactorily.

$$\boxed{l = l_m = \kappa \cdot y \qquad \text{if} \quad 1 < 0.09 \cdot \delta} \quad (3.65)$$

otherwise

$$\boxed{l = l_m = 0.09 \cdot \delta} \quad (3.66)$$

The boundary layer height δ is defined as the distance from the wall where the velocity is equivalent to 99% of the free stream velocity. The value of the von Karman constant κ was set to be equal to 0.41.

3) Dissipation rate

Using the eddy-viscosity concept, Boussinesq (1877), for a two dimensional boundary layer flow the Reynolds stress reduces to:

$$\boxed{-\overline{uv} = \upsilon_t \frac{\partial U}{\partial y}} \quad (3.67)$$

Assuming a state of local equilibrium for non-buoyant shear layers (see Hinze, 1959: p. 498) the production is equal to the dissipation rate of turbulence. In the k-equation (see Section 3.5) the rate-of-change-term and both convective and diffusive transport terms are negligible. If the production is equal to the dissipation then:

$$\boxed{\varepsilon = \upsilon_t \left(\frac{\partial U}{\partial y}\right)^2} \quad (3.68)$$

Jet Inlet Boundary

The incoming jet velocity was defined to be a plug profile. The magnitude of the jet velocity was defined as a fraction of the free stream velocity U_0; i.e.,

$$\boxed{U_{jet} = VRAT \cdot U_0} \quad (3.69)$$

The jet flow inlet turbulent kinetic energy was assumed to be given by:

$$\boxed{k_{jet} = 0.002 \cdot U_{jet}^2} \quad (3.70)$$

This is a reasonable approximation for a relatively small inlet issuing into a large solution domain and is recommended in the CFX 4 Manual (1995).

The dissipation rate was assumed to be given by;

$$\boxed{\varepsilon_{jet} = \frac{k_{jet}^{3/2}}{0.3 D_{jet}}} \quad (3.71)$$

where D_{jet} is equal to the jet diameter

Upper and Outlet Boundary for Local Models V1, V2, D1, D2

The upper and the outlet boundary conditions were defined as constant pressure boundaries, i.e. the pressure is set to zero.

Upper Boundary for the Local Model D3

Axis-symmetric boundary conditions were imposed at the upper boundary.

Side boundary for Local Models V1, V2

Symmetry boundary conditions were imposed at the sides of the solution domain. The width of the solution domain was very large compared to the diameter of the generated vortex, thus the vortex behaved as an isolated vortex. As a result, the side boundary conditions were assumed not influence the vortex.

Side Boundary for Local Models D1, D2, D3

On each side of the solution domain either symmetry (set of counter-rotating vortices) or periodic (set of co-rotating vortices) boundary conditions were imposed.

3.8 Local Model Grids

Grid generation of Model V1 and V2

The grid generation code, 'JETGRID', written in Fortran 77, generates a multi-block structured three dimensional grid in an algebraic manner. The solution domain is divided into 17 grid blocks, as shown in Figure 3.21.

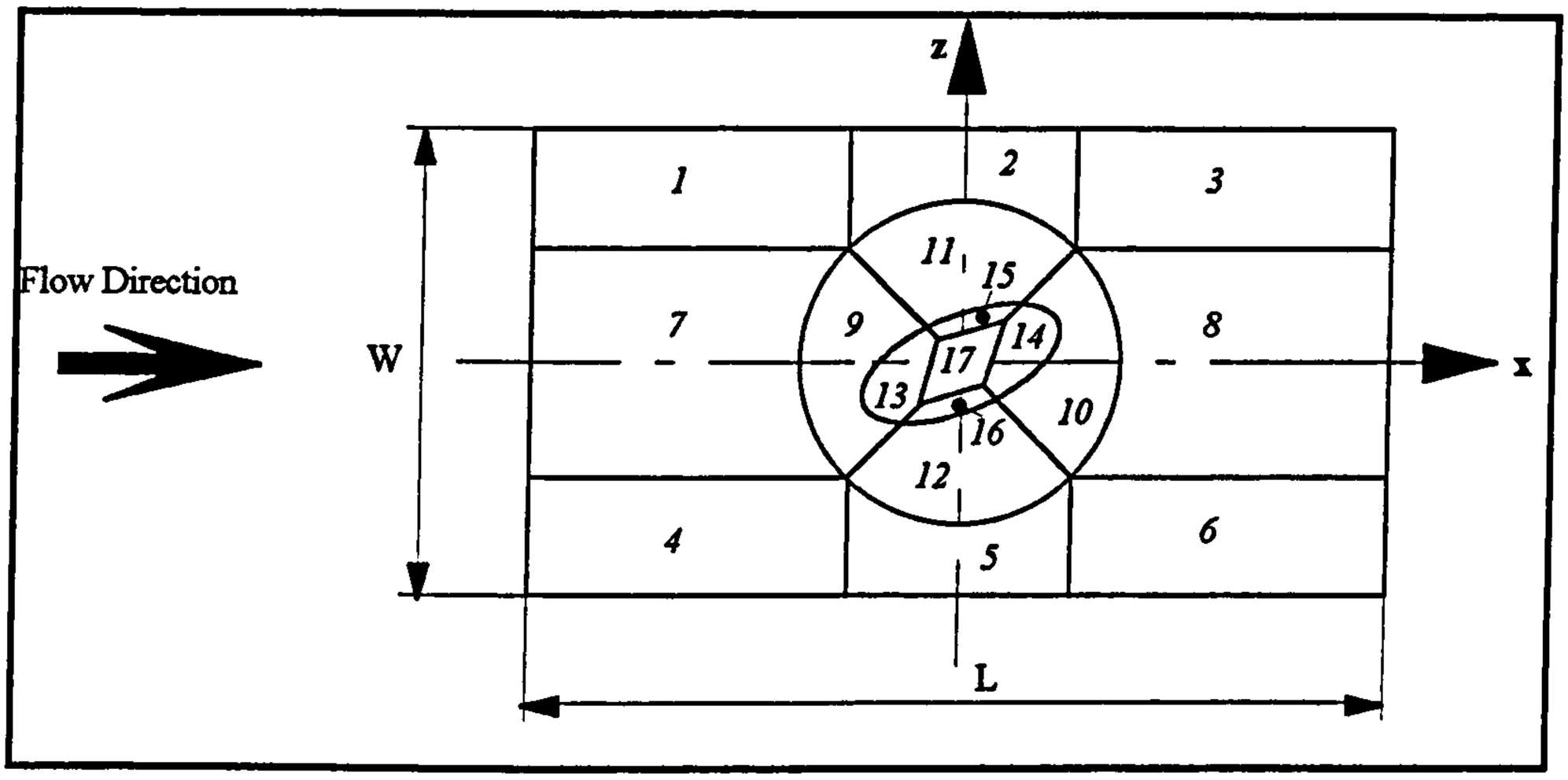

Figure 3.21: Plan view of the grid block configuration of the solution domain

The central ellipse comprising a diamond-shaped block (No.17) and the four surrounding blocks (No.13 - 16) constitutes the grid for the jet exit orifice. The four blocks (No.9 - 12) surrounding the ellipse and forming a circular grid facilitate the

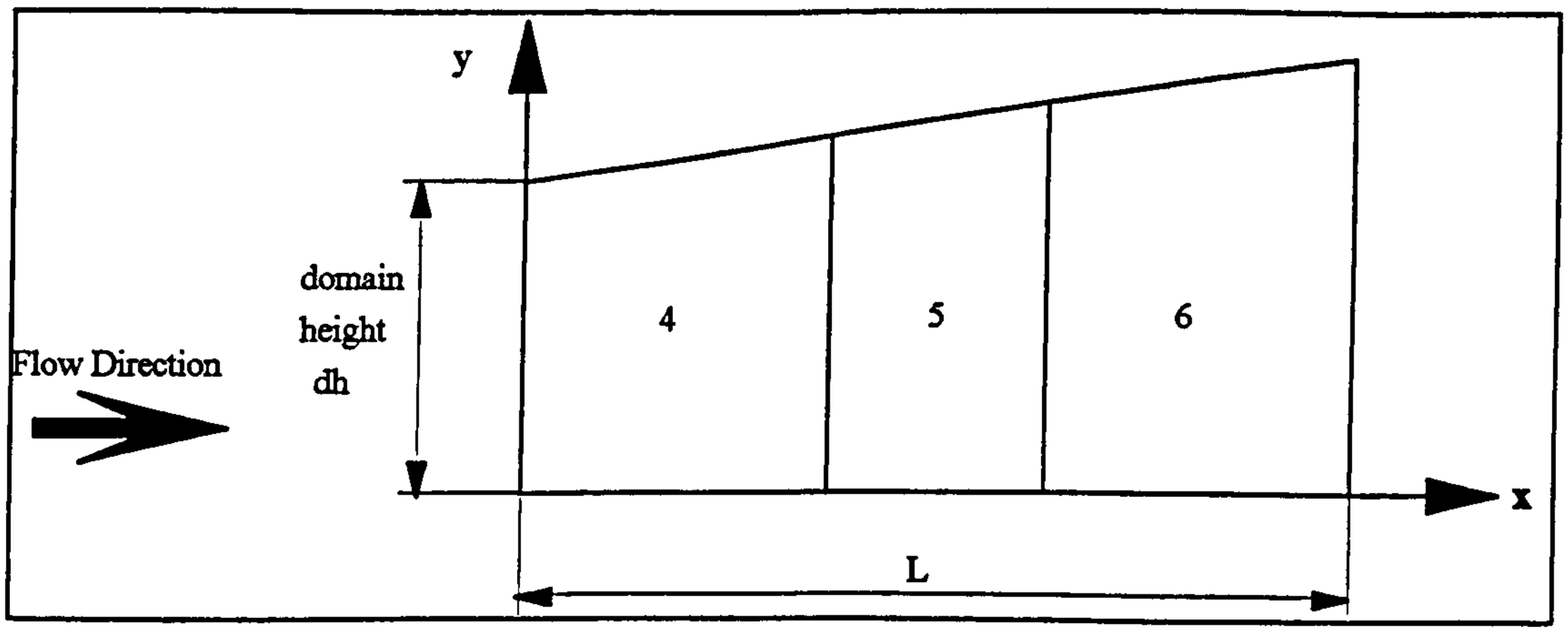

Figure 3.22: Side view in positive z-direction

requirement that the grid be periodic in the z-direction. This is required so that side periodic boundary conditions can be applied. Two geometric parameters, the solution domain length L, and width W, define the physical domain. The lower surface of the domain is a flat rectangular plate. In the third dimension (y-direction) the domain height, dh, is a multiple of the local boundary layer height δ and therefore increases in the flow direction (x) (see Figure 3.22). For clarity, only blocks 4 to 6 are shown. At the solution domain inlet, the boundary layer height is greater than zero, because the boundary layer height at the centre of the air jet orifice has to match the experimental value, as previously mentioned in Section 3.7.2.

dhr was set to 5. The correlation for the domain height is:

$$\boxed{dh = dhr \cdot \delta} \quad (3.72)$$

For any physically defined flow, the code generates a block structured grid, with a cell distribution fixed by the following geometrical parameters:

Geometrical parameters

L:	length of the flat plate in x-direction (see Figure 3.21)	⎫ dimension
W:	width of the flat plate in z-direction (see above)	⎬ in
D_{jet}:	diameter of the airjet orifice (see Figure 3.13)	⎭ meter
θ:	pitch angle (see Figure 3.13)	⎫ these angles
ϕ:	skew angle	⎭ are in degrees

ESF: expansion factor for calculating the radius of the circle (see Figure 3.23)

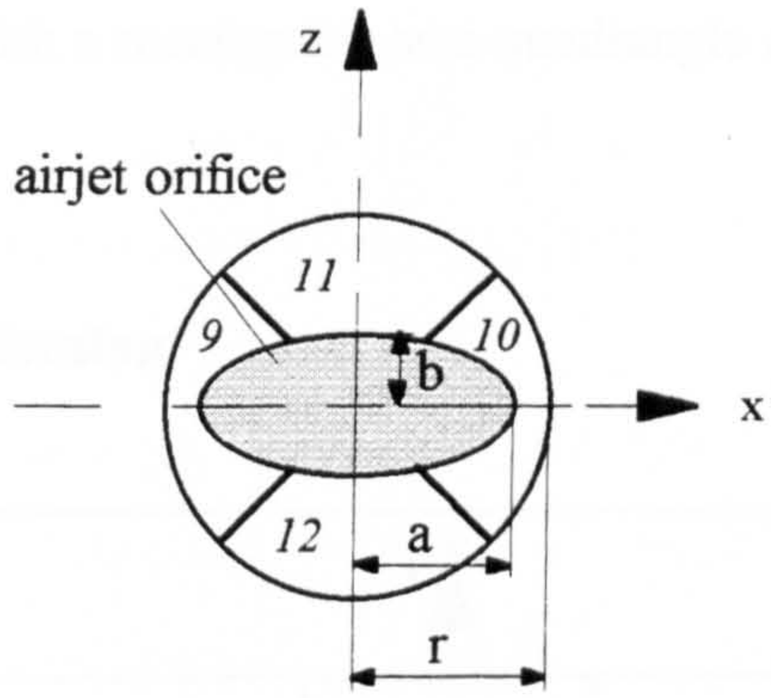

Figure 3.23: Block structure within the circle

$$\boxed{r = a + (a \cdot ESF)} \quad (3.73)$$

where, a = half major axis of the ellipse

r = radius of the circle

The chosen expansion factor ESF defines the size of the four grid blocks (Nos.9 - 12) around the airjet orifice. Depending on the size of the circle, the area around the airjet orifice within the circle expands or contracts to ensure a homogenous distribution of cells.

DIST: factor for defining a constant distance between the four diamond vertices and the four intersections of the straight 45° lines and the ellipse (see Figure 3.24).

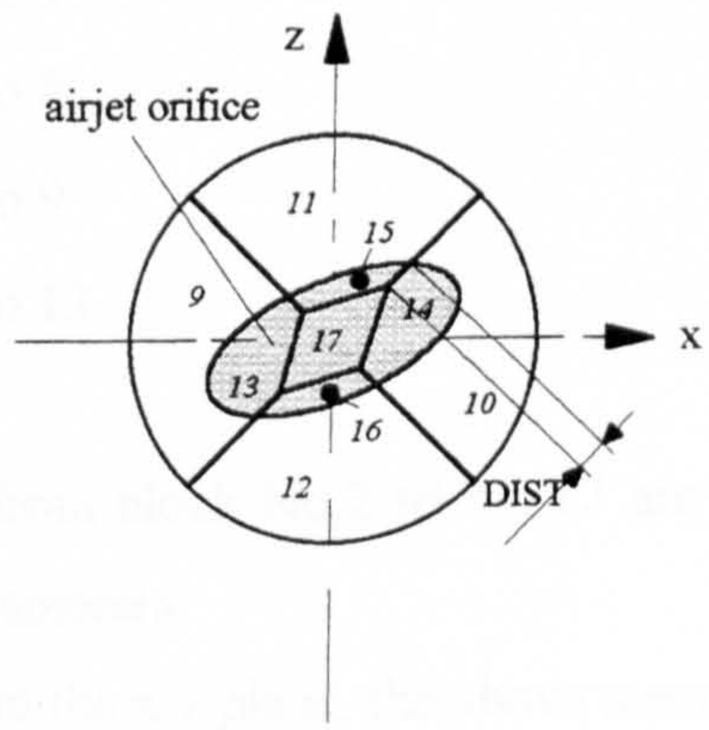

Figure 3.24: Block structure within the airjet orifice

The distance factor DIST defines four similar grid blocks (Nos.13 - 16) within the airjet orifice around the diamond. The diamond was found to give the best grid node distribution, compared with a rectangular or a quadrangle at a defined pitch angle, θ, for all skew angle, ϕ.

Input data for cell distribution

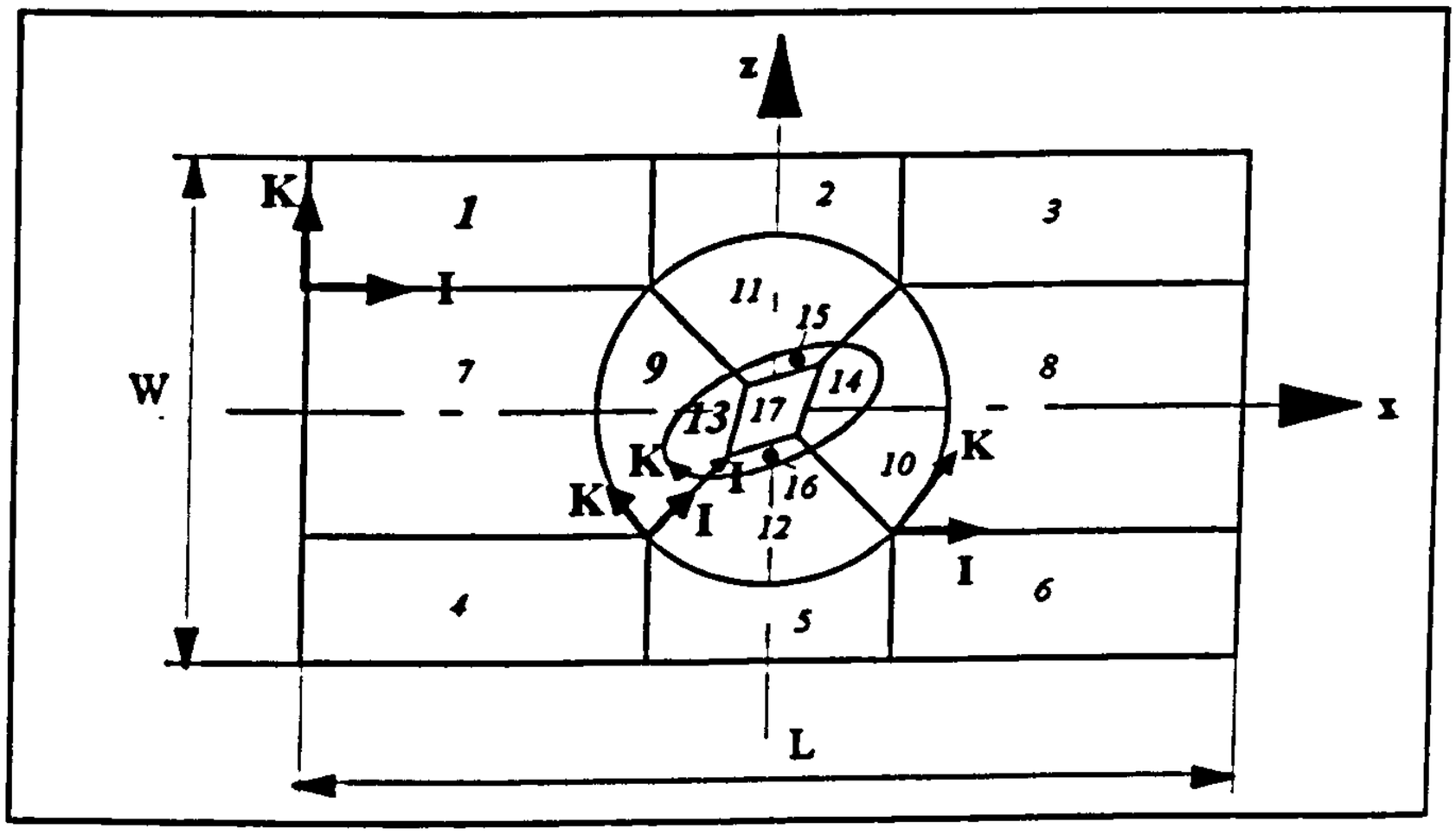

Figure 3.25: Plan view with block defined I, K notation

The following number of grid nodes NI and NK describe the total number of grid nodes in I- and K-direction for the grid blocks No.1, 8, 9 and 13 (see Figure 3.25). They have to be given as an input data file; i.e.,

NI(1), NK(1) → block No.1
NI(8) → block No.8
NI(9) → block No.9
NI(13) → block No.13

All the other grid points from block No.2 to No.17 are generated automatically by applying the geometric parameters.
To define the grid density in the x-z plane, the above mentioned number of grid nodes have to be defined. NI and NK for block No.1 define the density of the upstream

outer blocks (Nos.1, 4, 7)). NI(8) defines the downstream axial grid density of the outer grid blocks (Nos.3, 6, 8). By fixing NI(9) the grid distribution within the circle, i.e. blocks Nos.9 to 12, will be created. The last number of grid points NI(13) defines the density in the airjet orifice for block Nos.13 to 16. The number of grid points in J-direction is calculated within the code by ensuring of y^+ values (see Section 3.5) in the range of $30 \leq y^+ \leq 100$.

The code generates a multi-block structured grid. For numerical investigations of different diameters of airjet orifices, see Figure 3.13, and any combinations of a pitch angle $\boxed{0^0 \leq \theta \leq 90^0}$ with a skew angle $\boxed{0^0 \leq \phi \leq 90^0}$.

It is computationally essential when applying periodic boundary conditions to ensure that the grid is periodic about the boundaries. This was achieved by restricting any grid distortion caused by the skewed ellipse representing the pitched jet orifice to be kept within the central circular area of the grid. In spite of this, the accuracy is not impaired, because there is a smoothly expanding grid (see Figure 3.26) from the circle to the outer boundaries in x-direction, i.e. in blocks No.7 and No.8. In Figure 3.27 smooth transition between blocks, No.13 to No.16, may be seen, which are located in the airjet orifice, to the surrounding blocks (Nos.9 to 12). At the boundary between these blocks, all increments are equal. It was considered unnecessary to expand the gird blocks No.1 to No.8 in z-direction. In order to optimise the cpu-time for running the flow solver the number of grid blocks were reduced from 17 to 13 by joining blocks No.1 to 3 and blocks No.4 to 6.

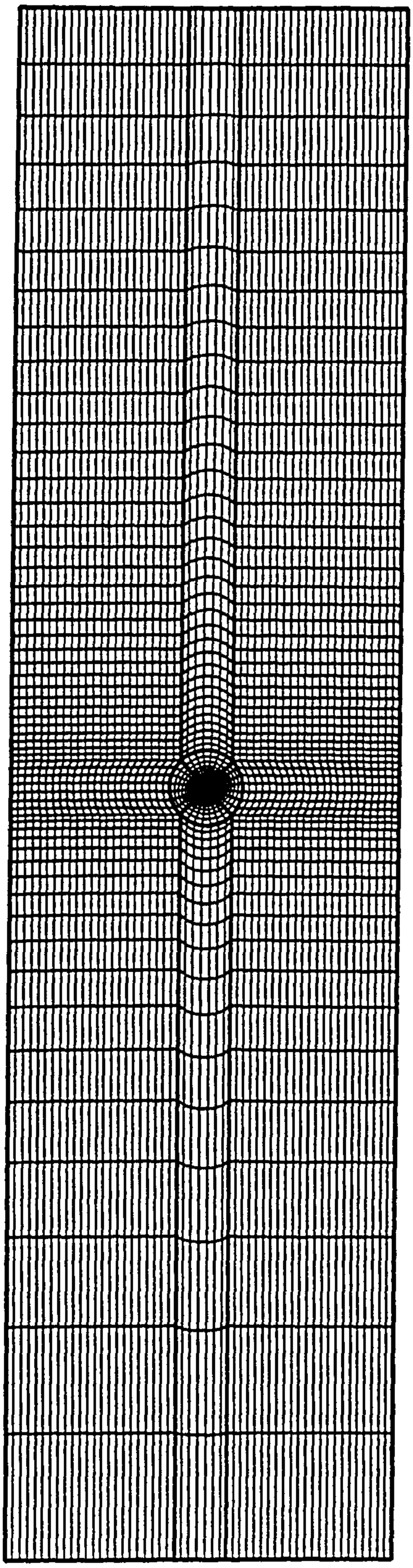

x-z plane

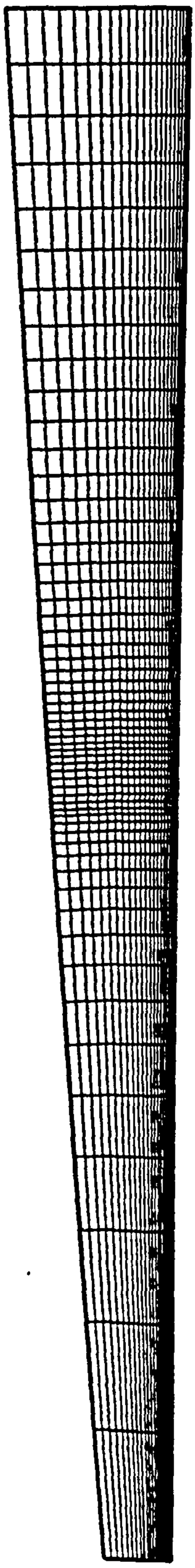

x-y plane

3.26: View of the grid of model V1 and V2 in (x-z) and (x-y) plane

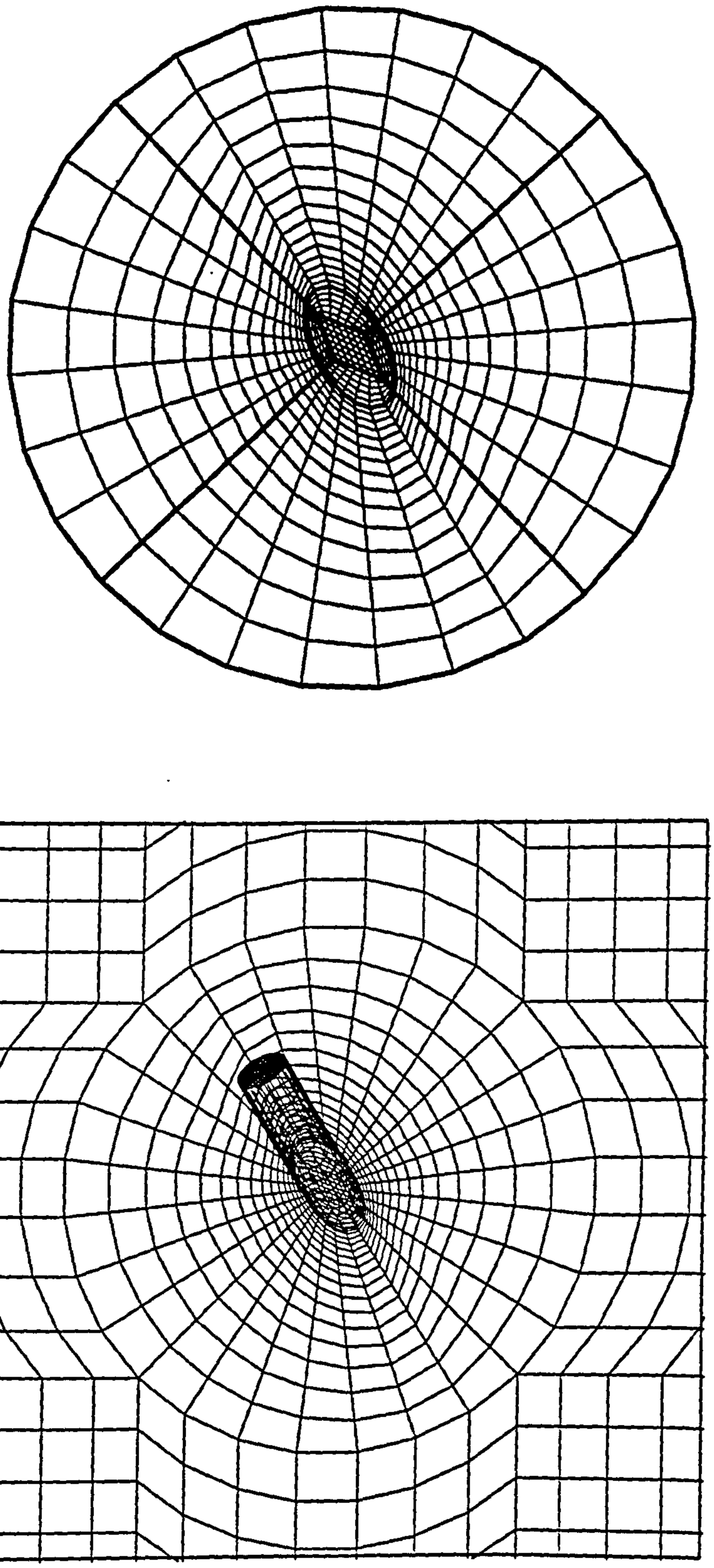

3.27: Detailed view of the inner block configuration with and without jet inlet tube, of model V1 and V2

Grid of Model D1

The structure of the numerical grid (see Figure 3.28), for the flat plate model is similar to the grid produced for Model V2.

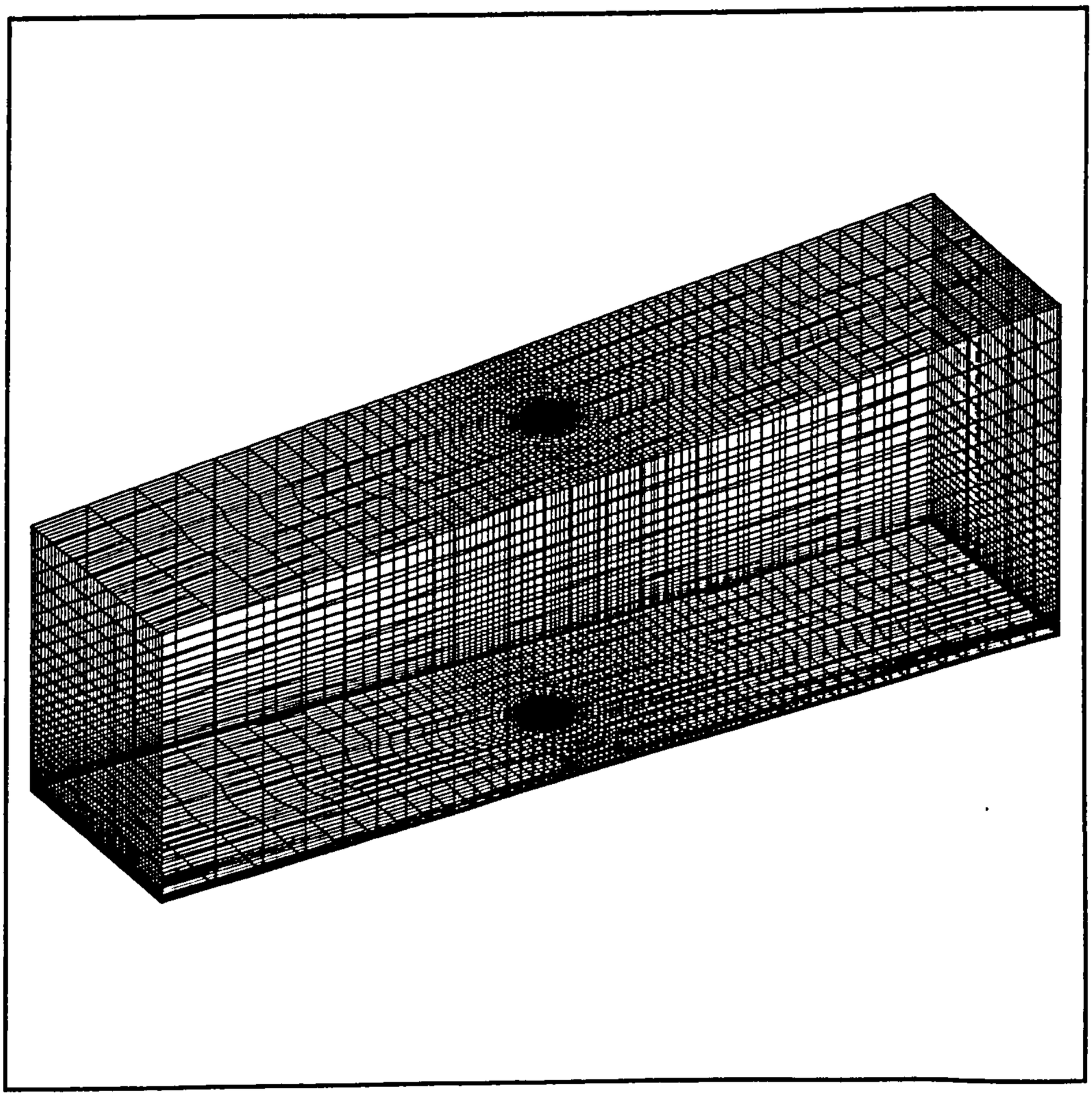

Figure 3.28: Isometric view of the solution domain of model D1

Grid generation of Model D2

The grid generation code 'VANEGRID', written in Fortran 77, generates a one-block structured three dimensional grid in an algebraic manner. For any physically defined flow, the code generates a grid, with a cell distribution fixed by the following geometrical parameters:

Geometrical parameters

L:	length of the solution domain in x-direction	⎫	
dh	height of the solution domain (see Figure 3.22)	⎪	
l_v	⎫	}	in meter
h_v	} vane dimensions	⎪	
t_v	⎭	⎪	
W	width of the domain	⎭	
ϕ	skew angle	}	in degrees

Input data for cell distribution

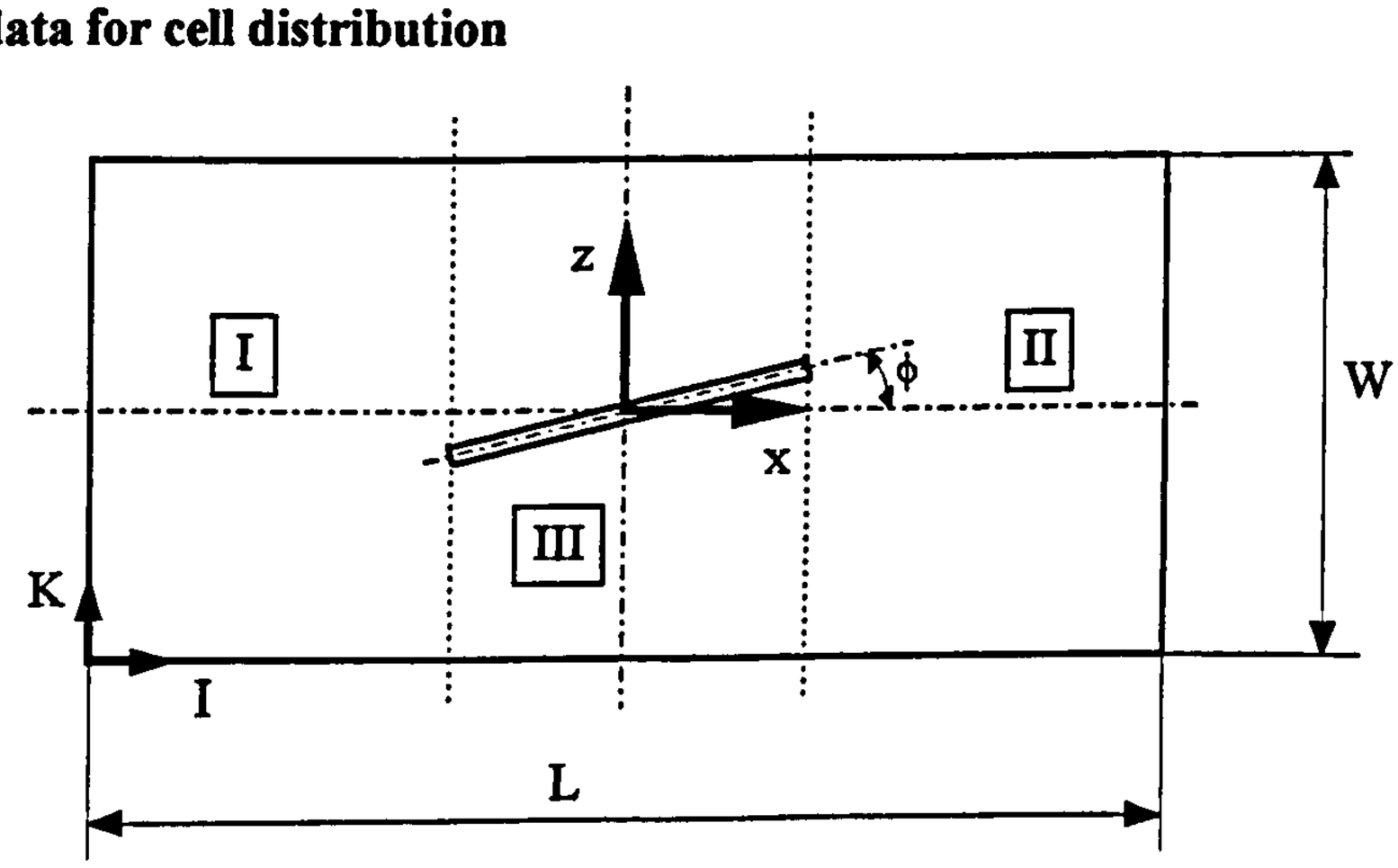

Figure 3.29: Plan view with I, K notation

The grid is divided in three areas (see Figure 3.29), having a common grid density in K-direction, i.e. NK. Area (I), i.e. NI(I), defines the upstream axial grid density. NI(II) defines the downstream axial grid density. The axial mesh density of area (III)

is defined by the number of cells NI(III) along the vane. For numerical investigations of different skew angles $\boxed{0^0 \leq \phi \leq 90^0}$, the Fortran code is capable of generating a one-block structured grid. The grid generation in the y-direction (see Figure 3.31) is equivalent to that in 'JETGRID' described previously. In Figure 3.30 smooth transition between the areas (I) to (III) may be seen.

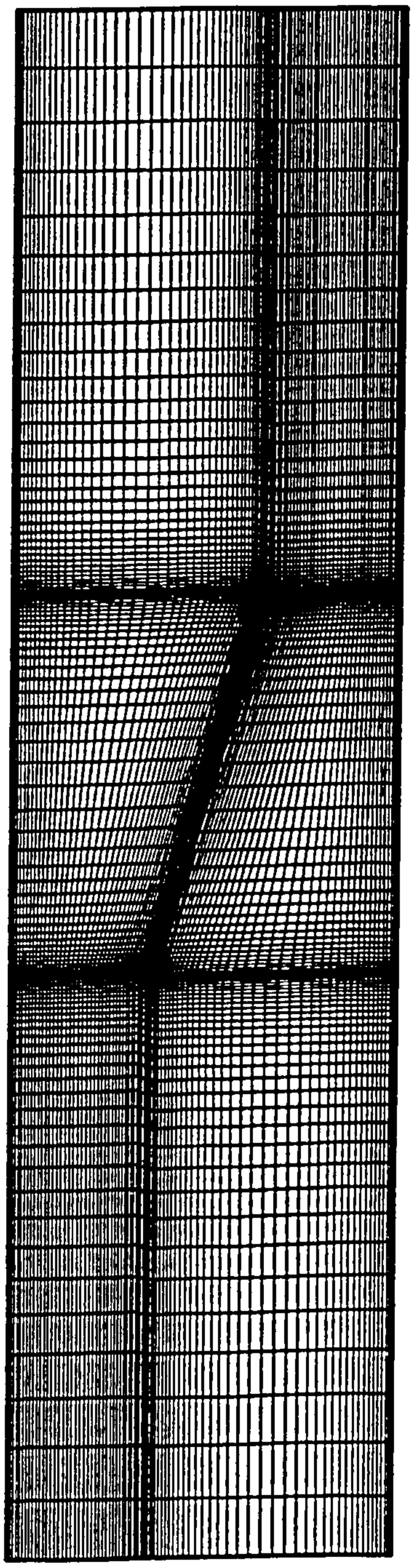

Figure 3.30: View of the VVG grid of model D2 in positive y-direction

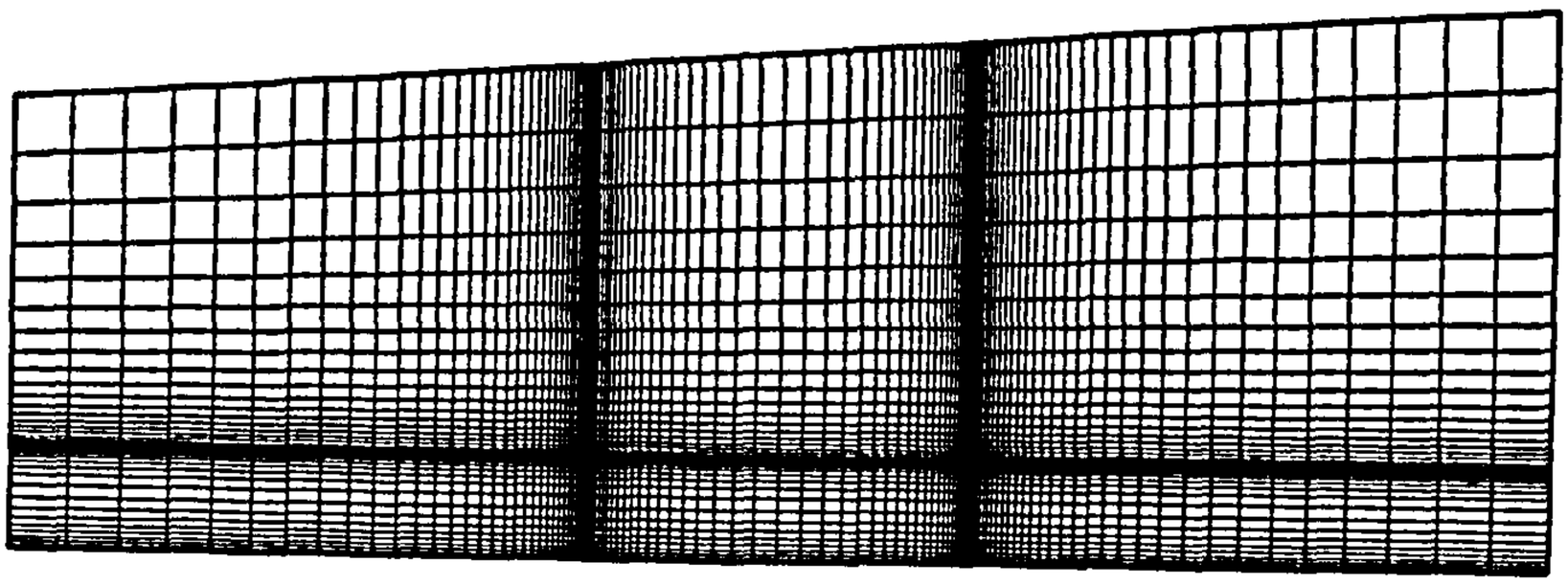

Figure 3.31: Side view of the VVG grid of model D2 in positive z-direction

Figure 3.32 shows a three-dimensional view of the one block grid of the vane VG.

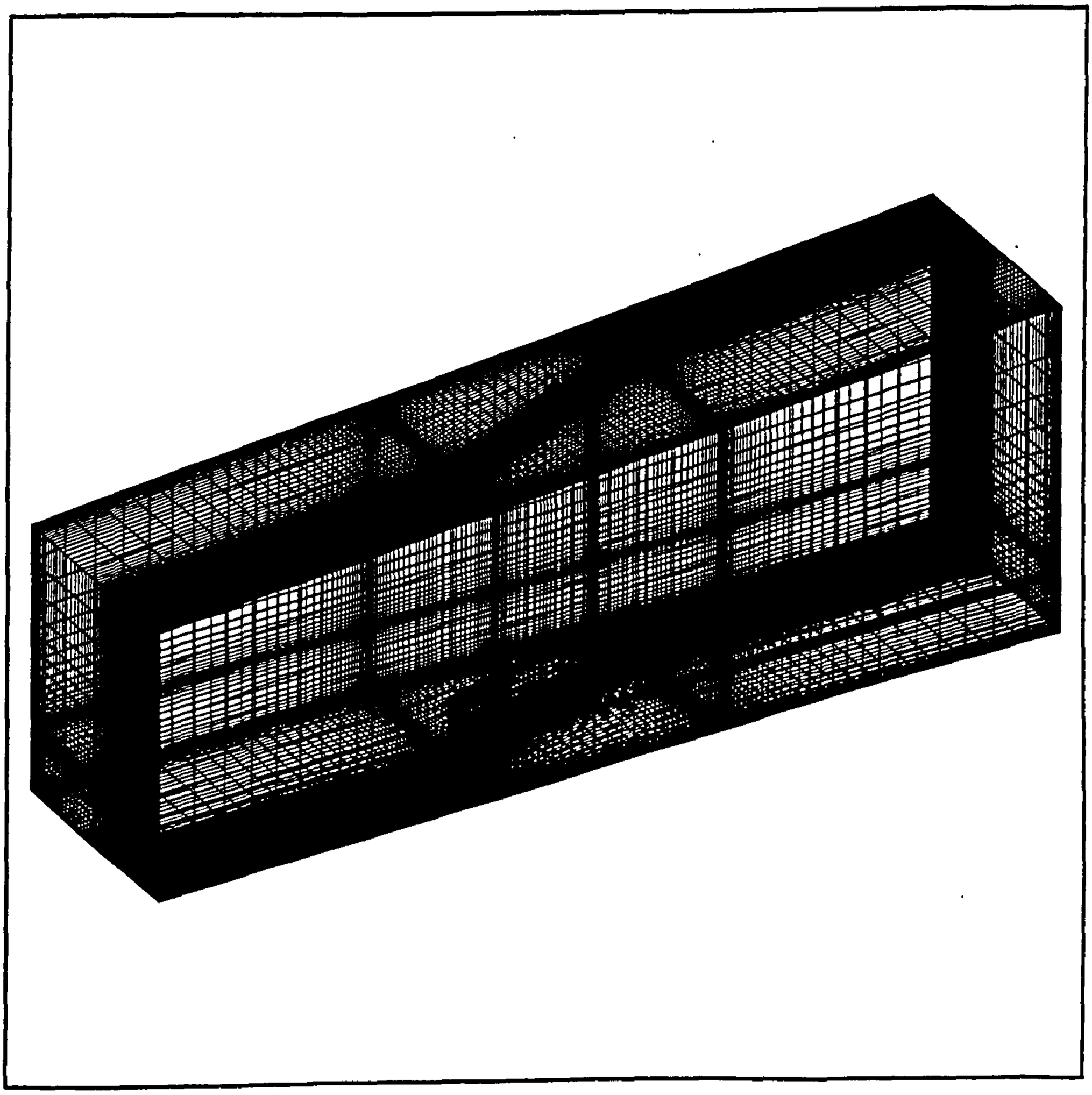

Figure 3.32: Isometric view of the solution domain of the VVG of model D2

Grid generation of Model D3

The structure of the numerical grid, for the sector model is topologically equivalent to the grid produced for the Model D1. The only difference is the coordinate system employed, which is changed from Cartesian to polar coordinates. The 15° sector domain (see Figure 3.33) has a constant height, which is equal to the radius of the duct (r = R).

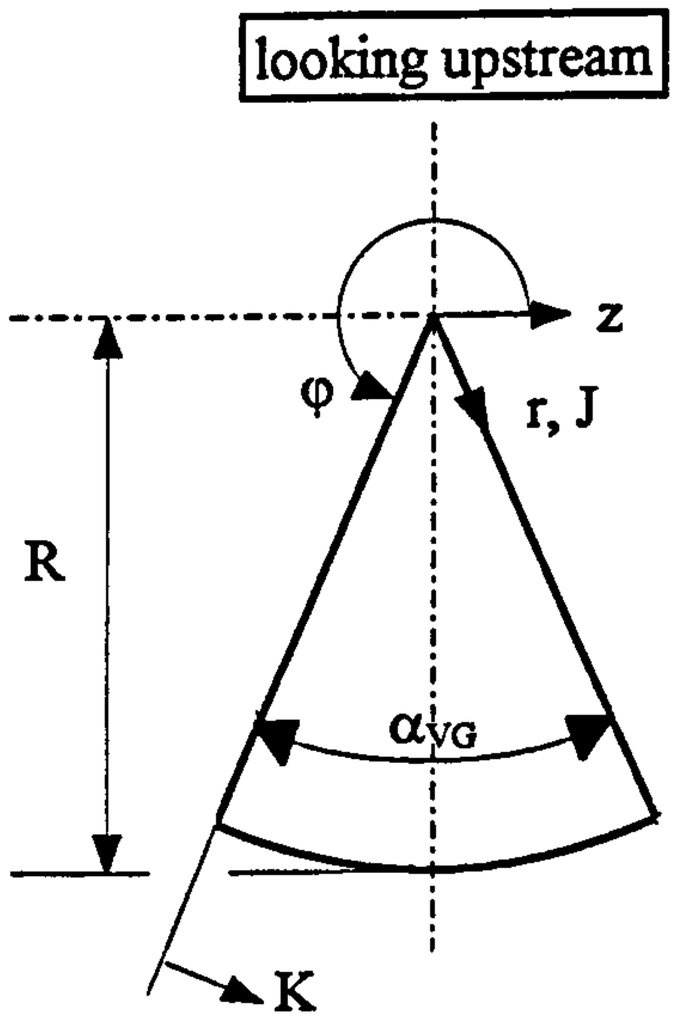

Figure 3.33: z-r-plane of the grid sector of model D3

The number of grid points in the J-direction is calculated within the code by ensuring of y^+ values (see Section 3.5) are in the range of $30 \leq y^+ \leq 100$. Smooth transition between the grid blocks and from the wall may be seen in Figures 3.34 to 3.37.

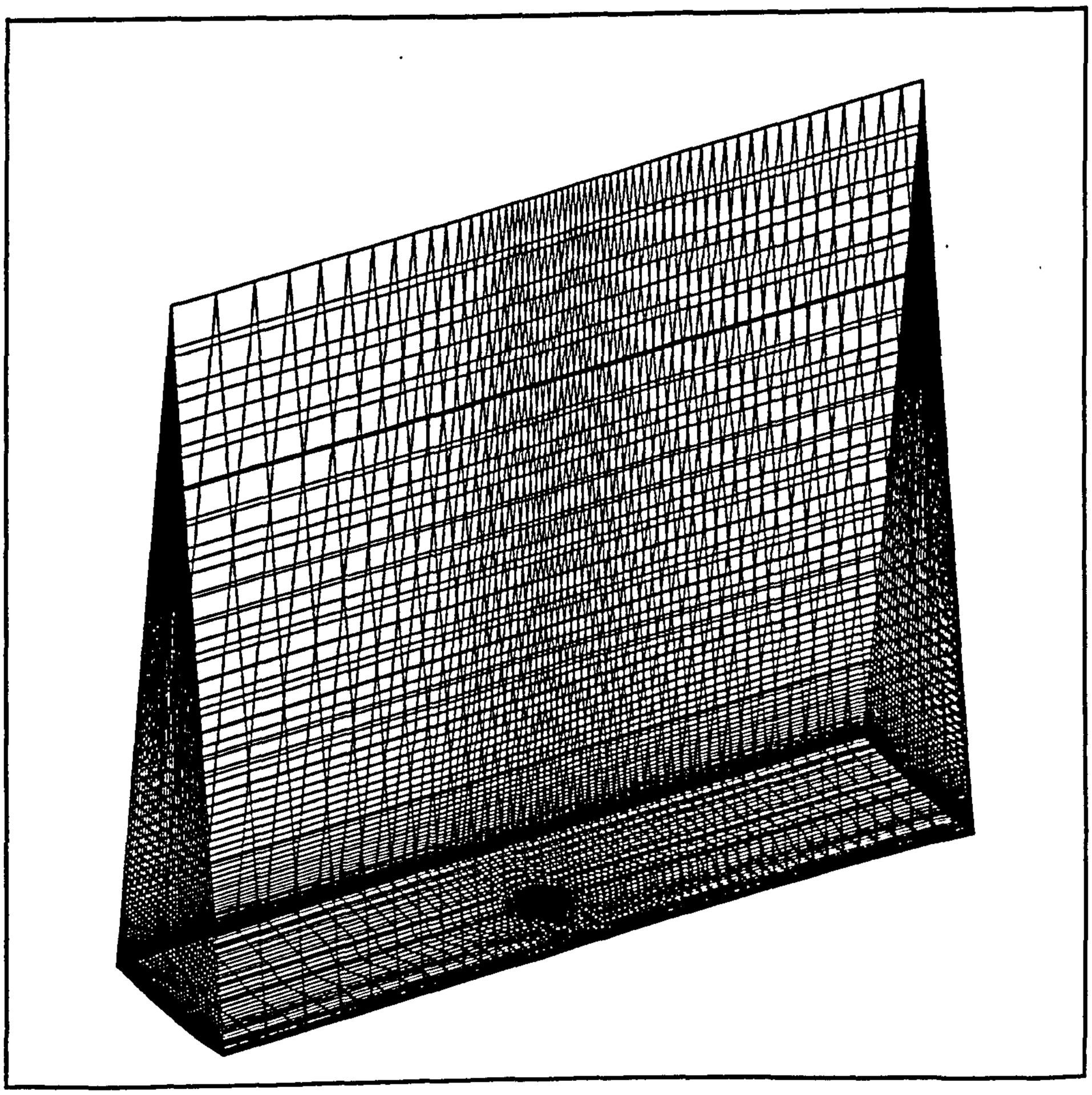

Figure 3.34: Isometric view of the grid sector of model D3

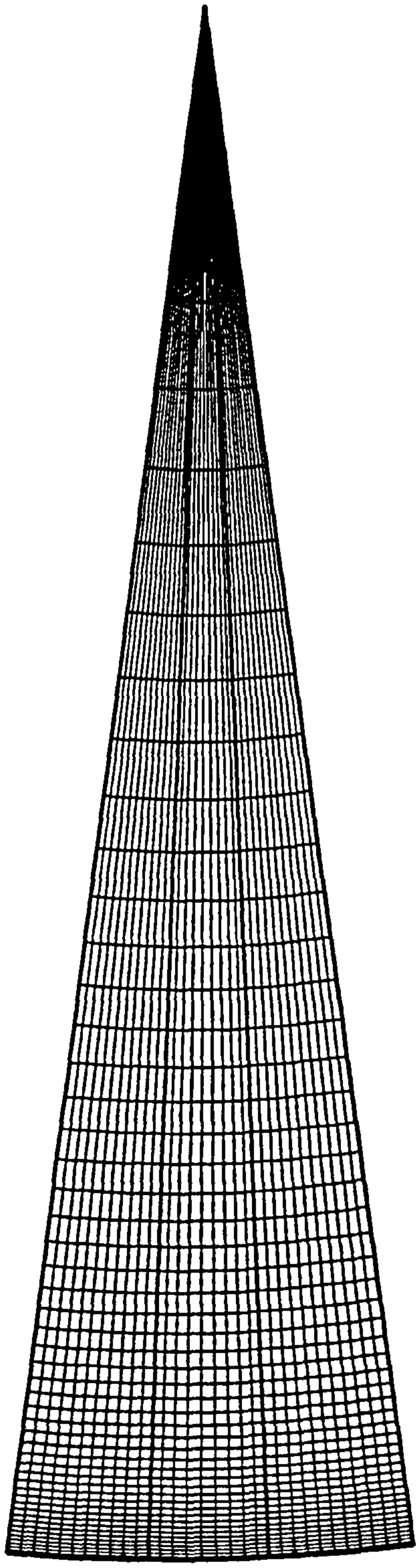

Figure 3.35: y-z plane of the grid sector of model D3

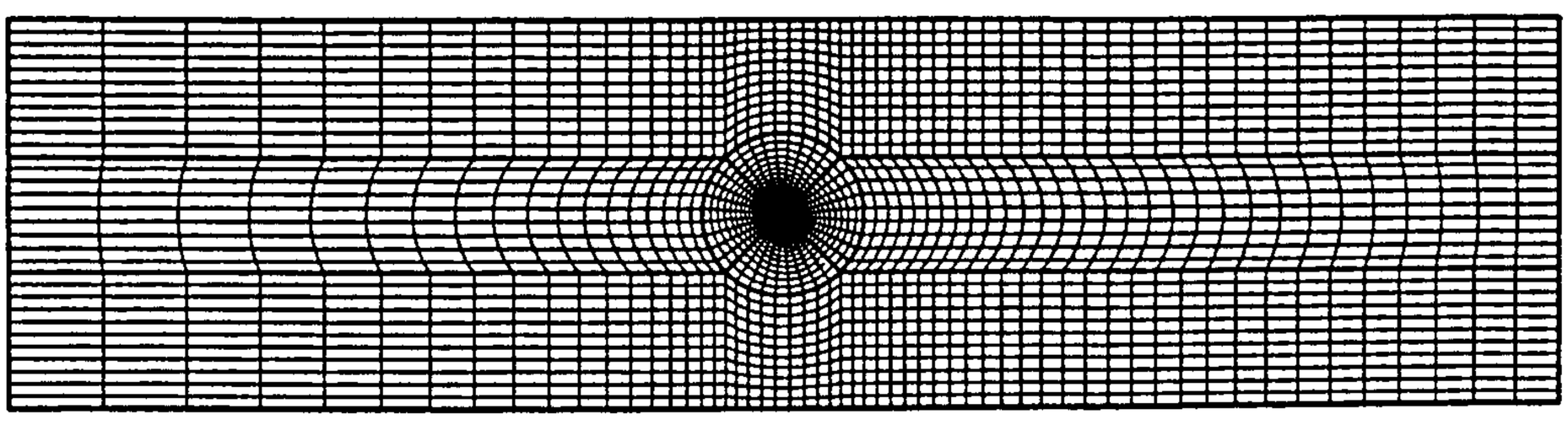

Figure 3.36: Plan view of the grid of model D3

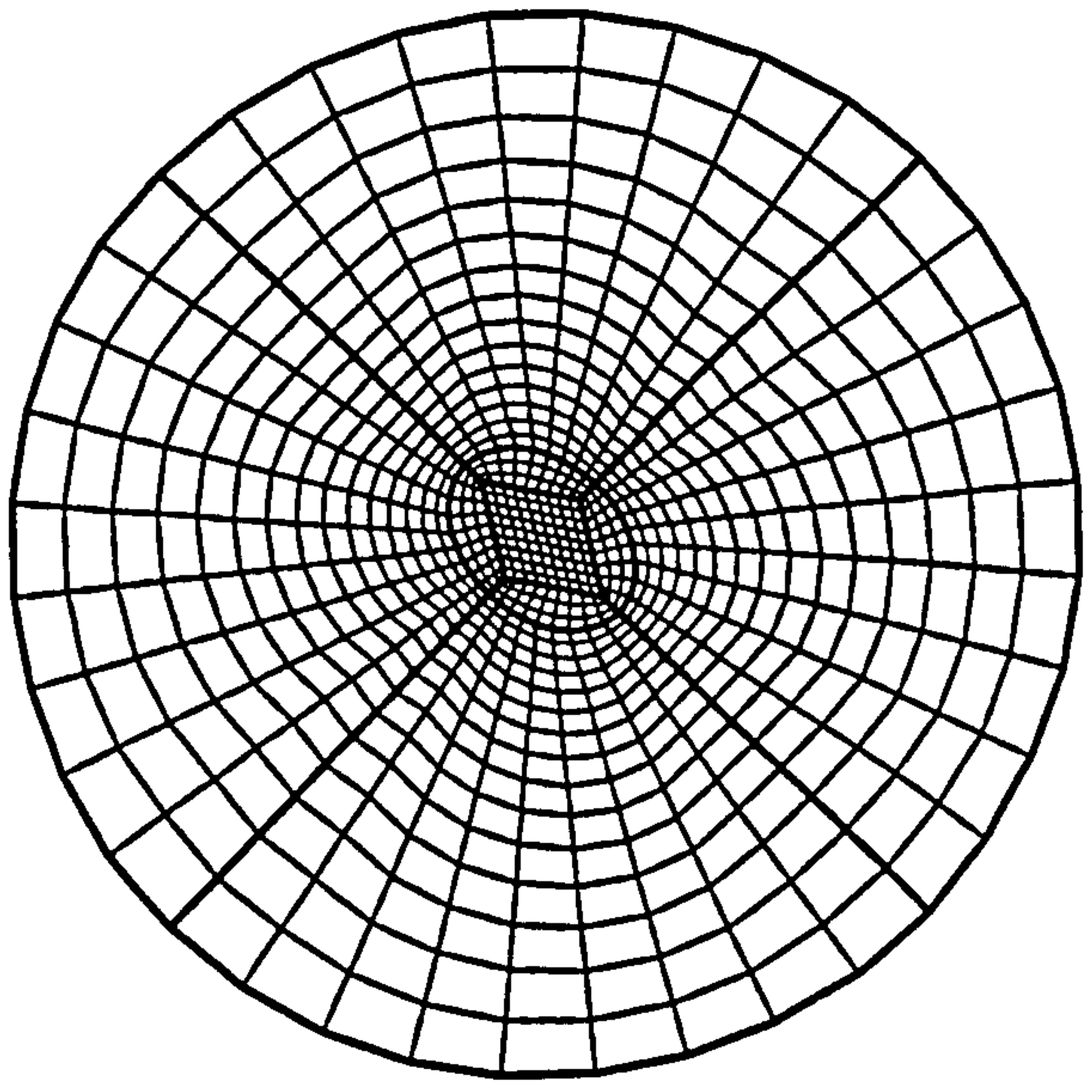

Figure 3.37: Detailed view of the inner block configuration of model D3

Calculation of the maximum and minimum skewness ζ_{max} / ζ_{min}

The intention was to create a routine in which the local distortion of the physical grid was estimated. Both the maximum and minimum skewness were calculated to check that the generated grid represented an acceptable discretisation. The most important value is the maximum skewness which may cause an inaccurate solution due to discretisation errors.

Skewness

In the literature, several definitions of skewness appear to be used. The definition employed in JETGRID was chosen for its simplicity.

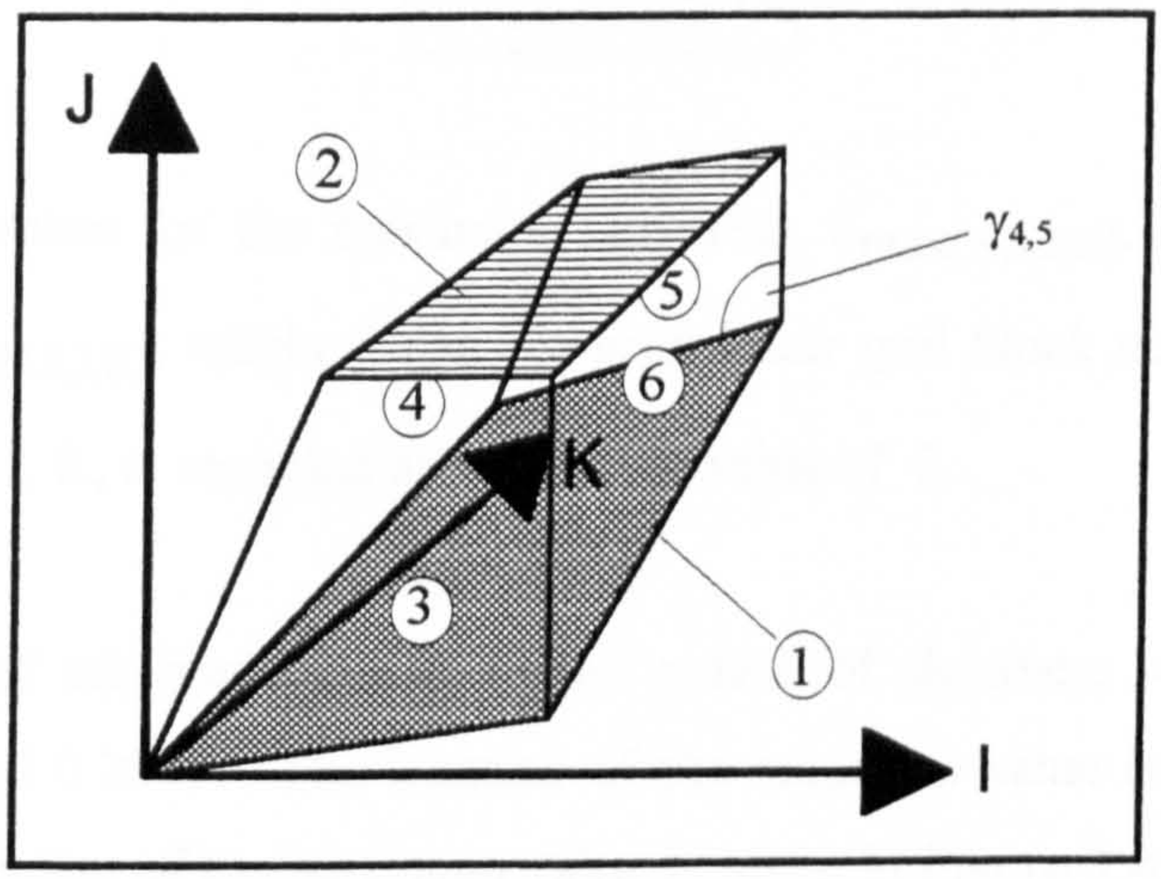

Fig. 3.38: Arbitrary distorted grid cell

Consider the typical cell of the physical grid, as shown in Figure 3.38. Its shape consists on 24 angles, i. e. six faces or planes each with four angles, where 18 angles are independent. The location of each angle is defined by the indices a and f of $\gamma_{a,f}$. The first subscript, a, defines the angle the second index, f, is the face number.

The skewness routine is defined as the sum of the square of the cosine of each angle $\gamma_{a,f}$ divided by the total number of angles per volume (i.e., 24).

$$\frac{1}{a \cdot f} \cdot \sum_{i=1}^{f} \sum_{i=1}^{a} \left(\cos\gamma_{a,f}\right)^2 = \zeta_{N,I,J,K} \tag{3.74}$$

$a \equiv$ *number* of angle

f ≡ face of a particular volume

N ≡ grid block No.

I, J, K ≡ notation

This provides a characteristic skewness scale ζ in a range between 0.0 and 1.0. If all angles are right angles, the skewness scale is exactly $\zeta = 0.0$. For a completely collapsed grid cell $\zeta = 1.0$. Hence,

$$\boxed{0 \leq \zeta_{N,I,J,K} \leq 1.0}$$

The routine searches for the maximum skewness, $\zeta_{max(N,I,J,K)}$, and the minimum skewness, $\zeta_{min(N,I,J,K)}$, within the whole grid. Their grid block number, N, and the local position, I, J, K, is recorded as well as the value of ζ.

Typical results of minimum and maximum values of skewness were found to be between zero and 0.27570. The location of the minimum value is shown in Figure 3.39, and the location of the maximum value is given in Figure 3.40. It is noted that the skewness in the diamond-shaped block is approximately the same for all cells and the maximum occurs at the location in Figure 3.40, because the contribution to skewness in the y-direction is greatest there.

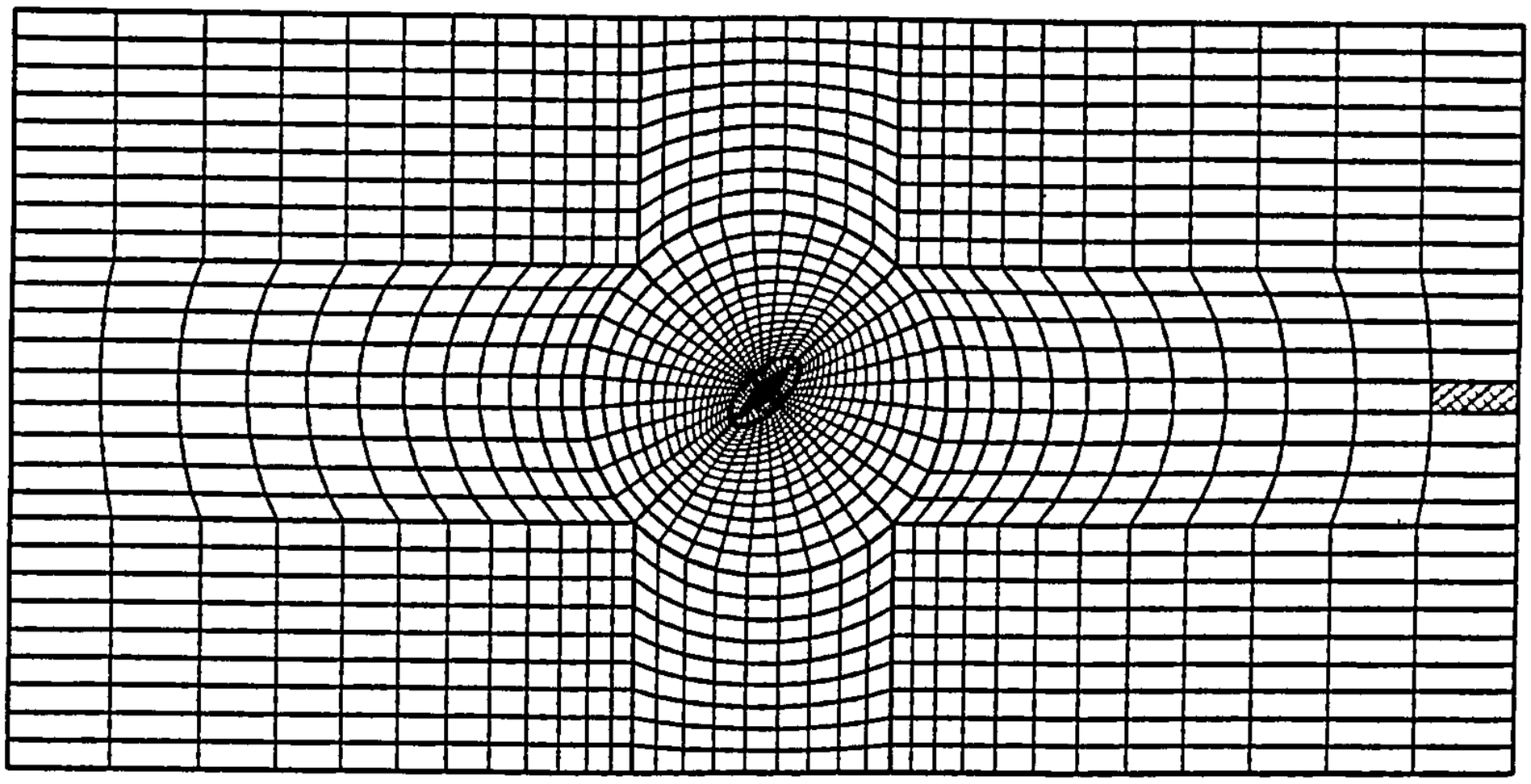

Figure 3.39: Position of cell with minimum distortion

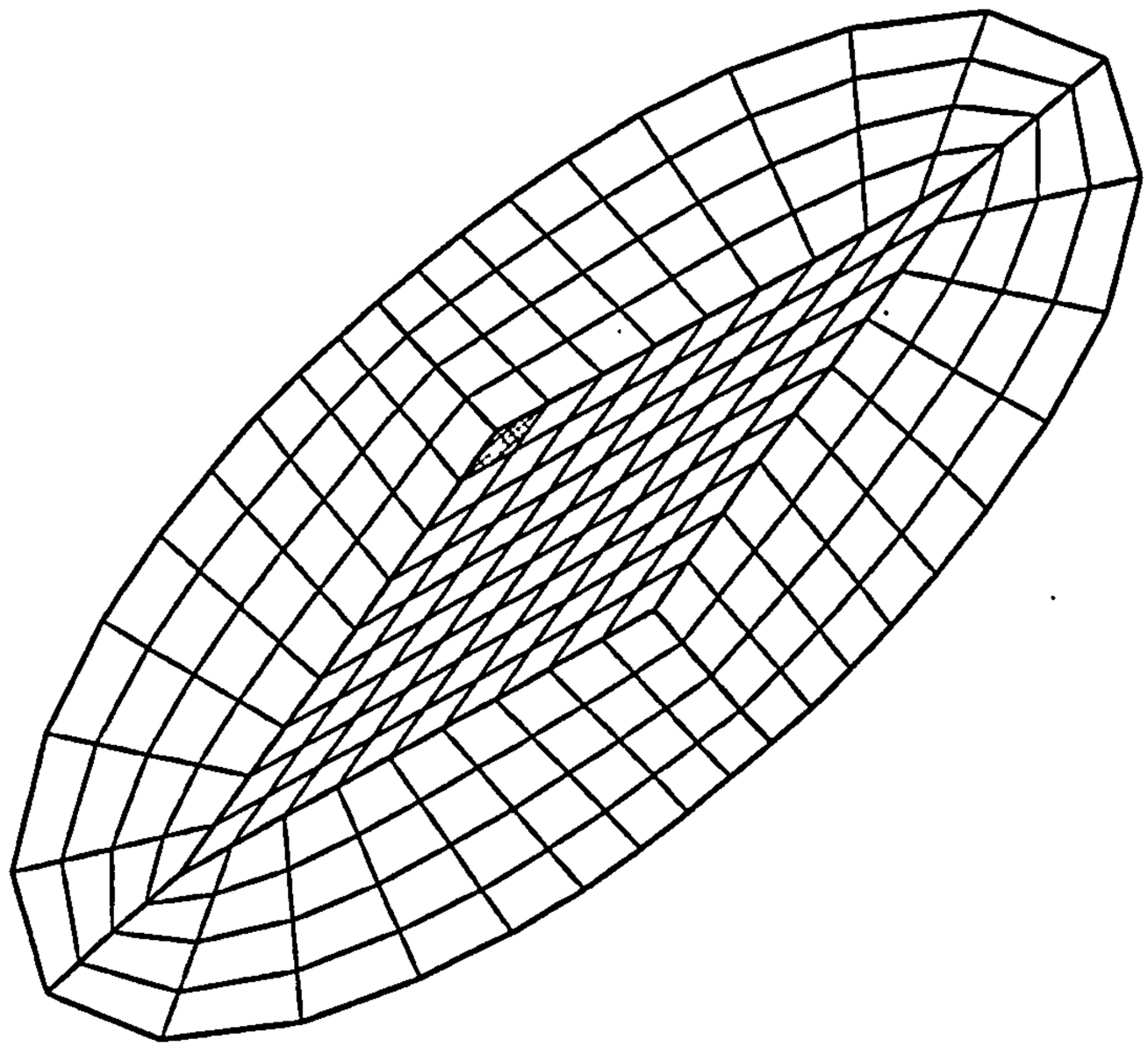

Figure 3.40: Position of cell with maximum distortion

4 Initial Prediction and Validation

4.1 Introduction

Numerical results for this thesis were validated against experimental data provided by Bray (1999) which were conducted at Cranfield University. The numerical solution domain was equivalent to the geometry of the experiment in terms of the size of both the domain and the airjet (see Section 3.7.2).

However, before prediction can be validated, a grid independence check has to be considered. That is not always possible to achieve because of hardware limits defining the maximal available computing capacity. The second factor in reducing the discretisation error is the choice of an advection scheme. In CFX 4 the diffusion terms of the Navier-Stokes equation are discretised in space with second-order accuracy. For the advection terms (see Section 3.4.2) a range of first, second and third order methods are available. Higher-order schemes are more accurate in terms of discretisation error but that does not necessarily mean better agreement with experiments. Once an adequate advection scheme is chosen the comparison of experimental and numerical data can follow. The strength of the secondary motion and the local position of the vortex were used for these comparisons.

4.2 Code Validation

4.2.1 Grid Dependence

Grid dependence tests comprise computations on grids with differing densities. The shear stress distribution at one chosen downstream location of Local Model V2, x/δ_{VG}, (see Figure 4.1) was used as a criterion to judge grid independence.

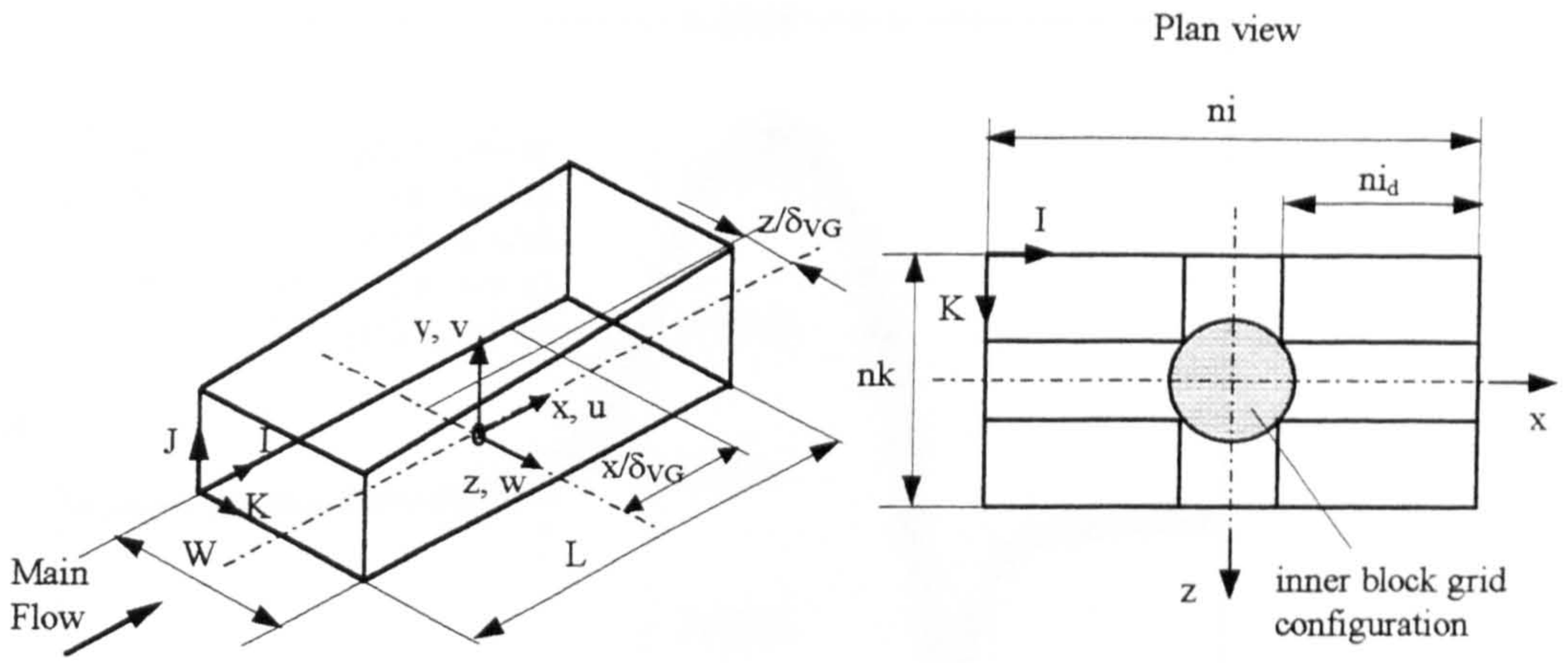

Figure 4.1: Local model V2 with the reference downstream location and I, J, K notation

The predicted shear stress distribution for varying grid densities is shown in Figure 4.2; The graph (looking upstream) shows the number of nodes used has an impact between $-4.5 < z/\delta_{VG} < 1.5$ on the predicted shear stress in the cross-stream direction (K-direction). Little effect can be seen with further refinement from nk = 53 to 70 cells. Keeping the number of nodes in J- and K-direction, nj and nk, respectively, constant and refining the grid density of the outer downstream grid blocks in I-direction, ni_d, from 22 to 33 cells show negligible difference in shear stress. However, the finer grid distribution in the I-direction was chosen to keep the aspect ratio constant in the x-z plane. No change of shear stress was observed when the grid was refined in the J-direction (i.e. the number of grid nodes was increased from 28 to 38). The final cell distribution of the outer grid blocks was ni = 58 (ni_d = 33), nj = 28, nk = 53 and this was chosen for subsequent predictions. The total number of cells in the grid was 98812 without the inlet tube modelled and 101458 with the inlet tube.

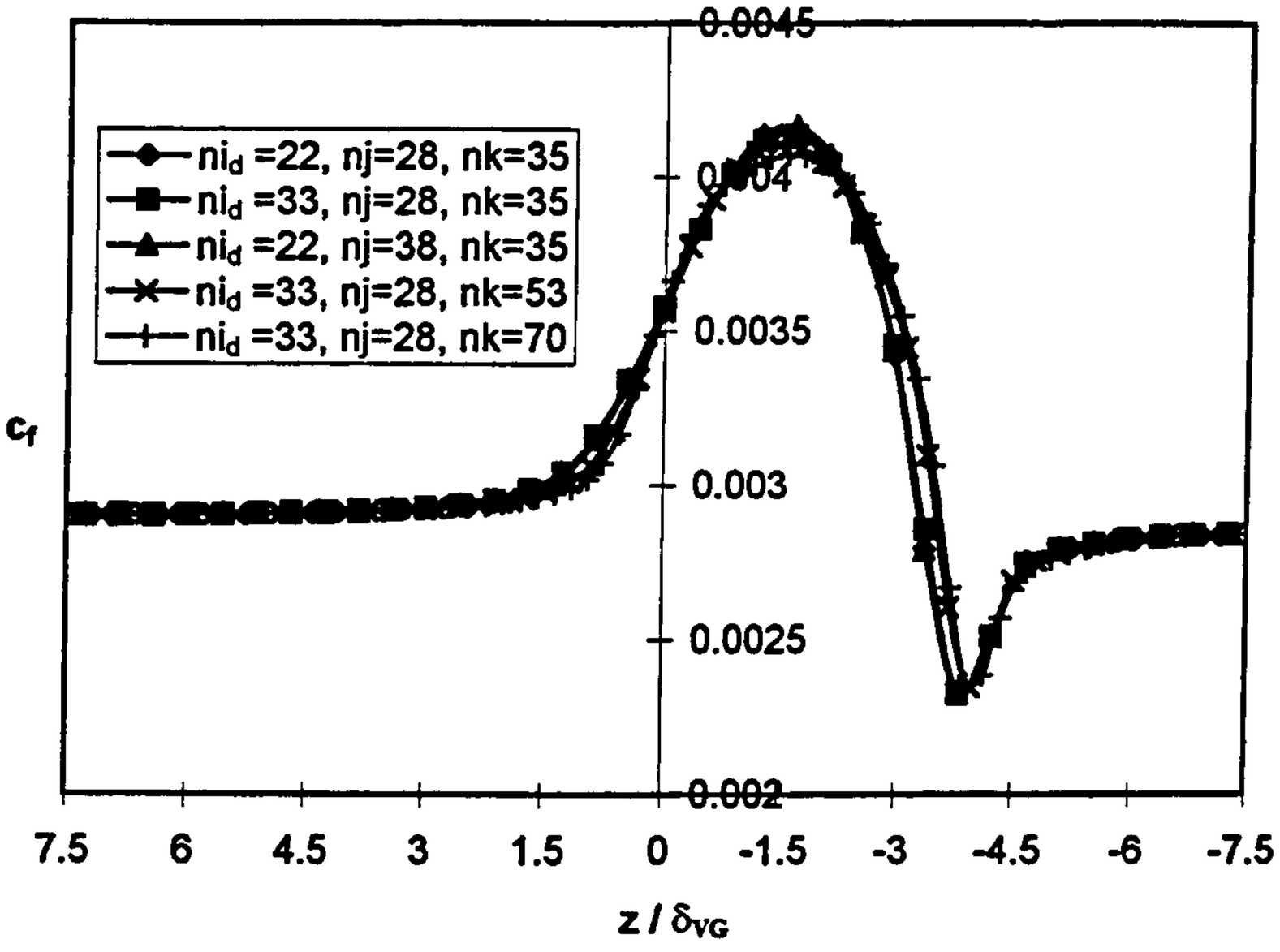

Figure 4.2: Shear stress distribution at x/δ_{VG} = 19 for various grid densities where ni_d defines the number of cells of the downstream part of the domain

4.2.2 Advection Terms Discretisation

In all aforementioned grid dependence tests the Hybrid discretisation scheme was employed. This scheme is employed by default. In the fully turbulent flow considered $Re_C > 2$ for most of the flow and therefore the first-order UDS dominated. Based on the results provided by the Hybrid discretisation scheme a grid independent solution was achieved.

Higher-order advection schemes may be employed to further reduce the discretisation error. In Section 3.4.2 the five available discretisation schemes employed by the FVM code CFX 4 are described in detail. The CONDIF-method is a modification of the Hybrid scheme but it did not improve the accuracy of the prediction. QUICK and CCCT are third-order advection schemes but both methods failed to reach the same level of convergence as the second-order accurate HUW scheme. In the Figures 4.3 to 4.5 the three velocity components u, v, and w are shown at one downstream location x/δ_{VG} = 19, (where δ_{VG} is the undisturbed boundary layer height of 41.5mm at the centre of the air jet orifice). The velocities were predicted by using the five different advection schemes and compared to the experimental data.

In Figure 4.3 the results of each of the advection schemes plus the experimental data are shown at the cross-stream location of the vortex core ($z/\delta_{VG} = -2.1$). All of the predicted results, except those of the Hybrid scheme, reflect the shape of the experimental velocity profile. Hybrid did not predict the strong velocity gradient at the solid surface. The Condif method predicted a similar velocity shape as the experiment but it is shifted to a lower velocity magnitude. The two third-order schemes, Quick and CCCT, accurately predicted the strong velocity gradient close to the solid surface but showed a much stronger velocity deficit than the experimental data and the HUW method. The HUW results show the best overall agreement with the experimental data, i.e. the velocity gradient shape at the wall is to a certain extent close to the experiment, the velocity deficit is reflected and returns to free stream conditions in accordance with the experimental profile.

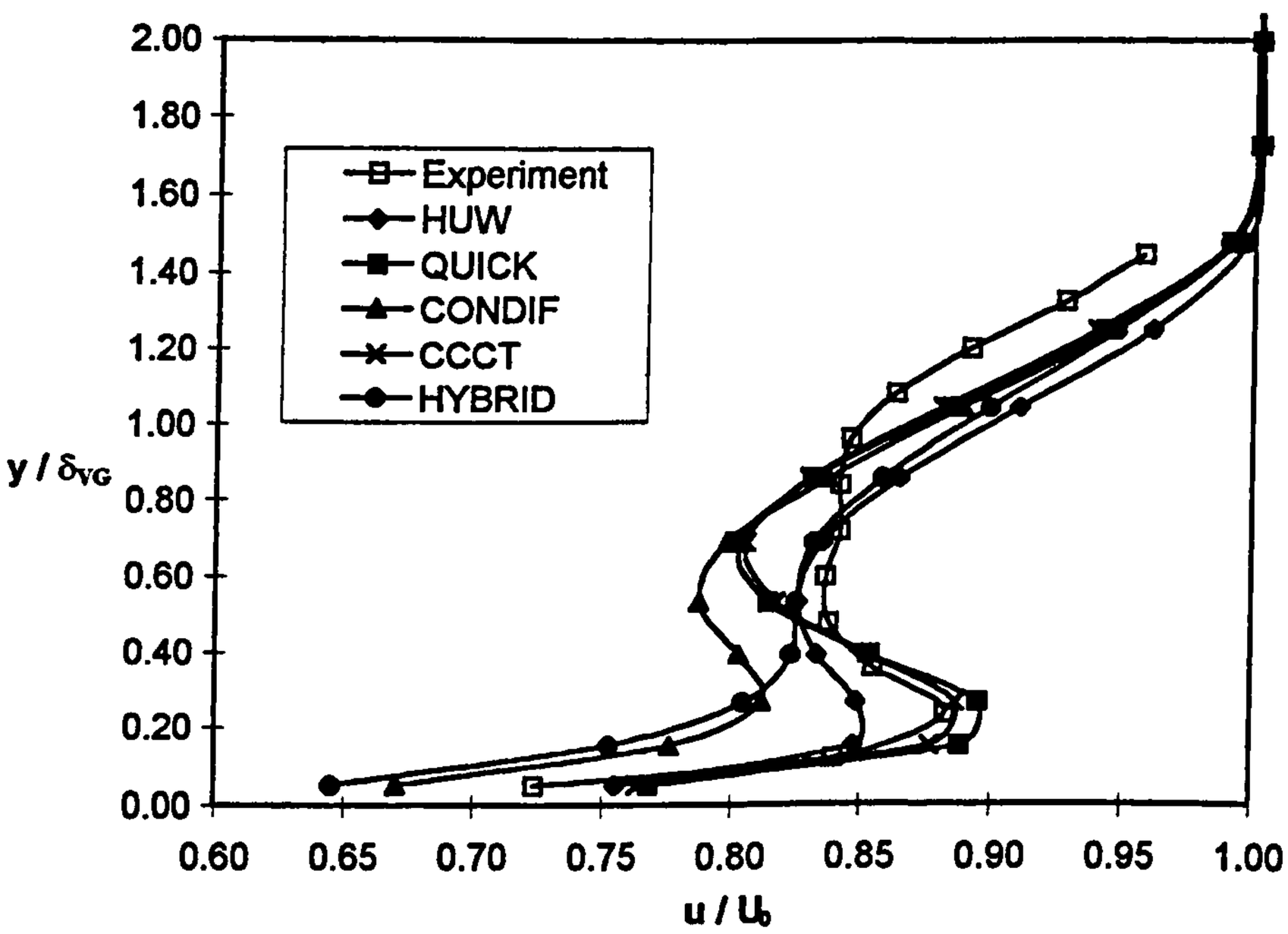

Figure 4.3: Streamwise component of velocity (u) at $x/\delta_{VG} = 19$ and $z/\delta_{VG} = -2.1$

Figure 4.4 shows the cross-stream distribution of the velocity component v/U_0 at $y/\delta_{VG} = 0.69$ above the plate. This corresponds to the height of the experimental vortex core. All the advection schemes underpredict the strength of the v-velocity component of the longitudinal vortex. The numerical predictions are in general over

60% lower than the experimental data. The predicted core locations in the cross-stream direction; i.e. where the profiles cross the v/U_0 axis, differ from each other but are relatively close to the experimental position. The Hybrid and Condif schemes predict the lowest velocity peaks. All higher-order schemes predict approximately 50% higher-velocity peaks than Hybrid and Condif.

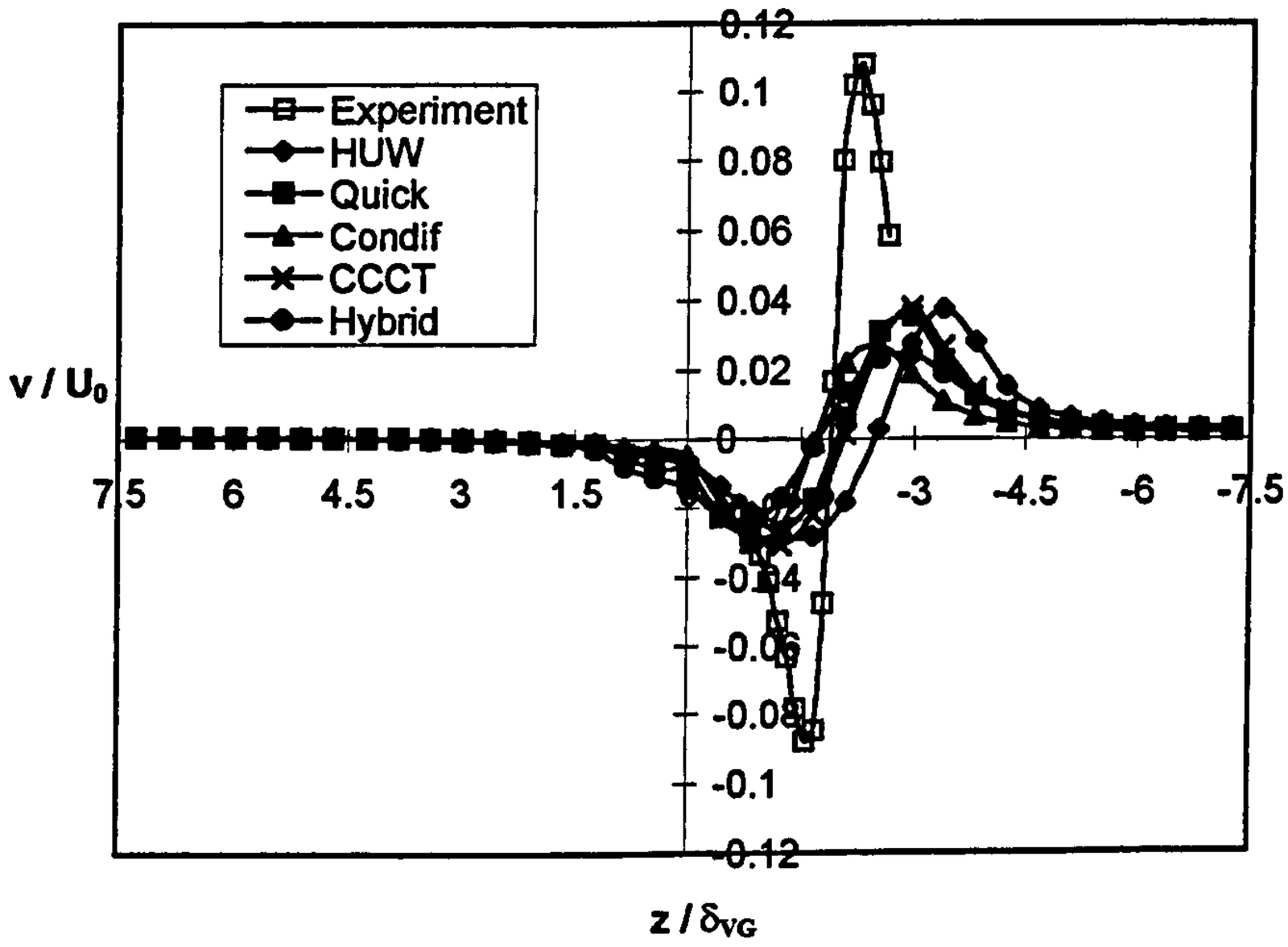

Figure 4.4: Cross-stream component of velocity (v) at $x/\delta_{VG} = 19$ and $y/\delta_{VG} = 0.69$

In Figure 4.5 the cross-stream velocity component w/U_0 is shown at the same location ($z/\delta_{VG} = -2.1$ and $x/\delta_{VG} = 19$) as the streamwise component u/U_0 in Figure 4.3. Notice that the solution domain height is normalised with the undisturbed boundary layer height at the centre of the air jet orifice. Thus the maximum value is greater than five times the local boundary layer thickness (see Section 3.8). All schemes predict approximately the same vortex core position in the y-direction; i.e., where the velocity profiles cross the y axis. The predicted values of the Hybrid and Condif advection schemes of the velocity peak are approximately 74% lower than the experimental value above the core. The higher-order scheme results (HUW, Quick, CCCT) are 59% lower than the experimental data. Underneath the core the higher-order schemes Quick and CCCT velocity profiles are 4% lower than the experimental data and the HUW values are 10% lower than the experimental. The Hybrid profile maximum is

approximately 36% less than the experiment and the Condif peak value is 39% lower than the experimental.

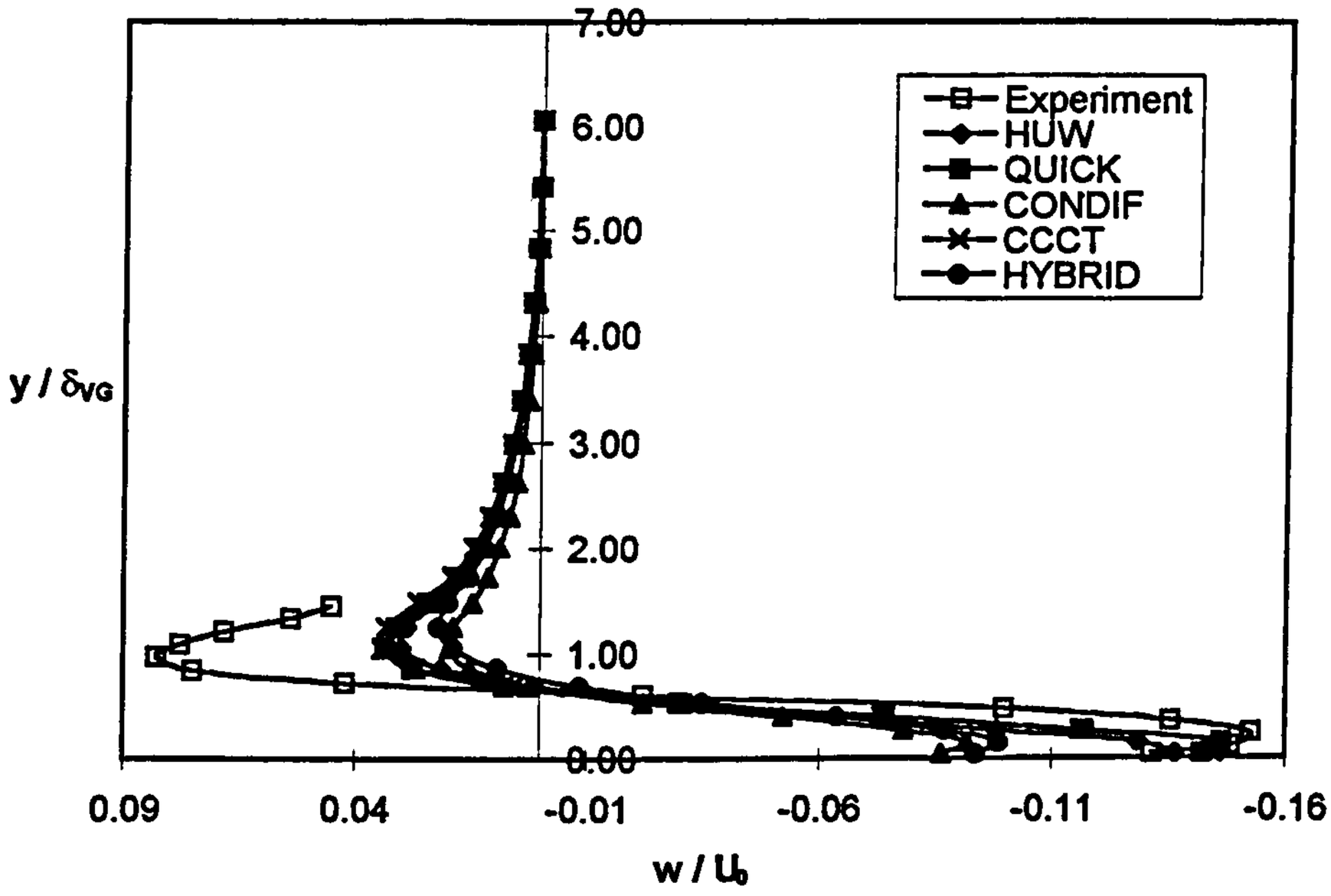

Figure 4.5: Cross-stream component of velocity (w) at x/δ_{VG} = 19 and z/δ_{VG} = -2.1

The results show in general, that the higher-order advection schemes predict the experimental vortical flow structure more closely than do the Hybrid and Condif methods. Even though the Quick scheme provided the closest results to the experimental data the HUW scheme offered the best compromise between accuracy and stability. An average number of 500 iterations was needed to achieve convergence for both Verification Models, V1 and V2. The error in continuity, i.e. the mass source residual was reduced by an average reduction factor of approximately 6×10^{4}. All subsequent predictions for this project were obtained using the second-order HUW method. In the next Section (4.3) a detailed comparison between experimental measurements and numerical predictions will be discussed.

4.3 Results and Discussion

The numerical results will be discussed at four downstream locations, i.e. X1 to X4 (see Figure 4.6).

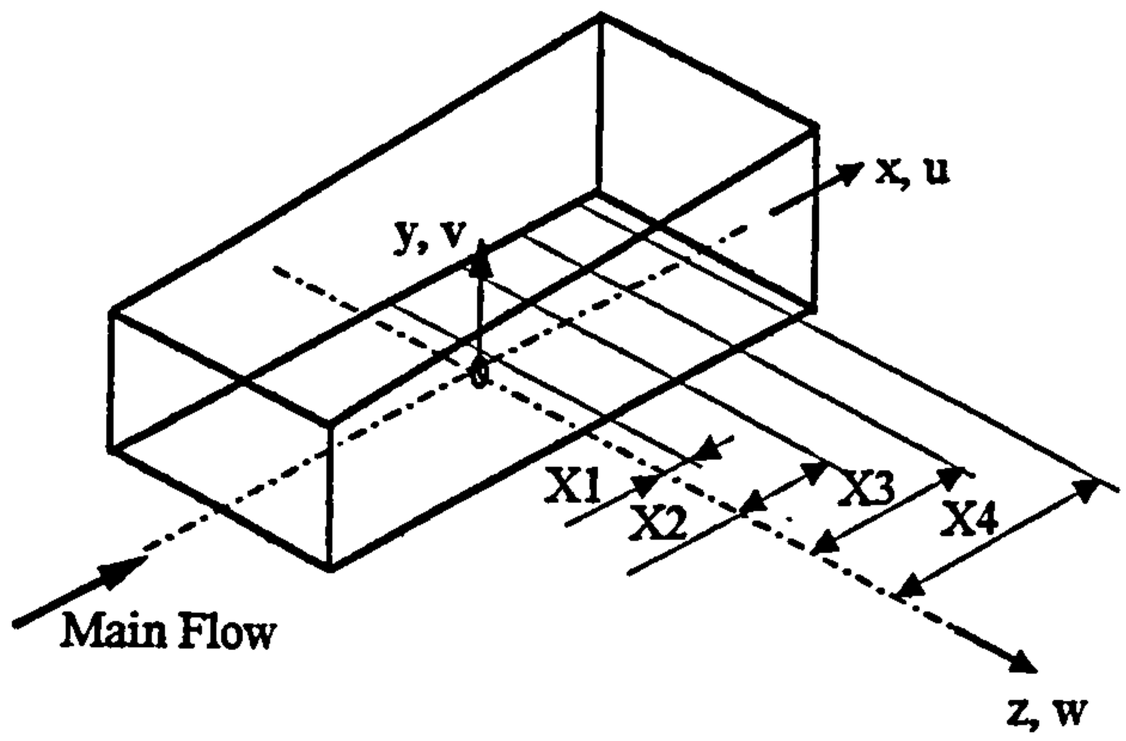

Figure 4.6: Local airjet models V1 and V2 with the four downstream stations defined by experiment

These locations were chosen to correspond to the experimental data of Bray (1999) and are as follow:

- X1 = 0.16m (3.86 δ_{VG}), see Figures, 4.7 to 4.9
- X2 = 0.50m (12.05 δ_{VG}), see Figures, 4.10 to 4.12
- X3 = 0.80m (19.28 δ_{VG}), see Figures, 4.13 to 4.15
- X4 = 1.10m (26.51 δ_{VG}), see Figures, 4.16 to 4.18

The flat plate model with and without the jet inlet tube (see Figure 3.14) will be discussed in comparison with the experimental data.

In the above mentioned Figures (4.7 to 4.18) the three velocity components u, v and w were nondimensionalised with the free stream velocity component U_0 = 20m/s. The solution domain height y and the cross-stream direction z was nondimensionalised with the undisturbed boundary layer thickness δ_{VG} at the jet centre, determined experimentally to be 41.5mm. At five cross-stream locations Z1 to Z5 the streamwise components of velocity u (see e.g. Figure 4.7) and the cross-stream components of velocity w (see e.g. Figure 4.9) will be compared. The comparison is between the two numerical models (i.e., with and without inlet tube) and the experimental data. Z3 represents the experimental location of the vortex core while the other four cross-

stream locations are divided into two on either side of the experimental vortex core location. The locations Z1 and Z5 represent the extent of the experimental measuring plane in the cross-stream direction whereas Z2 and Z4 are equidistant from the core and within the vortex. The cross-stream components of velocity, v, will be compared at three vertical (Y1, Y2, Y3) distances from the solid surface. The location Y2 is coincident with the experimental vortex core position. The other two positions are equidistant above and below the experimental vortex core.

Figure 4.7 shows the streamwise velocity profiles provided by the two numerical models and the experimental model at five cross-stream locations within the experimental measuring plane. At position Z1, which represents the edge of the experimental measuring plane, all velocity distributions match and show undisturbed profiles. At locations Z2 to Z5 the velocity shapes reflect the influence of the longitudinal vortex produced by the AJVG. The vortex mixes high momentum fluid from the flow outside or at the edge of the boundary layer (i.e., depending on the strength and the vertical positions of the vortices cores) with low momentum fluid close to the solid surface. As a result the velocity gradients at the solid surface are enhanced and by continuity velocity deficits occur at the vortices cores locations. The vortical flow structure produced by longitudinal vortices is often called secondary motion because it is perpendicular to the main flow direction. The secondary motion ceases at a vertical (y-direction) location where the velocity ratio u/U_0 shows unity. On the upwash side of the vortex at the edge of the experimental measuring plane (location Z5) the experimental data shows the flow at free stream conditions whereas the numerical models predict vortical flow. At the experimental core location Z3 the predicted and experimental velocity profiles are of similar shape but have different magnitudes. The two numerical models (i.e., with and without inlet tube) predict approximately the same results at the two edges of the experimental measuring plane (Z1 and Z5). At the experimental vortex core location Z3 and at the two locations Z2 and Z4 (equidistant from the core) the predicted velocity deficit without the inlet tube is approximately 12% more in magnitude than the value of the velocity deficit with the inlet tube.

In Figure 4.8 the cross-stream velocity components v against the solution width are shown. All vortices cores positions, i.e. where the velocity profiles cross the z-axis,

are relatively close to each other. However, the predicted vortices are stretched in the cross-stream direction compared to the experimental vortex. Little difference is observed between the two numerical model predictions. As shown in Section 4.2.2, the magnitudes of the numerically predicted peak velocities are approximately 50% less than the experimentally measured velocities. However, the decrease of magnitudes of measured and predicted velocities in both directions away from the core position Y2 (i.e., at location Y1 and Y3) is of the same rate.

Figure 4.9 shows the cross-stream velocity components w against the solution domain height y and the difference between the widths of the predicted and measured vortices can be seen. At cross-stream position Z1 all data are aligned whereas at position Z5 the measured velocity magnitude is negligible compared to those of the predictions. Although the predicted velocities are approximately 50% lower above the core (i.e., where the velocity profiles cross the y-axis) at location Z3, the locations Z2 and Z4 show satisfactory agreement between prediction and experiment. Except at location Z5, no difference between the two numerical predictions can be observed.

Figures 4.10 to 4.12 show measured and predicted data at the second downstream location X2 (see Figure 4.6) which is 3.86 δ_{VG} downstream of location X1. Figures 4.13 to 4.15 describe the flow situation 8.20 δ_{VG} further downstream of X2 and Figures 4.16 to 4.18 reflect the vortical flow structure a further 7.23 δ_{VG} downstream of X3.

At all downstream locations (X1 to X4) the strength of the predicted longitudinal vortices of both numerical models, measured by the vertical cross-stream velocity component v, is always approximately 50% lower than the experimentally produced vortex.

In Figure 4.10, i.e. at location X2, both numerical models provide approximately identical results apart from the cross-stream position Z5. At position Z5 both numerical predictions indicate a velocity deficit but with slightly different magnitudes. This indicates secondary motion, whereas the experimental data already shows a return to free stream conditions. The difference in velocity deficit between the numerical models with and without the inlet tube is because the cross-stream positions of the vortices were slightly shifted (see Figure 4.11).

In Figure 4.11 the two predicted vertical cross-stream velocity profiles are slightly shifted in cross-stream direction as they were upstream at location X1 (see Figure 4.8). The difference between the results at locations X1 and X2 to X4 (see Figures 4.8, 4.11, 4.14 and 4.17) is that at location X1 the velocity peaks of the model without the inlet tube are slightly higher than those of the model with the inlet tube. This effect disappeared further downstream. Although the predicted vortices of the two numerical models were always slightly shifted from each other in the cross-stream direction, their downstream decay is similar. This argument is supported by the almost identical velocity profiles further downstream, shown in Figures 4.13 to 4.18.

The shift between the measured vortex position and those of the predicted vortices in cross-stream direction increased further downstream. Between downstream location X1 (see Figure 4.8) and X2 (see Figure 4.11) the shift between experimental and numerical vortices increased by approximately 100%. The predicted vortices migrate from location X1 to X2 much more than the experimental vortex. From location X2 further downstream to locations X3 (see Figure 4.14) and X4 (see Figure 4.17), the translation of the predicted and measured vortices is parallel.

Comparing the cross-stream velocity component w at the three downstream locations X2 (see Figure 4.12), X3 (see Figure 4.15) and X4 (see Figure 4.18) three features can be observed. Firstly, the vertical positions of the experimental and computational vortices cores are approximately the same. Secondly, the velocity profiles are similar in shape and finally, the different cross-stream cores positions can be seen at the w-velocity profile especially at cross-stream location Z5. This location is approximately the core position of the predicted vortices. In all three Figures 4.12, 4.15 and 4.18 the magnitudes of the predicted velocities at Z5 are close to the experimental velocity magnitude at location Z3 which is the vortex core position of the experimental vortex.

The predicted streamwise velocity profiles at the downstream locations X2 (see Figure 4.10), X3 (see Figure 4.13) and X4 (see Figure 4.16) reflect the same trend as the experimental profile. The reason why the magnitudes of measured and predicted profiles do not match at each of the five cross-stream locations Z1 to Z5 is that the vortices cores are at different cross-stream locations. However the vortical flow structure is significantly different in the y-direction (i.e., the predicted velocity peaks are 50% lower than the experimental) but less different in z-direction.

Figure 4.7: Streamwise velocity at X1 and various cross-stream positions

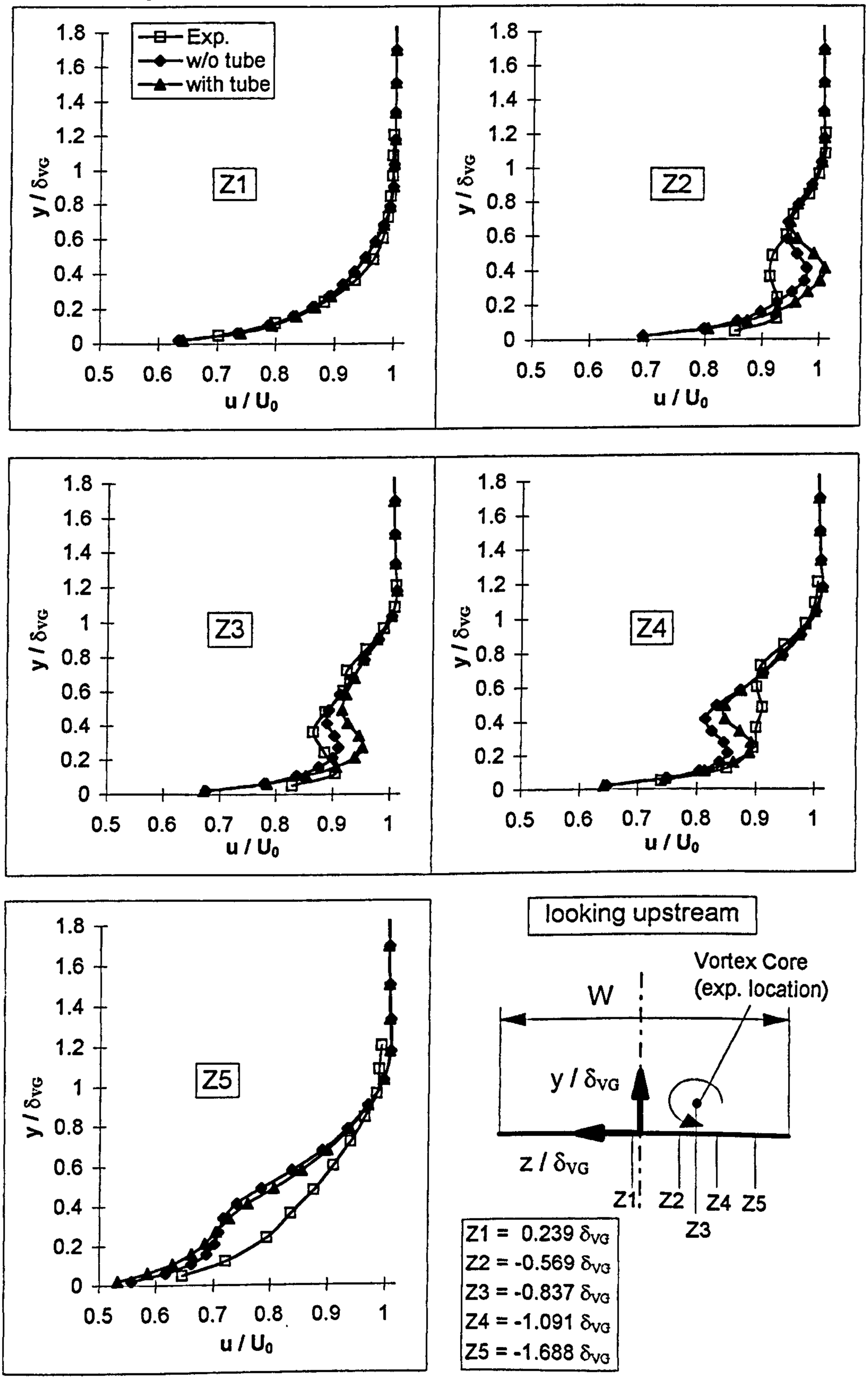

Figure 4.8: Vertical cross-stream velocity at X1 and various cross-stream positions

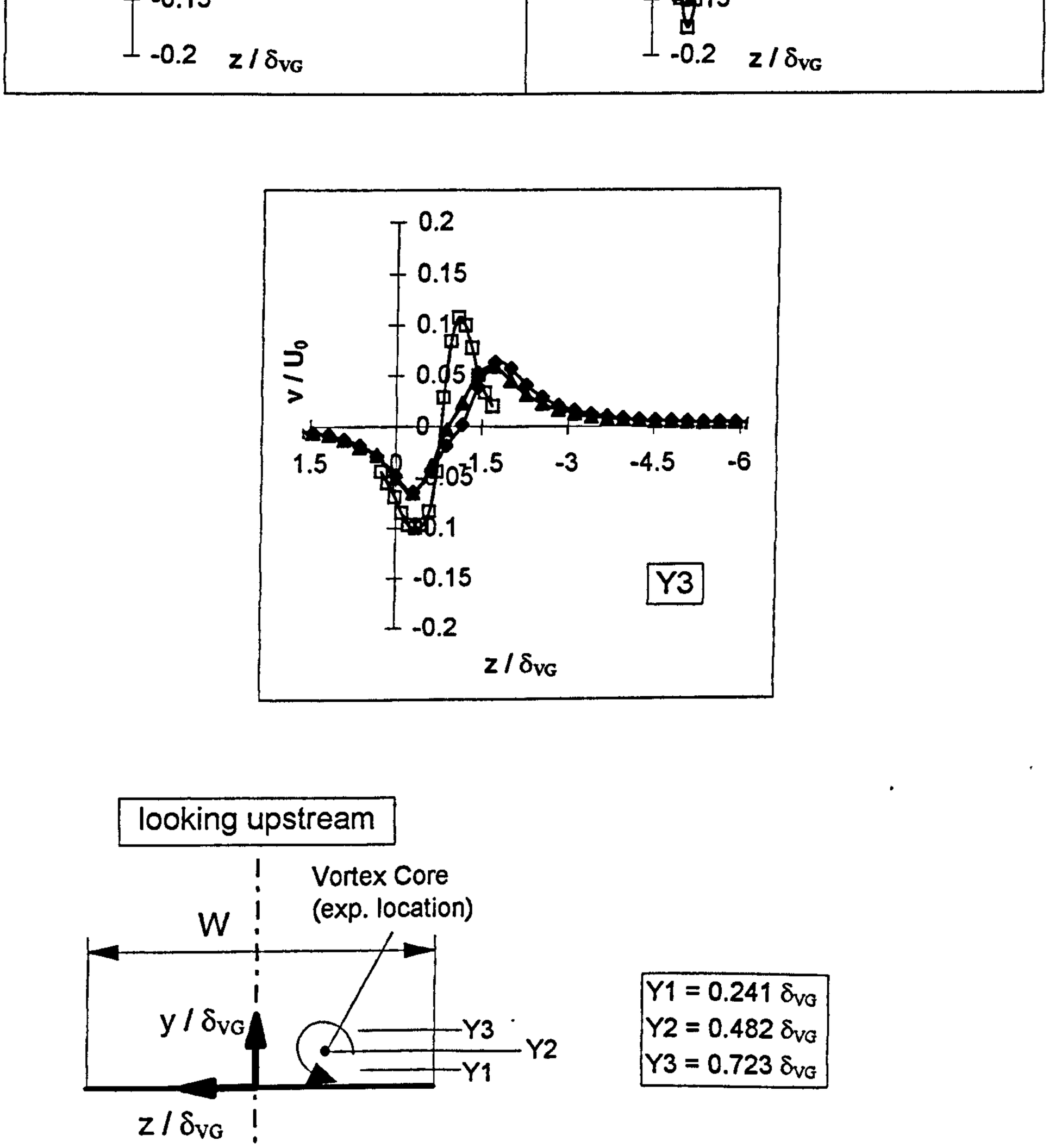

Figure 4.9: Horizontal cross-stream velocity at X1 and various cross-stream positions

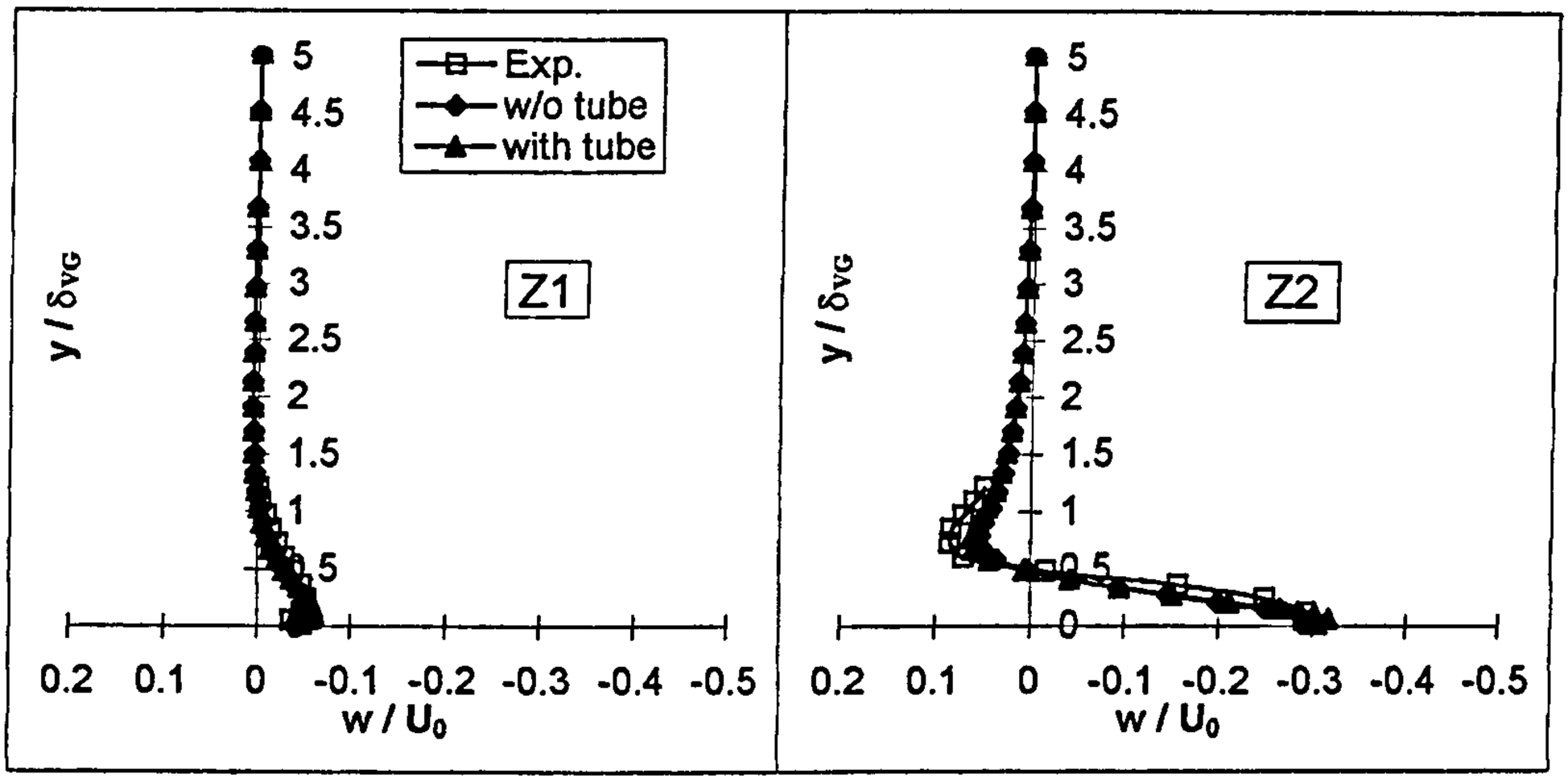

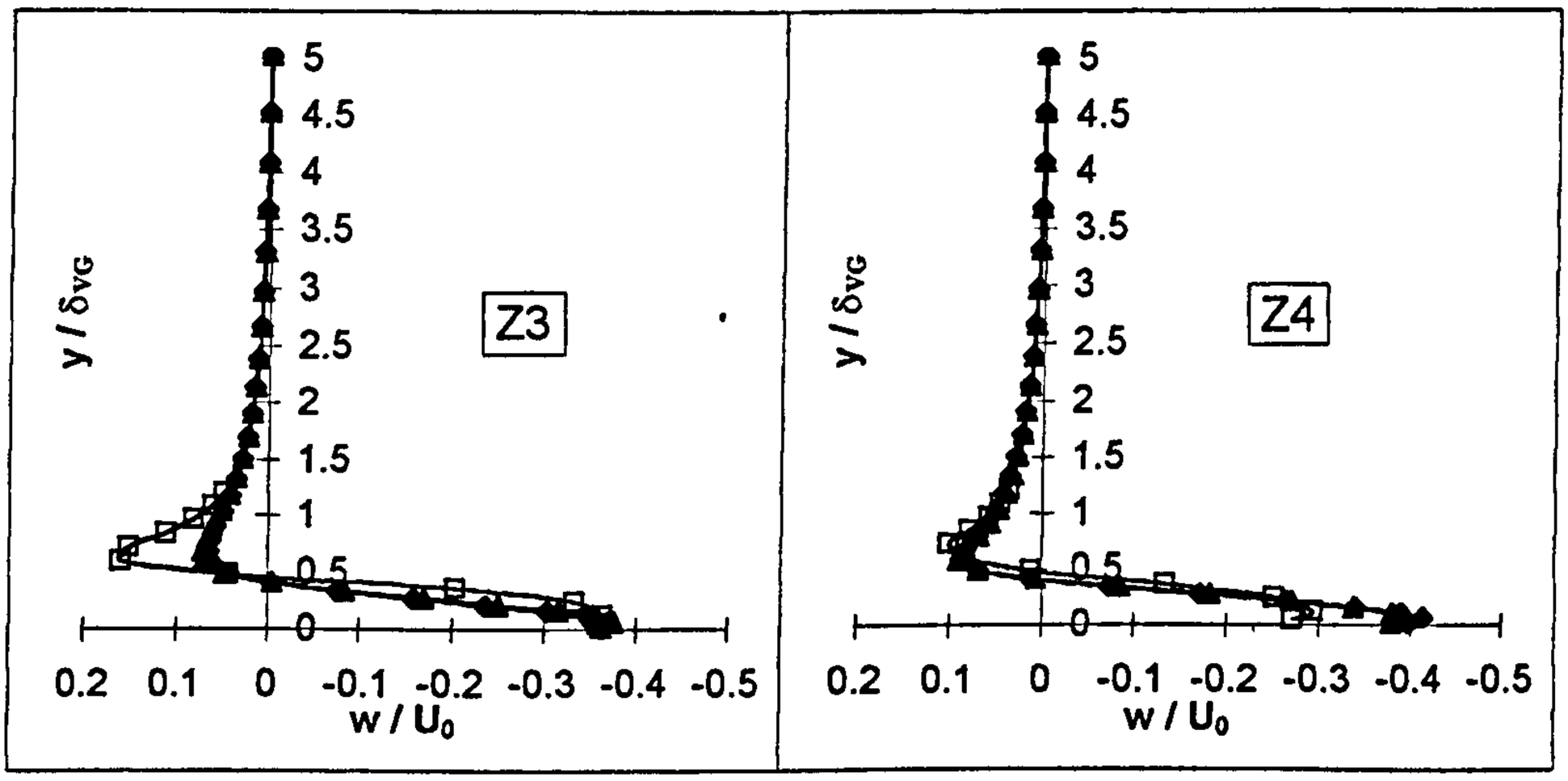

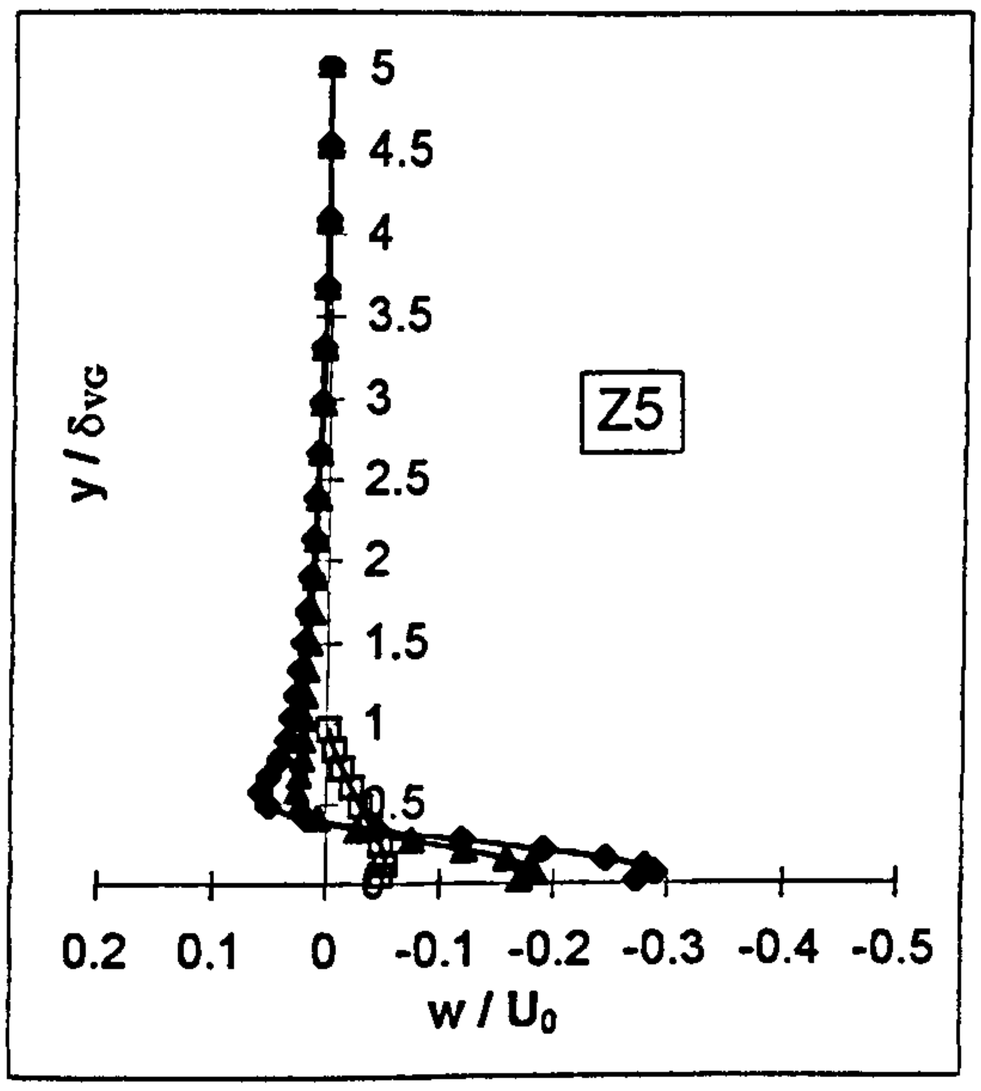

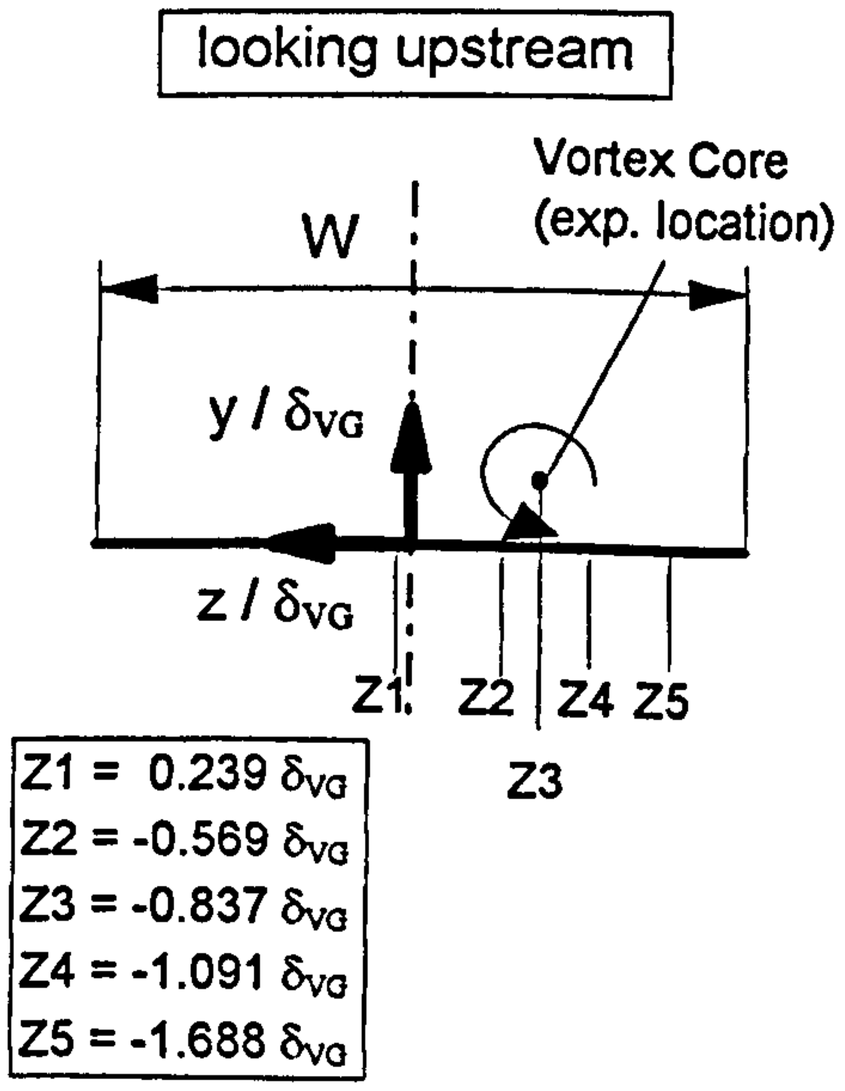

Z1 = 0.239 δ_{VG}
Z2 = -0.569 δ_{VG}
Z3 = -0.837 δ_{VG}
Z4 = -1.091 δ_{VG}
Z5 = -1.688 δ_{VG}

Figure 4.10: Streamwise velocity at X2 and various cross-stream positions

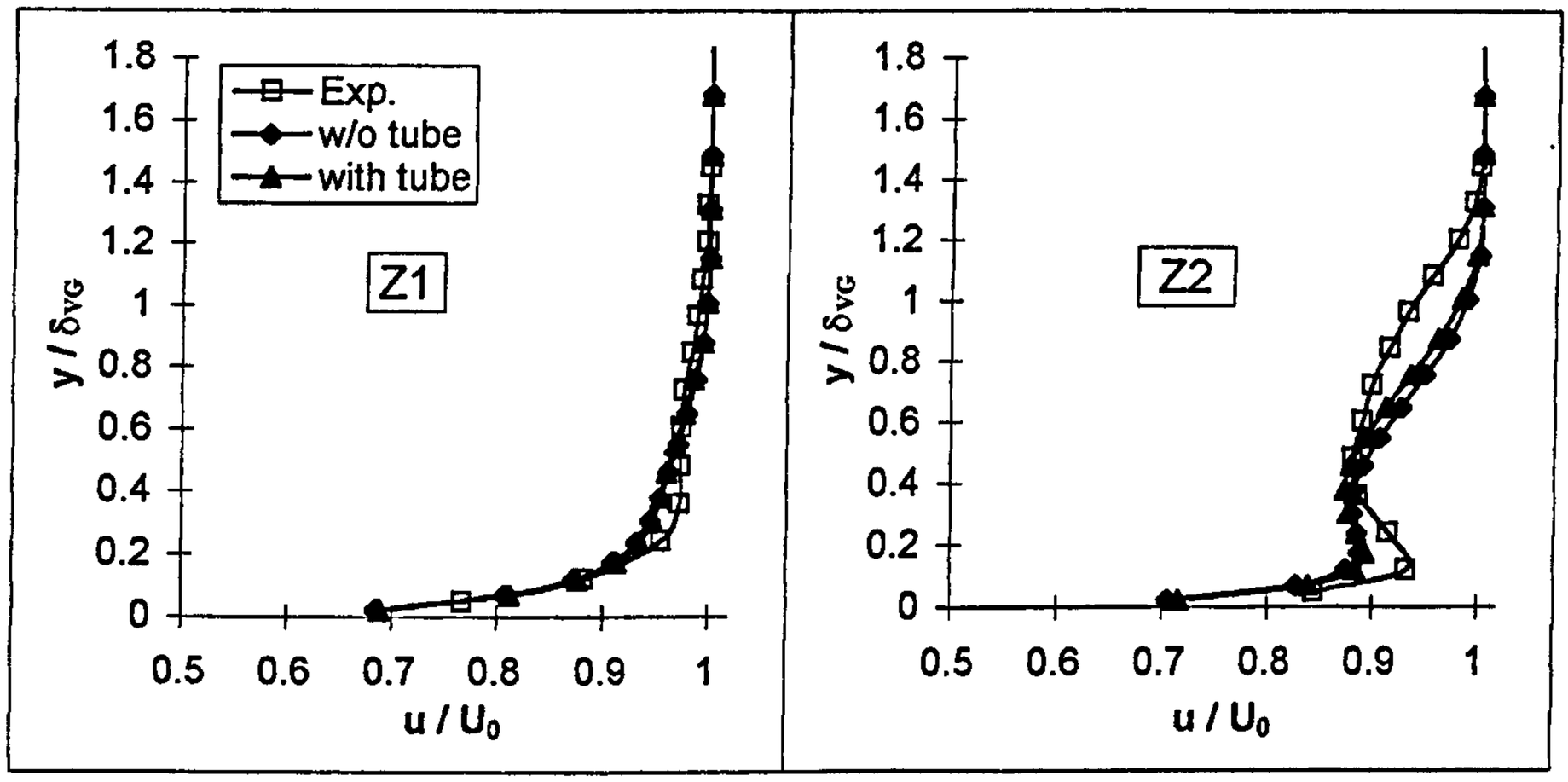

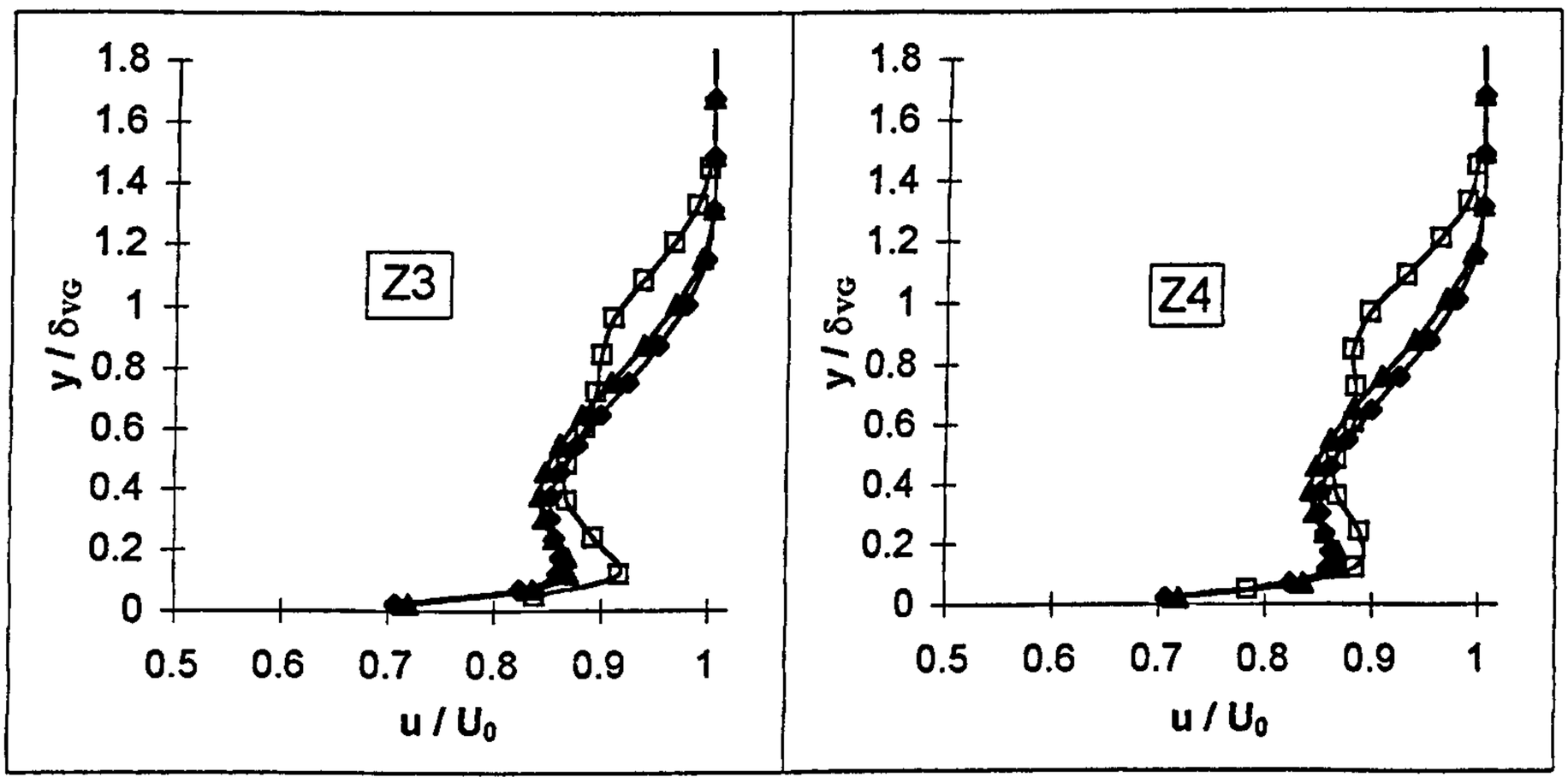

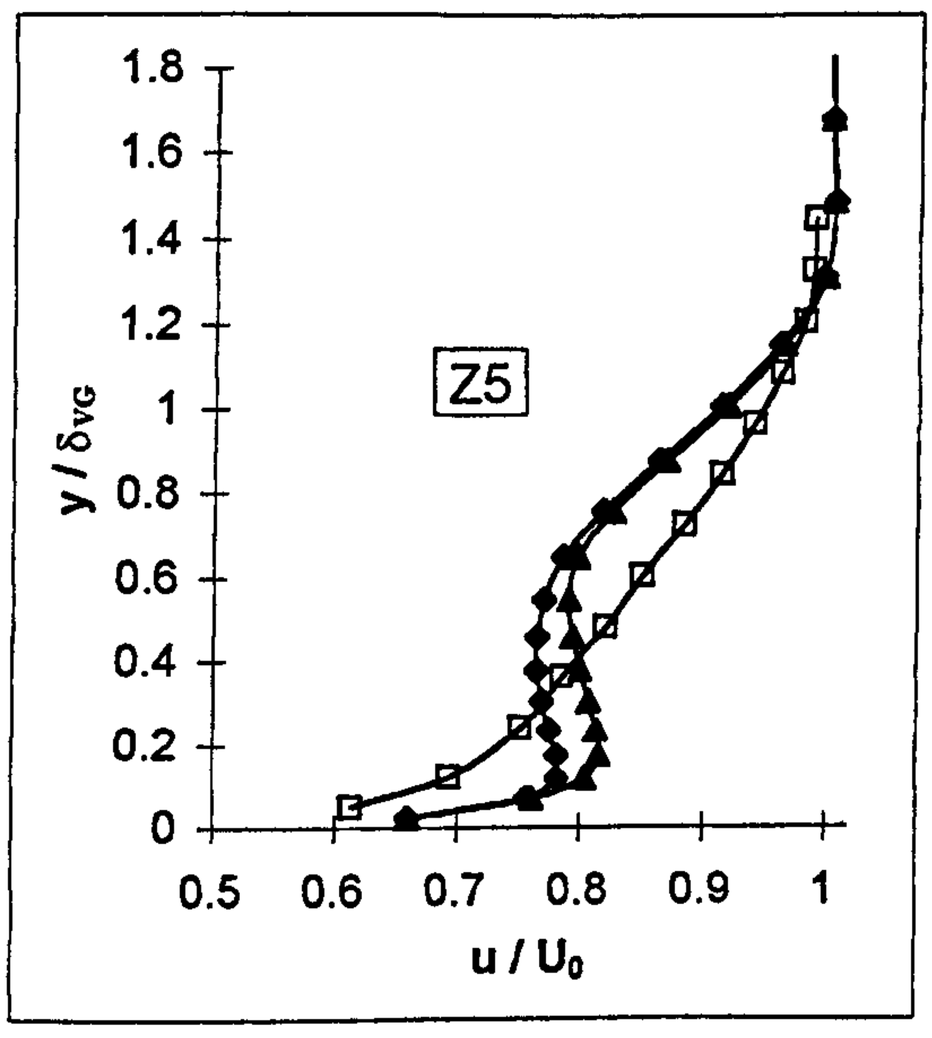

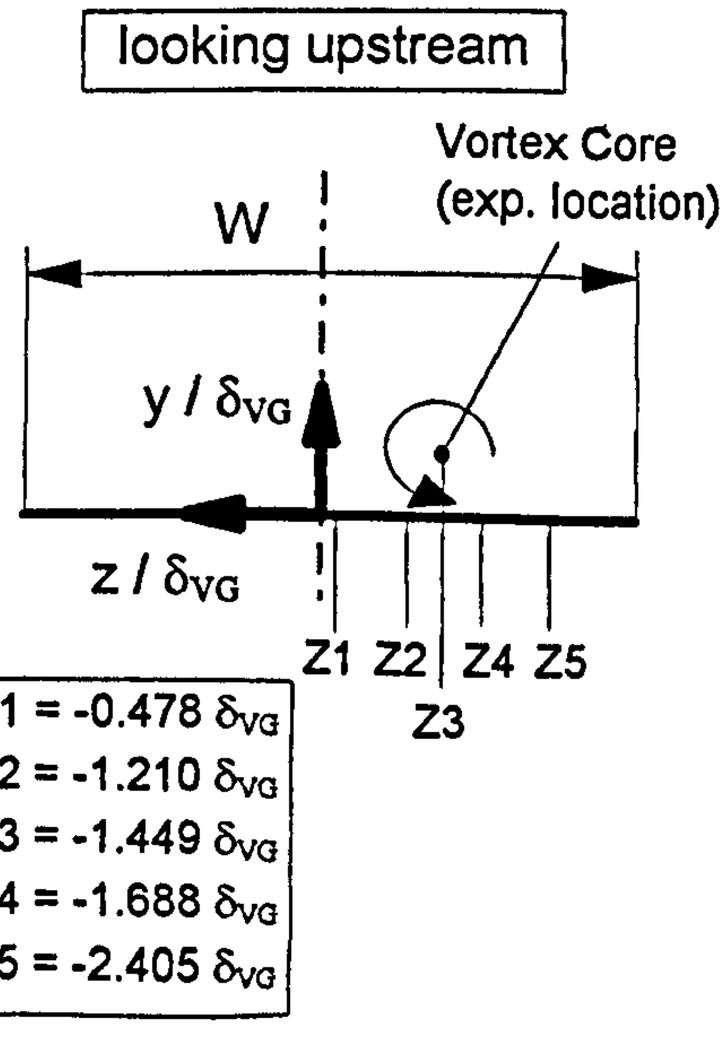

Figure 4.11: Vertical cross-stream velocity at X2 and various cross-stream positions

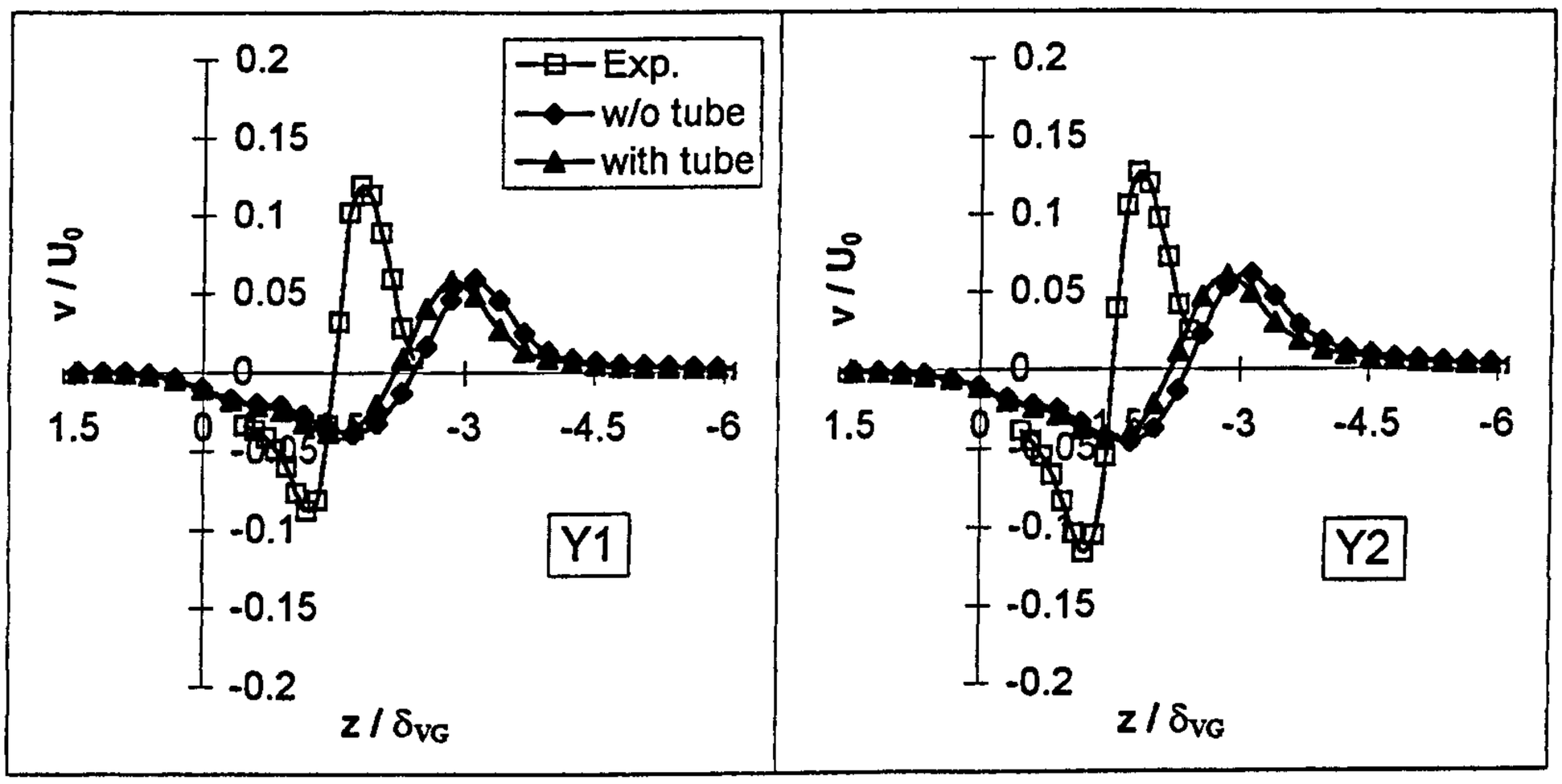

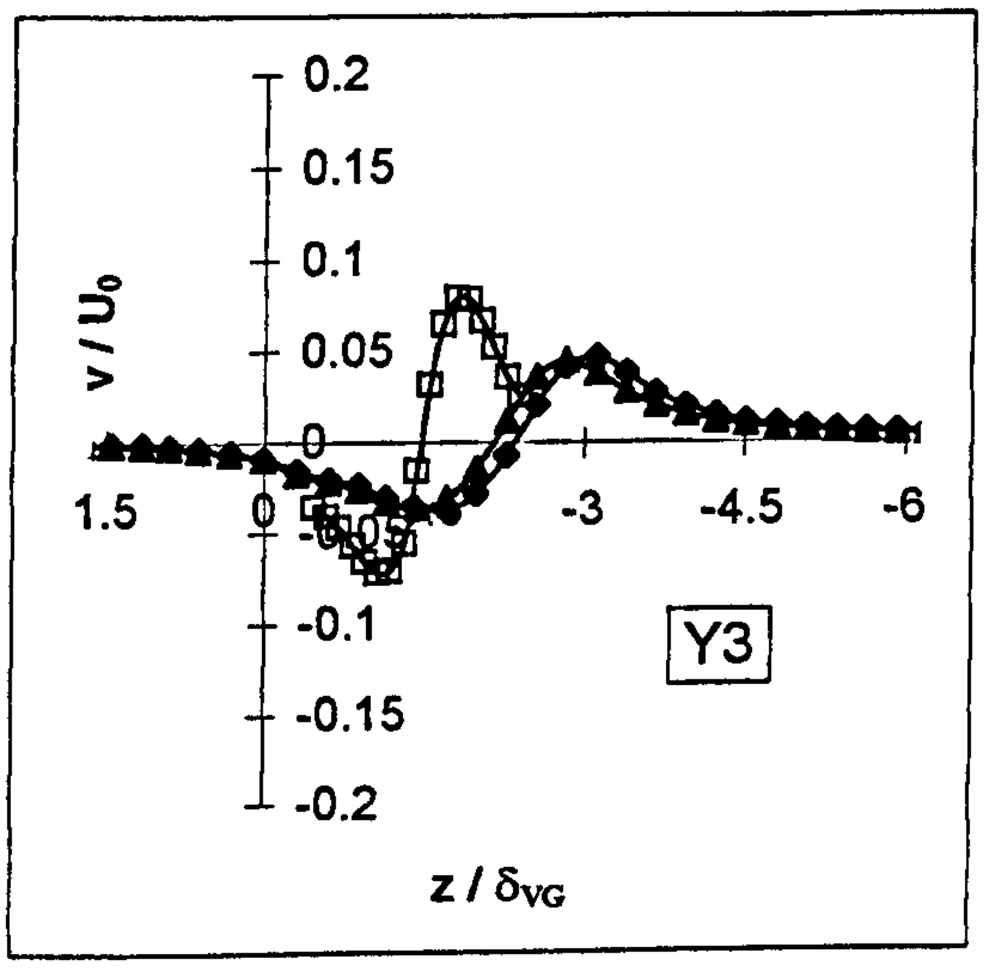

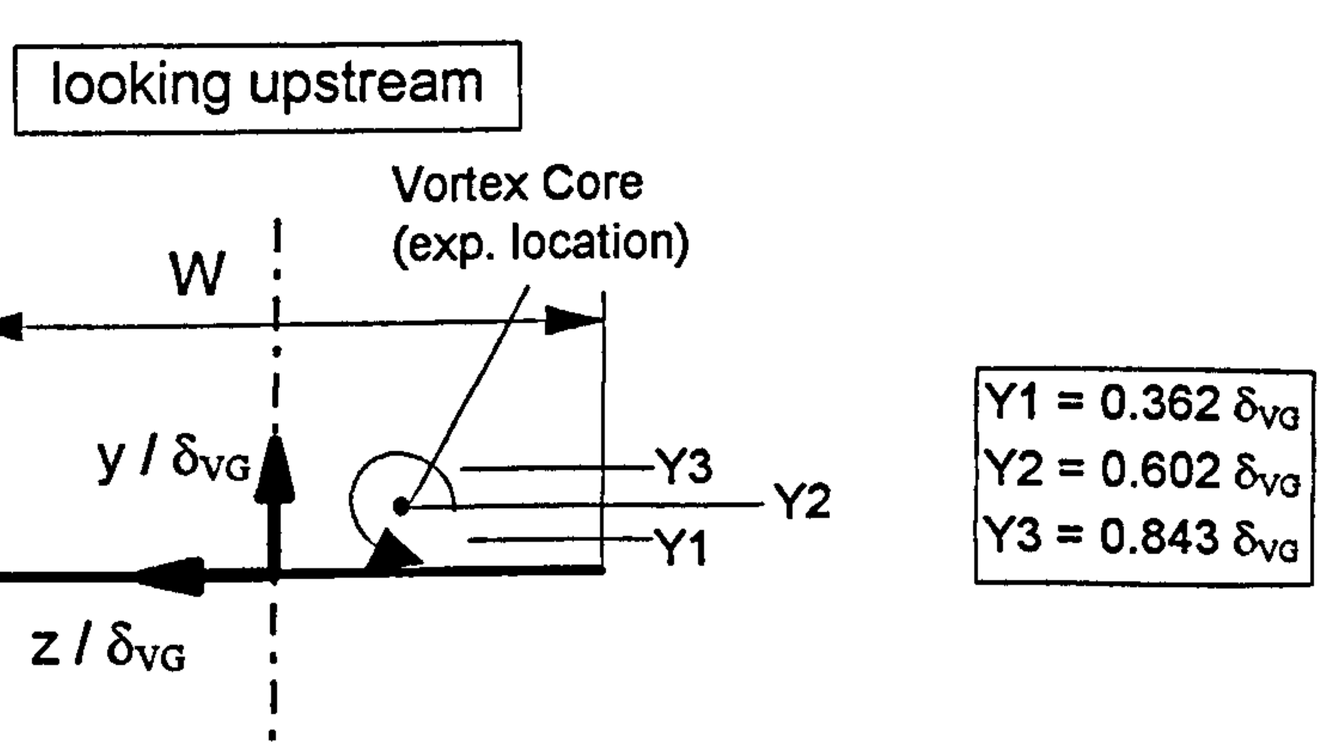

Figure 4.12: Horizontal cross-stream velocity at X2 and various cross-stream positions

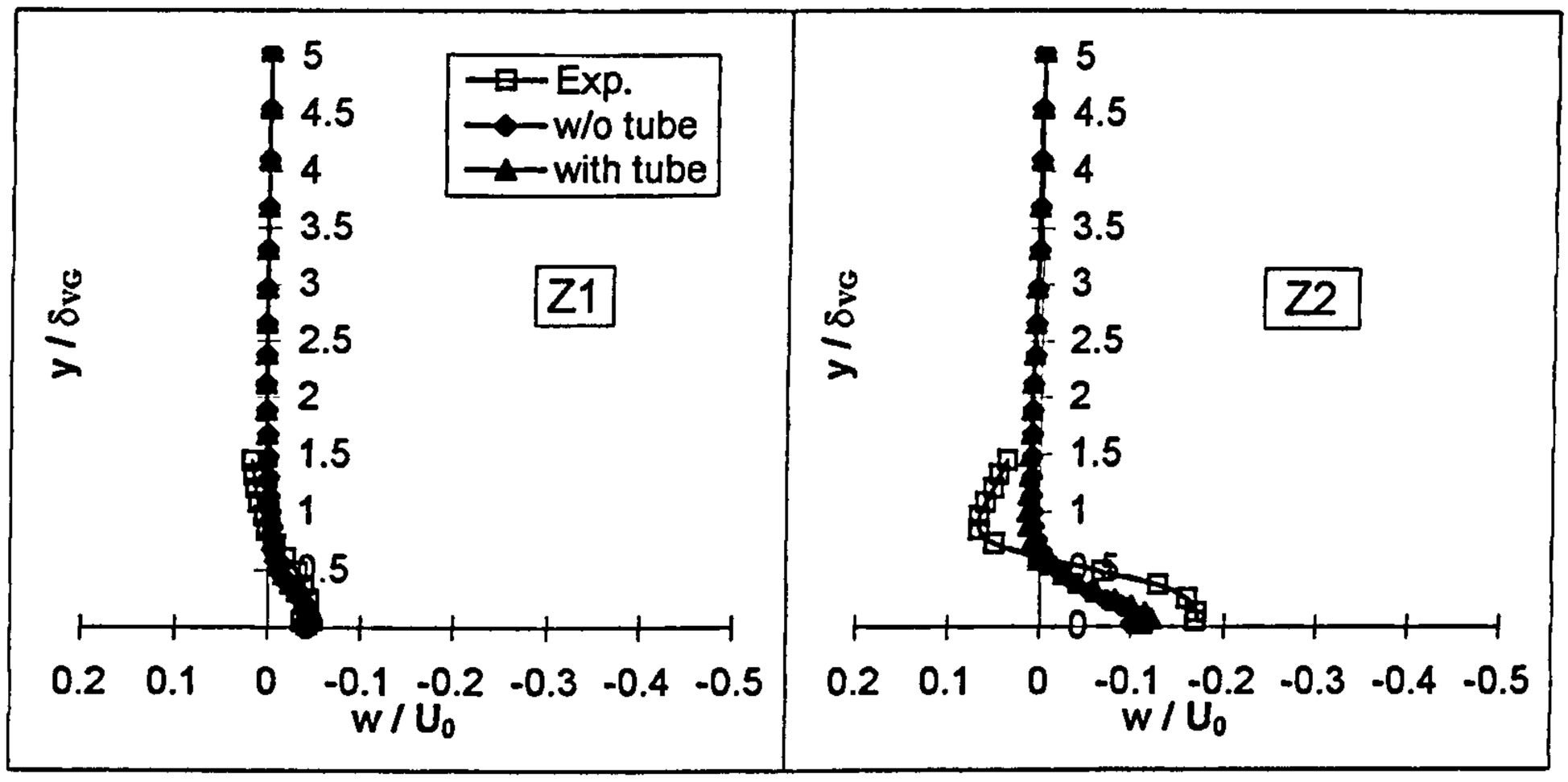

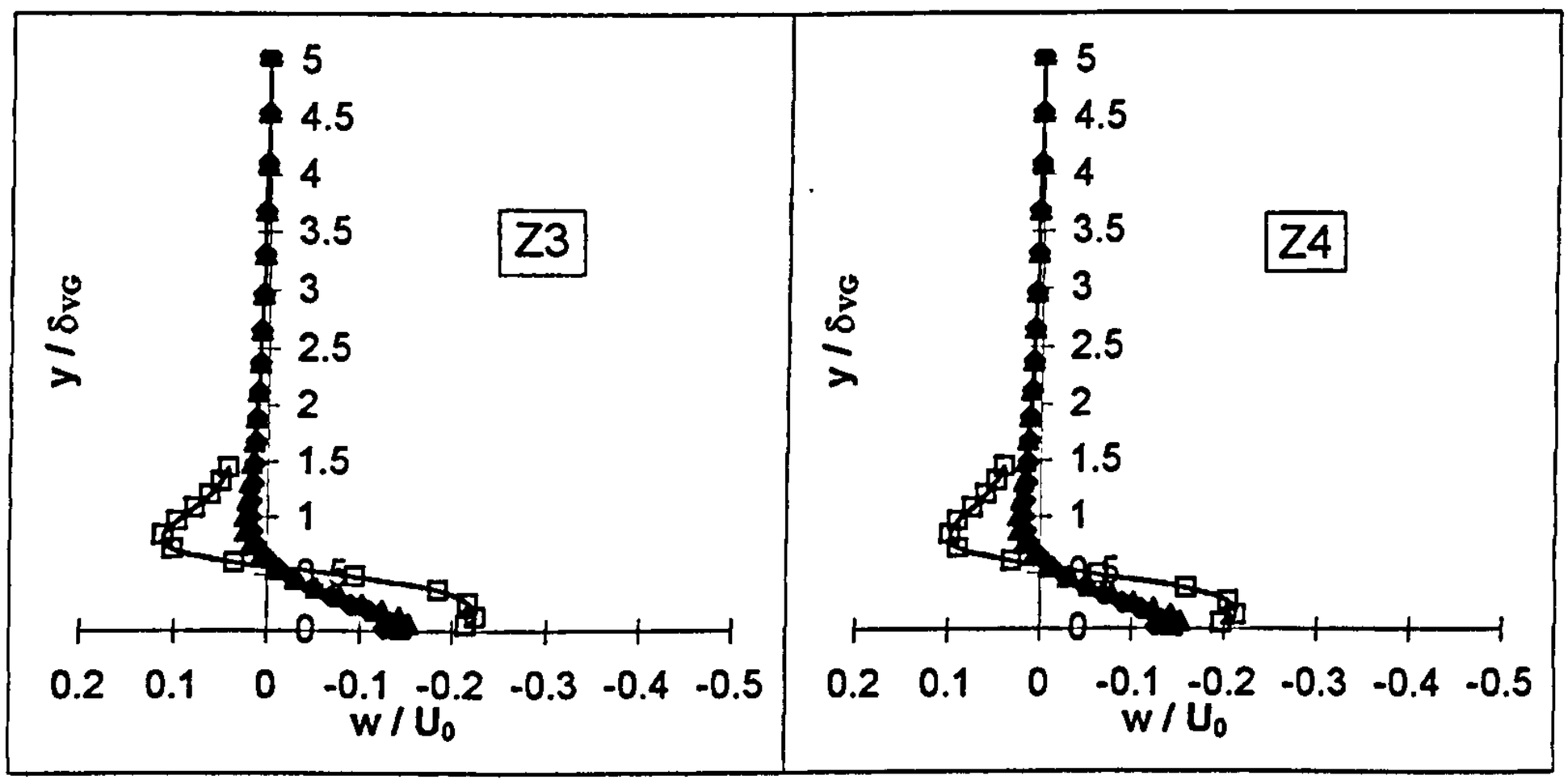

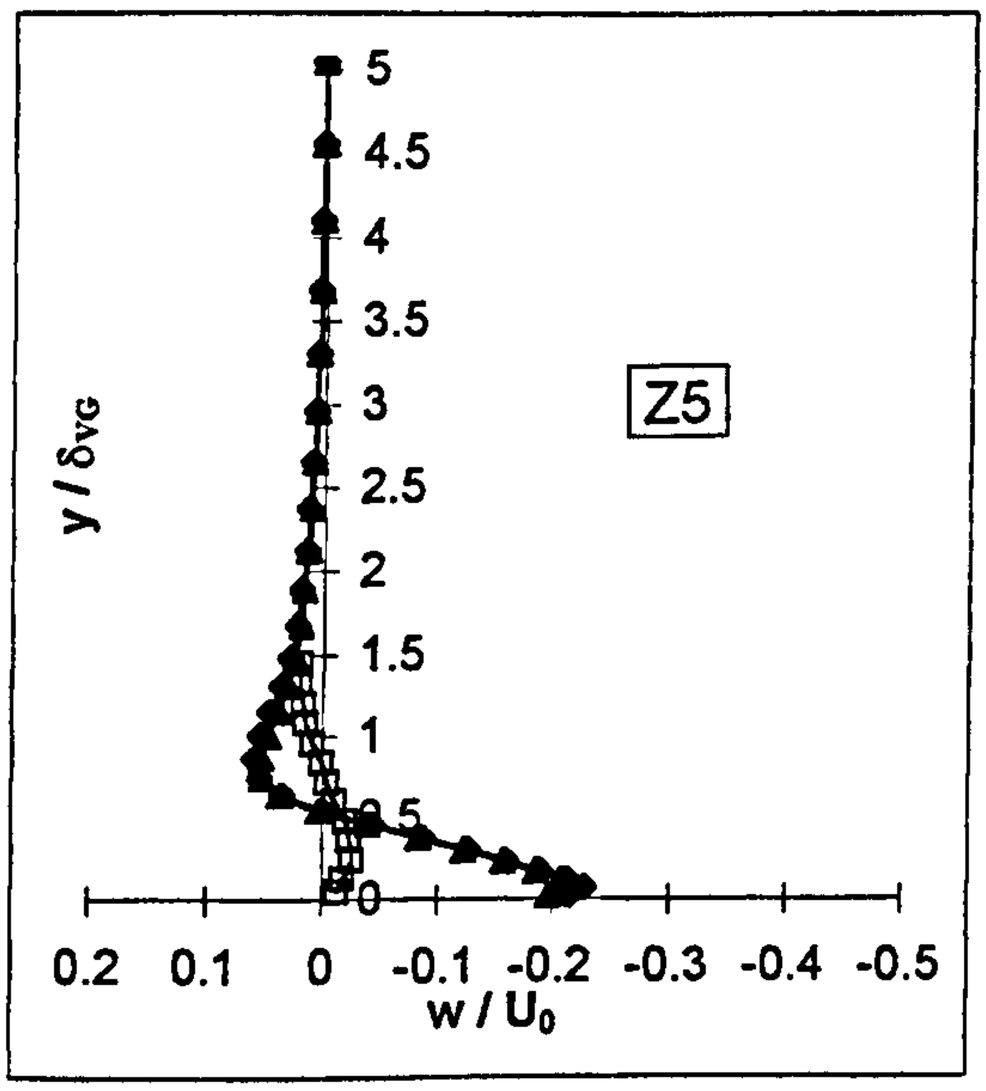

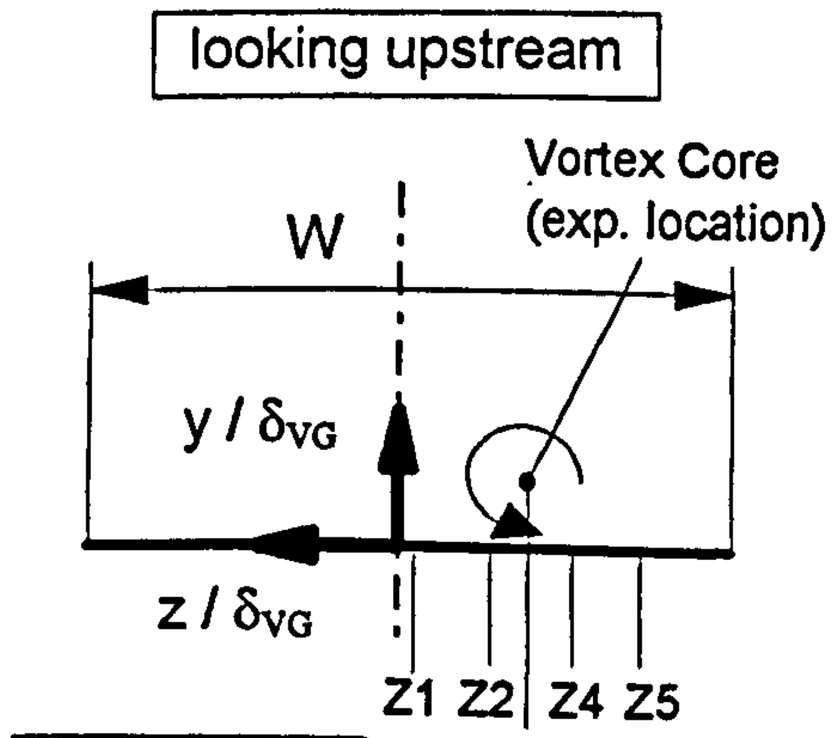

Z1 = -0.478 δ_{VG}
Z2 = -1.210 δ_{VG}
Z3 = -1.449 δ_{VG}
Z4 = -1.688 δ_{VG}
Z5 = -2.405 δ_{VG}

Figure 4.13: Streamwise velocity at X3 and various cross-stream positions

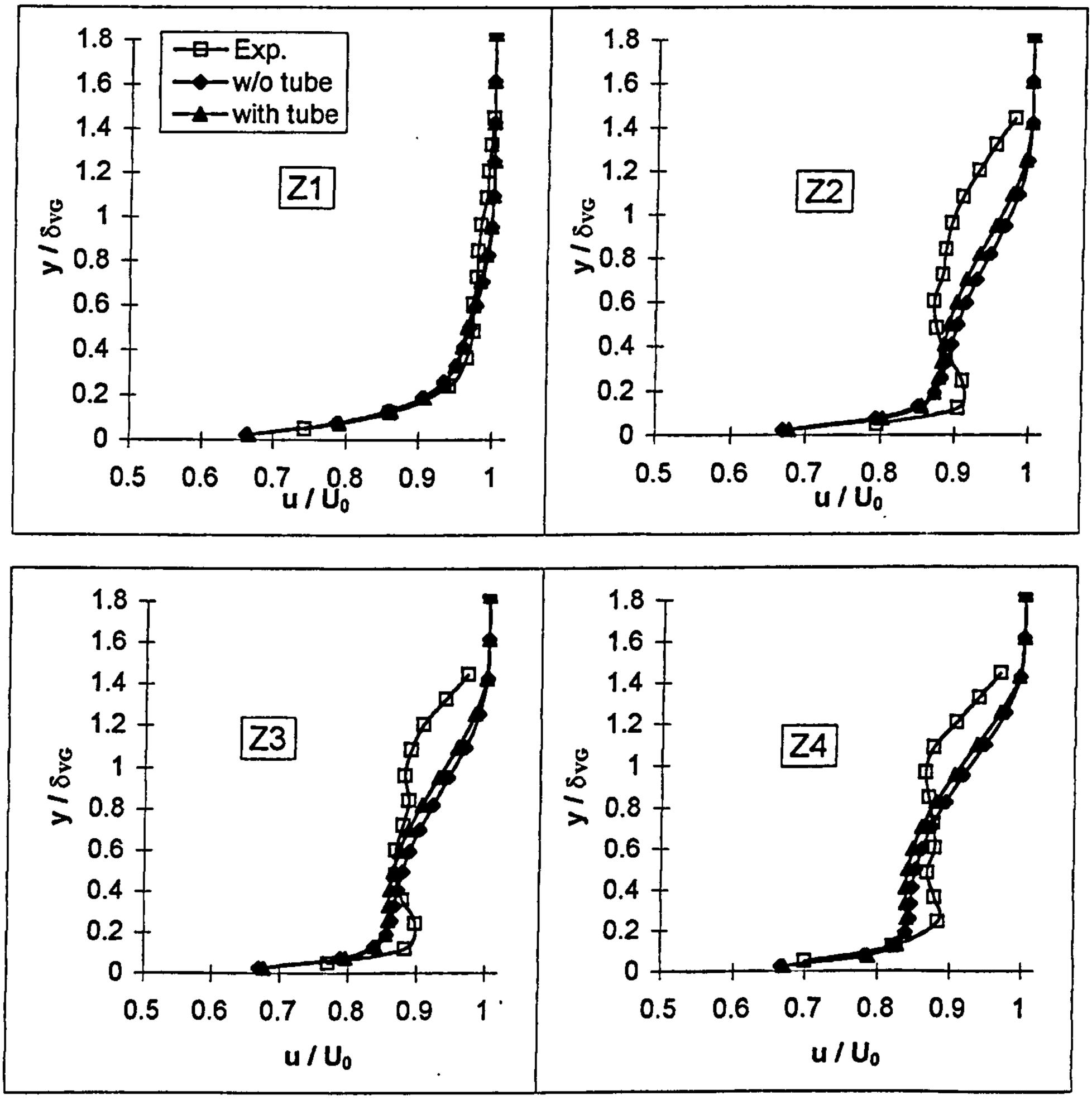

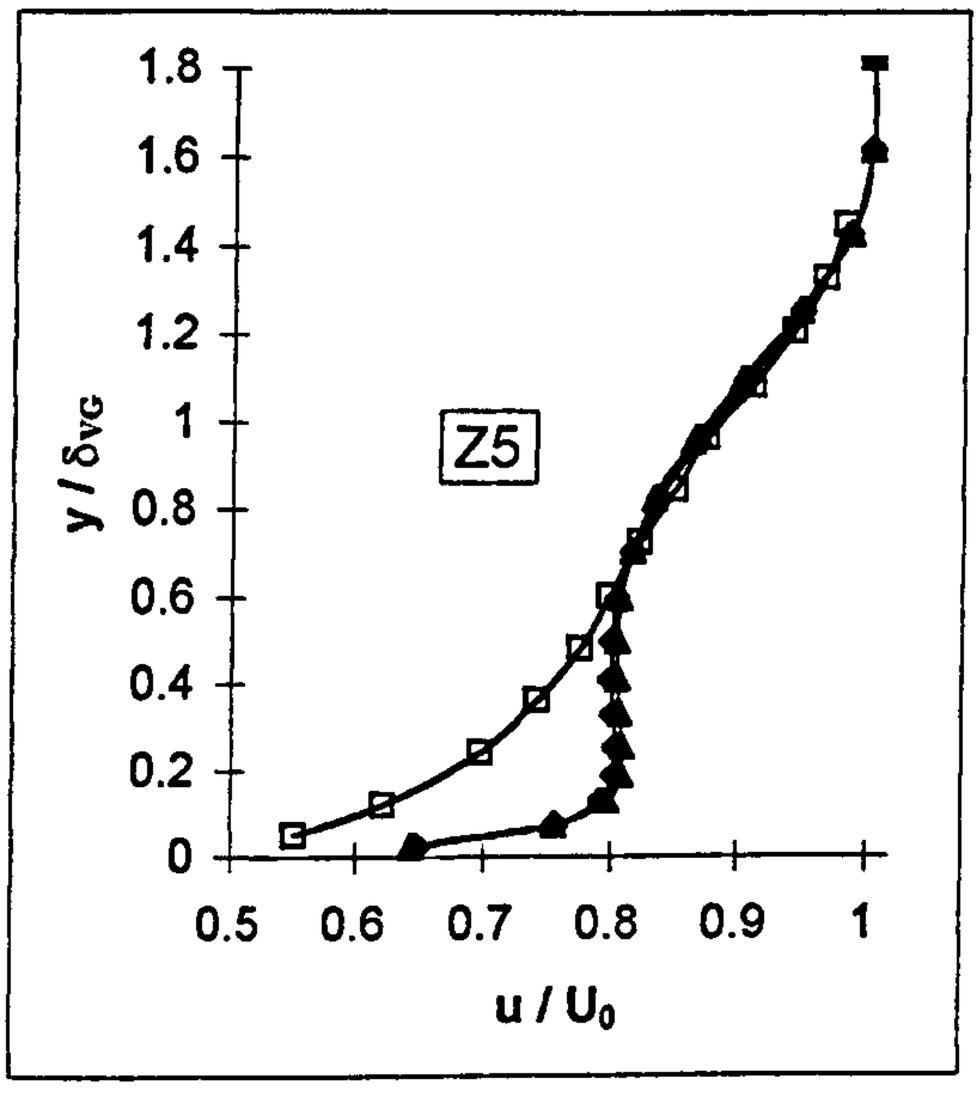

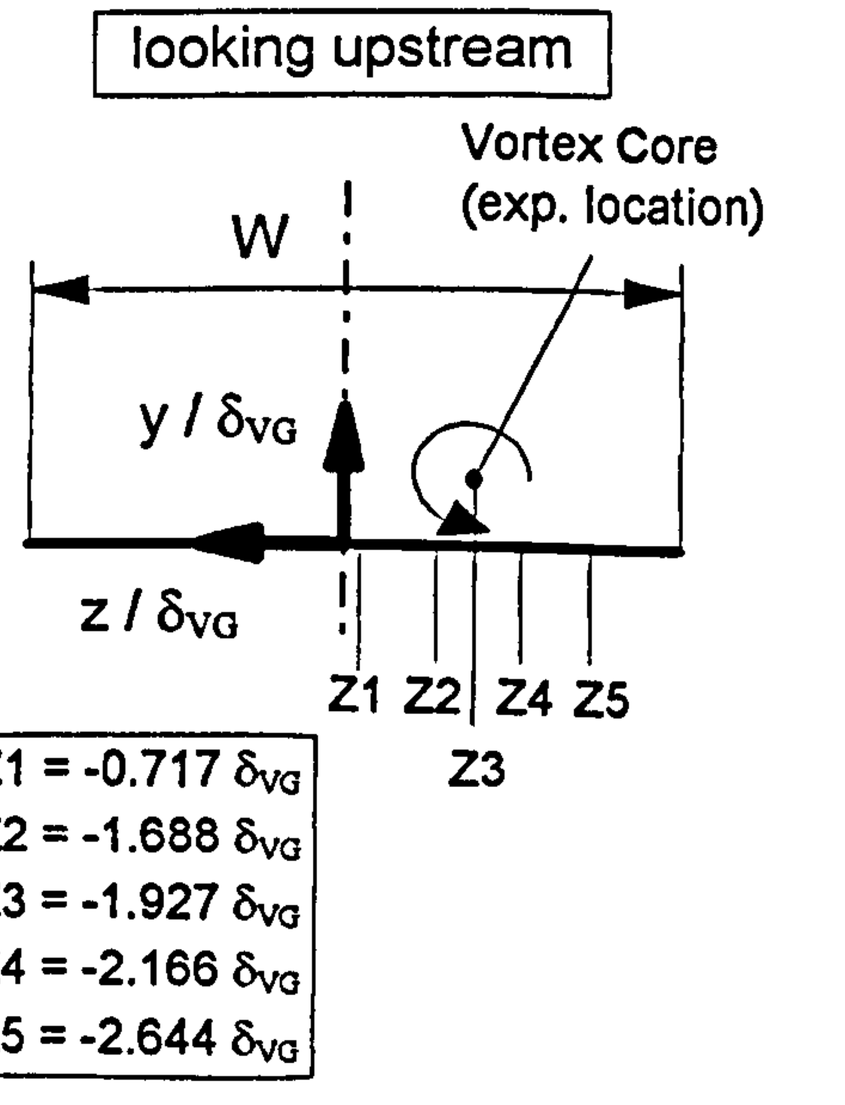

Z1 = -0.717 δ_{VG}
Z2 = -1.688 δ_{VG}
Z3 = -1.927 δ_{VG}
Z4 = -2.166 δ_{VG}
Z5 = -2.644 δ_{VG}

Figure 4.14: Vertical cross-stream velocity at X3 and various cross-stream positions

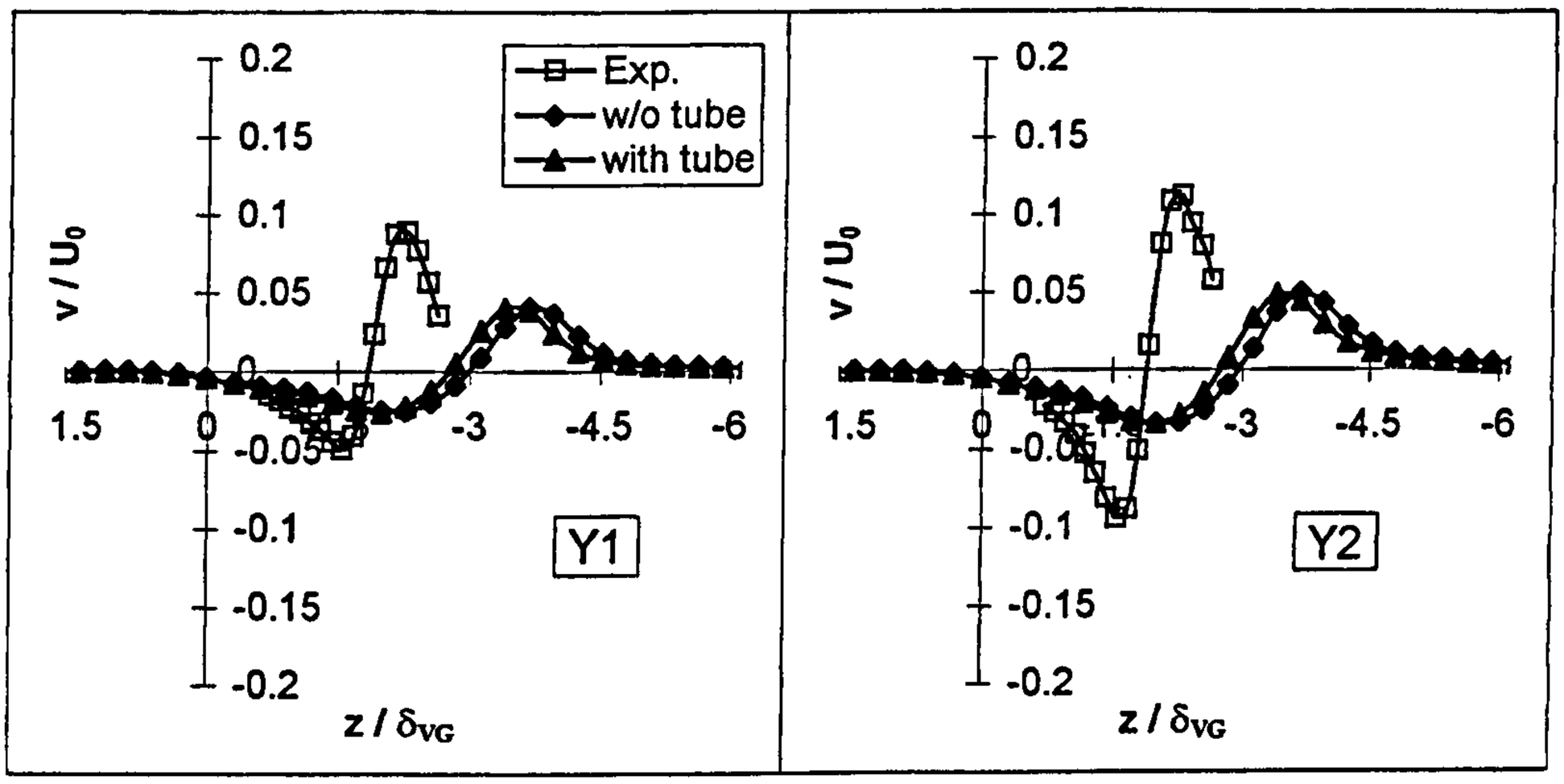

Figure 4.15: Horizontal cross-stream velocity at X3 and various cross-stream positions

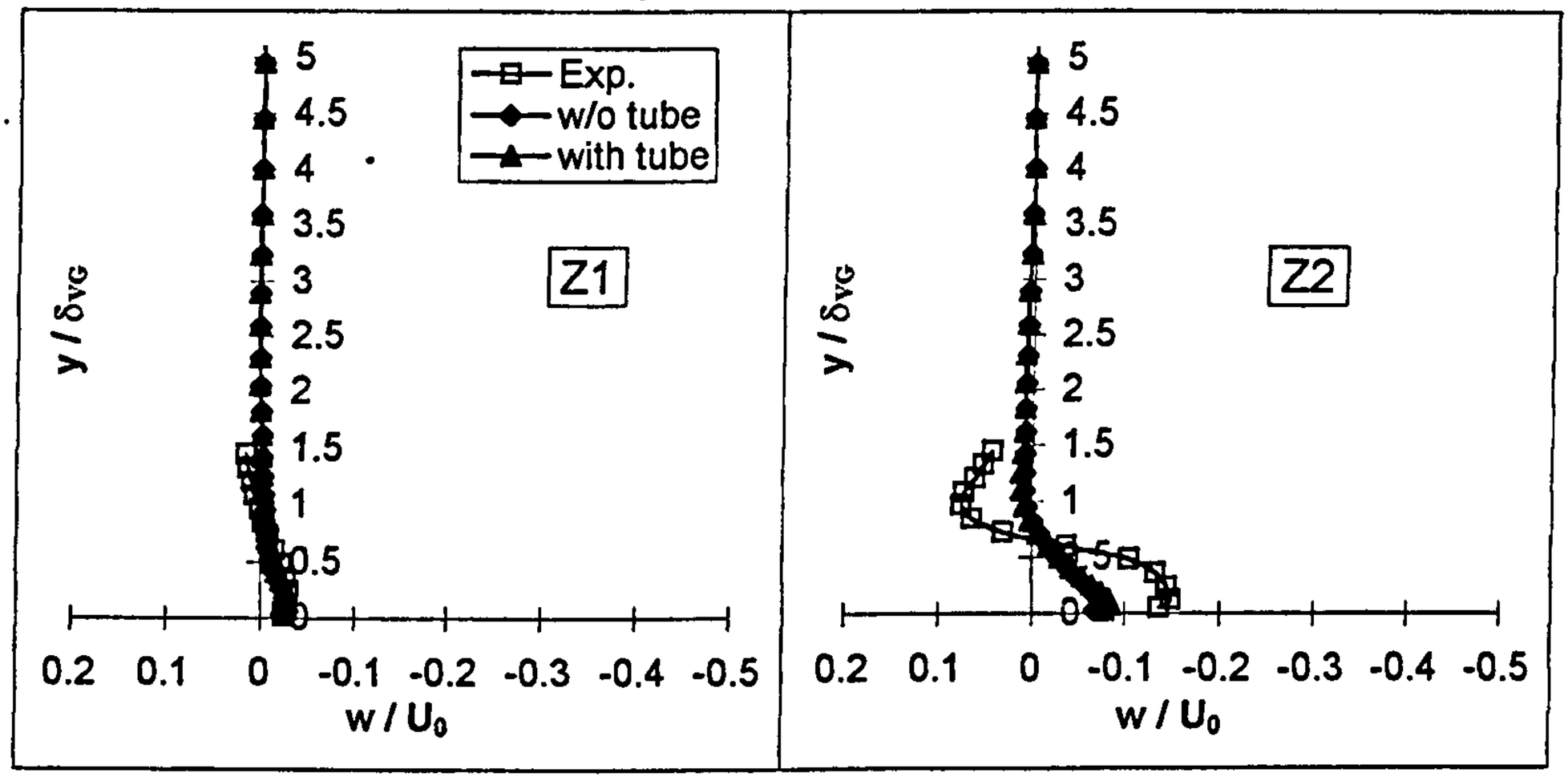

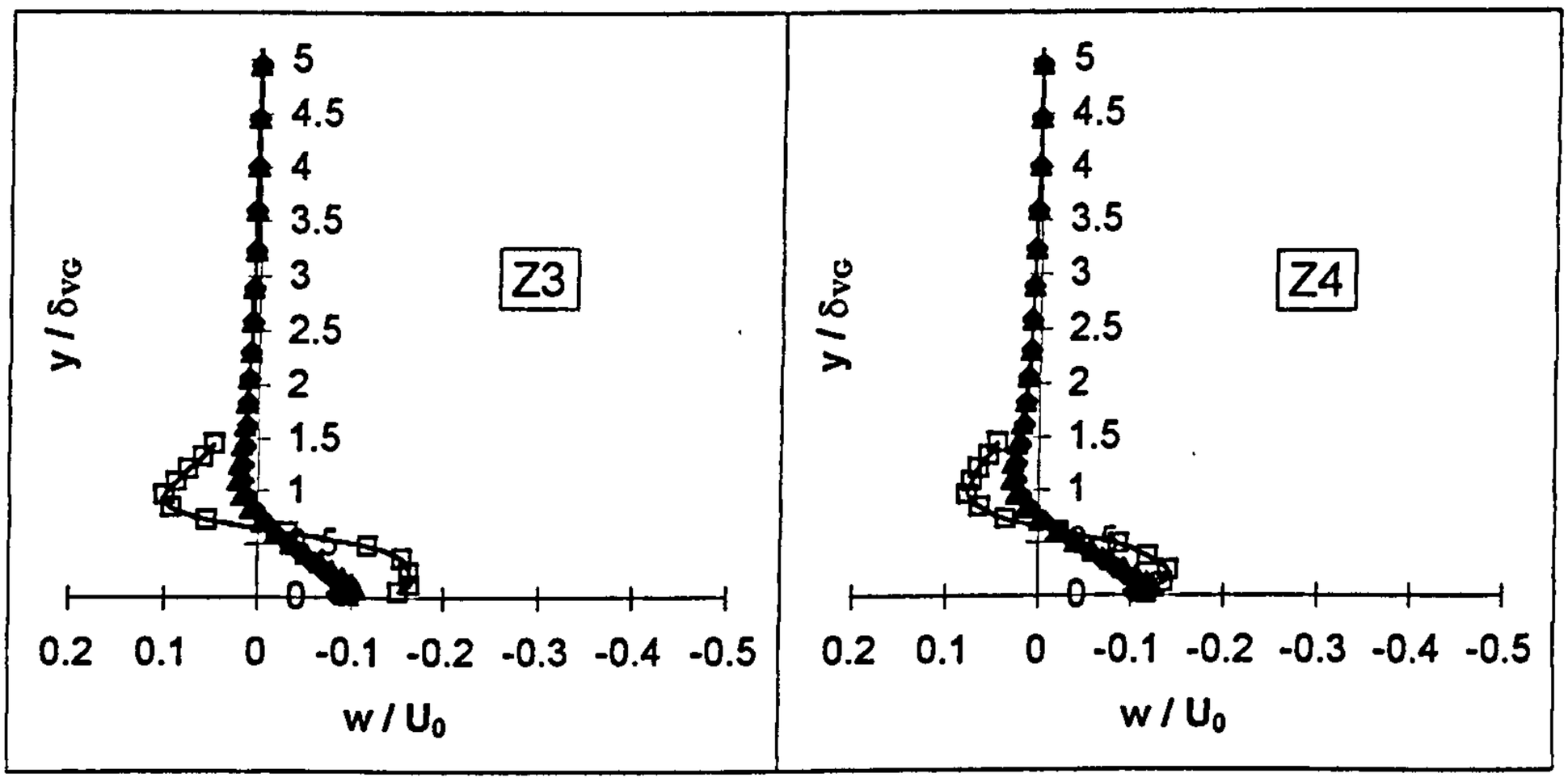

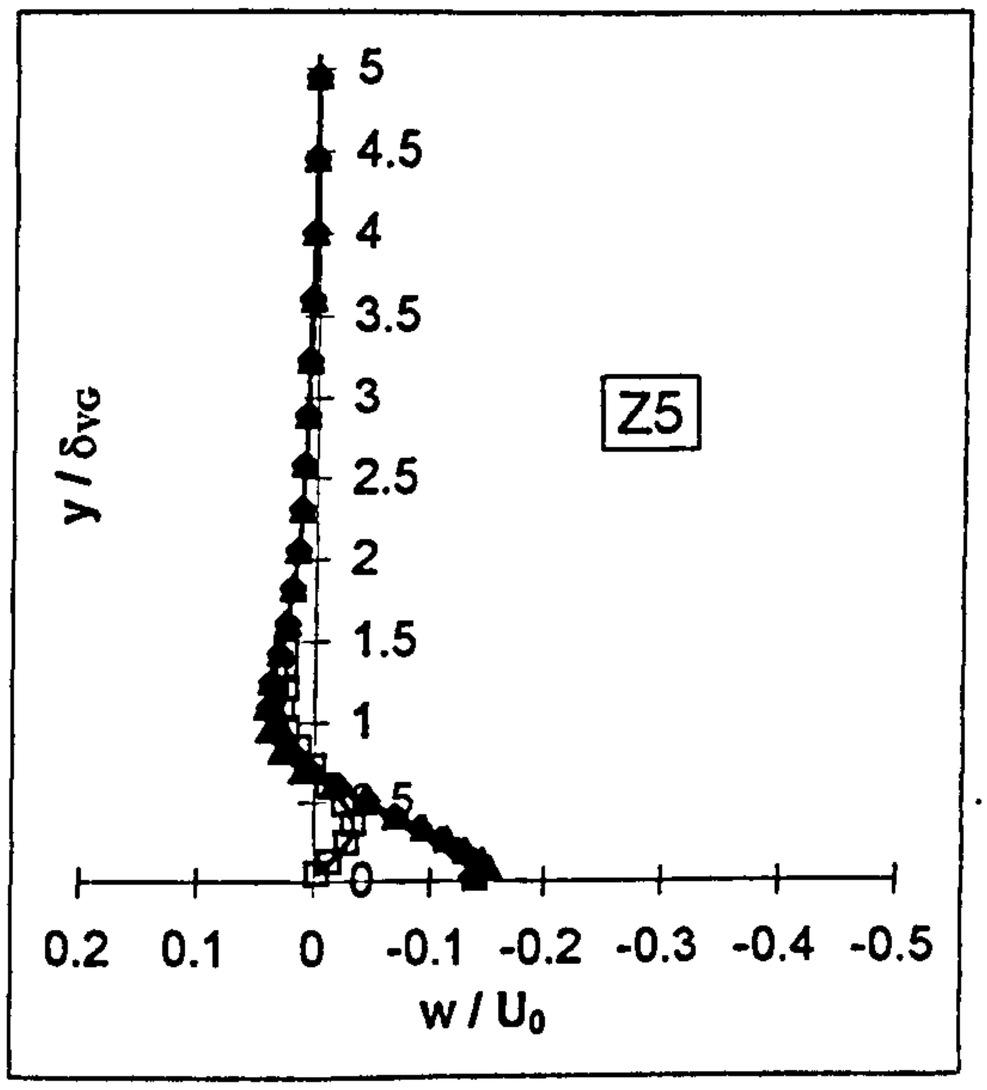

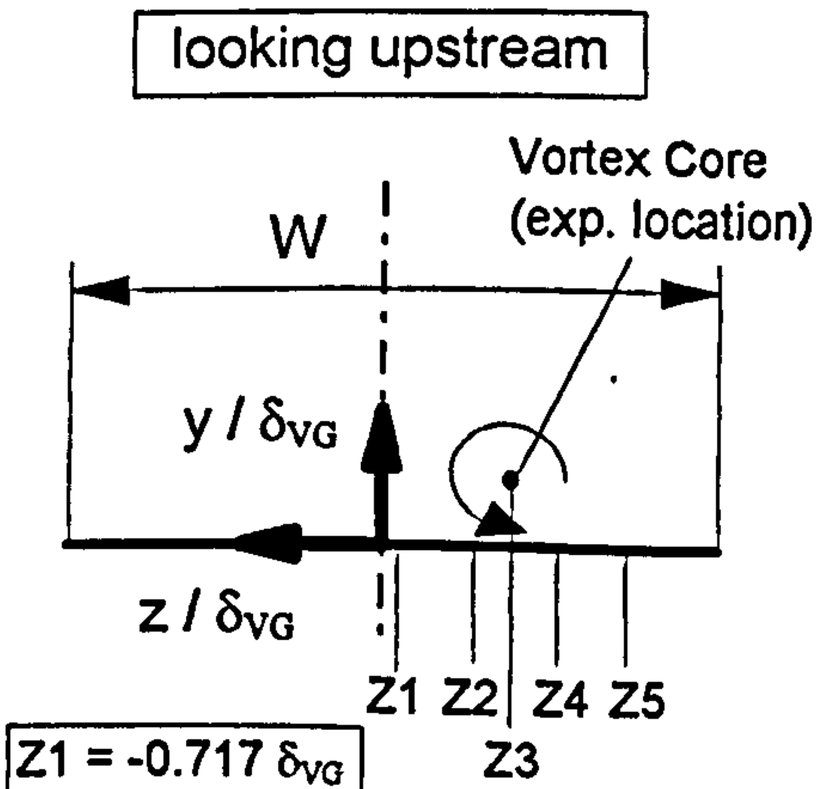

Z1 = -0.717 δ_{VG}
Z2 = -1.688 δ_{VG}
Z3 = -1.927 δ_{VG}
Z4 = -2.166 δ_{VG}
Z5 = -2.644 δ_{VG}

Figure 4.16: Streamwise velocity at X4 and various cross-stream positions

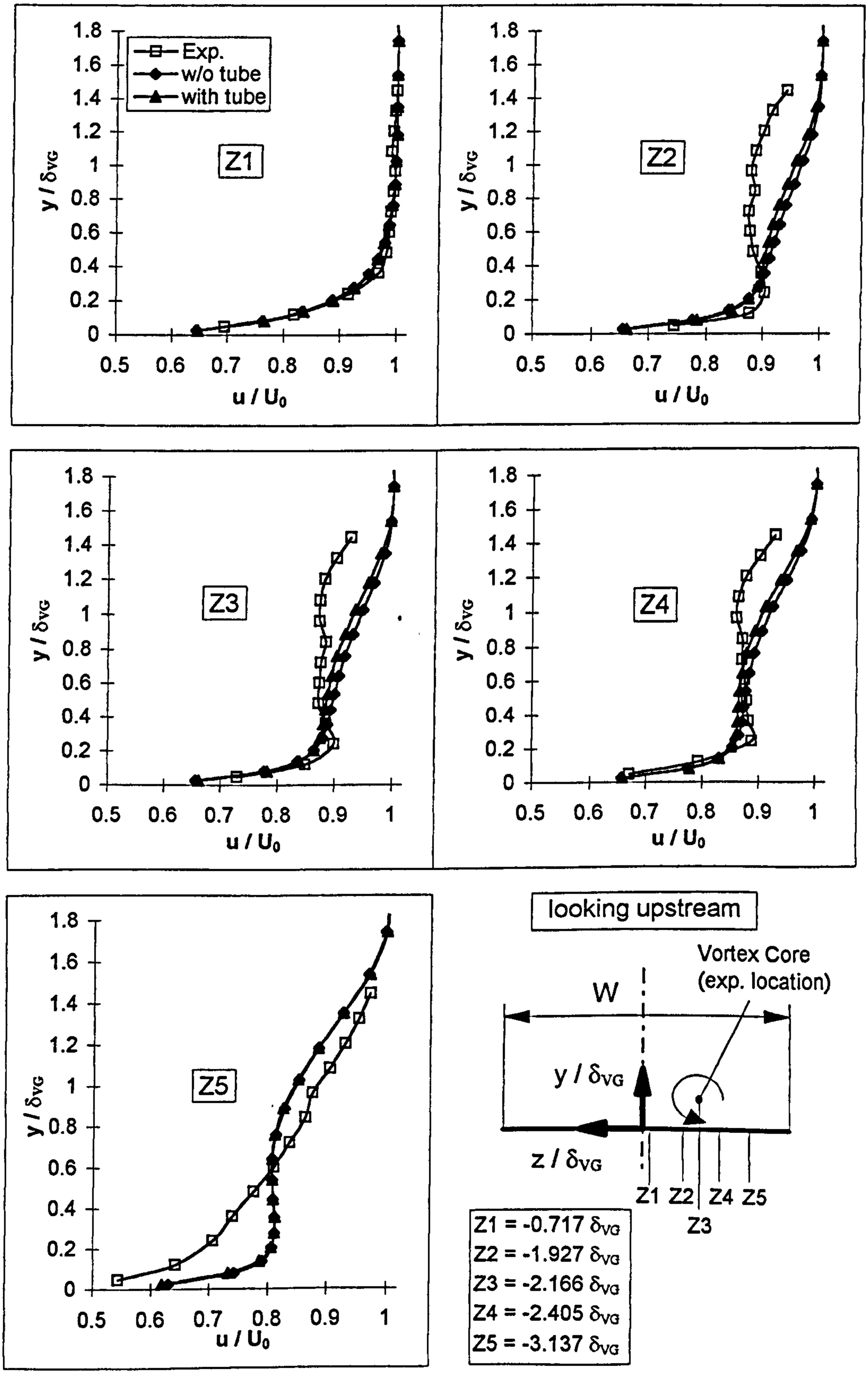

Figure 4.17: Vertical cross-stream velocity at X4 and various cross-stream postions

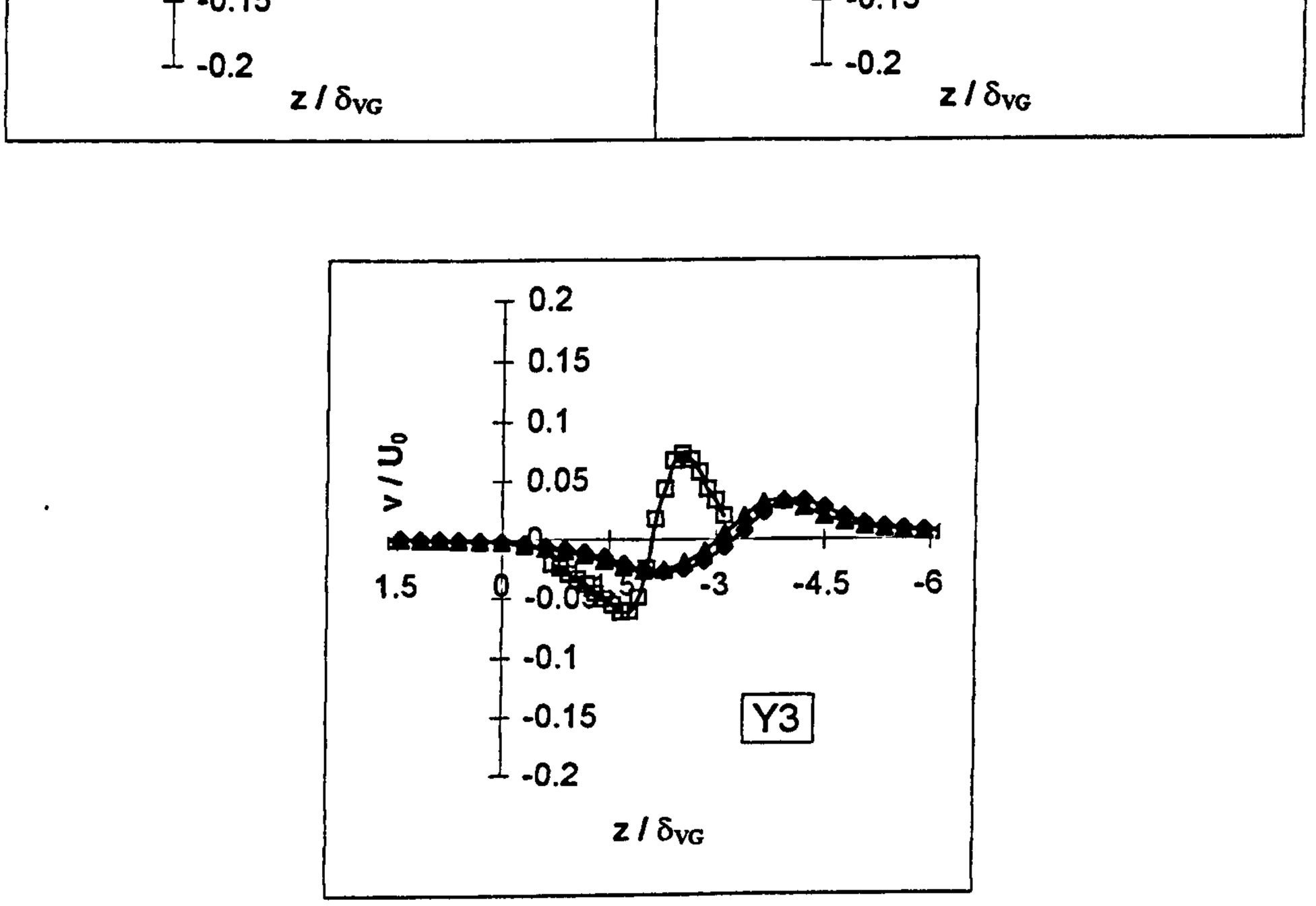

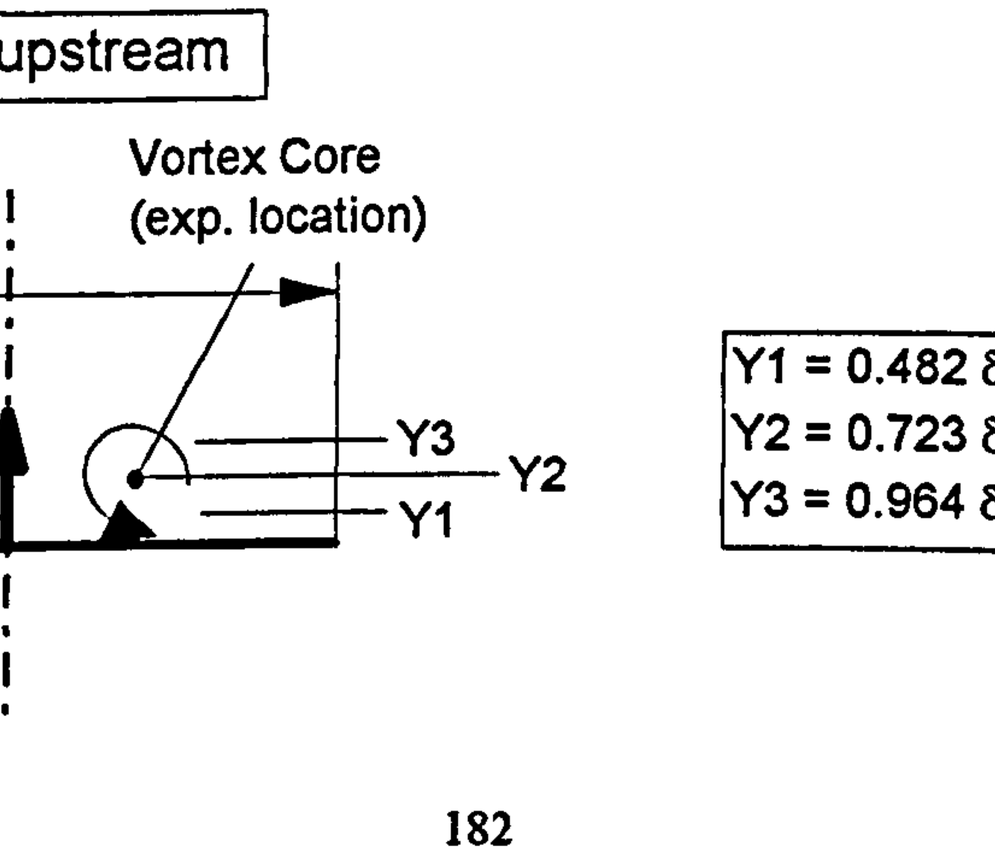

Y1 = 0.482 δ_{VG}
Y2 = 0.723 δ_{VG}
Y3 = 0.964 δ_{VG}

Figure 4.18: Horizontal cross-stream velocity at X4 and various cross-stream positions

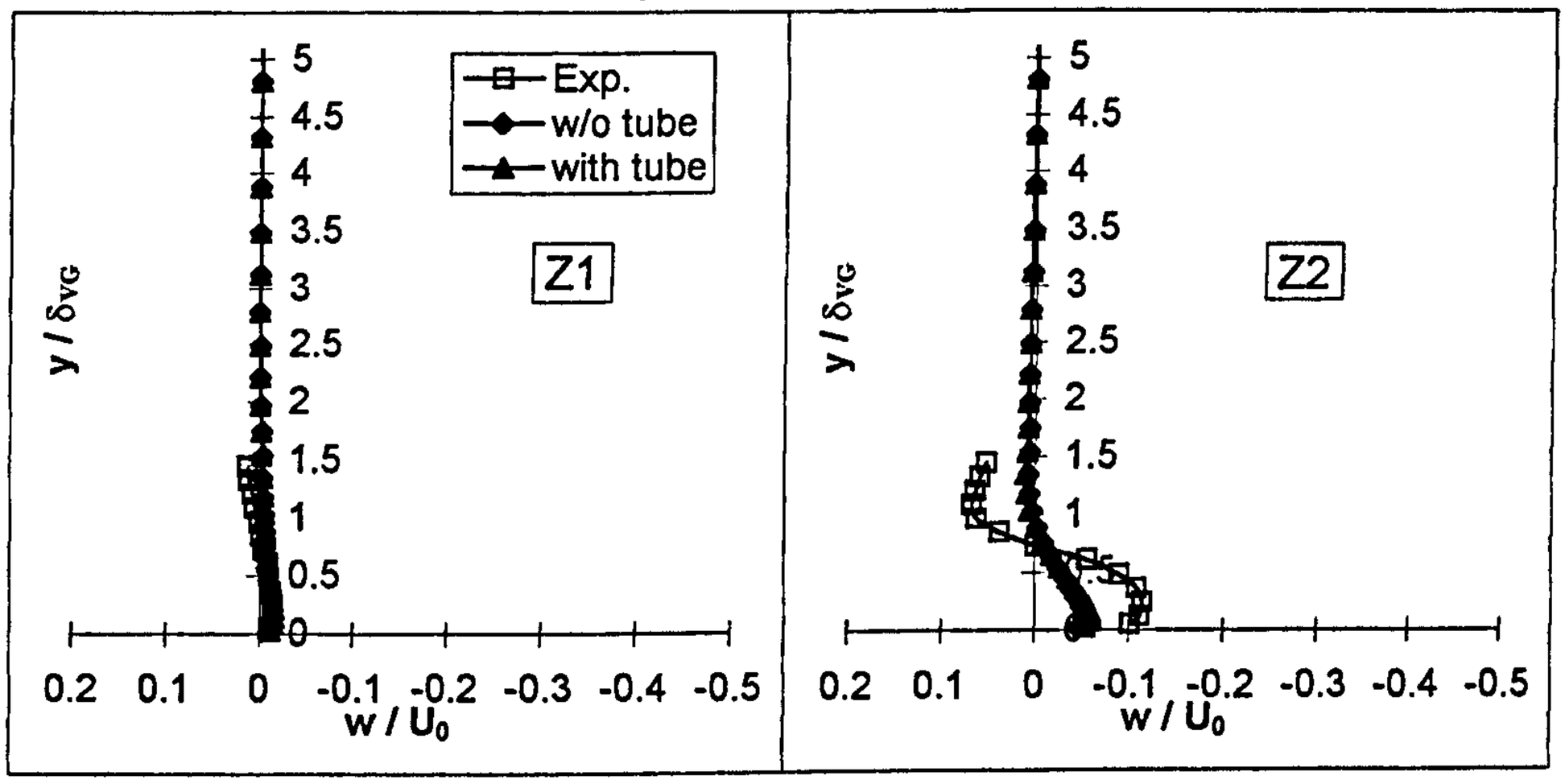

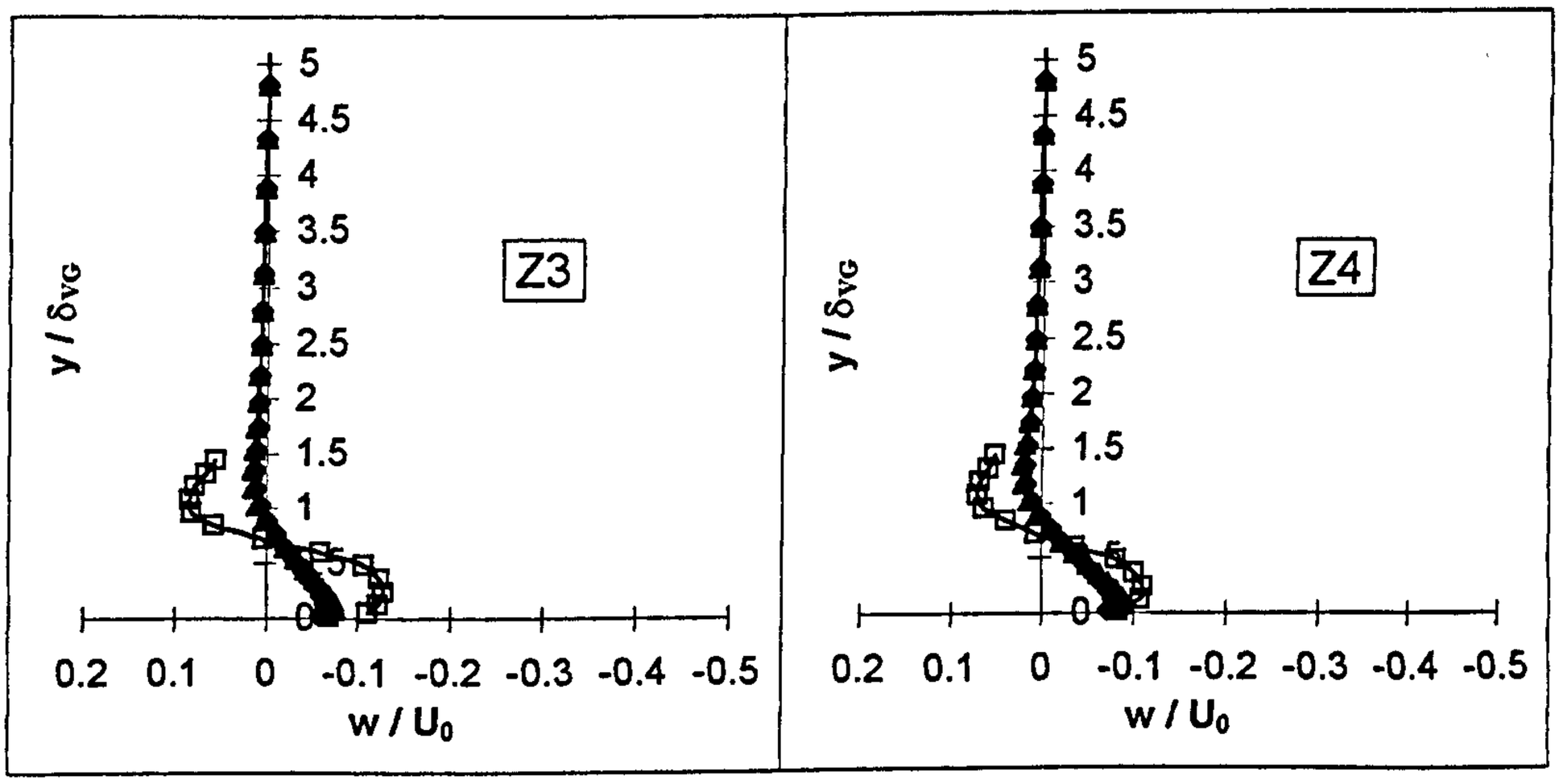

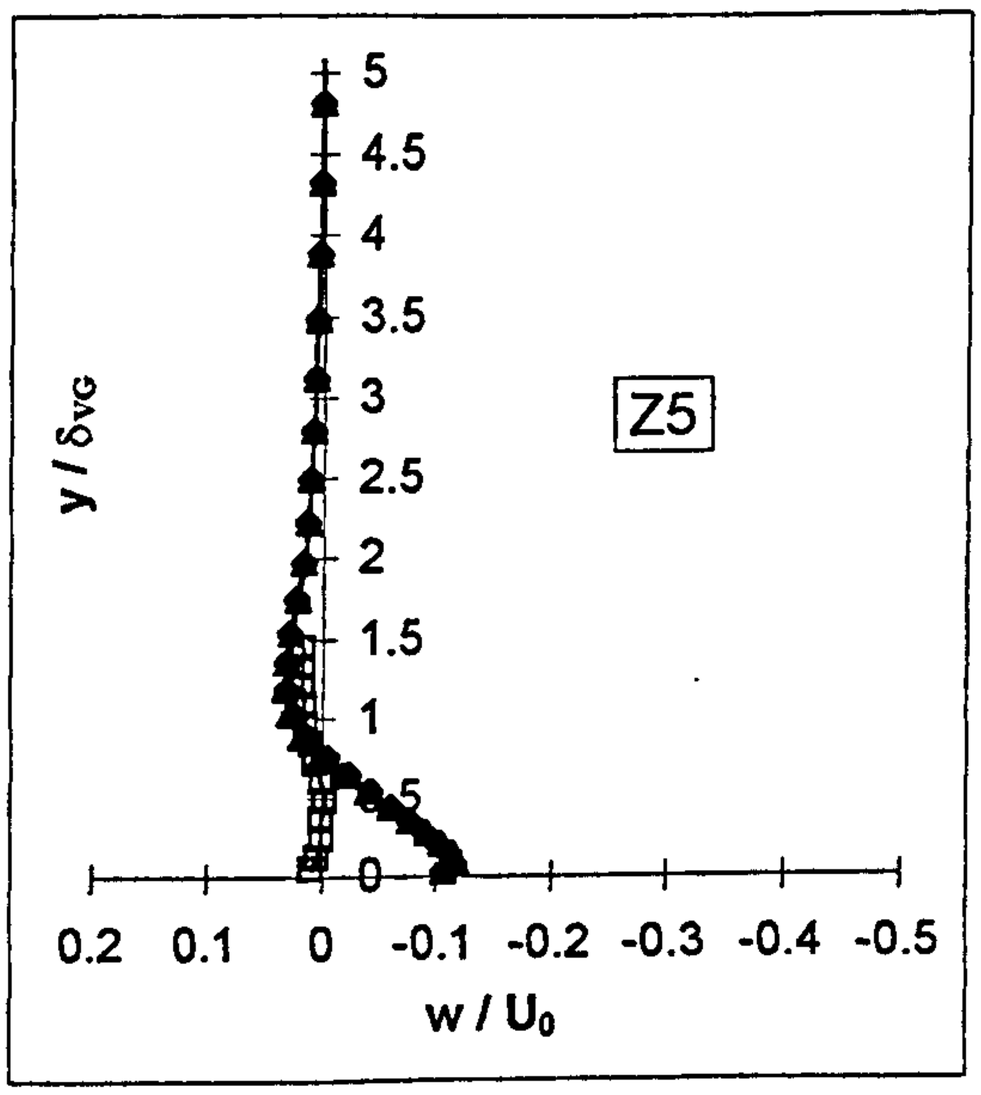

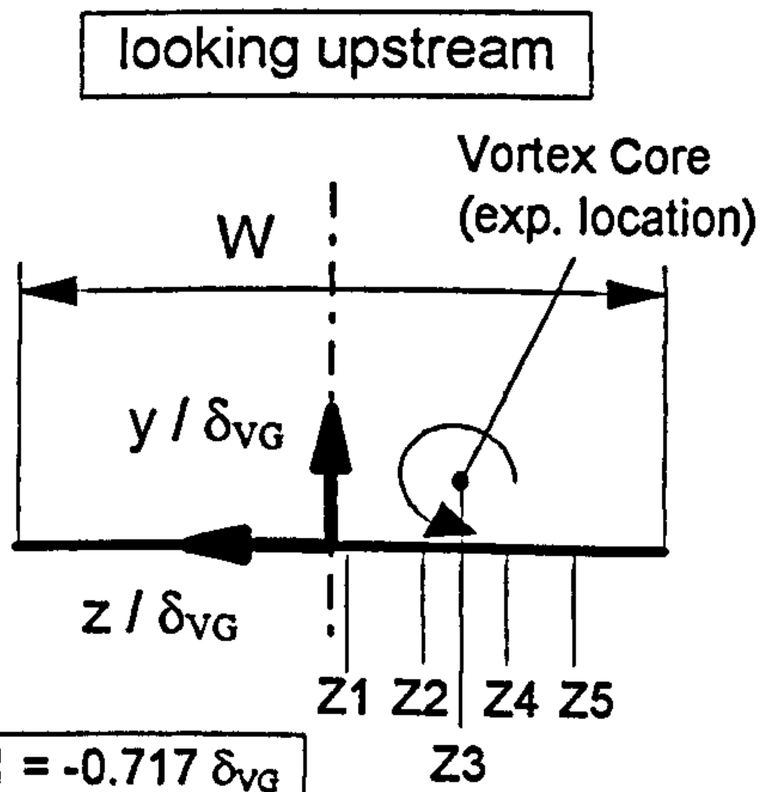

Z1 = -0.717 δ_{VG}
Z2 = -1.927 δ_{VG}
Z3 = -2.166 δ_{VG}
Z4 = -2.405 δ_{VG}
Z5 = -3.137 δ_{VG}

4.4 Summary

In this Chapter predictions of two numerical models were compared to experimental data provided by the Cranfield University. Both numerical models, described in Section 3.7.2, were designed to match the experimental model in terms of dimensions and boundary conditions. Both numerical models comprise an incompressible, turbulent, boundary layer over a flat plate into which a pitched and skewed airjet is issuing. In the first model the airjet is defined as a velocity plug profile issuing into the solution domain from the solid surface. In the second numerical model a jet inlet tube (see Figure 3.14) is modelled where the velocity plug profile is defined at the inlet of the tube. This feature allows the jet velocity profile to develop over the length of the tube. It also allows the main flow to influence the jet velocity profile as it enters the main flow.

Section 3.8 describes briefly the grid generation code 'JETGRID', written in Fortran 77. The code generates a thirteen block structured three dimensional grid. The grid generation code also calculates the local distortion of the physical grid, both the maximum and minimum skewness are determined to check the state of discretisation.

In Section 4.2.1 grid dependence was investigated and discussed by using the shear stress distribution at one chosen downstream location. Five advection schemes were tested against experimental data by using streamwise and cross-stream velocity profiles at one defined downstream location. The higher Upwind scheme (HUW) was found to provide the best compromise between accuracy and level of convergence. The numerical and experimental results were discussed and compared in Section 4.3. At four downstream locations (see Figure 4.6) experimental data was available in terms of streamwise and cross-stream velocity profiles. The data of the two numerical models, with and without the inlet tube were compared with the measured results. The most significant difference between measured and predicted data was the magnitude of the cross-stream velocity components v. The magnitude of the predicted cross-stream velocity component v was approximately 50% lower than that of the measurement (see Figure 4.8). The predicted cross-stream positions of the vortices cores were slightly shifted from the experimental position at the first downstream location. Between the first and second downstream (see Figure 4.11) location, the predicted vortices travelled approximately 30% further in the cross-stream direction

than the experimental vortex. Thus the shift between the experimental vortex and the predicted vortices grew by approximately a factor of 2. The downstream development of measured and predicted vortices from the second downstream location onwards was similar in terms of decay and migration. Little difference between the two numerical models could be observed at the first downstream location but the velocity magnitudes of the model without the inlet tube were slightly higher. Further downstream, the two numerical models predicted approximately the same results.

5 Flat Plate Models

5.1 Introduction

The numerical results for the two vortex generators, i.e. the airjet and the vane VGs, will be discussed and compared at two downstream locations, i.e. X1 and X2 (see Figure 5.1).

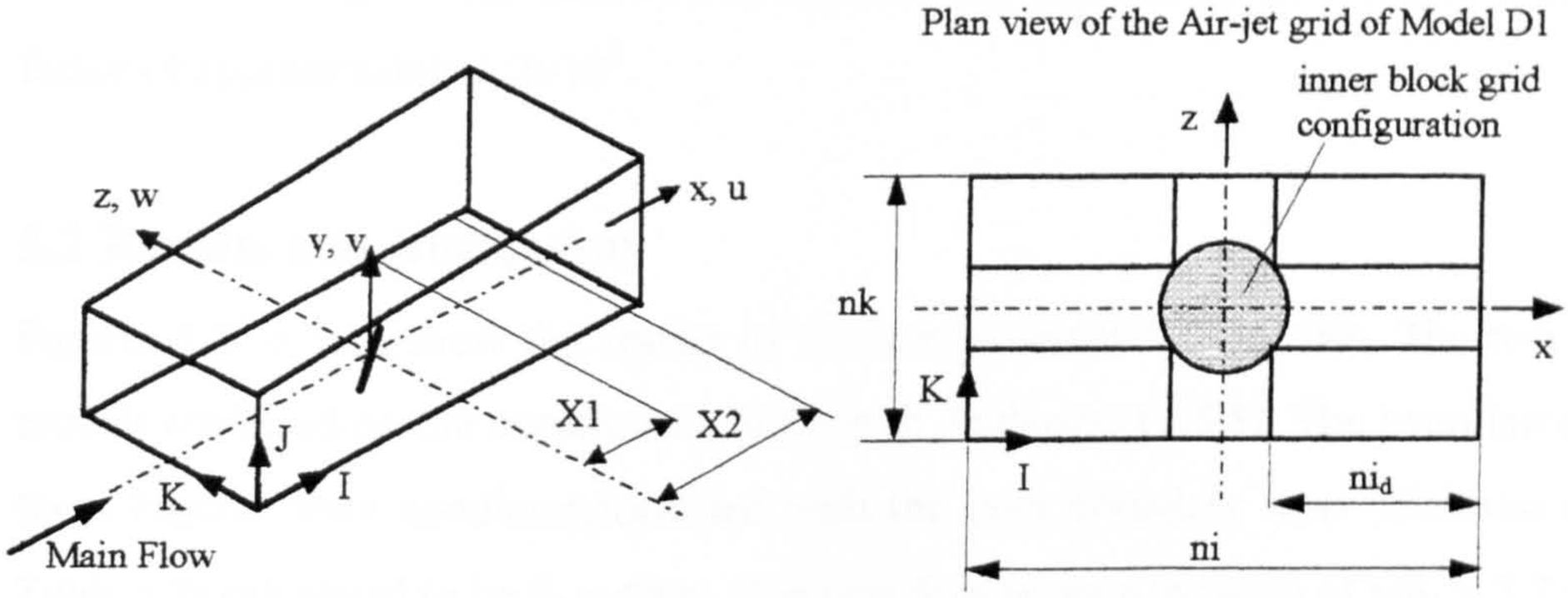

Figure 5.1: Local VG models (D1 and D2) with the two downstream stations and I, J, K notation

These downstream locations were defined as follow:

- X1 = 0.25 L (4.2 δ_0)
- X2 = 0.46 L (7.7 δ_0) remembering that $\delta_0 \equiv$ inlet condition as we see in the following Figures 5.5 to 5.12.

A grid dependence test was carried out for both numerical models, D1 and D2. The shear stress distribution at the downstream location X1 was used as a criterion to judge grid independence.

For the vane VG model D2 a one-block grid was used with a total number of grid cells of 299520. A cell distribution of (ni = 104, nj = 36, nk = 80) was found to provide shear stress results independent of further refinement.

The Air-jet VG model D1 was discretised with a thirteen block grid and a cell distribution of the outer grid blocks of (ni = 60 (ni_d = 30), nj = 29, nk = 40). The total number of grid cells including the inner block configuration (see grey shaded area in Figure 5.1) is 89088 cells. This grid size provide shear stress results independent of

further refinement. All predictions in this section were calculated using the aforementioned grids and a second-order Upwind (HUW) dicretisation scheme (see Section 4.2.2). From previous calculations (see Section 4.3) it was decided that it was unnecessary to grid the jet inlet tube. An average number of 1000 iterations was needed to achieve convergence in the case of the two local models, D1 and D2. The error in continuity, i.e. the mass source residual was reduced by an average reduction factor of approximately 1.2×10^5.

5.2 Results and Discussion

Figures 5.2 to 5.12 show the results of the two different VG models. The two VG models are based on the experiments of Gibb & Anderson (1995). The coordinates in these Figures were nondimensionalised with the inlet boundary layer thickness (see Table 3.2) calculated to be $\delta_0 \approx 4$mm. The first downstream location of $x/\delta_0 \approx 3.2$ was chosen because it was the closest downstream location to the vane at which the vortex was properly developed.

Figure 5.2 shows the significant difference between the strength of the counter-rotating vortices produced by the Air jet Vortex Generators (AJVG) and by the Vane Vortex Generators (VVG). The velocity scales are the same in both vector plots.

Figure 5.3 shows the decay of circulation and peak vorticity in the streamwise direction downstream of the VG's centre. The calculation of peak vorticity and peak vorticity position is given in Appendix B. The lowest circulation was predicted for the counter- and co-rotating vortices of the Air jet. As can be seen, the circulation for both jet configurations was the same. The co-rotating vanes were predicted to produce vortices with circulation values four times that produced by the jet vortices. However, even larger circulation values, six times that of the jets, were predicted for the counter-rotating vane configuration.

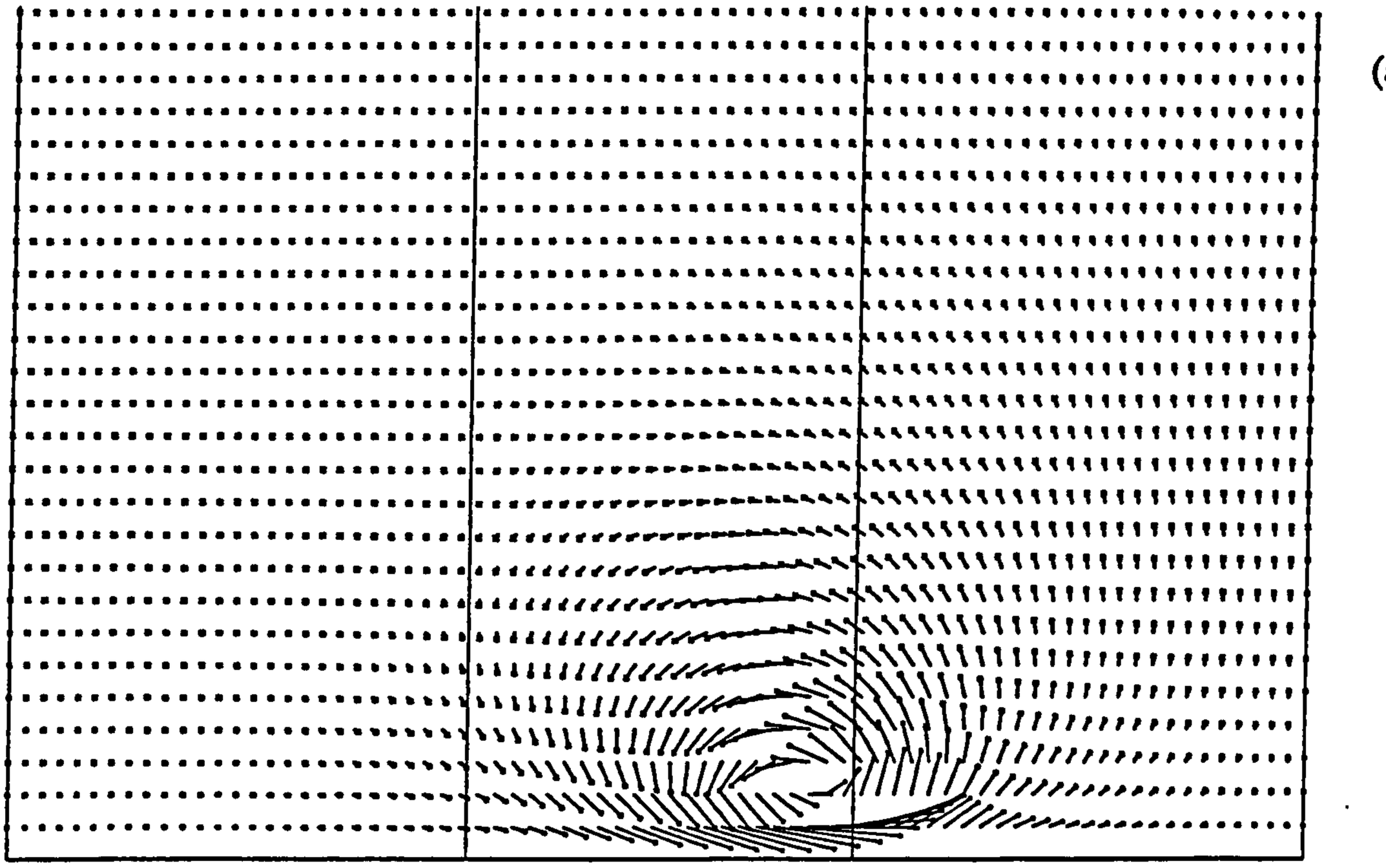

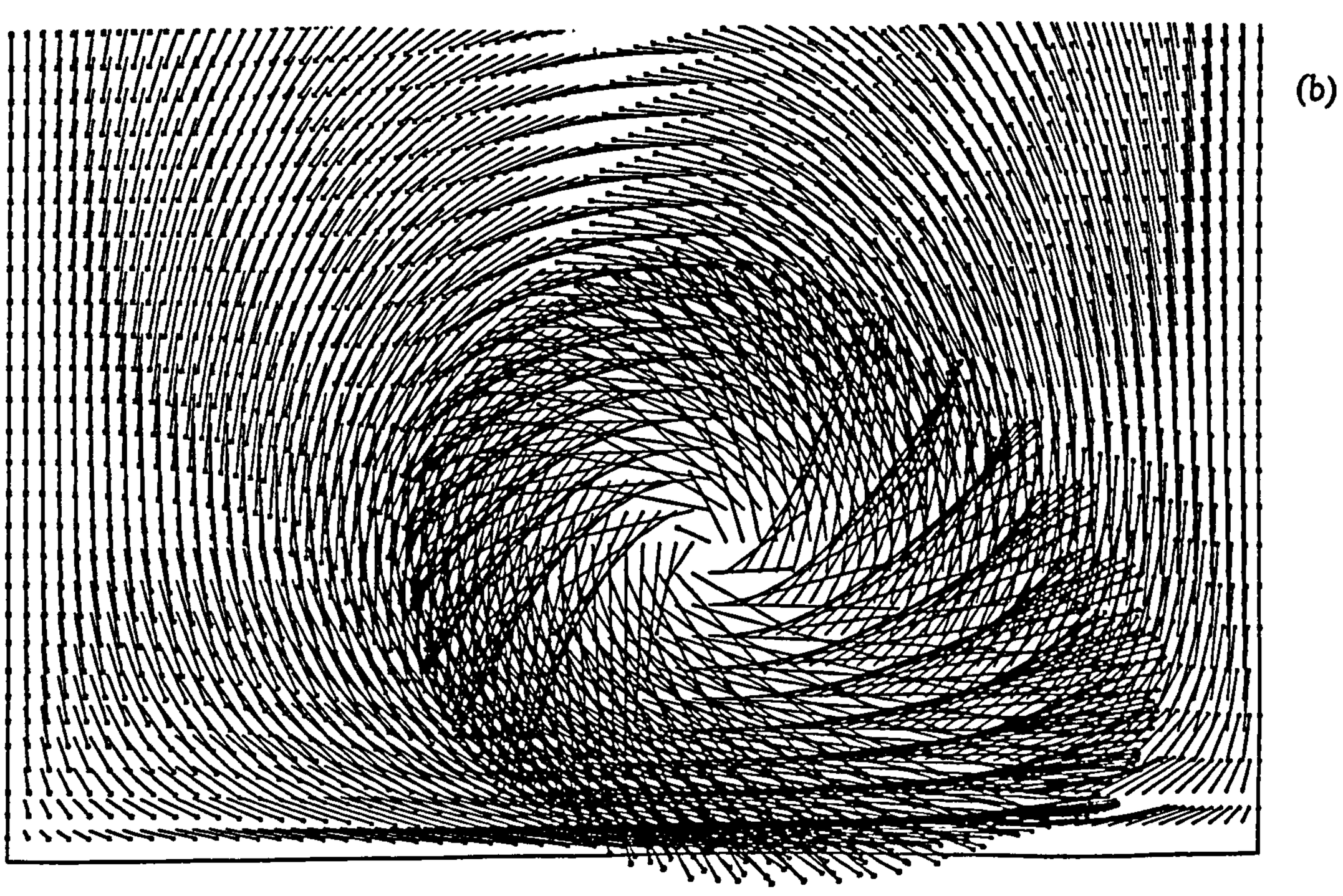

Figure 5.2: Velocity vector plots of counter-rotating vortices produced by (a) AJVG (model D1) and (b) VVG (model D2) at the downstream location X1 = 4.2δ_0

Figure 5.3: Circulation and peak vorticity decay for vane and airjet VGs

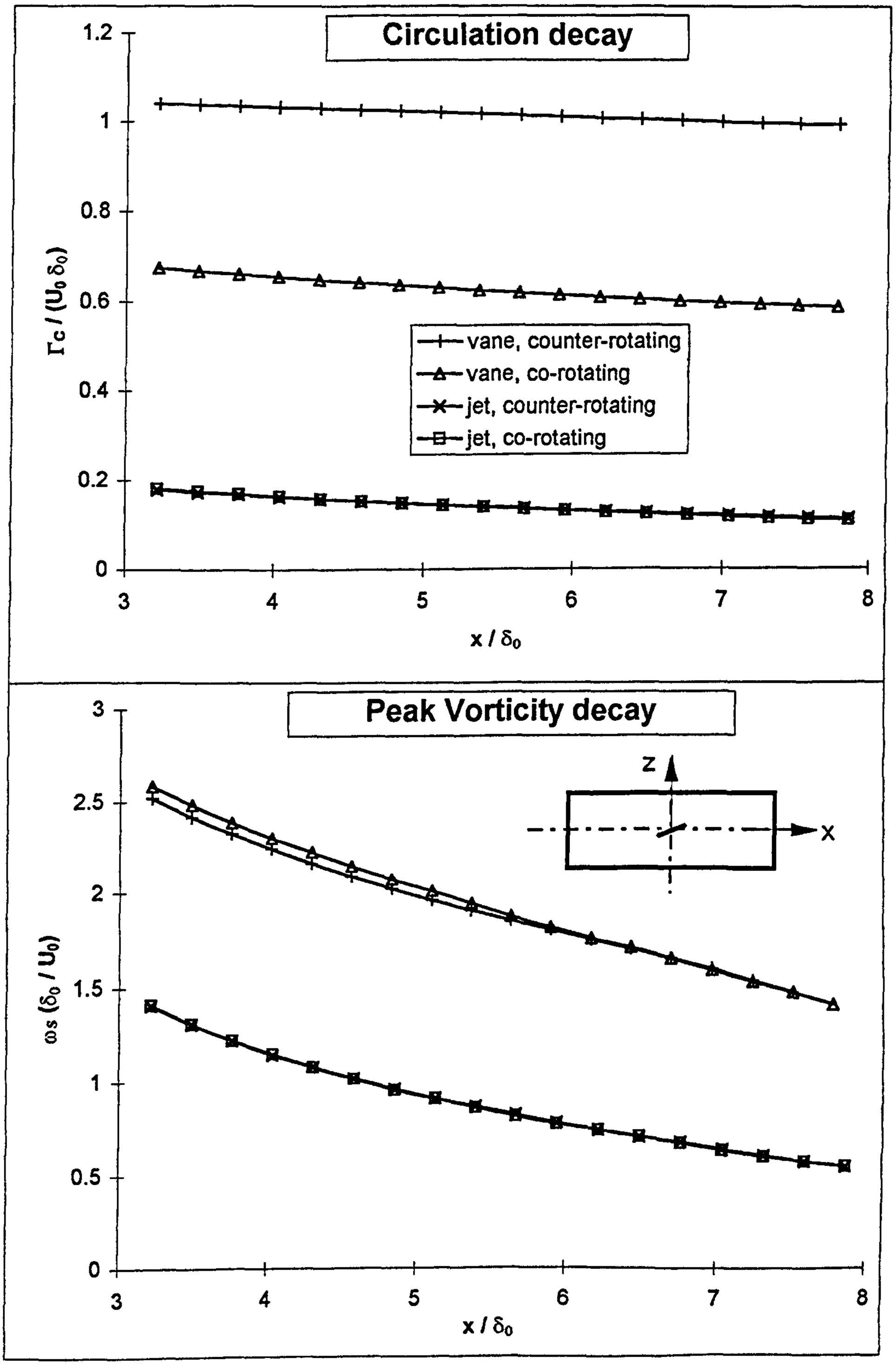

The difference in circulation magnitudes between the two vane cases is caused by interaction of the co-rotating vortices, as shown schematically in Figure 5.4. The lower value of circulation for the co-rotating vane vortices compared to the counter-rotating case, is believed to be due to the interaction of the vortices. The periodicity provides interference between the co-rotating vortices with a result of reducing the individual vortex strength. In contrast the vortices with symmetric boundary conditions (i.e. counter-rotating vortices) enhance each other.

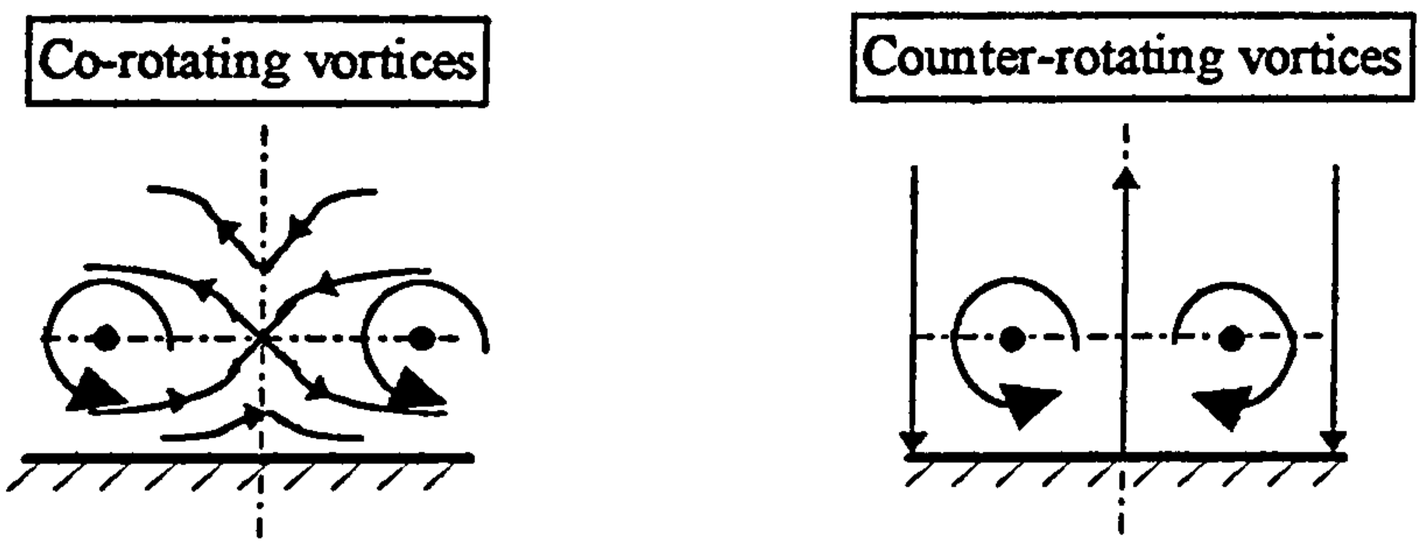

Figure 5.4: Interaction of co- and counter-rotating vortices

Figure 5.5 shows velocity vector plots of the co- and counter-rotating vortices produced by the VVG. It can be clearly seen that the diameter of the counter-rotating vortex is significantly larger than the diameter of the co-rotating vortex. No difference in both jet cases is seen because the individual vortex strengths are too low for the spacing used for any interaction between the vortices to occur.

The peak vorticity decay provides distinctive differences in the results between jet and vane but a negligible difference between the two vane configurations. The peak vorticity magnitudes of the counter- and co-rotating vortices of the jet are identical and approximately 50% lower than the vane cases. The peak vorticity decay rate is approximately the same for both VG models but more rapid than that of the circulation decay rate.

In Figure 5.6 paths of peak vorticity for the counter- and co-rotating vortices for vane and airjet VGs are shown. It was found that the peak vorticity and the vortex core location is approximately the same in the case of the VVGs. However, in the case of the AJVGs the peak vorticity locations, normal to the solid surface, were slightly

below the vortex core position. In the x-z plane it can be seen that the counter-rotating vortex produced by the vane travelled parallel to the counter- and co-rotating vortices initiated by the AJVG. The two jet vortices are almost on the same path. Again, this is due to the relatively large spacing in the airjet cases. The exception is the co-rotating vane vortex which exhibits a greater cross-stream translation compared to the counter-rotating vane vortex and to those created by the AJVGs. The line of peak vorticity in the x-y plane for the vane vortices is significantly different from that of the jets. This graph shows clearly that the vortices produced by the jet are five times lower, i.e. much closer to the solid surface, than those produced by the vane. Specifically, the cores of the vortices generated by the vane are approximately on the edge of the boundary layer, whereas the cores of the vortices initiated by the jet are within the boundary layer (see Figure 5.8). The diameter of the co-rotating vortex produced by the vane remains constant over the distance calculated, thus travelling downstream on an approximately horizontal line (see Figure 5.6). The counter-rotating vane vortices lift each other off the surface thus increasing their diameters.

The cross-stream vorticity distribution produced by the VVGs and the AJVGs are shown in Figure 5.7 at two downstream locations X1 and X2. The first location X1 is exactly half way downstream from the VG centre to the domain exit plane. The second location X2 is just upstream of the domain exit plane. The vorticity peaks of the vortices produced by the jet are 50% less than the vorticity peaks produced by the vane, as already shown in Figure 5.3. The counter-rotating vane vortex is the most effective in terms of providing a high level of vorticity distribution. Comparing the two downstream locations X1 and X2 in Figure 5.7 it can be seen that the co-rotating vane vortex travelled more in the cross-stream direction than the counter-rotating vortex. This effect was also shown in Figure 5.6. Vorticity profiles through the vortices cores produced by both VG models at two downstream locations, X1 and X2 are shown in Figure 5.8. The vorticity distribution can be divided into two main groups, i.e. the vorticity profiles produced by the vane and the 50% less strong vorticity profiles initiated by the jet. In terms of vorticity magnitudes, i.e. the area underneath the vorticity profile, the counter-rotating vane vortices are the most effective. As would be expected from above, both air jet vortices produced identical

vorticity distributions. As already observed in Figure 5.6, the vertical positions of the vortices produced by the vane and those initiated by the jet were significantly different. Figure 5.8 shows very clearly the height of each vortex in the vertical direction. Both vane configurations produced vortices which influenced the main flow over a height of $y \approx 2\delta$. These vortices were able to mix the low momentum flow within the boundary layer with high momentum fluid from the main flow. In contrast, the vortices produced by the jet were active within the lower half of the boundary thickness and thus no mixing of low and high momentum fluid of the free stream could take part. An additional difference between the vorticity distribution produced by vane or jet in horizontal and vertical cross-stream directions, i.e. z- and y-direction, is the occurrence of negative vorticity. Both Figures 5.7 and 5.8 show negative vorticity areas in case of the VVG. Pauley & Eaton (1988) described this phenomenon as secondary vorticity compared to the main positive vorticity.

Cross-stream shear stress distributions produced by VVGs and AJVGs at the two downstream locations X1 and X2 are shown in Figure 5.9. This Figure might explain the findings of Anderson & Gibb (1995). That is, they achieved slightly more reductions of flow field distortion at the engine face of an S-bend intake duct (see Figure 3.16) by employing the AJVG than the VVG configuration. For the first time in this investigation, the influence of VVGs and AJVGs on the main flow appears similar. Although the widths of the vortices produced by the vane are significantly larger than those produced by the jet, the magnitudes of shear stress are of a similar order. The shear stress magnitudes of the counter- and co-rotating jet vortices at X1 are between the co-rotating and counter-rotating vane results. Through the interference of the co-rotating vane vortices, the shear stress magnitudes are approximately 20% lower than those of the counter-rotating vane vortices. In Figures 5.7 and 5.8 secondary vorticity, i.e. negative vorticity can be seen in case of both vane VG configurations. Further downstream at location X2, the secondary vorticity in the case of the vane VG has almost disappeared and the magnitude of the shear stress is increased by approximately 12% (see Figure 5.9). In contrast, the shear stress magnitude provided by the AJVG decreased from location X1 to X2 by approximately 8%. These results indicate that the vortices produced by the VVG were still developing in the longitudinal direction whereas the vortices introduced by the jet

were fully developed at or before location X1 and decay further downstream to location X2. The observed secondary vorticity (see Figures 5.7 and 5.8) at location X1 in the case of the VVG seems to feed the main vorticity as the vortices developing downstream.

The streamwise velocity profiles through the vortices cores produced by VVGs and AJVGs at the two downstream locations X1 and X2 are given in Figure 5.10. At location X1 the velocity profiles of the vane vortices support the argument that the vortices are not fully developed because two velocity deficits occur. Further downstream at X2 the two velocity deficits produced by the vane at X1 are joined to one main velocity deficit. The streamwise velocity deficits are less significant for the co-rotating vane vortices than those generated by the counter-rotating vortices. The increase of skin friction provided by the vane vortices can be seen by comparing the two velocity gradients at each downstream location. As shown in Figure 5.10 the counter-rotating vane vortices provide a steeper velocity gradient and thus greater shear stress than the co-rotating vane vortices. The velocity deficits produced by the AJVG configurations appear negligible in terms of magnitude compared to that of the vane data. A clear velocity deficit can be seen for the jet vortices at location X1 but not at X2. Even if the vortices produced by the jet are small in diameter compared to the strong vortices produced by the vane, the velocity gradients at the solid surface are similar. Therefore, the skin friction is of similar magnitude in both VG cases as shown in Figure 5.9.

The cross-stream velocity profiles (v, w) in z- and y-directions are shown in Figures 5.11 and 5.12. These Figures reflect the main differences between the vortices produced by the VVG and those by the AJVG in relation to the magnitude and the vertical positions of the vortices. All vortices travelled and stretched in the cross-stream direction (see Figure 5.11) but did not significantly alter in their proximity to the solid surface (see Figure 5.12). The difference observed between the magnitudes of the co- and counter-rotating vane vortices is due to a number of factors. These include the interference effect of the co-rotating vortices reducing the magnitudes of each other. Conversely the counter-rotating vortices tend to enhance each other rotation. Referring to Figure 5.8 it could be seen that most of the vorticity in the case of the AJVG was found within half of the boundary layer thickness whereas the VVG

configurations provided mixing with the main flow. Figure 5.12 shows the same significant difference in magnitudes and positions between the vane vortices and the jet vortices as also can be seen in Figure 5.8 for the vorticity distribution. However, in Figure 5.12 the cross-stream velocity w of the AJVG spread into the flow at a vertical distance form the solid surface close to the boundary layer height. Even though the velocity magnitude of the w-component is weak close to the boundary layer thickness, Figure 5.12 shows, compared to Figure 5.8, that the whole boundary layer is affected by the jet vortices.

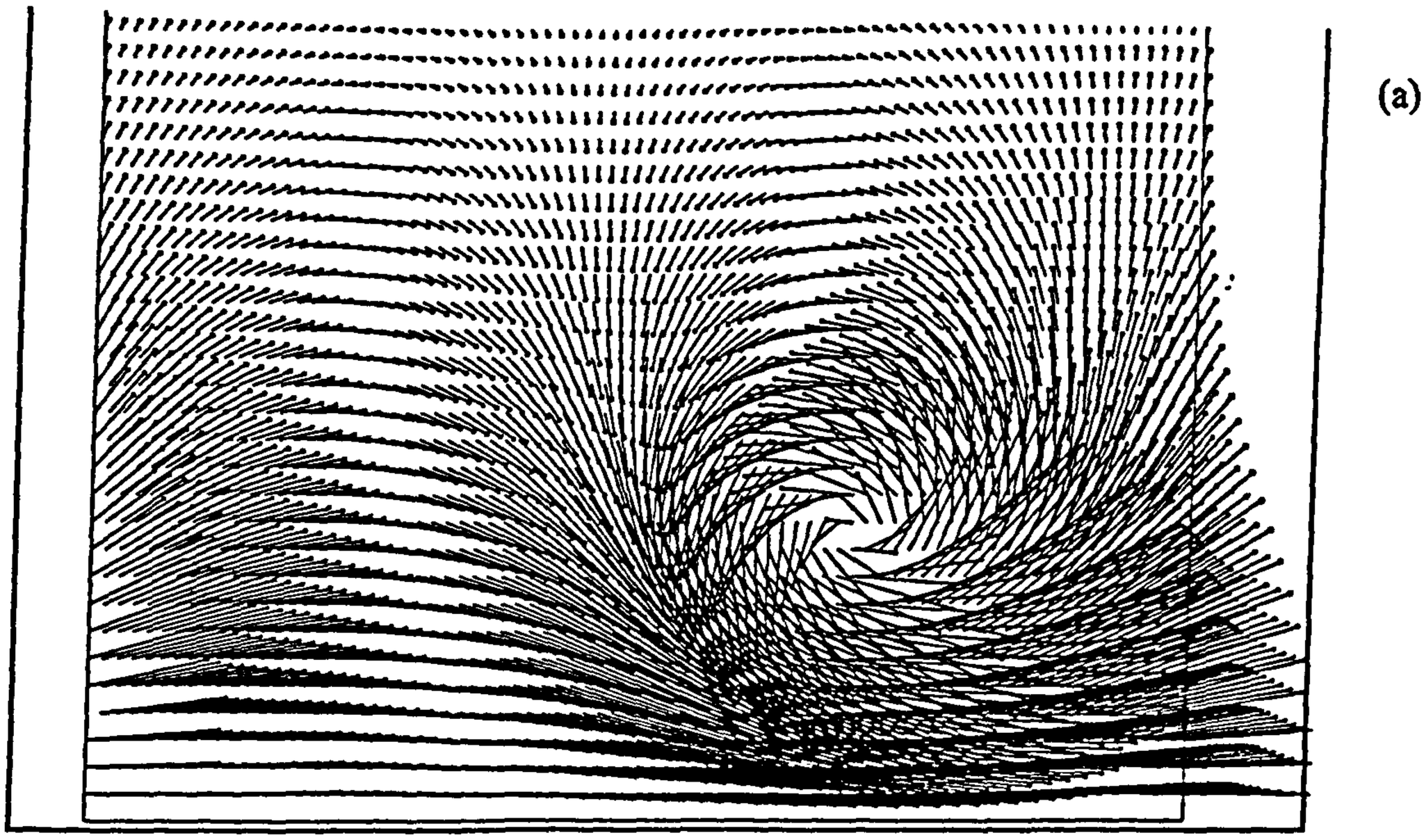

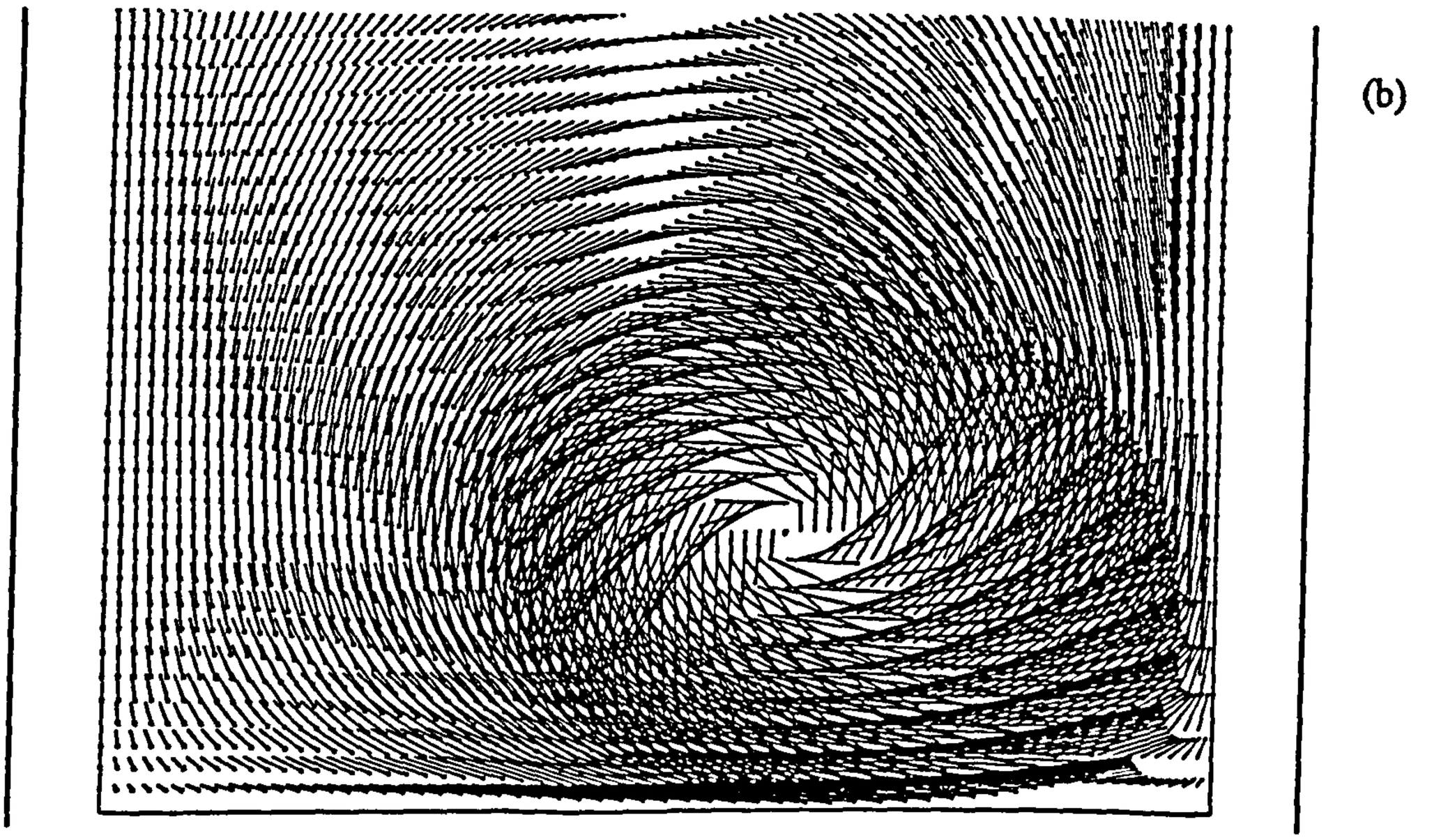

Figure 5.5: Velocity vector plots of (a) co- and (b) counter-rotating vortices produced by the VVG of model D2 at the downstream location $X2 = 7.7\delta_0$

Figure 5.6: Peak vorticity paths for vane and airjet VGs

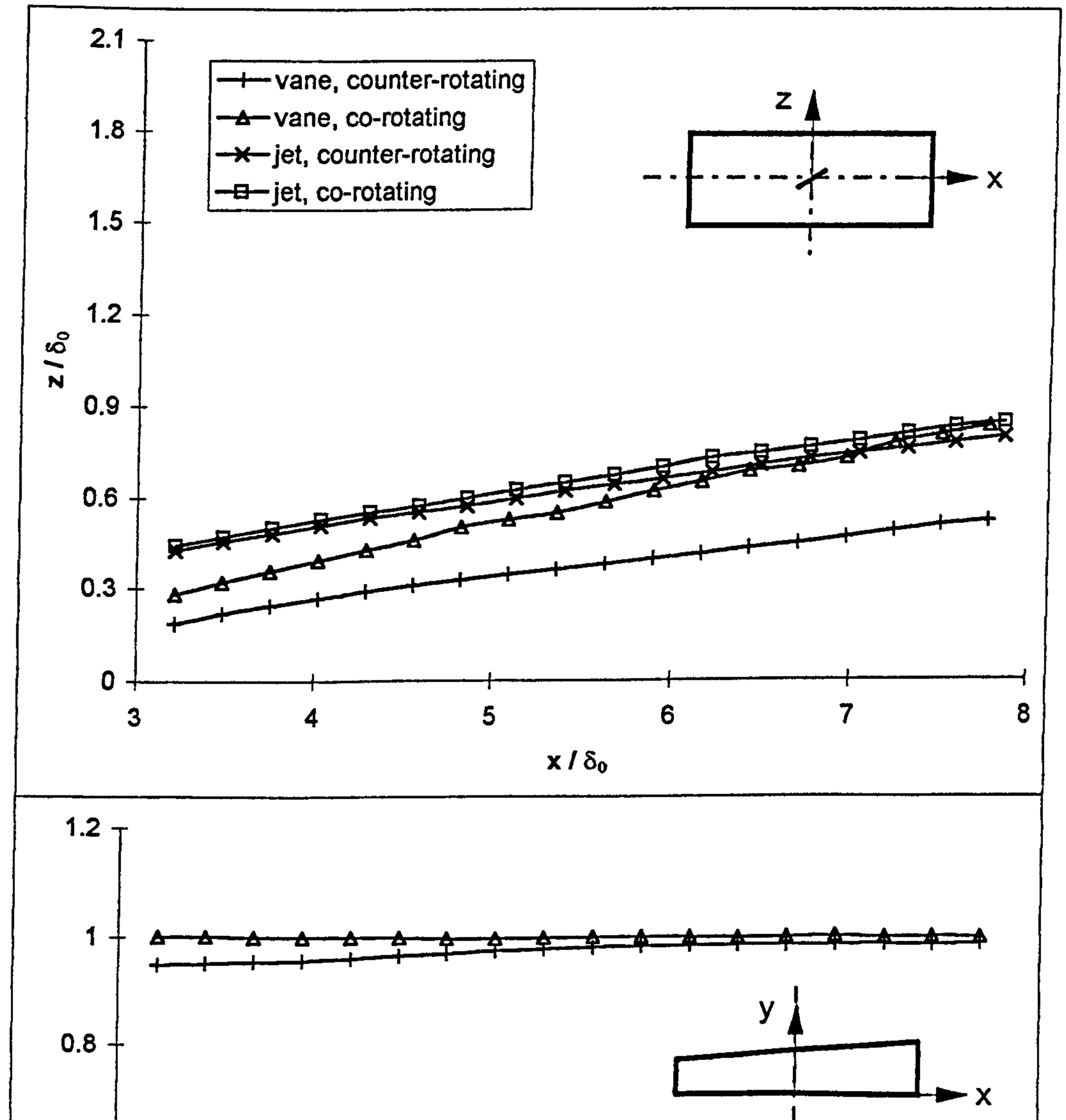

Figure 5.7: Cross-stream vorticity distributions for vane and airjet VGs at two downstream locations, X1 and X2

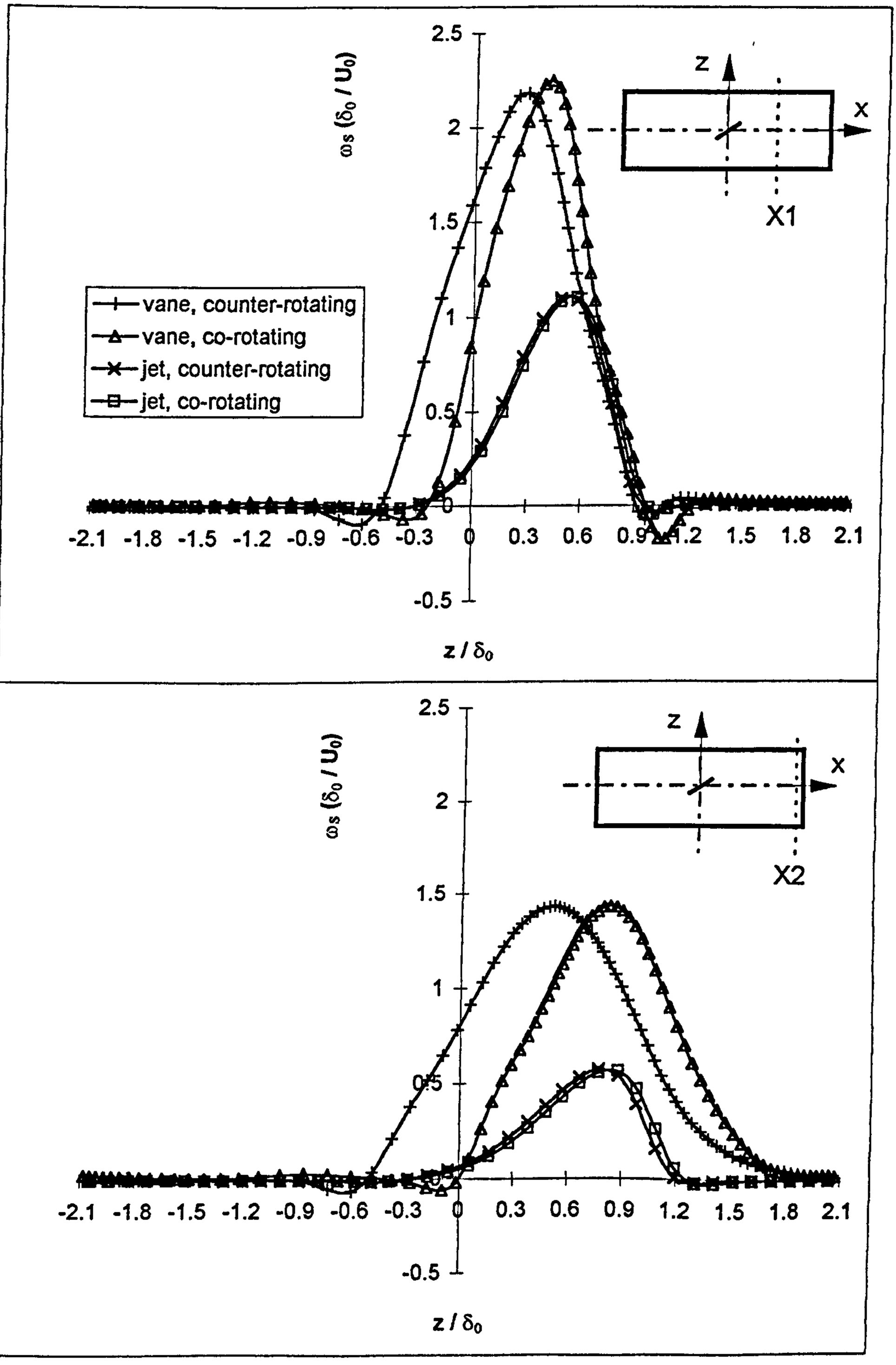

Figure 5.8: Vorticity profiles through vortex cores for vane and airjet VGs at two downstream locations, X1 and X2

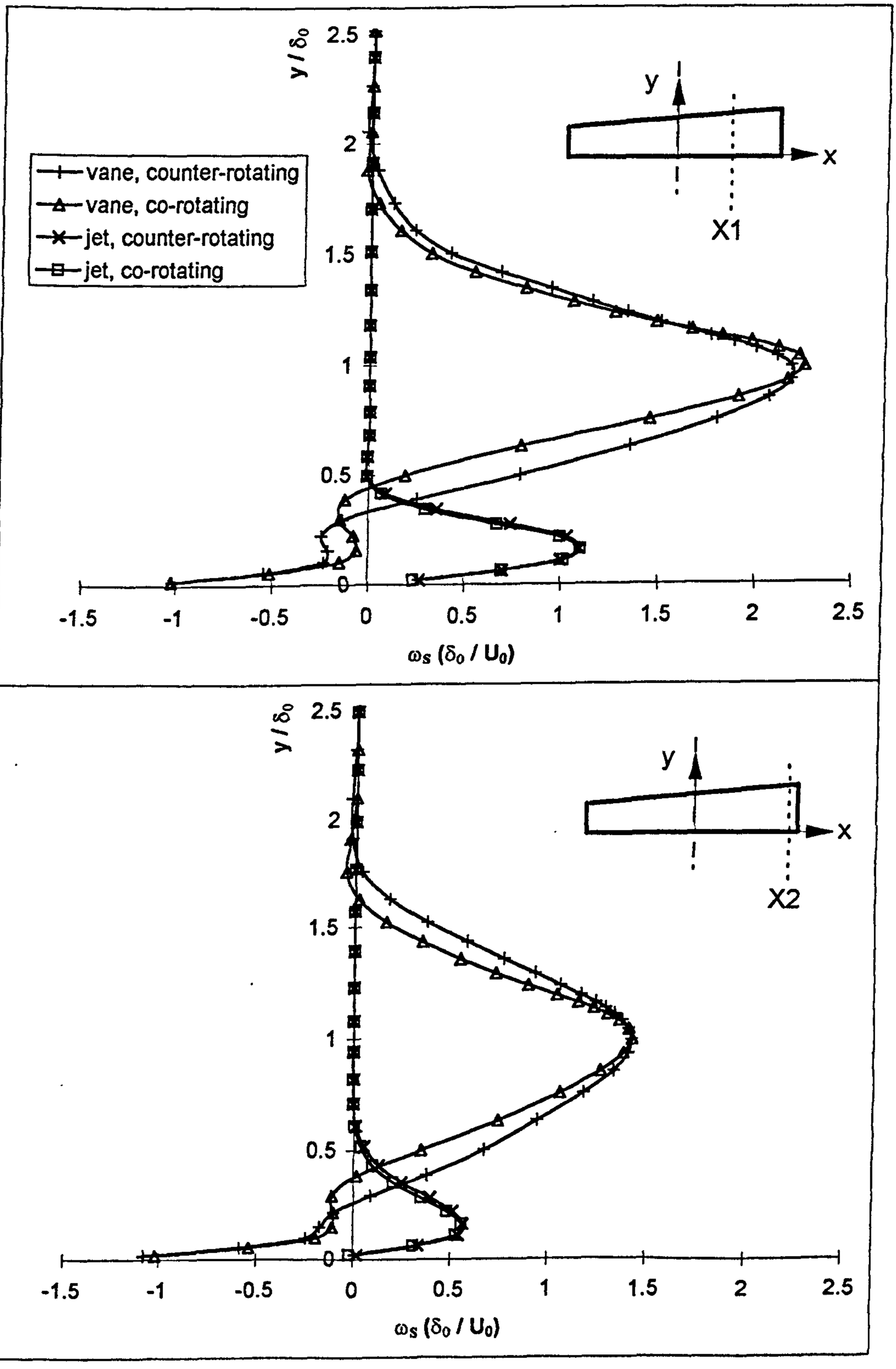

Figure 5.9: Cross-stream shear stress distributions for vane and airjet VGs at two downstream locations, X1 and X2

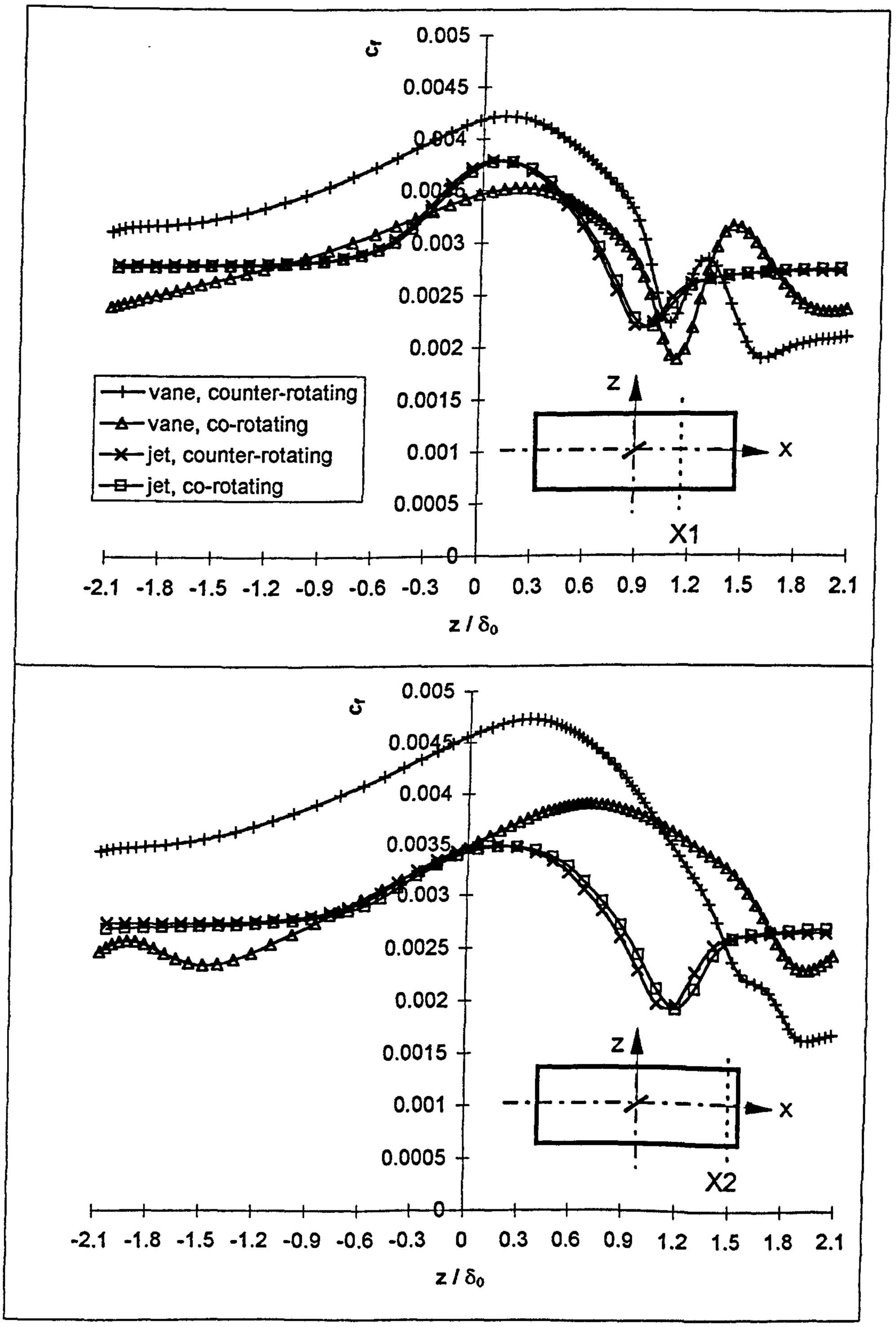

Figure 5.10: Streamwise velocity profiles through the vortex cores for vane and airjet VGs at two downstream locations, X1 and X2

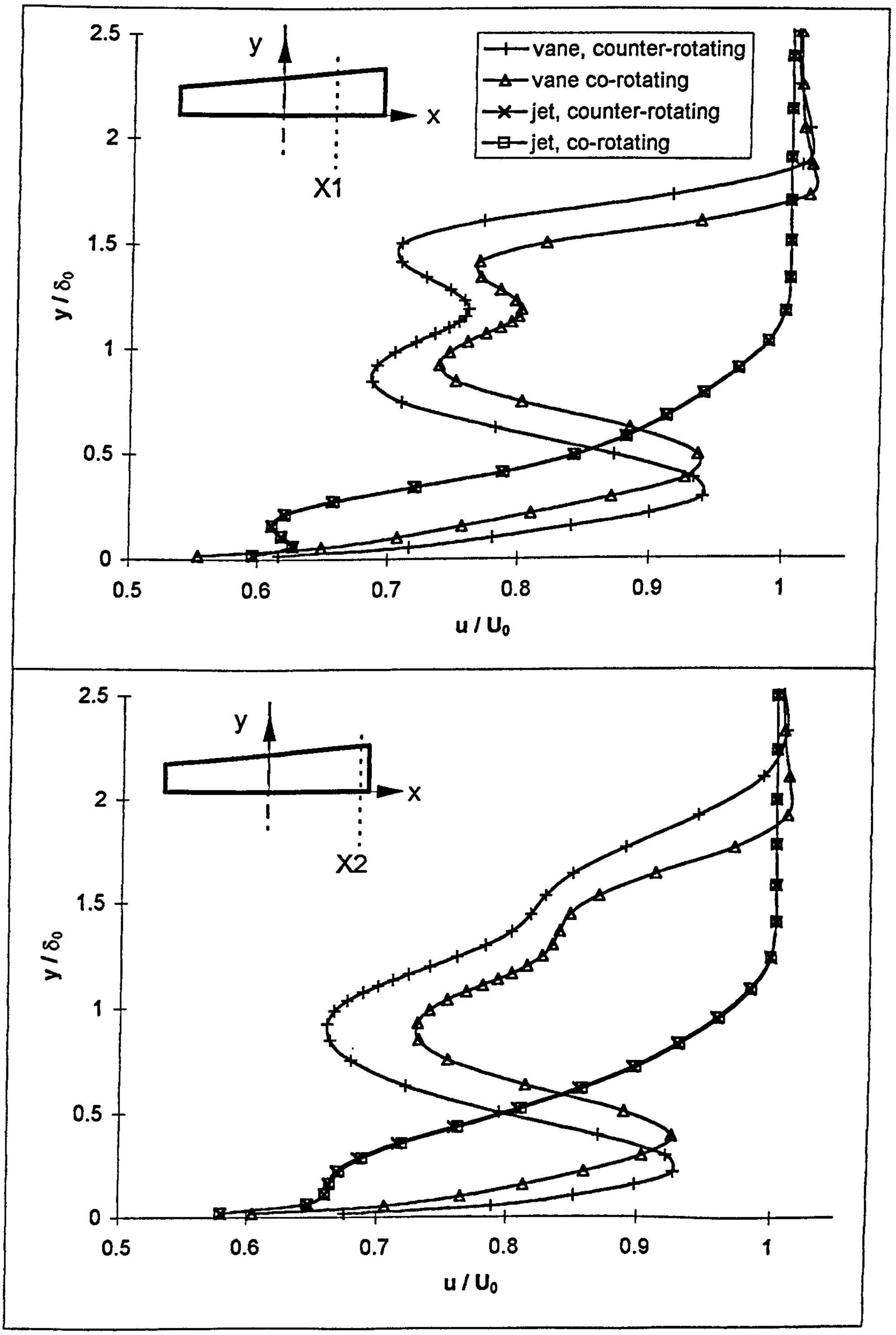

Figure 5.11: Vertical cross-stream velocity for vane and airjet VGs at two downstream locations, X1 and X2

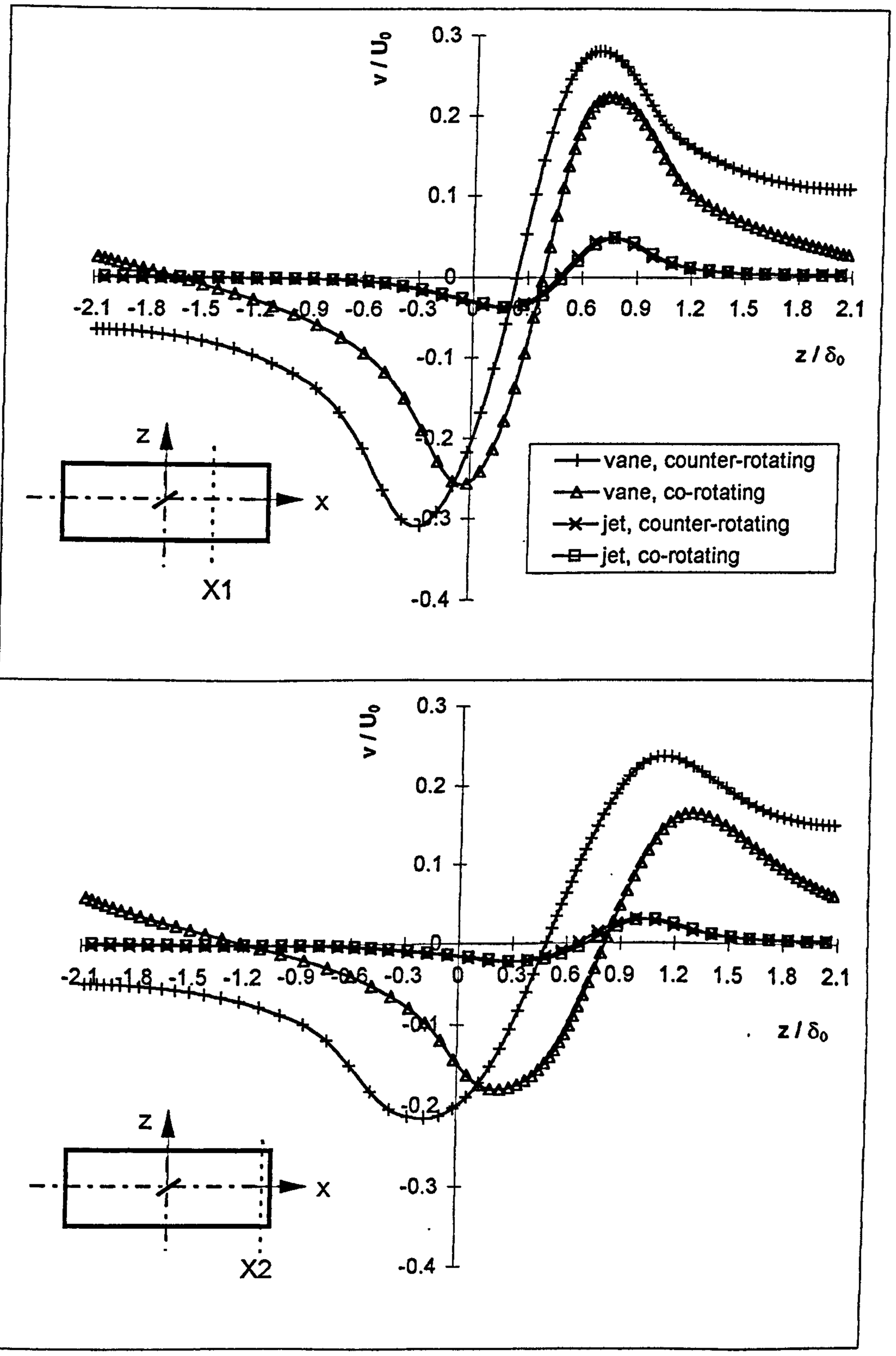

Figure 5.12: Horizontal cross-stream velocity for vane and airjet VGs at two downstream locations, X1 and X2

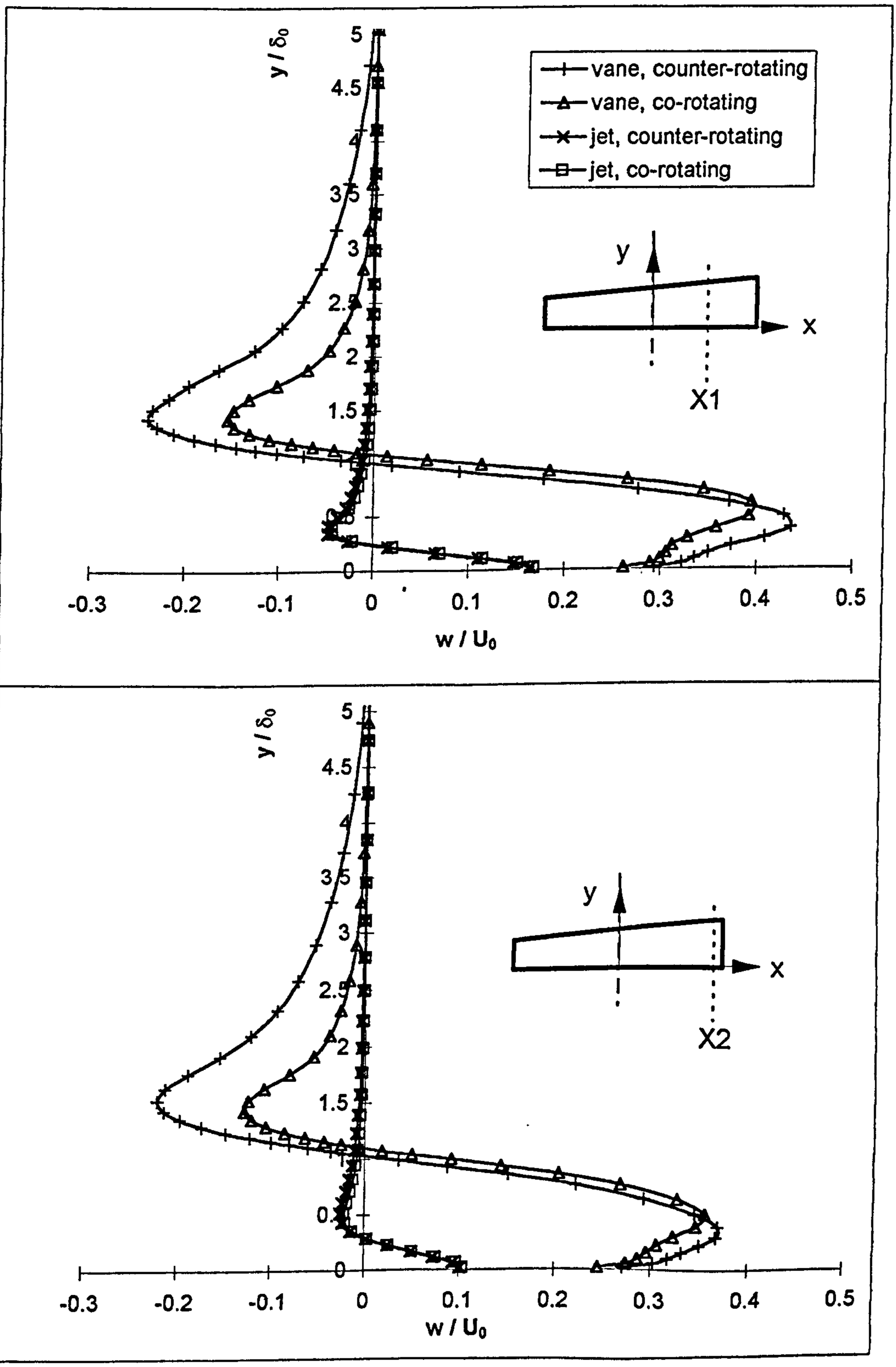

5.3 Summary

In Chapter 5 two local numerical models, D1 and D2 described the vortical flow structure in the vicinity of a VG array. The location of the VG array is approximately two inlet diameters downstream in a S-bend intake duct (see Figure 3.16). The two models comprise an incompressible, turbulent, boundary layer over a flat plate.

In the first model (No: D1-airjet, see Table 3.2) an airjet issued into the solution domain whereas in the second model (No: D2-vane, see Table 3.2) a vane was employed as a VG. Section 3.7 provides all the details and boundary conditions for the two models which are based on experiments by Gibb & Anderson (1995). The numerical grid for the airjet model was generated by the fortran code 'JETGRID' which was described in Section 3.8. A second grid generation code 'VANEGRID', also written in Fortran 77, generated a one-block structured three dimensional grid for the Vane VG model (see Section 3.8). The results of the two numerical VG models were discussed and compared in section 5.2 at two downstream locations (see Figure 5.1). A grid dependence study was examined for both models by using the shear stress distribution as a criterion to judge independence.

The second-order Upwind (HUW) discretisation scheme was used for the predictions based on previous tests (see Section 4.2.2). Circulation and peak vorticity decay, peak vorticity paths in cross- and streamwise directions, cross-stream vorticity profiles, shear stress distributions, streamwise and cross-stream velocity profiles (see Figures 5.5 to 5.12) were used to analyse the longitudinal vortices produces by the two VGs. Counter- and co-rotating vortices were predicted with both models.

- In the case of the AJVG no significant differences in results produced by either counter- or co-rotating vortices could be observed. This was because these vortices were relatively weak and spaced too far apart; consequently hardly any interaction between the counter- or co-rotating partner took place.
- In the case of the VVG, significant differences between counter and co-rotating vortices were observed. The magnitude and the close spacing of the longitudinal vortices produced by the vane provided strong interaction between the co-rotating vortices. Thus the difference in magnitudes of circulation (see Figure 5.3) between the co-rotating and counter-rotating vane vortices increased from 36% initially to 47% at the domain exit. Similar differences between the strengths of the velocity components

(see Figures 5.10 to 5.12) can be seen in terms of counter- and co-rotating vane vortices. As would be expected, the co-rotating vane vortices travelled further than the counter-rotating vortices in the cross-stream direction. The increase of skin friction above free stream conditions (see Figure 5.9) produced by the VVG was approximately 20% higher for the case of counter-rotating vortices compared to co-rotating vortices. The shear stress distributions also shows clearly that the vane vortices were still in a state of development at the first downstream location. This was indicated by an increase of shear stress further downstream at the second downstream location. Negative or secondary vorticity (see Figures 5.7 and 5.8) was observed in the case of the VVG but this disappeared downstream.

- All results, except circulation and shear stress, provided by the AJVG were approximately 50% less than those produced by the vane. The skin friction enhancement provided by the co- and counter-rotating AJVG vortices at the first downstream location was slightly higher than that produced by the co-rotating VVG vortices.
- The core positions (see Figure 5.12) of the vortices produced by the VVG were approximately equal to the undisturbed boundary layer height whereas the core positions of the vortices produced by the AJVG were at approximately a quarter of the undisturbed boundary layer height.
- The amount of circulation provided by both AJVG configurations was six times lower than that produced by the counter-rotating VVG vortices and four times lower than that of the co-rotating values.

6 Duct-Sector Model

6.1 Introduction

The numerical results of eight different pitch and skew angle configurations will be discussed and compared at one downstream location, i.e. X1 = $0.25L$ ($4.2\delta_0$) (see Figure 6.1).

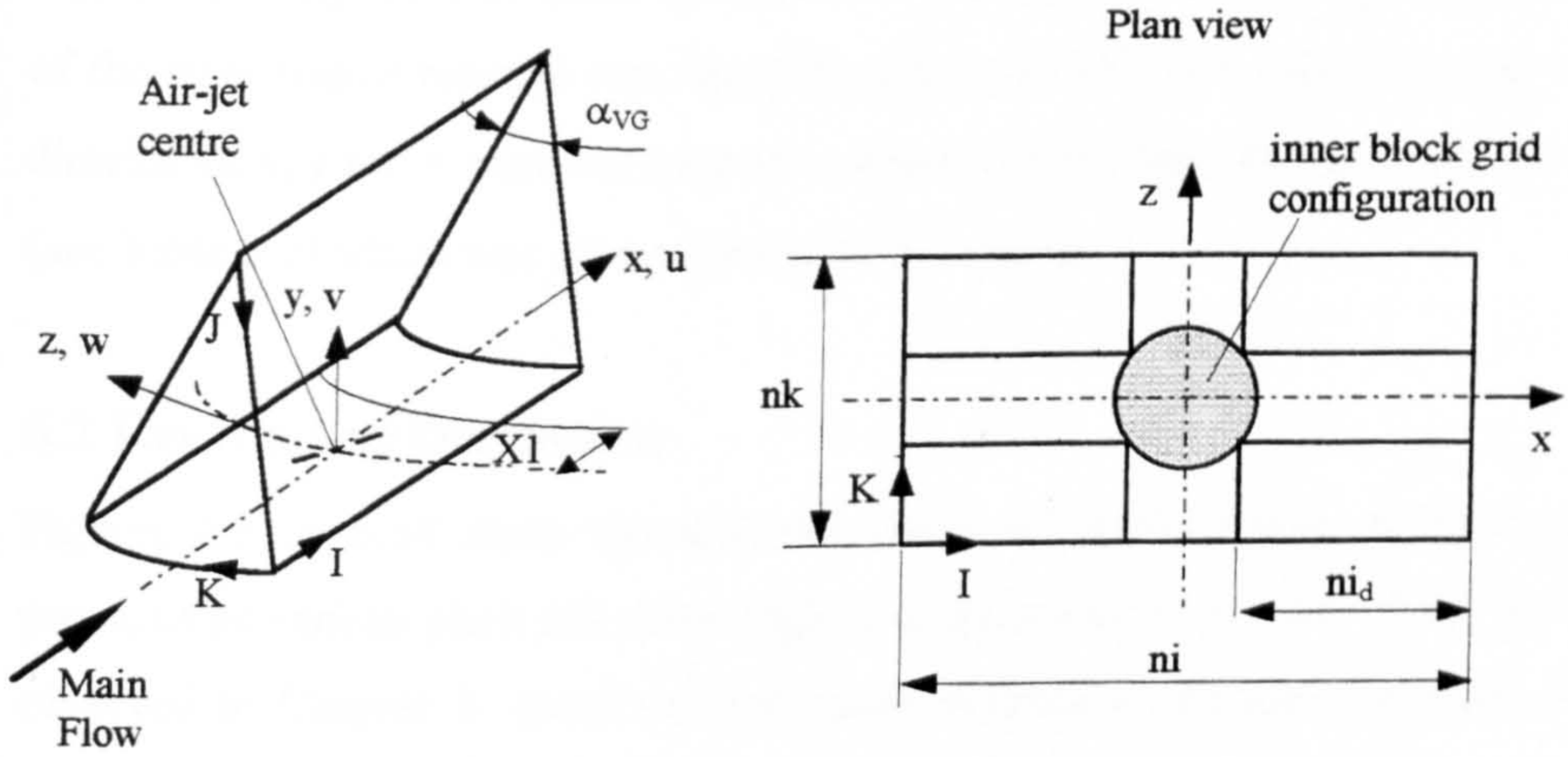

Figure 6.1: Local airjet sector model D3 with the downstream station and I, J, K notation

A grid dependence test was conducted for the numerical sector model. The shear stress distribution at the downstream location X1 was used to judge grid independence. The local airjet sector model was discretised with a thirteen block structured three dimensional grid with polar coordinates. The computational hardware capacity restricted the test to the current grid with a cell distribution of the outer grid blocks of (ni = 57 (ni_d = 30), nj = 52, nk = 31). The total number of grid cells including the inner grid blocks (see grey shaded area in Figure 6.1) is 119964. Further refinement by keeping the aspect ratio of the grid cells constant generated a grid size which was not possible to compute to convergence. However, it was found in the grid dependence study of the flat plate model (see Chapter 5) that only minor shear stress enhancement was achieved by refinement of the cross-stream cell distribution from nk = 31 (sector model D3) to nk = 40 (flat plate model D1) nodes. The streamwise cell distribution of the downstream grid blocks of ni_d = 30 nodes was equal to the flat plate

model in Chapter 5. The cell distribution in domain height of nj = 52 was necessary to achieve a similar cell aspect ratio for the sector model than for the flat plate. The solution domain height which is equal to the radius of the S-bend duct was the main cause of the computational limit being exceeded. All predictions in this Section were calculated using a second-order Upwind (HUW) differencing scheme (see Section 4.2.2). Convergence was achieved after 2500 iterations. The average reduction factor of the mass source residual was approximately 1.1×10^{5}. The coordinates in the three dimensions x, y and z were nondimensionalised with the inlet boundary layer thickness (see Table 3.2) which was determined to be $\delta_0 \approx 4$mm.

6.2 Results and Discussion

Figures 6.2 to 6.14 show the different levels of enhancement of the flow field provided by various pitch and skew angle configurations of the airjet VG (AJVG). As observed in Chapter 5, there are only small differences between counter- and co-rotating vortices produced by the jet. The reason for the negligible difference between the co -and counter-rotating vortices is because of the individual size of the vortices compared to the solution domain width. Therefore each vortex produced by the jet behaved independently without any major interaction with its co- or counter rotating neighbour. The first cross-plane examined was defined to be $x/\delta_0 \approx 0.94$ which is much closer to the VG centre than it was in Chapter 5 ($x/\delta_0 \approx 3.2$). The vortices introduced by the jet were already fully developed at this downstream location.

The highest level of circulation (see Figure 6.2) downstream of the VG was achieved with a pitch angle of 30° and a skew angle of 75°, followed by a configuration of 30° pitch and 60° skew angle. The pitch/skew angle configurations of 45°/75°, 45°/60° and 30°/45° provided the third, fourth and fifth highest initial circulation but all three decayed approximately to one value at the end of the solution domain. The pitch/skew angle configurations of 45°/45°, 30°/30° and 45°/30° provided the lowest flow field enhancement. By changing the pitch and skew angle configuration from 45°/30° to 30°/75° the initial level of circulation can be increased by a factor of approximately 2.75. Even the final level of circulation at the end of the solution domain is increased by a factor of approximately 2.2. Inspection of the circulation decay profiles reveals that the value of the skew angle is the most important factor to influence the

magnitude of the circulation. The four pitch and skew angle configurations which enhance the flow field most have high skew angles of 75° and 60°. The level of circulation is further decreasing with skew angles of 45° and finally 30°. It seems also to be important to issue the air into the flow field with a pitch angle of 30° rather than 45° to achieve a higher level of circulation.

The sequence of pitch and skew angle configurations in terms of the level of peak vorticity strength (see Figure 6.3) is the same as observed for the circulation in Figure 6.2. Although the distinction between the various angle configurations is not as clear as it was in terms of circulation. However, the pitch and skew angle configurations with the highest and lowest level of peak vorticity, of 30°/75° and 45°/30° can be clearly differentiated. The factor between the maxima of peak vorticity strengths is approximately 1.3 compared to 2.75 for the circulation. The decay of the peak vorticity describes approximately an exponential function and all configurations reached a similar level of peak vorticity strength at the solution domain exit. Comparing the peak vorticity decays for the flat plate model (see Figure 5.3) of the case of 45°/45° with the sector model in this Section, a significant difference of initial peak vorticity magnitudes and profiles can be seen. This difference is caused by the fact that the first downstream cross-plane is at $x/\delta_0 \approx 0.94$ for the sector model and $x/\delta_0 \approx 3.2$ for the flat plate model. Thus the vortices further downstream were already more decayed.

The locus of peak vorticity can be seen in Figure 6.4 as a planview onto the solid surface of the sector. The two groups of angle configurations, (1) 30°/75° and 30°/60° and (2) 30°/30° and 45°/30° described the longest and the shortest way of travelling from the centre line of the solution domain towards the domain boundary. These two groups produced the highest and lowest levels of circulation and peak vorticity as mentioned above. Three configurations, i.e. 45°/60°, 30°/45° and 45°/75°, described similar paths. The angle configurations of 45°/75° and 30°/60° coincided at the first downstream location.

A side view of the locus of peak vorticity is given in Figure 6.5. The peak vorticity paths of the longitudinal vortices are displayed in the streamwise direction against the solution domain height. The two angle configurations of 30°/75° and 30°/60° which provided the highest level of circulation, shown in Figure 6.2, describe the most

monotonic ascending peak vorticity paths. Their peak vorticity paths rose by approximately 66% from their initial position in the streamwise direction until a downstream location of $x/\delta_0 \approx 5.5$ is reached. The peak vorticities of the angle configurations of 30°/75° and 30°/60° travelled further downstream on approximately horizontal paths. Except for the case of 45°/30°, all configurations produced peak vorticity paths which rose by approximately 20 to 40% from their initial positions to a downstream location of $x/\delta_0 \approx 3$ and continued travelling slightly towards the solid surface. The 45°/30° case initiated peak vorticity paths which rose rapidly about approximately 30% from the initial position over the first quarter of the solution domain length and continued travelling back towards the solid surface to a final position of approximately 14% further away from the solid surface than the initial position. It has to be emphasised that all peak vorticity paths against the solution domain height described very small changes in vortex height. Comparing the scales of the streamwise axis with the domain height axis it can be seen that the peak value of the y-axis is only 2.5% of the total downstream length of the solution domain; i.e., the y-axis is greatly magnified.

The cross-stream vorticity distribution is shown in Figure 6.6. Assuming the area underneath the vorticity profiles are equal to the magnitudes of vorticity distribution, the two configurations, 30°/75° and 30°/60° provided the highest level of voritcity. These results conform with those of Figure 6.2 where the highest level of circulation were achieved with the angle configurations of 30°/75° and 30°/60°. Small amounts of negative or secondary vorticity can be observed for all predictions.

In Figure 6.7 the vorticity profiles through the vortices cores are displayed against the solution domain height. Negative or secondary vorticity can be observed only for the case of 45°/30°. The different heights of the peak vorticities of various pitch and skew angle configurations can be seen. Figure 6.7 shows clearly that for all cases the secondary motion took place in the first half of the boundary layer thickness.

The cross-stream shear stress distribution is shown in Figure 6.8. The data shows that the two angle configurations of 30°/75° and 30°/60° provided the highest level of skin friction. The lowest magnitude of shear stress was initiated by the vortices of a pitch and skew angle configuration of 45° and 30°. The co-rotating vortices provided slightly different shear distribution than the contra-rotating vortices. The small

difference is only visible for the cases of 30°/75° and 30°/60° because these vortices travelled in closer proximity to the domain boundary, and hence interacted with each other, than did vortices in the other configuration.

The streamwise velocity profiles through the vortices cores are shown in Figure 6.9. The velocity deficits are coincident with the positions of the vortices cores in the vertical distance from the solid surface. It can be observed that the velocity gradients from the solid surface to the inflection points of the profiles are depending very much on the magnitudes of the skew angles. All angle configurations with high skew; i.e., 60° and 75°, have very steep and short gradients between the first and the second data point above the solid surface. The velocity profiles with high skew angles also had lower magnitudes. The case of 45°/75° described the velocity profile with the lowest magnitude and the 30°/30° configuration produced the highest velocity magnitude with the biggest velocity difference between the first and the second data point. In all cases the velocities returned smoothly to free stream conditions with increasing boundary layer height.

The cross-stream velocity profiles of the component v can be seen in Figure 6.10. The difference of counter- and co-rotating vortices is more visible as it was in Figure 6.8 but it is small. The periodicity in the case of the co-rotating vortices can be seen, especially for high skew angles of 60° and 75°. The strongest cross-stream velocities are produced by the angle configurations of 30°/75° and 30°/60° whereas the weakest were initiated by the configurations of 45°/30° and 30°/30°. Figure 6.10 demonstrates the various vortices cores positions in the cross-stream direction. The core positions and velocity magnitudes coincide with the results of the previously discussed figures in this section.

Figure 6.11 shows the cross-stream velocity component w for all angle configurations through the vortices cores. The sequence of velocity magnitudes conforms to the results presented in Figure 6.10. The two configurations of 30°/75° and 30°/60° provided the highest magnitudes and the lowest magnitudes were produced by the angle configurations of 45°/30° and 30°/30° .The counter-rotating vortices were slightly stronger above their cores whereas the co-rotating vortices produced slightly higher velocity magnitudes below their cores. All vortices were positioned at approximately the same distance from the solid surface while the counter-rotating

spread slightly more into the main flow above the boundary layer thickness than the co-rotating vortices.

Figures 6.12 and 6.13 show the cross-stream velocity profiles at each side of the solution domain. Comparing the two counter-rotating profiles in Figures 6.12 and 6.13 the difference of velocity magnitudes can be clearly seen. On the downwash boundary (see Figure 6.13) the magnitudes of velocities are about one order less than the values on the upwash side (see Figure 6.12). The vortices travelled to the upwash side. The magnitudes of cross-stream velocities on the upwash side were approximately 10% of the cross-stream velocities in the case of the co-rotating vortices and approximately 1% in the case of the counter-rotating vortices, shown in Figure 6.11, through the vortices cores. As a result, it can be seen that even though the vortices on both domain boundaries (see Figures 6.12 and 6.13) have decayed they still influence the main flow, especially above the boundary layer. The periodicity of the co-rotating vortices was reflected in Figures 6.12 and 6.13 where the velocity profiles are of the same shape.

In Figure 6.14 the peak vorticity paths of the counter- and co-rotating vortices of the pitch and skew angle configuration 30°/75° are compared. This configuration showed the highest level of circulation, peak vorticity and increase of skin friction. As previously mentioned the difference of the boundary conditions played only a minor part. However, the co- and counter-rotating vortices pattern began to diverge at a downstream location of $x/\delta_0 \approx 2$. It must be emphasised that the magnitudes of travel distances in y-direction are negligible compared to those in cross-stream direction. The counter-rotating vortices enhance each other and lift off the surface (see Figure 5.4) whereas the co-rotating vortices inhibit each other. As a result, the co-rotating vortices move towards the solid surface and the cross-stream velocities below the cores (see Figure 6.11) has to increase by continuity. Thus the co-rotating vortices experience a greater translation in the cross-stream direction due to the influence of its neighbours.

Figures 6.15 and 6.16 show velocity vector plots (looking upstream) at the downstream locations, X1 (= $4.2\delta_0$) and X2 (= $7.7\delta_0$). Comparing the strengths and distribution of the vectors of the counter- (see Figure 6.15) and the co-rotating

vortices (see Figure 6.16), it can be seen that the counter-rotating vortices are slightly stronger than the co-rotating.

Both counter- and co-rotating vortices migrate to the side, as potential theory predicts. In both configurations, the vortices decay in the streamwise direction. This effect can be observed in terms of the vortices shapes and the lengths of the velocity vectors. It can be seen that the velocity vectors are decreasing in length (compare velocity vectors at locations X1 and X2 in Figures 6.15 and 6.16). The vortices shapes change from flattened elliptical (at location X1) to an approximately circular form (at location X2).

The results are tabulated in a form which can be used as input data for RNS3D in the form of vortex strengths (peak vorticities) and cross-stream locations for all investigated pitch and skew angle configurations is given in Appendix C.

Figure 6.2: Circulation decay for various pitch/skew angle configurations of the airjet VG

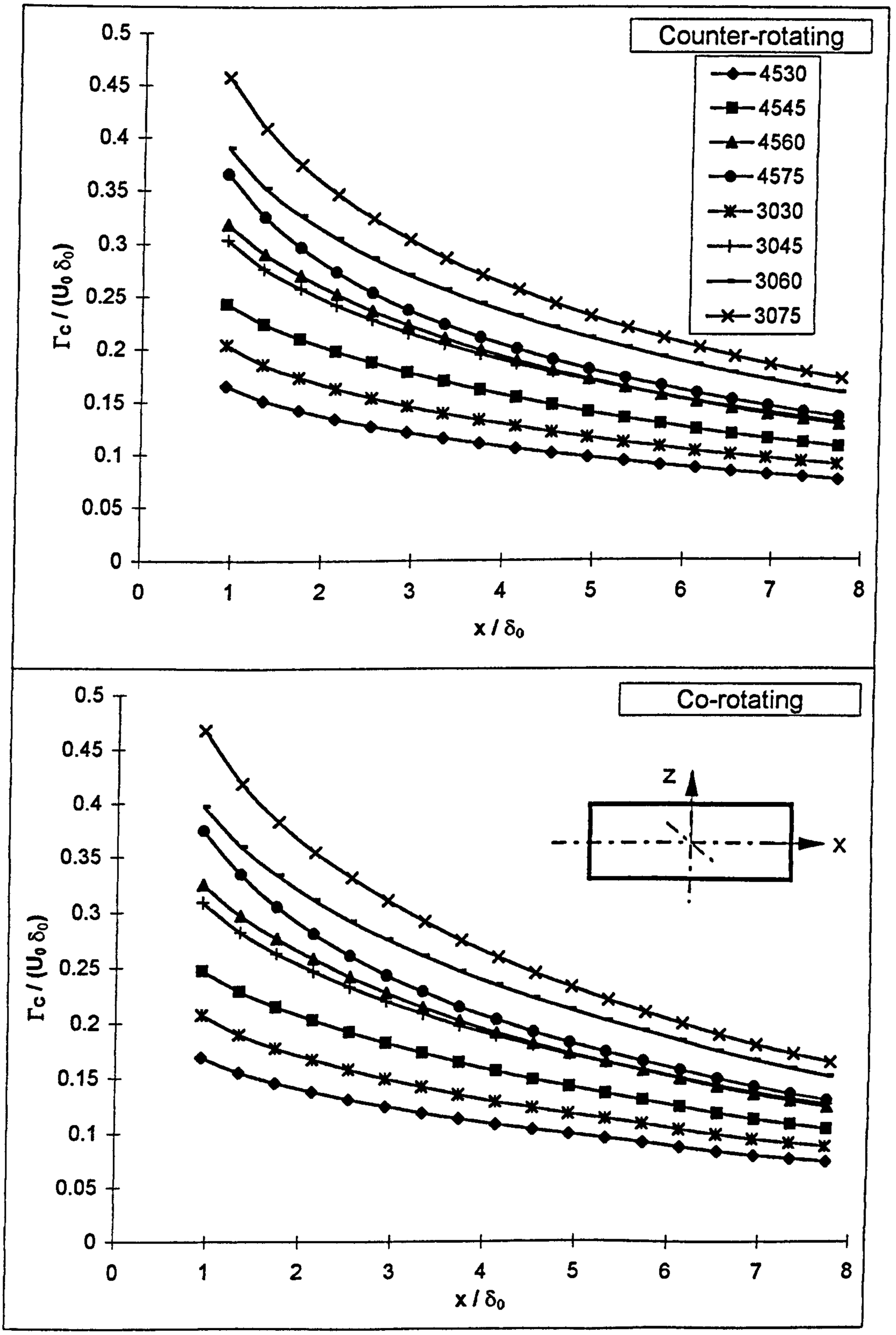

Figure 6.3: Peak Vorticity decay for various pitch/skew angle configurations of the airjet VG

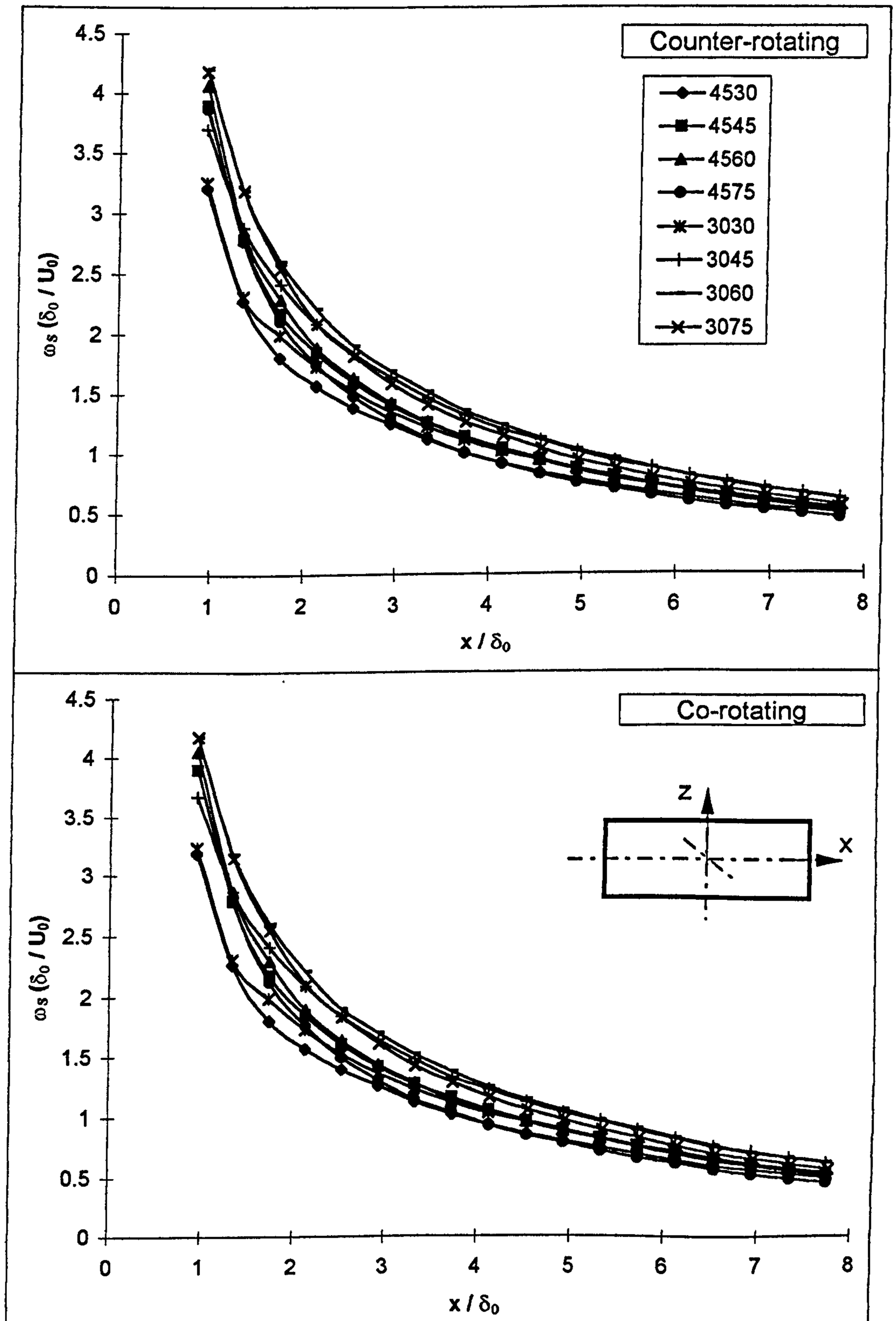

Figure 6.4: Peak Vorticity paths for various pitch/skew angle configurations of the airjet VG

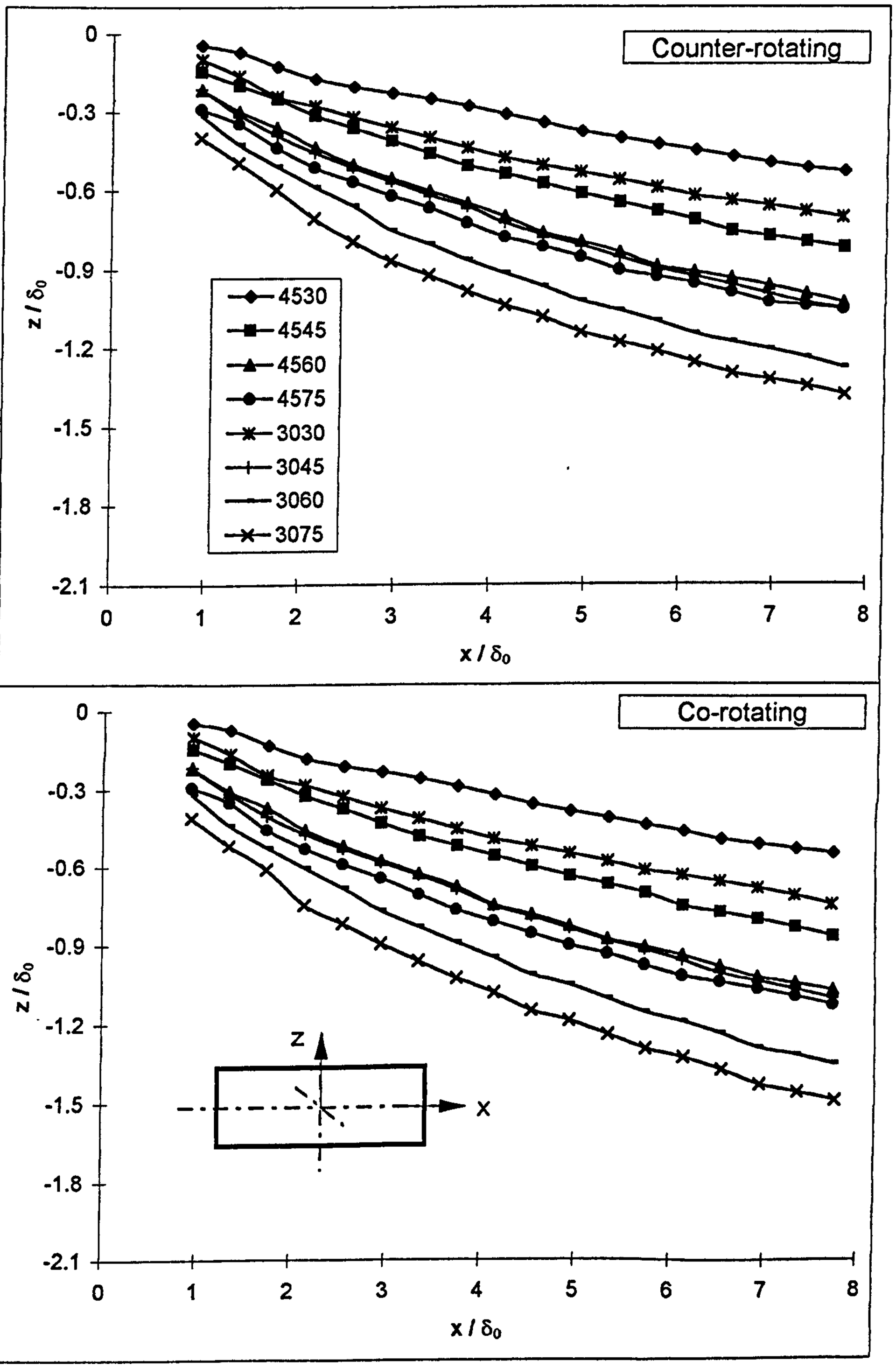

Figure 6.5: Peak Vorticity paths for various pitch/skew angle configurations of the airjet VG

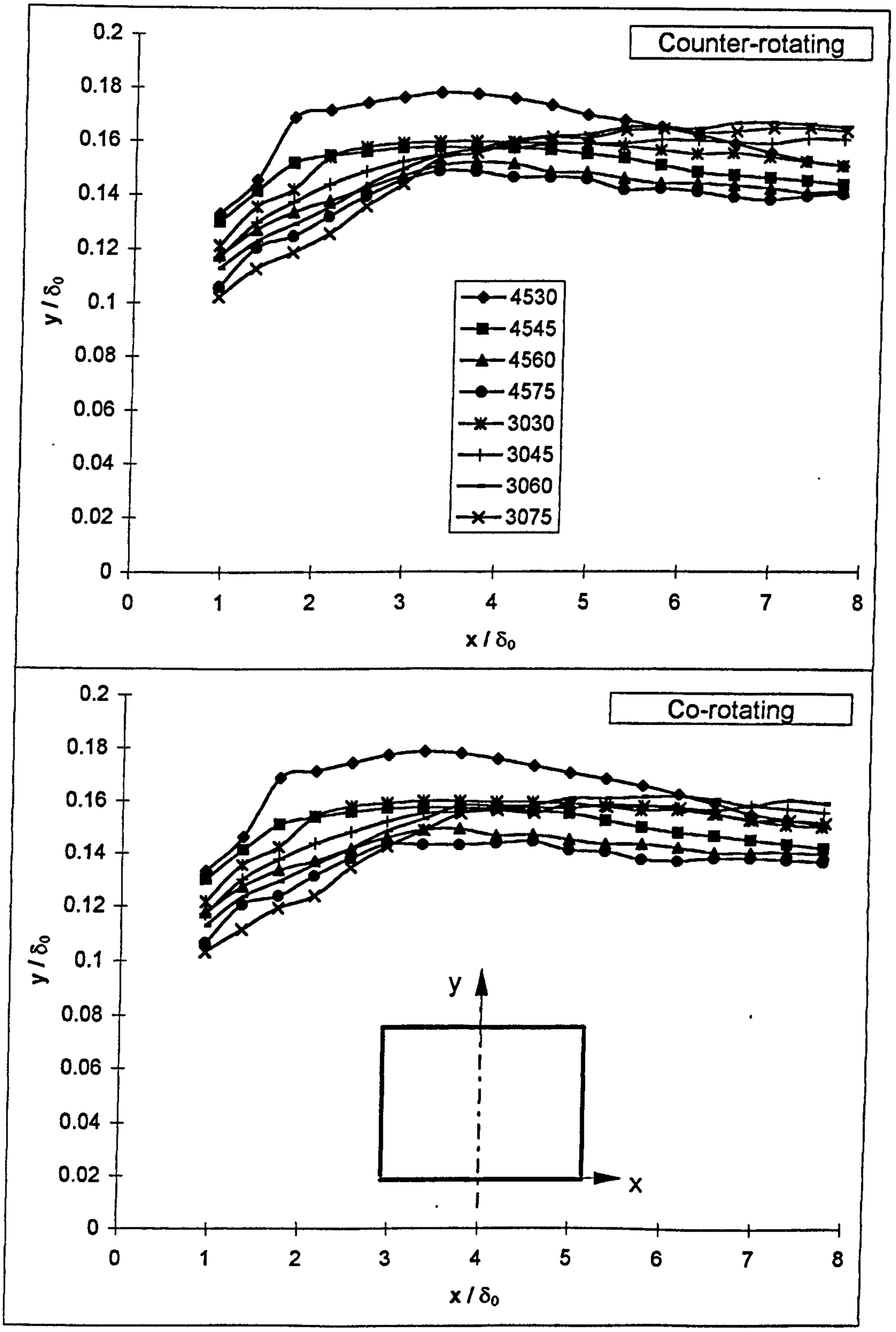

Figure 6.6: Cross-stream vorticity distribution for various pitch/skew angle configurations of the airjet VG at the downstream location X1

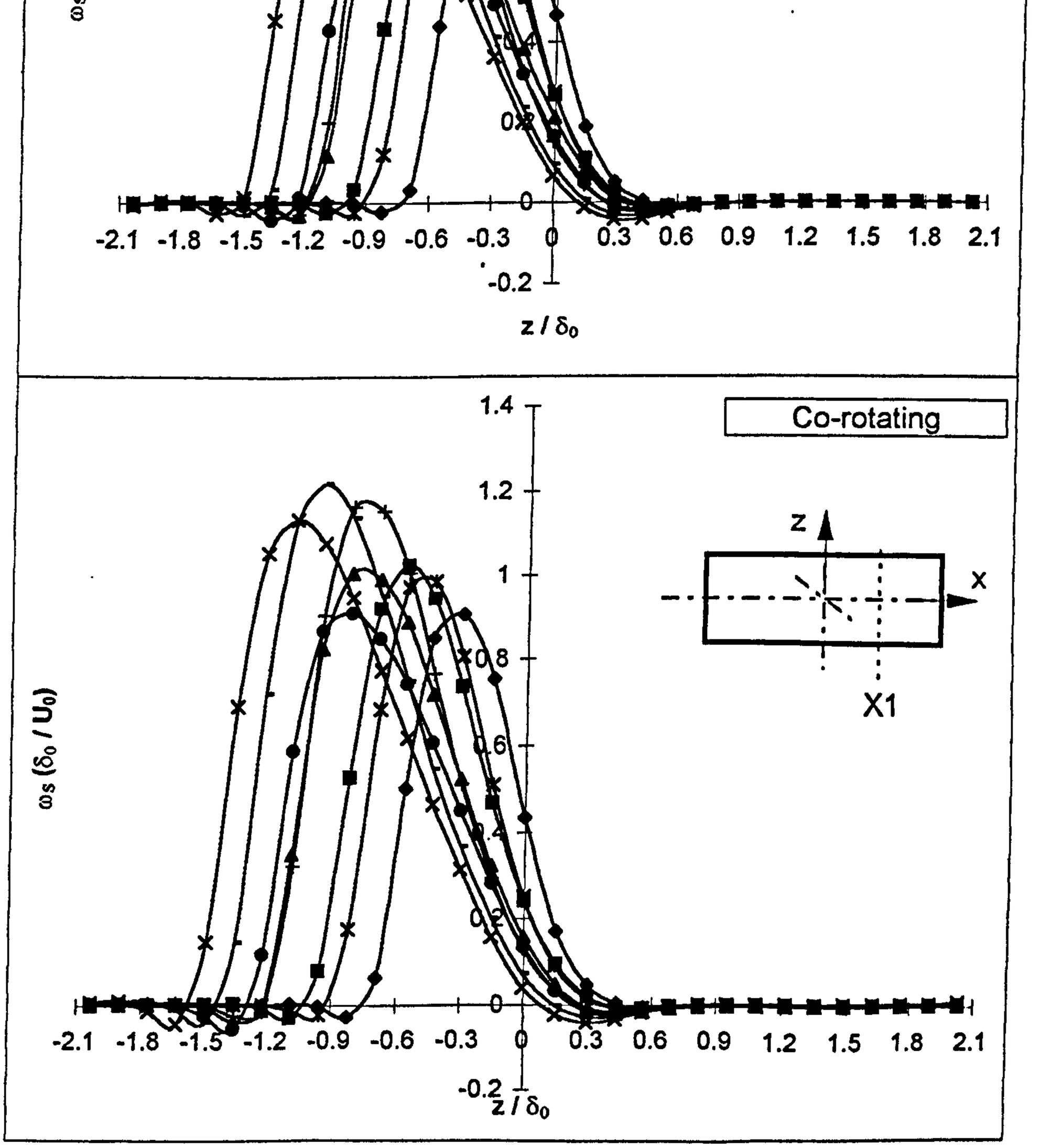

Figure 6.7: Vorticity profiles through vortex cores for various pitch/skew angle configurations of the airjet VG at the downstream location X1

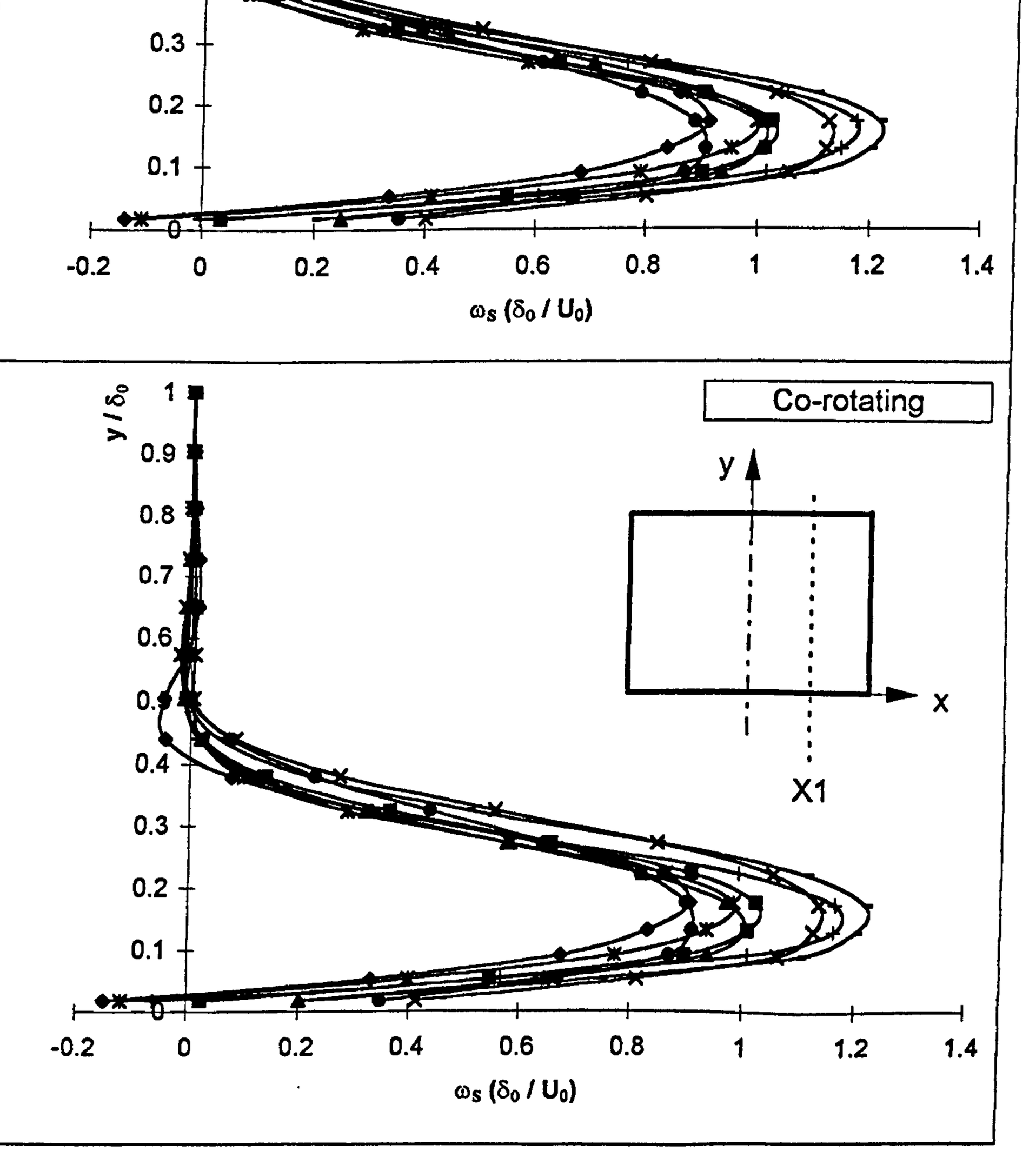

Figure 6.8: Cross-stream shear stress distribution for various pitch/skew angle configurations of the airjet VG at the downstream location X1

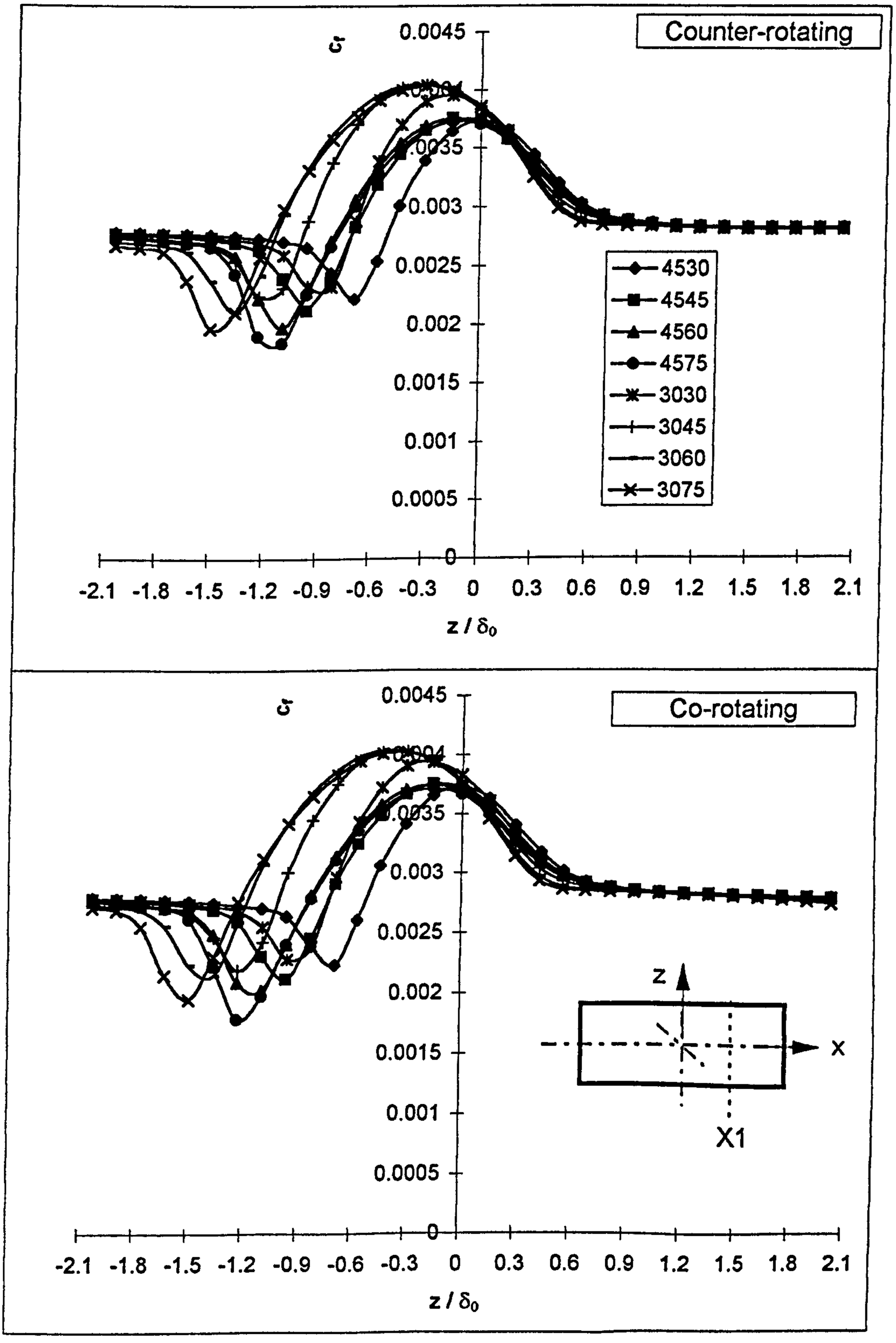

Figure 6.9: Streamwise velocity profiles through the vortex cores for various pitch/skew angle configurations of the airjet VG at the downstream location X1

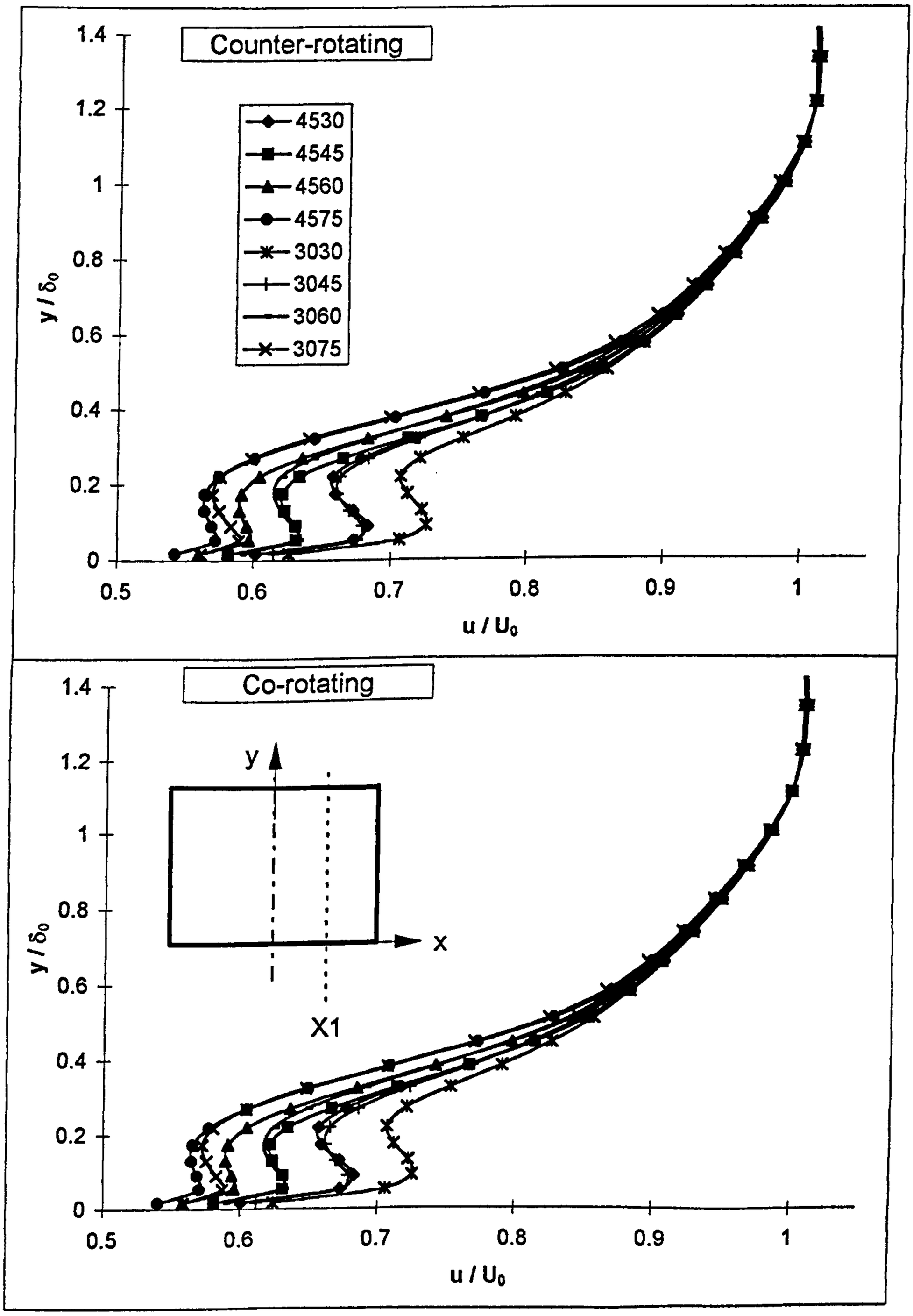

Figure 6.10: Vertical cross-stream velocity for various pitch/skew angle configurations of the airjet VG at the downstream location X1

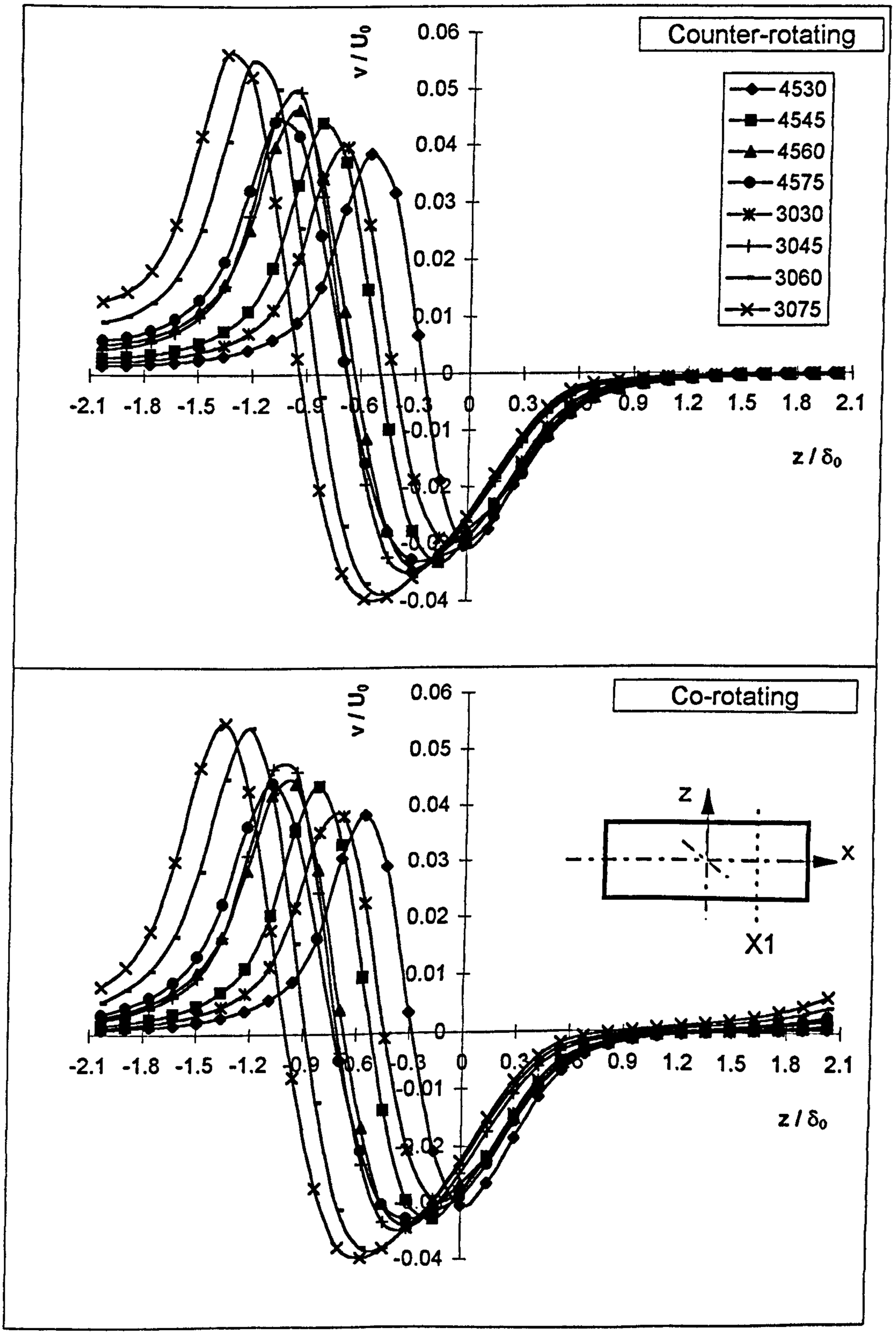

Figure 6.11: Horizontal cross-stream velocity for various pitch/skew angle configurations of the airjet VG at the downstream location X1

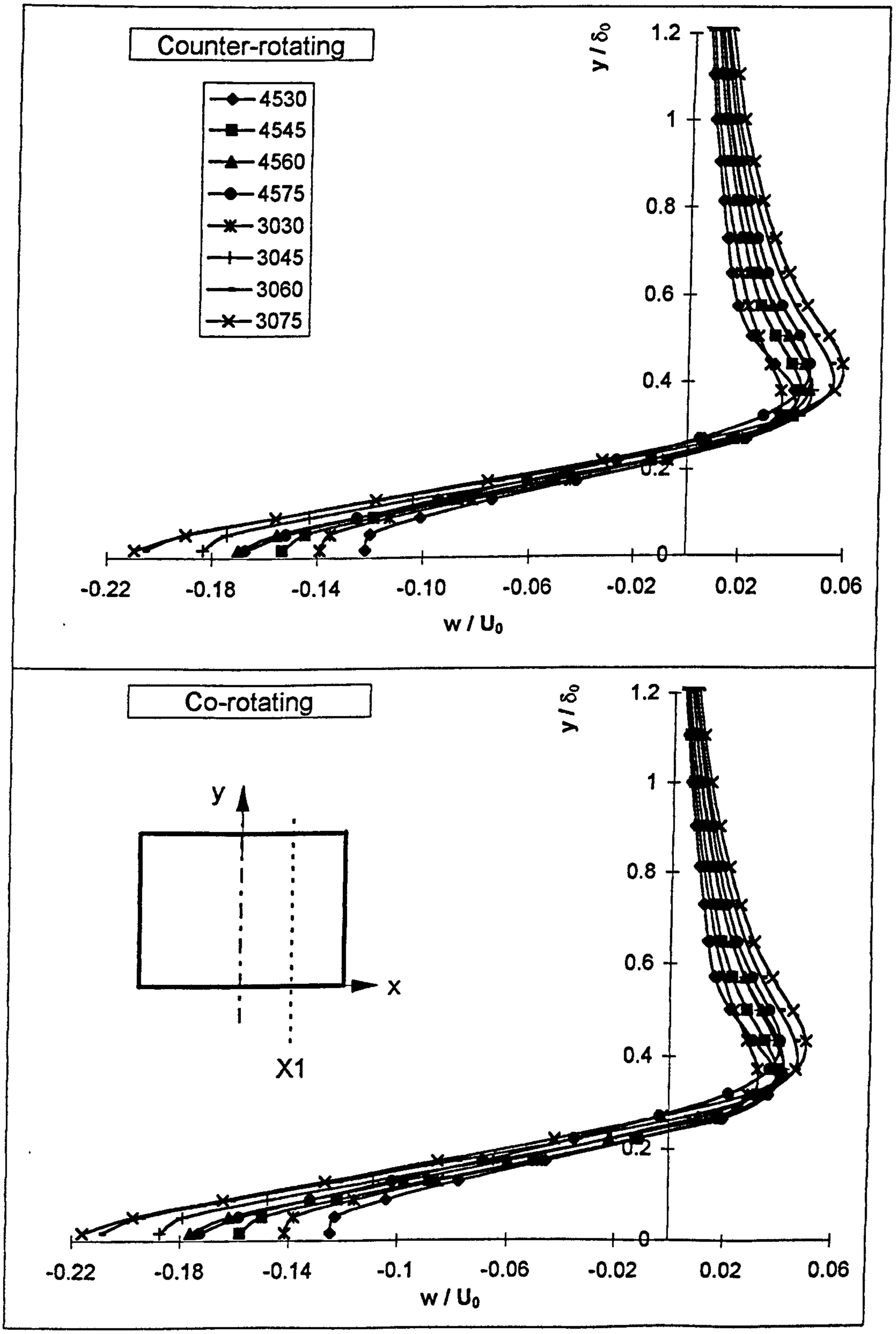

Figure 6.12: Horizontal cross-stream velocity for various pitch/skew angle configurations of the airjet VG on the upwash domain boundary Z_u and at the downstream location X1

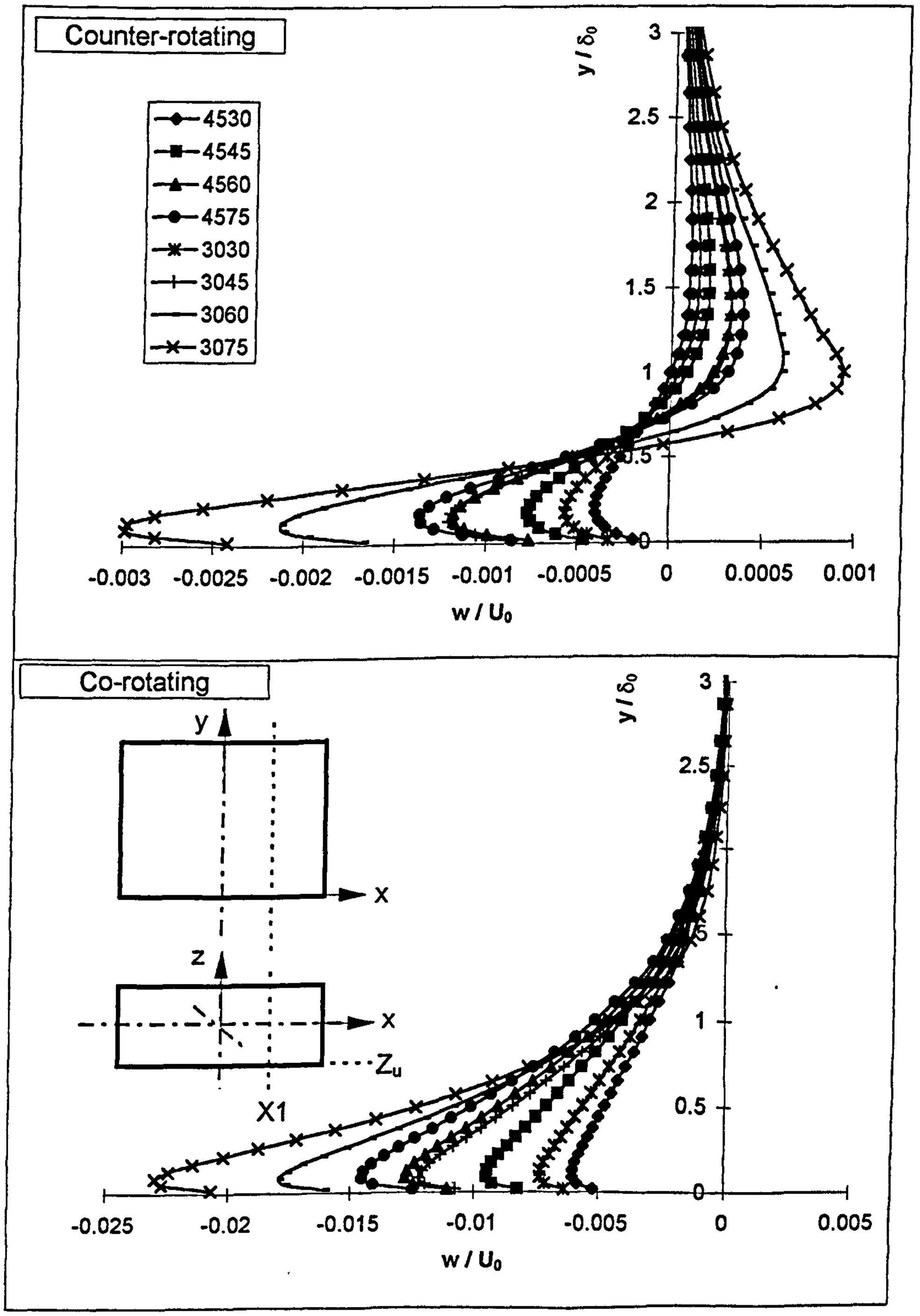

Figure 6.13: Horizontal cross-stream velocity for various pitch/skew angle configurations of the airjet VG on the downwash domain boundary Z_d and at the downstream location X1

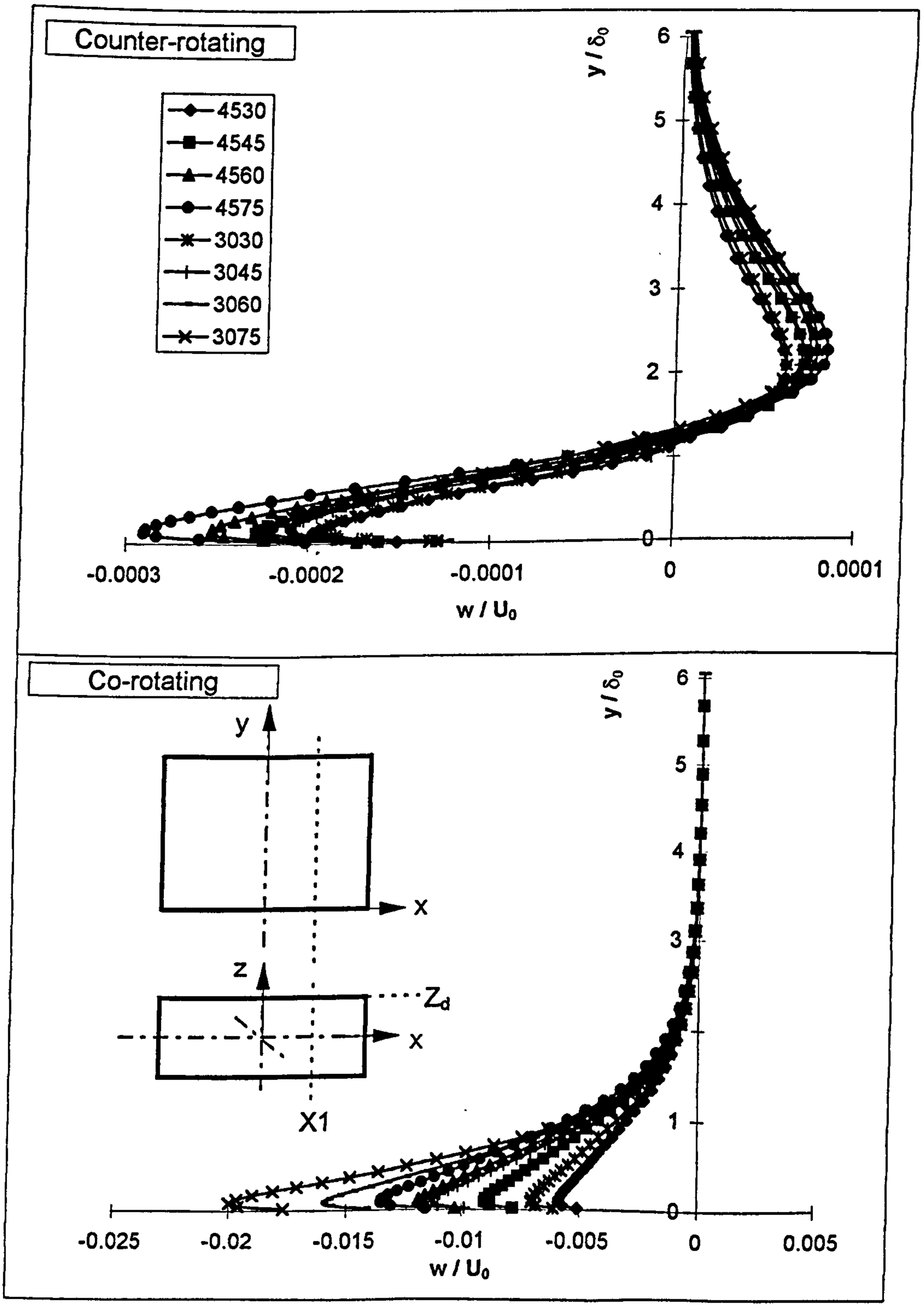

Figure 6.14: Peak Vorticity paths for the airjet VG with 30^0 pitch and 75^0 skew angle

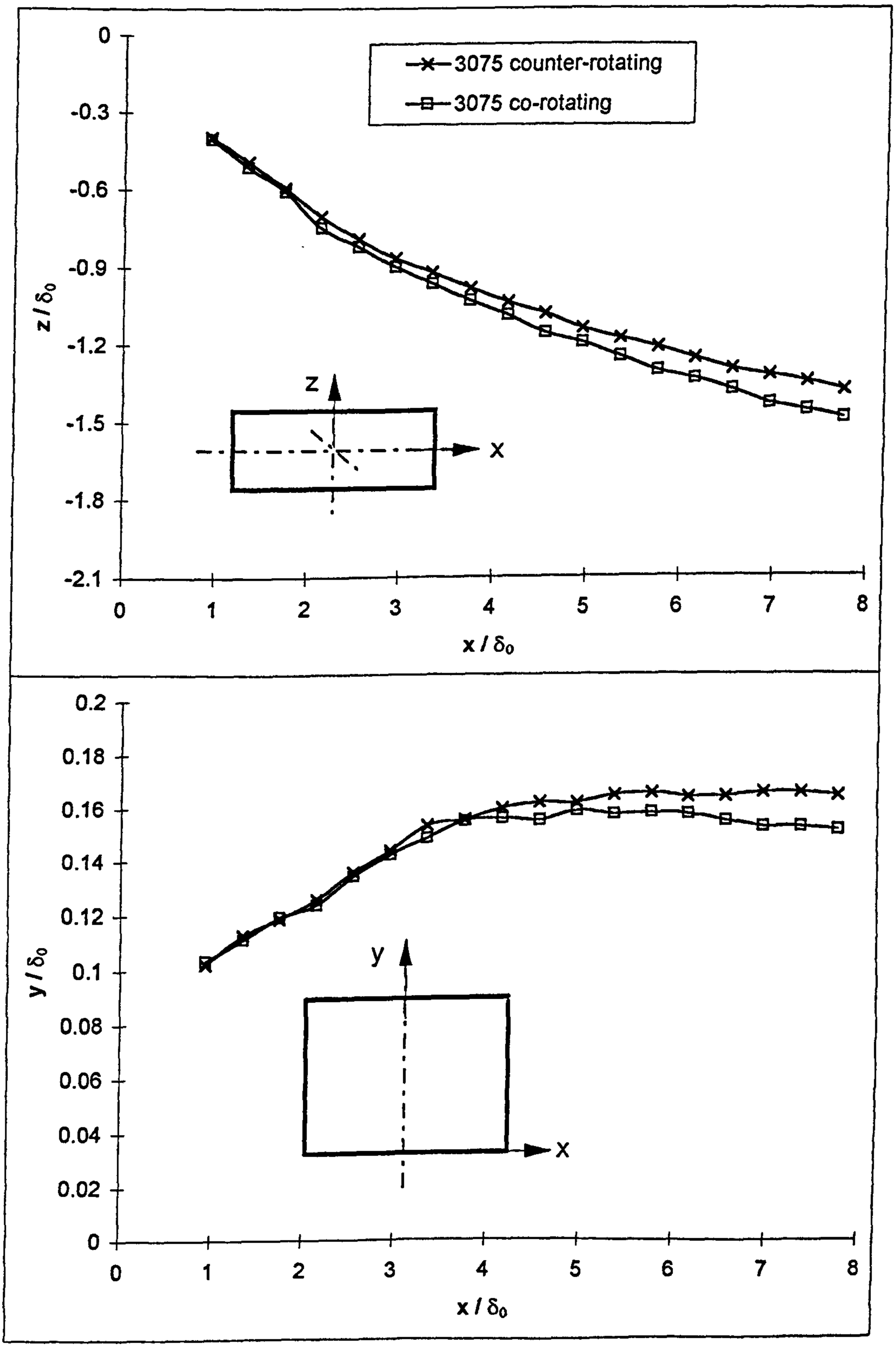

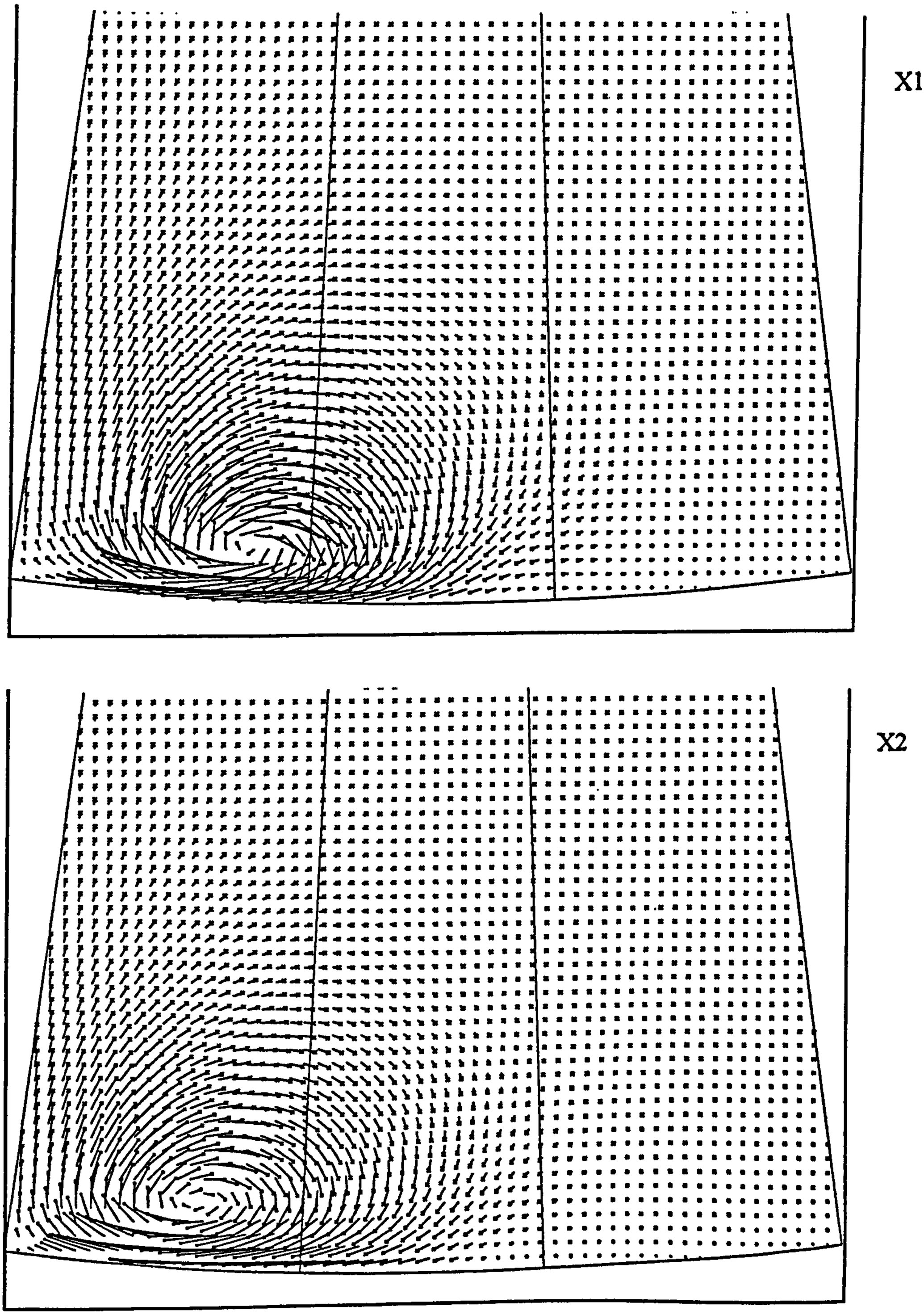

Figure 6.15: Velocity vector plots of the counter-rotating vortices of the pitch and skew angle configuration 30°/75° at the downstream locations, X1 (= 4.2δ_0) and X2 (= 7.7δ_0)

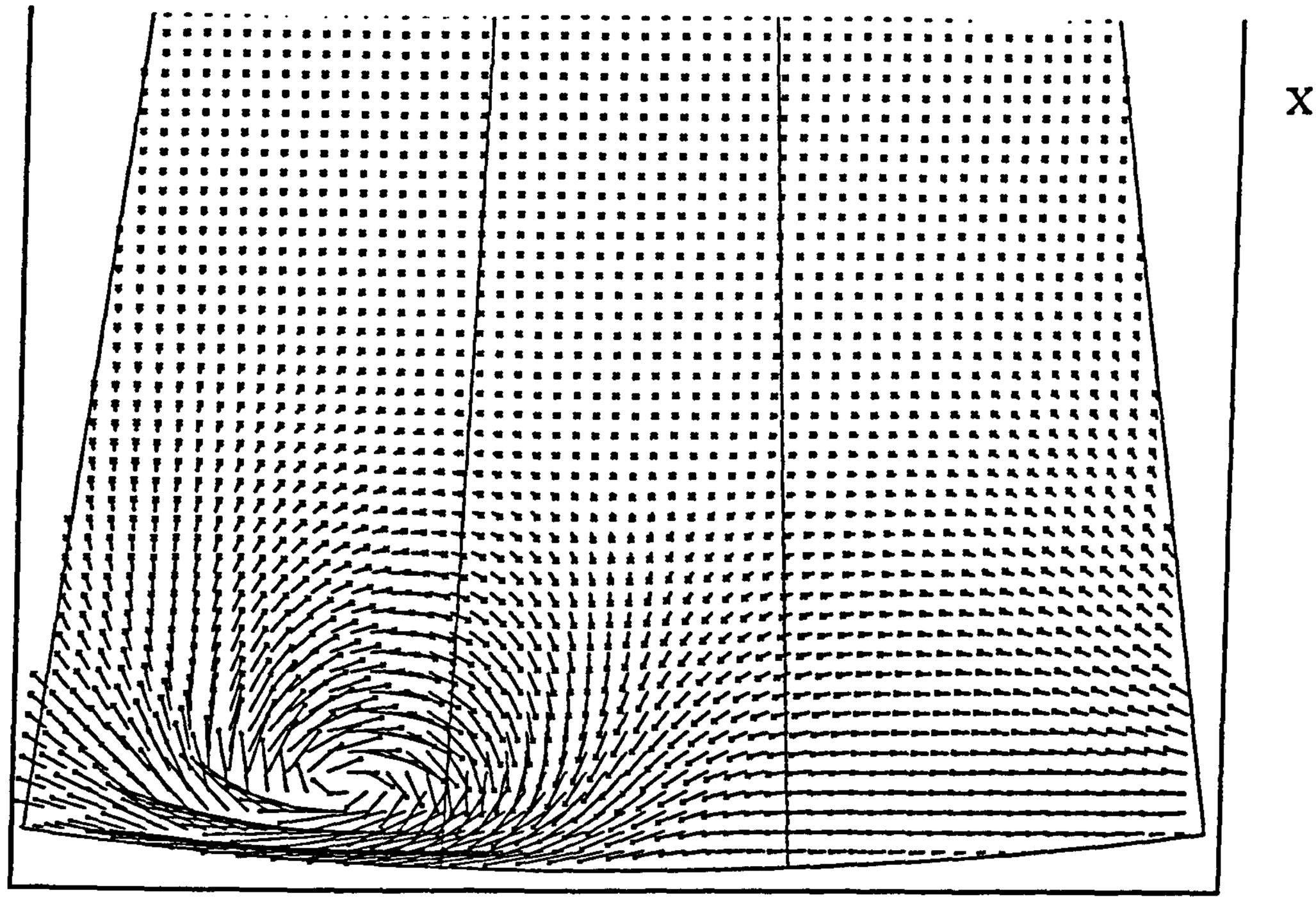

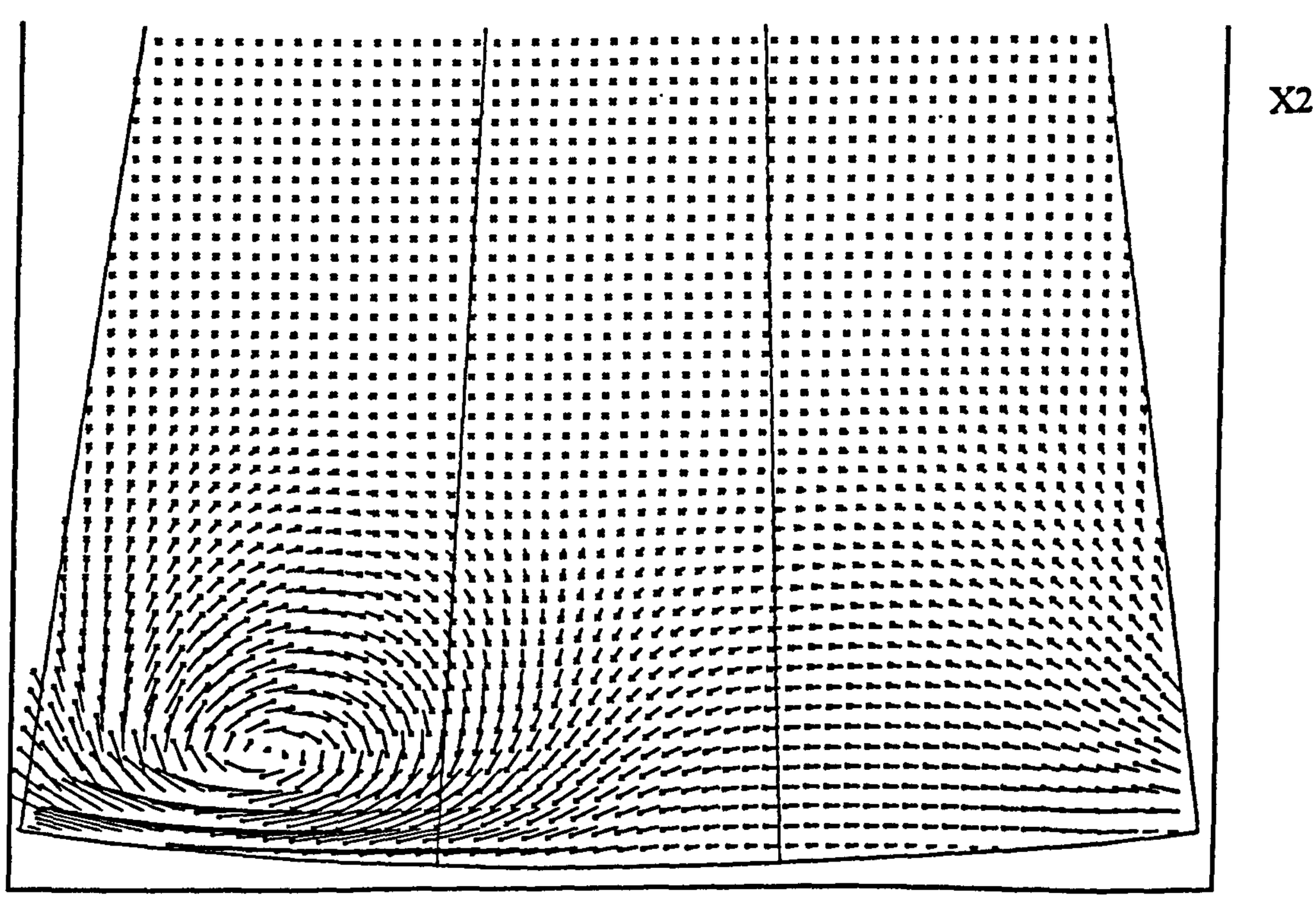

Figure 6.16: Velocity vector plots of the co-rotating vortices of the pitch and skew angle configuration 30°/75° at the downstream locations, X1 (= 4.2δ_0) and X2 (= 7.7δ_0)

6.3 Summary

In Chapter 6 the local sector model D3 (see Figure 6.1) was designed to investigate the performance of various airjet VG (AJVG) arrays at the same location in a S-bend intake duct (see Figure 3.16) as described in Chapter 5. The model describes one 15° sector of the S-bend duct with a solution domain height of the duct radius. Eight different pitch and skew angle configurations were predicted and analysed at one downstream location (see Figure 6.1) in Section 6.1. Details and boundary conditions of the sector model are described in Section 3.7.

The numerical grid for this AJVG model was generated by a modified version of the fortran code 'JETGRID' used for the grid generation in Chapter 4 and 5 and is described in Section 3.8. The modification comprises changing the coordinate system, i.e. from Cartesian to polar coordinates. Grid dependence was examined by using the shear stress distribution as a criteria to judge independence. The second-order Upwind (HUW) discretisation scheme was employed for the predictions.

Circulation and peak vorticity decay, peak vorticity paths in cross-stream and streamwise directions, cross-stream vorticity profiles, shear stress distributions, streamwise and cross-stream velocity profiles (see Figures 6.2 to 6.14) were used to analyse the performance of the different pitch and skew angle configurations. Both co- and counter-rotating vortices were predicted for each angle configuration. The differences between co- and counter-rotating vortices were negligible. However, at the upwash and downwash domain boundaries the difference between periodicity and symmetry in terms of cross-stream velocity profiles (see Figures 6.12 and 6.13) could be clearly seen.

Two groups of pitch and skew angle configurations, i.e. (1) 30°/75° and 30°/60° and (2), 30°/30° and 45°/30° defined always the highest and the lowest level of flow field enhancement downstream of the VG.

- Changing the pitch and skew angles from 45°/30° to 30°/75° increased the initial level of circulation (see Figure 6.2) by a factor of approximately 2.7. Enhancement in the flow field characteristics was achieved by altering pitch and skew angles of the AJVGs.
- The optimum configuration was observed to be the 30°/75° configuration.

- The initial level of peak vorticity (see Figure 6.3) could be increased by approximately 1.3 by changing the angle configuration from 45°/30° to 30°/75°.
- Changing the pitch/skew angle configuration from 45°/30° to 30°/75° resulted in an increase in the cross-stream translational movement (see Figure 6.4) proportional to that of the increase in vorticity strength. The cross-stream positions of the vortex cores (see Figure 6.10) reflected the same tendency as the vorticity paths.
- The vertical positions of the vortex cores (see Figure 6.11) were relatively independent of the pitch and skew angle configurations. In all cases the vertical distance from the solid surface of the vortex cores was approximately one quarter of the undisturbed boundary layer height. Therefore, most of the secondary motion was observed to occur within the boundary layer.
- The magnitude of the cross-stream velocity and the cross-stream vorticity was higher for the 30°/75° system than for the 45°/30° angle configuration (see Figures 6.6, 6.7, 6.11 and 6.12).
- The increase of skin friction (see Figure 6.8) was directly proportional to the cross-stream velocity results. The pitch and skew angle configurations of 30°/75° and 45°/30° provided the highest and the lowest shear stress distributions, respectively.

7 Comparison of Sector and Flat Plate Models

7.1 Introduction

The numerical results of the two VG models employed, i.e. the airjet vortex generator (AJVG) sector model D3 and the flat plate AJVG model D1 with 45° pitch and 45° skew angle, will be discussed and compared at two downstream locations, i.e. X1 and X2 (see Figure 7.1). This angle configuration was defined by the configuration for the flat plate model D1 of Chapter 5 from where the data is taken.

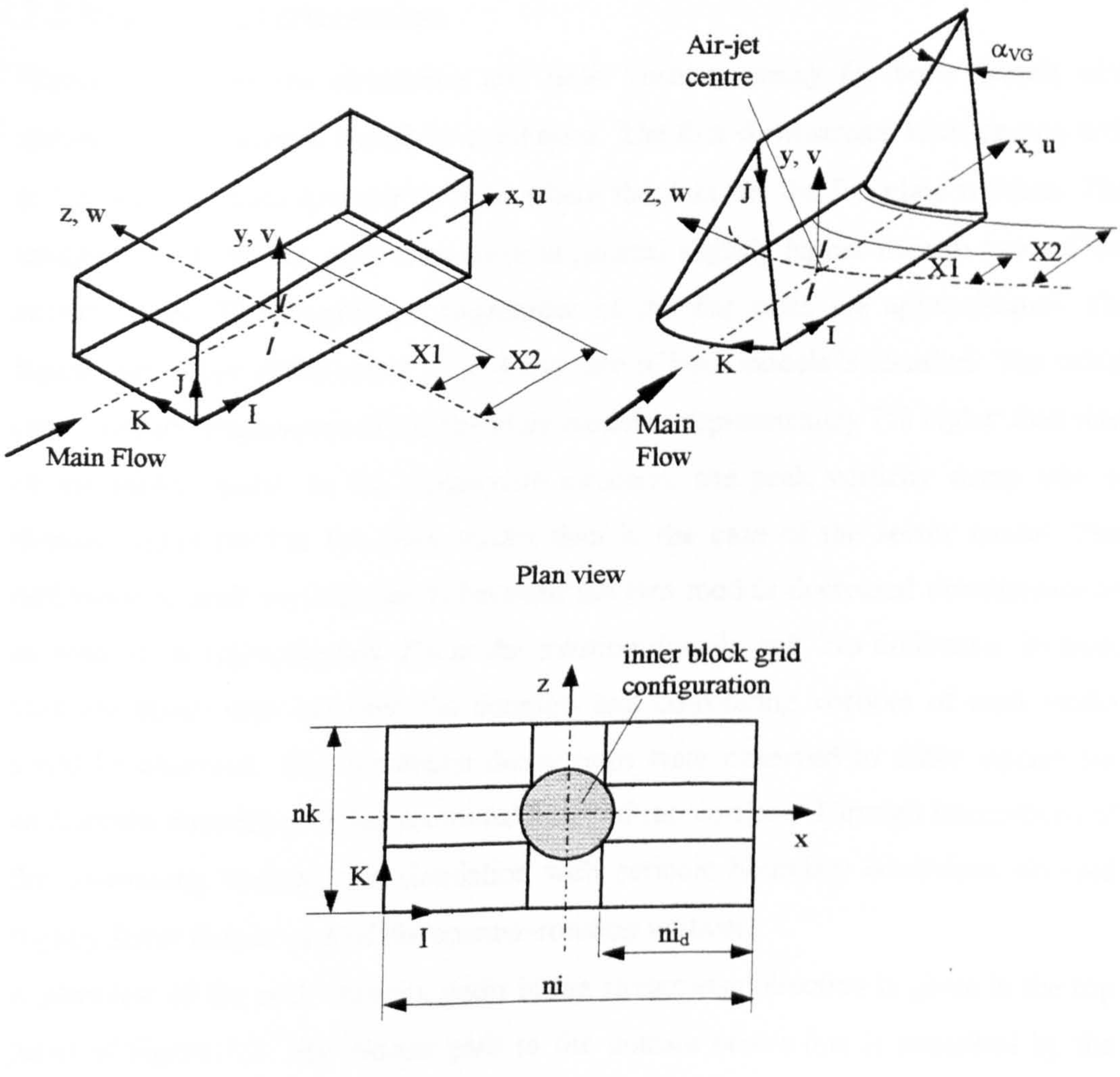

Figure 7.1: Local VG models D1 and D3 with the two downstream stations and I, J, K notation

These downstream locations were defined as follow:

- X1 = 0.25L ($4.2\delta_0$)
- X2 = 0.46L ($7.7\delta_0$)

see Figures 7.2 to 7.10.

Grid dependence was evaluated as was discussed in the previous Chapters 5 and 6. The total number of cells in the case of the sector model is 119964, whereas the flat plate model is discretised in 89088 finite volumes.

7.2 Results and Discussion

Figure 7.2 shows the circulation and peak vorticity decay for both models with symmetric and periodic boundary conditions. The first downstream location was $x/\delta_0 \cong 3.2$, adopted from Chapter 5, from where the data for the flat plate is taken. The magnitudes of the flat plate data were in general slightly higher than in case of the sector model. The circulation magnitudes of the flat plate are approximately 2% higher than those of the sector. The decay rate of both models is identical. The initial peak vorticity magnitudes of the flat plate model is approximately 7% higher than that of the sector model. In the streamwise direction, the peak vorticity decay rate is slightly higher for the flat plate model than in the case of the sector model. The difference in peak vorticity levels between the two models decreased downstream to an amount of approximately 2% at the solution domain end. No difference in peak vorticity decay rates between the counter- and co-rotating vortices of each model could be observed. The circulation decay rates were observed to differ equally for each model depending on the rotational sense of the vortices. Through interactions of the co-rotating vortices, the circulation with periodic boundary conditions decayed slightly faster than in case of the counter-rotating vortices.

A planview of the peak vorticity paths in the streamwise direction is given in the top panel of Figure 7.3. The closest path to the domain centre line is described by the counter-rotating vortex from the flat plate model. The next adjacent path is described by the co-rotating vortex of the flat plate model and by the counter-rotating vortex of the sector model. A third path is described by the co-rotating vortex of the sector model. The differences between the peak vorticity paths of the counter-rotating vortices predicted by both models is less than 1% and therefore negligible. The same

negligible difference is observed for the two co-rotating systems. A sideview of these paths is given in the lower panel of Figure 7.3. Comparing the vorticity paths in the streamwise direction against the solution domain height, the paths of the sector model separated from the paths of the flat plate model from a downstream location of $x/\delta \approx 5$. In the case of both models, negligible differences between the counter- and co-rotating vortices can be observed. As mentioned in Chapter 6 the difference in heights of the paths are negligible compared to the travelled distances of the vortices in the cross-stream direction. The total distance in y-direction is only 4% of the distance travelled downstream whereas the total cross-stream distance describes approximately 40% of the total downstream path. However, the peak vorticity paths of the sector model were closer to the solid surface than those of the flat plate model as the vortices predicted by the sector model were slightly weaker than those of the flat plate model (see Figure 7.3). The vortex is decaying in the streamwise direction and the core is lifting up. Through the restriction of the wall, i.e. by continuity, the vorticity will be stronger beneath the vortex core. The more the vortex decays, i.e. the weaker the vortex is, the more the remaining peak vorticity approaches the solid surface.

Figure 7.4 shows the cross-stream vorticity distribution at the two downstream locations X1 and X2, i.e. half way downstream and close to domain exit. No significant negative or secondary vorticity is observed in both cases. At the downstream location X1, the sector model predictions were approximately 7% less than those of the flat plate model. Further downstream at X2 the difference in vorticity prediction between the two models shrank to a negligible amount. This result conforms to Figure 7.2 where the peak vorticity, in the case of the flat plate model, is observed to decay slightly faster than that of the sector model. The difference between the data provided by counter- and co-rotating vortices appeared to be negligible for both Air-jet models. Figure 7.5 presents the vorticity profiles through the vortices cores for both models at the two downstream locations X1 and X2. The differences in vorticity magnitudes reflect in general the aforementioned results of Figure 7.4. At location X1 the sector model predictions are approximately 7% less that those of the flat plate model. The difference in prediction between the two models decreased to approximately 3% at the downstream location X2.

The cross-stream shear distribution, shown in Figure 7.6, supports the impression that the differences in predictions between the sector and the flat plate model are minor. There are no significant differences between the shear stress predictions of the two Air-jet models.

Streamwise velocity profiles through the vortices cores are presented in Figure 7.7. The velocity deficits predicted by the sector model are approximately 7% less than those predicted by the flat plate model at the downstream location X1, which supports the vorticity results (see Figure 7.4). At location X2 the two jet model predictions described approximately the same velocity profiles. No differences between the predictions of co- and counter-rotating vortices for each airjet model can be observed. The cross-stream velocity profiles at the two downstream locations are displayed in Figure 7.8. The flat plate predictions were approximately 7% higher than the sector predictions at location X1 and X2. The cross-stream positions of the vortices for both models were approximately the same. A minor difference between co- and counter-rotating vortices predicted by both models can be observed at location X2.

The cross-stream velocity profiles through the vortices' cores are presented in Figure 7.9. At location X1 the vertical distance of the vortices' cores are identically predicted from both airjet models. The flat plate model predicted co-rotating vortices which rose about approximately 25% between location X1 and X2, whereas the vortices cores predicted by the sector model rose by approximately 30% between location X1 and X2. The predictions of the flat plate model close to the wall are approximately 7% higher in magnitudes than those of the sector model at both downstream locations X1 and X2. The co-rotating vortices show slightly higher velocity magnitudes than the counter-rotating vortices for both models at the two downstream locations X1 and X2 close to the solid surface. The velocity profiles are approximately the same up to the cores centres, where the cross-stream velocities are zero. From the cores centres towards the negative velocity maxima the curves slightly diverge. At location X1 the counter-rotating vortices produced by the flat plate model describe the highest negative velocity maximum whereas the co-rotating vortices predicted by the sector model shows the lowest negative velocity maximum. The profiles of the negative velocity maxima of the counter-rotating vortices predicted by the sector model and the co-rotating vortices produced by the flat plate model are coincident at location

X1. Above the location of the negative velocity maxima the two models appear to describe identical results at location X1. Further downstream, at location X2, the two jet models describe already identical results from the location of the negative velocity maxima. Both models show slightly less strong velocities for the co-rotating vortices above the cores at the two downstream locations X1 and X2. At both locations, X1 and X2, it can be seen that the vortices spread above the boundary layer thickness but only slightly.

Figure 7.2: Circulation and peak vorticity decay for the sector and flat plate models with 45^0 pitch and 45^0 skew angle

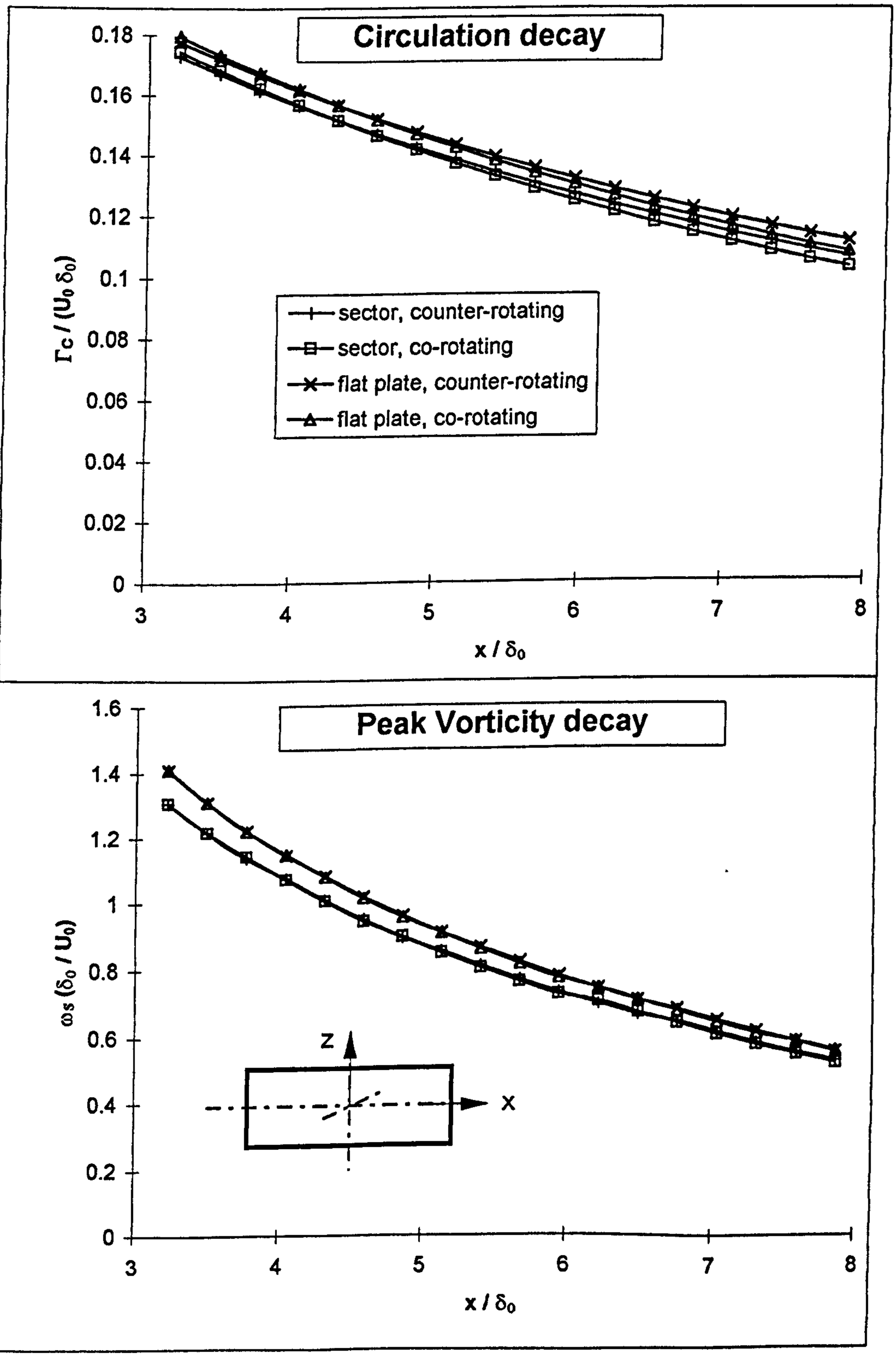

Figure 7.3: Peak vorticity paths for the sector and flat plate models with 45^0 pitch and 45^0 skew angle

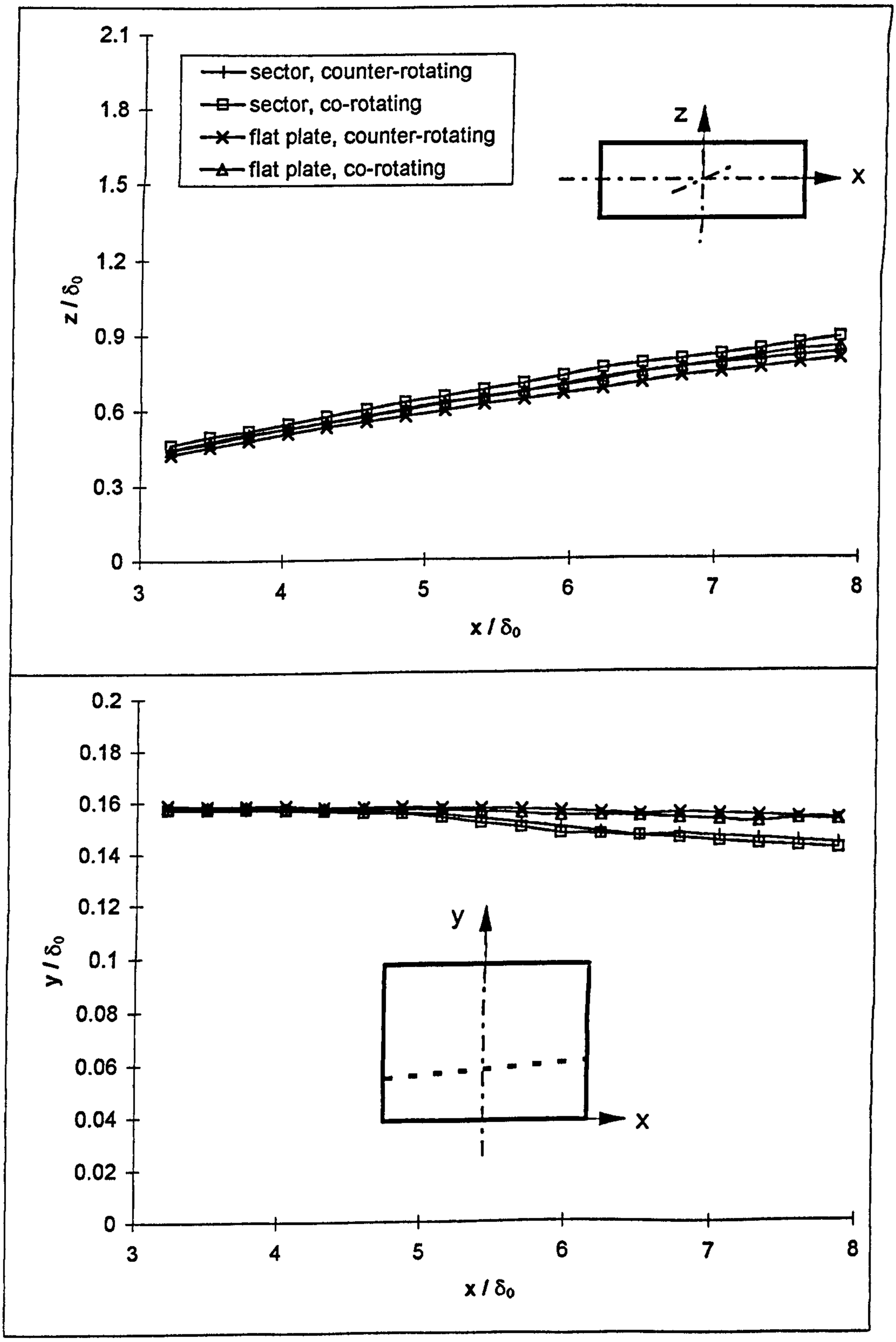

Figure 7.4: Cross-stream vorticity distribution for the sector and flat plate models with 45^0 pitch and 45^0 skew angle at two downstream locations, X1 and X2

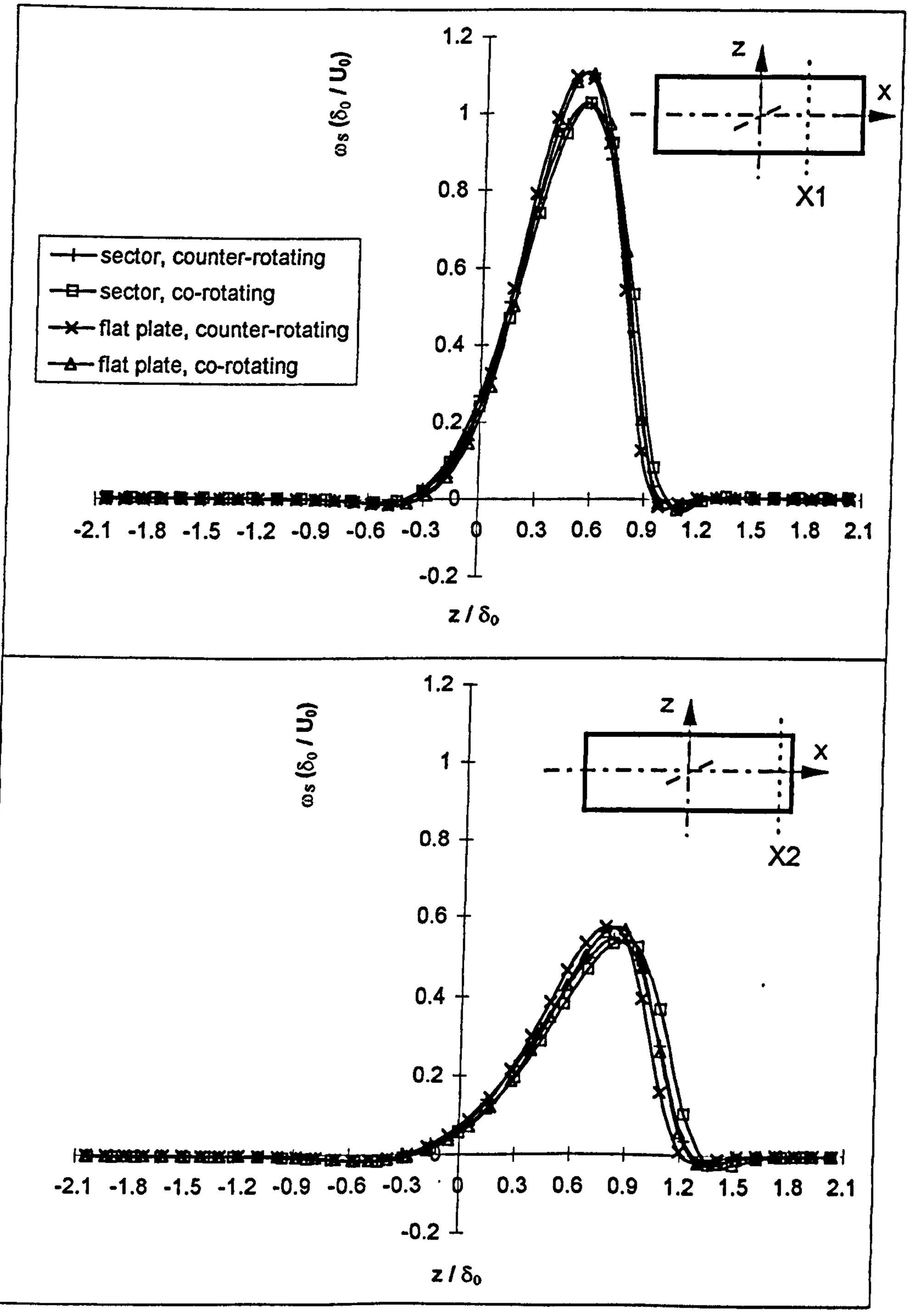

Figure 7.5: Vorticity profiles through vortex cores for the sector and flat plate models with 45^0 pitch and 45^0 skew angle at two downstream locations, X1 and X2

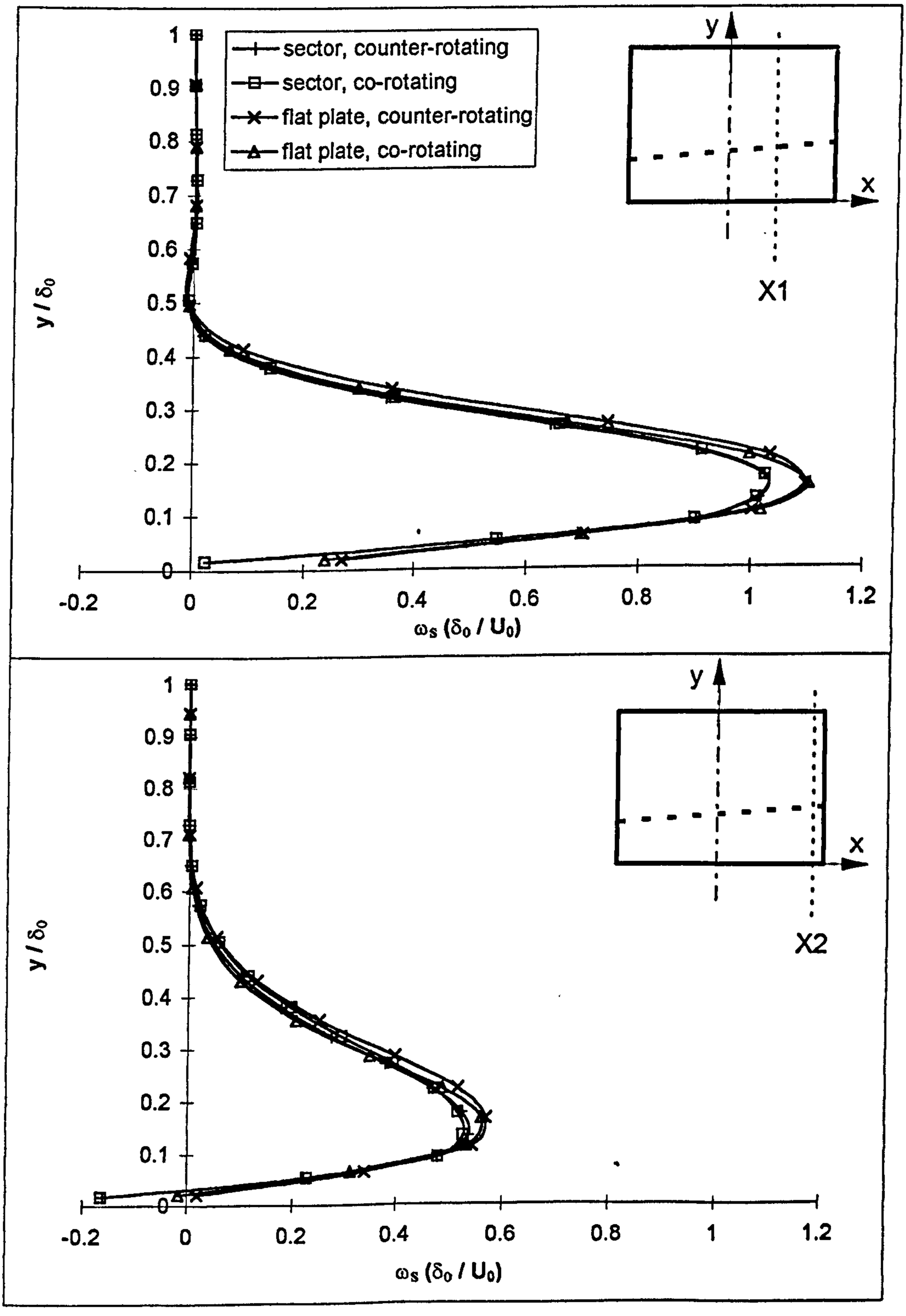

Figure 7.6: Cross-stream shear stress distribution for the sector and flat plate models with 45^0 pitch and 45^0 skew angle at two downstream locations, X1 and X2

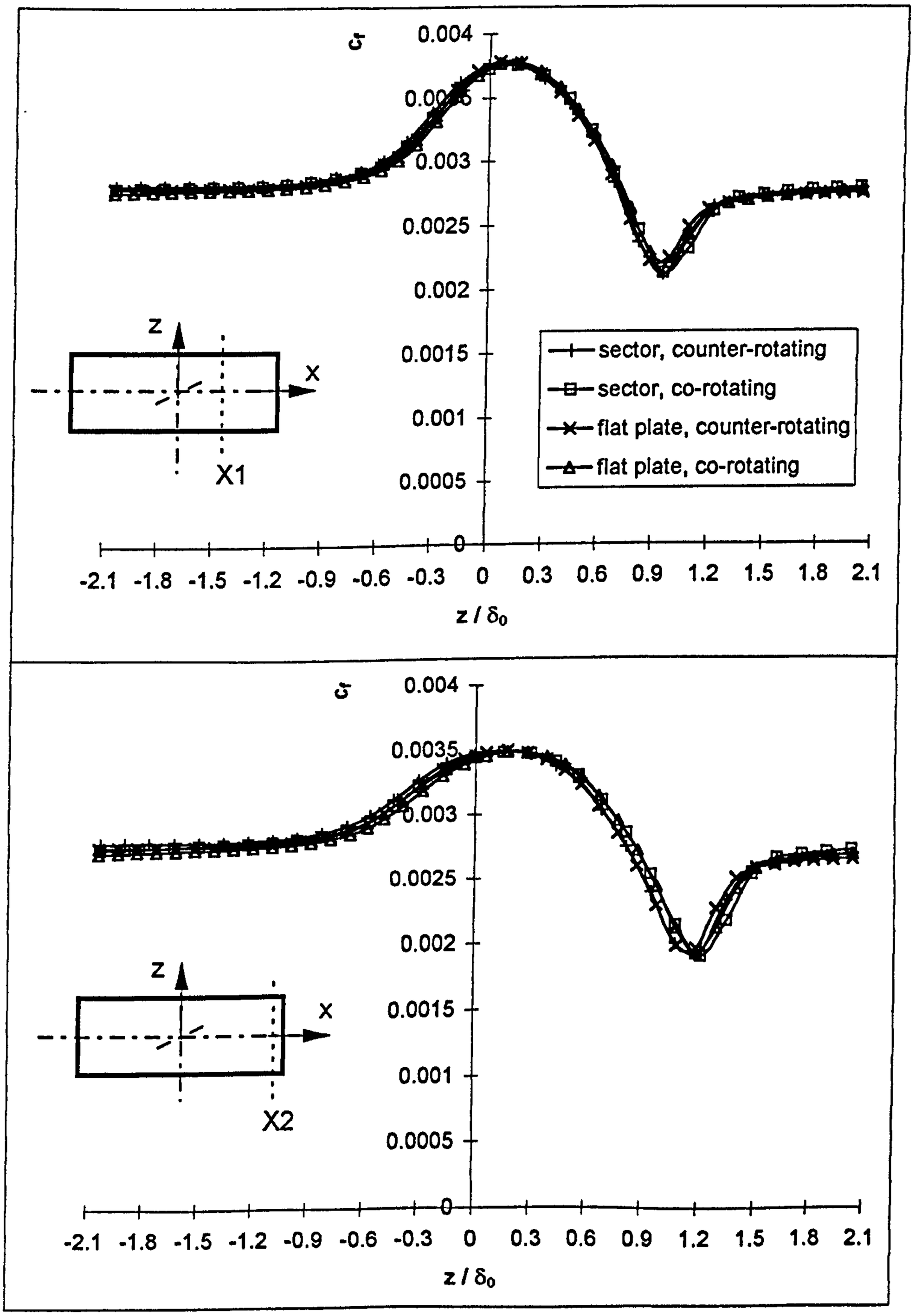

Figure 7.7: Streamwise velocity profiles through the vortex cores for the sector and flat plate models with 45^0 pitch and 45^0 skew angle at two downstream locations, X1 and X2

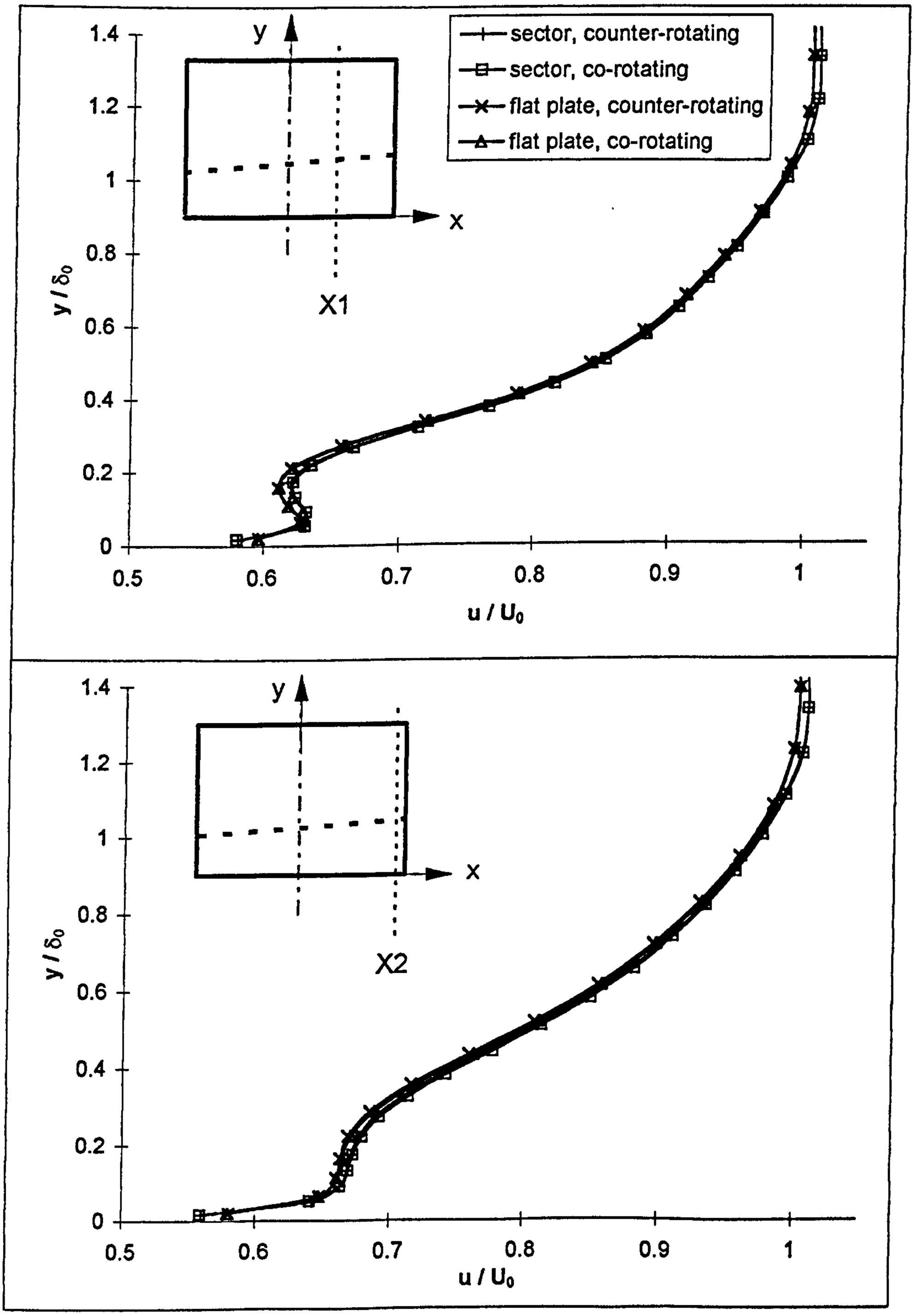

Figure 7.8: Vertical cross-stream velocity for the sector and flat plate models with 45^0 pitch and 45^0 skew angle at two downstream locations, X1 and X2

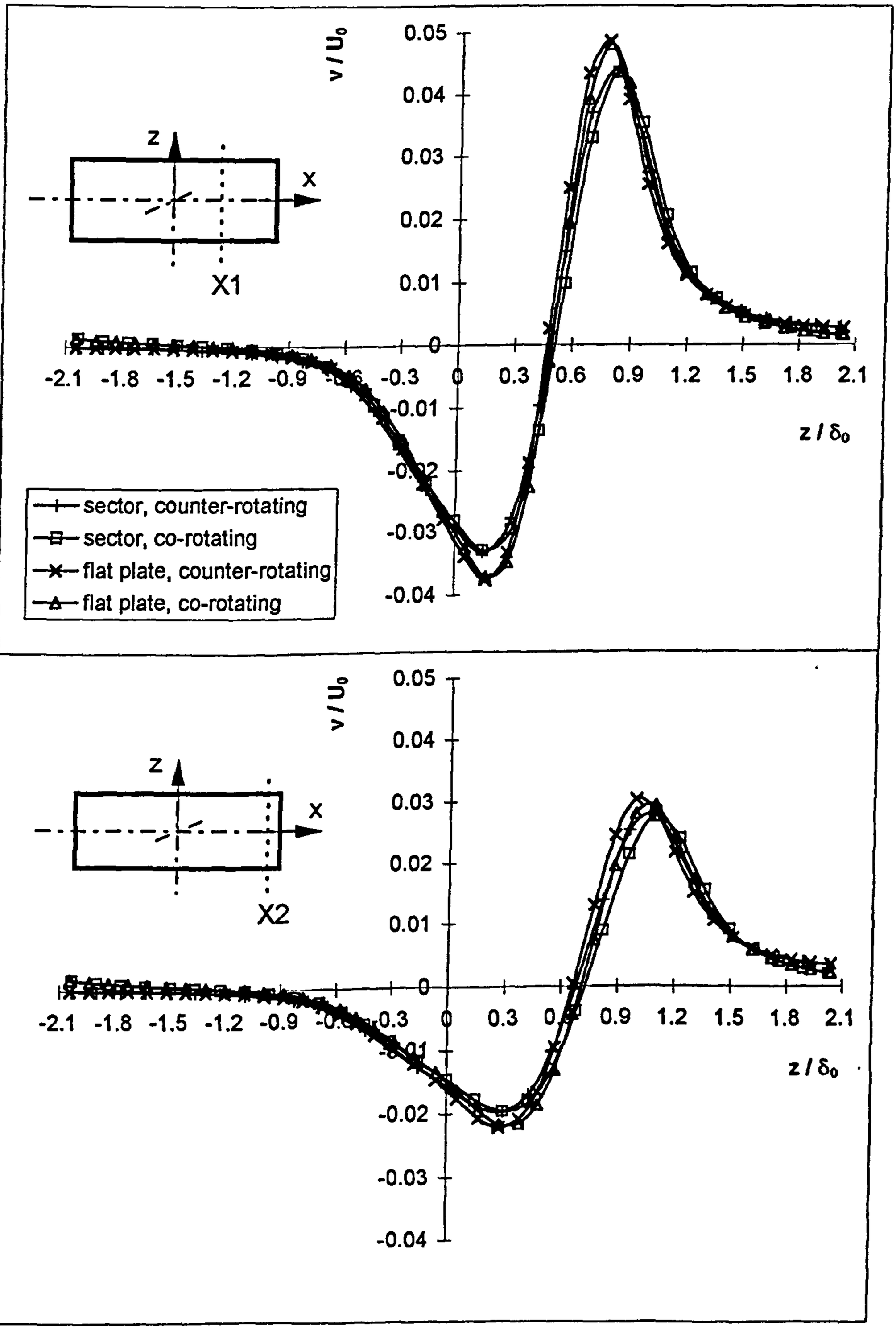

Figure 7.9: Horizontal cross-stream velocity for the sector and flat plate models with 45^0 pitch and 45^0 skew angle at two downstream locations, X1 and X2

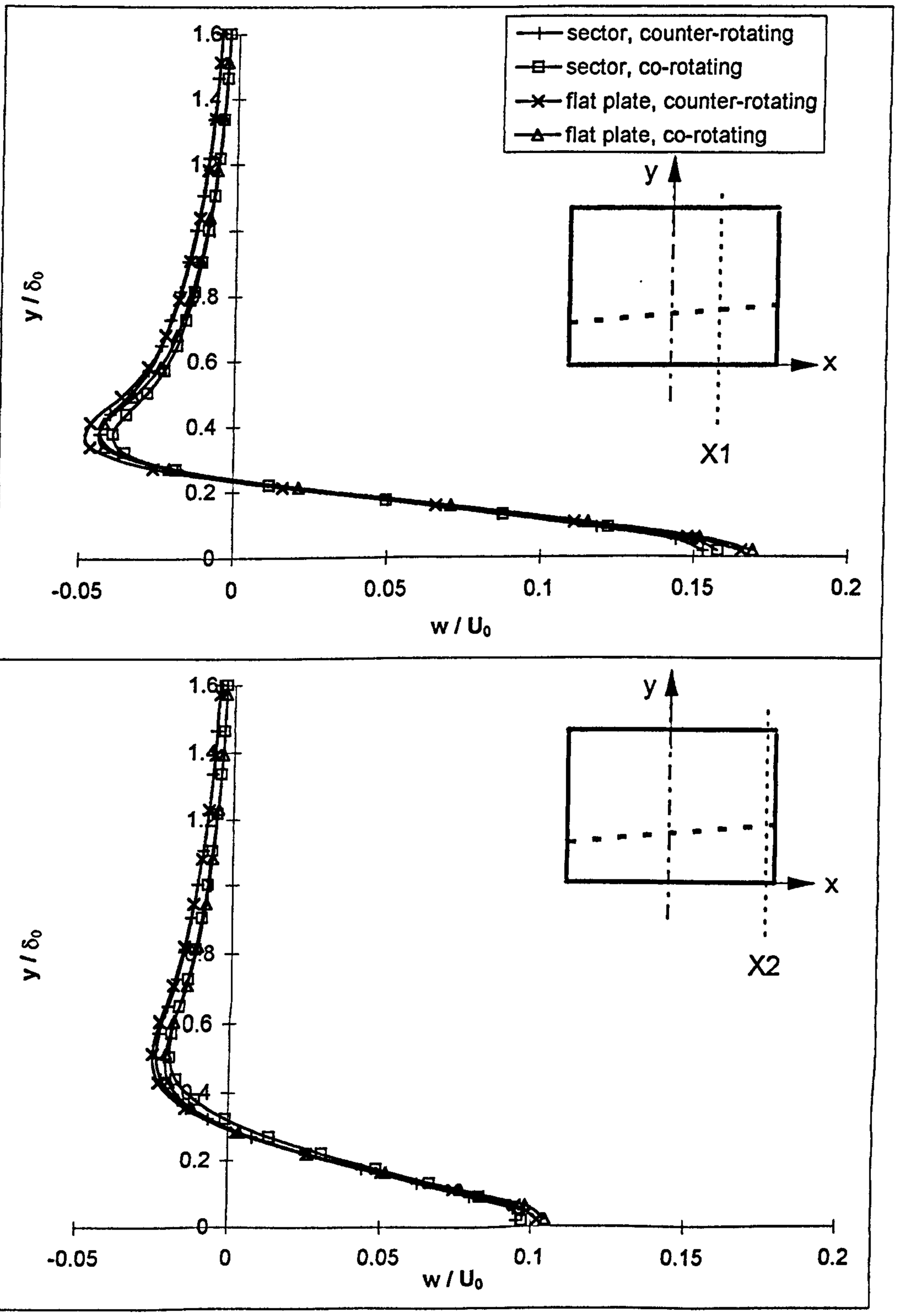

7.3 Summary

In Chapter 7 the airjet vortex generator (AJVG) flat plate model D1 and the AJVG sector model D3 (see Figure 7.1) with 45° pitch and 45° skew angle were compared and results discussed at two downstream locations. Details are described in Table 3.2 and the boundary conditions are defined in Sections 3.7.

The numerical grids were generated by using the two versions of the fortran code 'JETGRID' explained in Section 3.8. The main difference between the two grids is the coordinate system, which changes from Cartesian for the flat plate model to polar coordinates in case of the sector model. The solution domain of the flat plate model is growing in streamwise direction in accordance with the boundary layer thickness whereas the sector model comprises a constant solution domain height equal to the S-bend duct radius (see Figure 3.16). Shear stress distribution at the first downstream location was judged to be an acceptable criterion for grid independence. Throughout the numerical tests the second-order Upwind (HUW) discretisation scheme was employed for the predictions. Circulation and peak vorticity decay, peak vorticity paths in cross-stream and streamwise directions, cross-stream vorticity profiles, shear stress distributions and streamwise and cross-stream velocity profiles (see Figures 7.2 to 7.9) were used to analyse the differences between the two models.

Both co- and counter-rotating vortices were compared. Little difference between the results for co- and counter-rotating vortices for each of the models was observed.

The magnitudes of the flat plate data was in general marginally higher than in case of the sector model, except for the shear stress distributions (see Figure 7.6). The skin friction distribution was of the same order of magnitude. The difference between the two models in terms of level of circulation was approximately 2% whereas the decay rate was identical. The difference of initial peak vorticity was approximately 7% but decreased to 2% further downstream. The cross-stream peak vorticity paths of co- or counter-rotating vortices predicted by both models differed by less than 1%. The predicted vorticity profiles of both models (see Figures 7.4 and 7.5) showed, at the first downstream location, a difference in magnitudes of approximately 7% between each other, which decreased to approximately 3% further downstream. A constant difference of 7% between the two models in terms of cross-stream velocity v (see Figure 7.8) was observed. The difference between the cross-stream velocity

components w (see Figure 7.9) was negligible. The flat plate model predicted the co-rotating vortices lifted of the plate approximately 5% less than those produced by the sector model (see Figure 7.9). The streamwise velocity profiles (see Figure 7.7) showed a 7% difference in magnitudes at the first downstream location for the cross-stream component, v, whereas further downstream no significant difference was observed.

8 Discussion

The first aim of this project was to investigate the vortical flow structure in the vicinity of the Vane Vortex Generator (VVG) and the Air-Jet Vortex Generator (AJVG). The size and configuration of the VVG and AJVG were adopted from the experiments of Gibb & Anderson (1995). Their experimental results showed that the flow field distortion at the engine face was slightly more reduced by employing AJVGs than using VVGs. The pressure recovery at the engine face was also higher by using AJVGs than VVGs. This is expected because AJVGs do not cause any drag penalty in contrast to VVGs. Gibb & Anderson (1995) were unable to give a clear answer as to why the AJVGs perform slightly better than VVGs in terms of reducing the flow field distortion at the engine face.

The predictions of circulation, vorticity and velocity distributions showed two significantly different flow field enhancements generated by the VVG and AJVG. The VVG produced a strong vortex which travelled downstream along the top of the boundary layer. Thus the low momentum fluid within the boundary layer was mixed with the high momentum fluid of the free stream. Hence momentum was extracted from the inviscid free stream fluid into the viscous boundary layer fluid which was observed in terms of streamwise velocity profiles with relatively large velocity deficits. In contrast, the AJVG generated a vortex which was weak compared to the VVG vortex and centred at approximately one quarter of the boundary layer height. That implies almost no mixing of high momentum free stream fluid with low momentum fluid within the boundary layer. The streamwise velocity profile showed a small area of deficit. However, it could be seen from cross-steam velocity plots (parallel to the surface) that the AJVG vortex spreads into the free stream region, but with negligible strength.

Higher skin friction enhancement was predicted from our local model in the case of the co-rotating vortex produced by the AJVG compared to that provided by the VVG. Hence, the mixing within the boundary layer of low momentum fluid close to the surface with higher momentum fluid due to the AJVG may be more effective in terms of generating a steeper velocity gradient along the solid surface than the mixing due to the VVG of the boundary layer fluid with free stream flow. In the S-bend intake experiments of Gibb & Anderson (1995) two arrays of periodically arranged

VGs were placed symmetrically in the lower half of the duct (see Figures 3.16 and 3.17: pp. 137-138). These arrays produce two sets of co-rotating vortices which redirected the flow in the S-bend duct and tended to attenuate the naturally occurring pair of counter-rotating vortices. Gibb & Anderson (1995) experimental results showed that the flow field distortion at the engine face was better reduced by employing arrays of AJVGs than VVGs. Hence, it would appear that the reduction in engine face flow field distortion is linked to the higher skin friction produced by the AJVGs immediately downstream of the vortex generators.

The local model also showed that the vortices produced by the AJVGs behaved as individual longitudinal vortices because of their size and spacing. Thus each vortex keeps its identity in the array of co-rotating vortices travelling in the streamwise direction. According to the predictions and supported by potential theory the vortices travelled in the cross-stream direction. In terms of the S-bend configuration the generated vortices travel from the inside to the outside of the duct (see Figure 1.6) in a streamwise direction. Thus the boundary layer on the duct wall will be influenced by the two arrays of individual co-rotating vortices produced by the AJVGs in the circumferential direction depending on the magnitude of the circumferential velocity of the vortices.

In contrast, the vortices generated by the VVGs interfered strongly with each other thus reducing their individual strengths. In terms of the S-duct configuration the co-rotating vortices produced by the VVGs travel also from the inside to the outside of the duct in the streamwise direction but interact strongly with each other and thus tend to destroy each other. Hence the boundary layer on the duct wall might be also influenced over a certain circumferential extent depending on the circumferential velocity of the vortices but with strongly interfering vortices instead of individual vortices in the case of the AJVGs. The VVG vortices redirect momentum from the free stream and as a result of their mutual interference and mixing, less kinetic energy is available to convert into pressure at the engine face.

Based on the results from the local models discussed above, the redirecting process of the flow in the duct seems to be more balanced by the arrays of individual sub-boundary layer vortices produced by the AJVGs than by the strongly interfering vortices generated by the arrays of VVGs.

The second important aim was to determine the optimum pitch and skew angle configuration for the AJVGs in order to enhance the flow field in the most effective way. The sector AJVG model was used because it reflects the nature of the duct in two important respects. Firstly the circumferential curvature of the duct is approximated and secondly the height of the upper boundary of the local sector model is equal to the symmetry line of the duct. Thus the imposition of the upper boundary conditions could not suppress the resulting vortex. However, the comparison of the flat plate model with a fixed solution domain height of five times the local boundary layer height and the local sector did not show any significant differences in terms of flow field predictions.

All AJVG configurations showed individual sub-boundary layer vortices which were located at approximately one quarter of the undisturbed boundary layer height. The cross-stream shear stress distributions indicated the highest level of enhancement at a pitch and skew angle configuration of 30° and 75°, respectively. Cross-stream velocity plots, circulation and vorticity graphs supported the shear stress indications. Both an increase of the pitch angle to 45° or a decrease of the skew angle to 60° reduced the magnitude of flow field enhancement significantly. The flow field distortion at the engine face of the S-bend intake duct might be further reduced by adjusting the two co-rotating arrays of AJVGs with the optimum pitch and skew angle configuration of 30° and 75°, respectively. The interaction of the vortices was still insignificant thus they would keep their identity travelling downstream along the duct wall from the inside to the outside.

The third aim was to clarify whether modelling the AJVG inlet tube has any effect on the resulting vortex. The vortex produced by the local model without the inlet tube was slightly stronger close to the AJVG orifice. Further downstream the difference was negligible. Hence the mass flow rate seems to be more important than the velocity profile itself.

9 Conclusions and Future Work

Conclusions

The main objective of this research project was to design a local numerical model which reflects the physical geometry and conditions of the fully turbulent flow field in the vicinity of both Vane Vortex Generator (VVG) and an Air-Jet Vortex Generator (AJVG) array in an S-bend intake duct. The location of the Vortex Generator (VG) array is approximately two inlet diameters downstream of the inlet.

Two Flat Plate Models; one with and one without the jet inlet tube, were produced and predicted streamwise and cross-stream velocity profiles were compared to experimental data. The magnitude of the velocity component v (normal to the plate) in the experimental case is significantly higher than that of the predictions. Despite this difference, in general, the trend of the predicted velocity profiles are in agreement with experimentally measured results. Negligible differences between the results predicted by the two numerical models were observed, thus the simple flat plate model without the jet inlet tube was used for further predictions.

Two further local Flat Plate Models were constructed: one for rectangular VVGs and one for circular AJVGs. Both models predicted counter- and co-rotating vortices depending of the boundary conditions applied. The VVG model produced significantly stronger vortices than the array of AJVGs. As a result, the vortices produced by the VVGs interacted strongly with each other, whereas the vortices generated by the AJVGs behaved as isolated vortices. The VVG vortices' cores were approximately aligned with the undisturbed boundary layer height whilst the AJVG vortices' cores were located at a height of approximately one quarter of the undisturbed boundary layer thickness. Thus the VVG configuration provides mixing of low momentum fluid within the boundary layer with high momentum fluid of the free stream. In contrast, the AJVG vortices were seen not to provide significant mixing with free stream high momentum fluid.

Despite these differences, the enhancement of skin friction was similar for both types of VGs. In the case of co-rotating vortices, the AJVG and the VVG configurations produced shear stress distributions of similar magnitudes.

The sector AJVG model was constructed to reflect more closely the physical geometry of the VG array in the S-bend intake duct. A range of eight different pitch and skew angle configurations were modelled generating arrays of counter- and co-rotating vortices. The maximum level of flow field enhancement was predicted with a pitch angle of 30° and a skew angle of 75°. The lowest enhancement was observed for a pitch and skew angle configuration of 45°/30°. It appeared that decreasing the pitch angle, i.e. from 45° to 30°, and increasing the skew angle from 30° to 75° improves the flow field enhancement significantly. All the generated vortices' cores were located at approximately one quarter of the undisturbed boundary layer height. Thus little mixing between high momentum fluid of the free stream and low momentum fluid within the boundary layer was observed.

The Flat Plate AJVG Model and the Sector AJVG Model were compared for a pitch and skew angle configuration of 45°/45°. The differences between the generated results are insignificant, thus the simple flat plate model is suggested for further investigations.

Future Work

A parametric study of the jet orifice size would clarify the connection between the jet diameter and vortex strength. Work in progress at City University has highlighted the influence of the jet/free stream velocity ratio (VRAT) on the vortex position relative to the undisturbed boundary layer thickness. Preliminary results indicate that increasing VRAT (thus increasing the mass flow rate) increases the height of the centre of the vortex system above the surface. Similar trends may occur if VRAT were kept constant whilst increasing the area of the jet orifice.

The numerical model of VVG allows the same opportunity to study a variety of vane sizes and different skew angles. A comprehensive comparison study between vane and jets would indicate which size of a jet diameter will be comparable to a certain size of a rectangular vane.

Spacing of the VGs is another very important aspect needing further investigation. This affects the interaction between co- and counter-rotating vortices. Gibb & Anderson (1995) experiments showed that a slightly higher magnitude of reduction of

flow distortion at the engine face was achieved by employing an array of AJVGs than an array of VVGs. The configuration of the arrays of VGs were equal in terms of number and spacing. However, the predicted vorticity produced by the VVGs is significantly greater than that produced by the AJVGs. This seems to imply that the difference in magnitude of vorticity between the VVGs and AJVGs may not lead to any further reduction of distortion at the engine face. Thus it might be possible to reduce the surplus amount of vorticity by reducing the number of VVGs. This suggests that a larger spacing of VVGs might be sufficient enough to generate the necessary amount of vorticity needed for reduction of the flow field distortion at the engine face. Thus spacing of VGs becomes an important criteria to control the individual strength of vortices and the interaction between them.

The high free stream velocity provides a Mach number of approximately 0.7. The limit of incompressible flow is defined at a Mach-number of approximately 0.5. Thus the effects of compressibility (i.e. decrease of density and so decrease of mass flow rate) may produce a lower magnitude of circulation. As a result, skin friction enhancement may be less than that predicted for the incompressible case. Adjusting the local numerical model to include the effects of compressibility may generate results more representative of the experiment and is therefore a choice for further investigation.

References

Advisory group for Aerospace Research and Development (AGARD), "Air Intakes for High Speed Vehicles", AGARD-AR-270, Sept., 1991

Aftosmis, M. J., "Viscous Flow Simulation Using an Upwind Method for Hexahedral Based Adaptive Meshes", *AIAA Paper 93-0772*, 31st Aerospace Science Meeting, Reno, NV, 1993

Akanni, S. D. & Henry, F. S., "Numerical Calculations for Air jet Vortex Generators in Turbulent Boundary Layers", CEAS European Forum on High Lift & Separation Control, March, 1995, Bath, U. K.

Alderton, J. H. & Wilkes, N. S., "Some applications of new finite difference schemes for fluid flow problems", AERE-R 13234, 1988

Anderson, B. H., "The Aerodynamic Characteristics of Vortex Ingestion for the F/A-18 Inlet Duct", *AIAA Paper 91-0130*, Jan., 1991

Anderson, Jr. J. D., "Computational Fluid Dynamics", 1st ed., McGraw Hill, 1995

Anderson, B. H. & Gibb, J., "Application of Computational Fluid Dynamics to the Study of Vortex Flow Control for the Management of Inlet Distortion", NASA Technical Memorandum 105672, July, 1992

Anderson, B. H. & Gibb, J., "Study on Vortex Generator Flow Control for the Management of Inlet Distortion", *Journal of Propulsion and Power*, Vol. 9, No. 3, pp. 422-430, May-June, 1993

Anderson, B. H., Huang, P. S., Paschal, W. A. & Cavatorta, E., "Study on Vortex Flow Control of Inlet Distortion", *Journal of Propulsion and Power*, Vol. 8, No. 6, pp. 1266-1272, December, 1992

Anderson, B. H. & Reddy, D. R. & Kapoor, K., "A Comparative Study of Full Navier-Stokes and Reduced Navier-Stokes Analyses for Separating Flows Within a Diffusing Inlet S-Duct", *AIAA-93-2154*, June, 1993

Anderson, D. A., Tannehill, J. C. & Pletcher, R. H., "Computational Fluid Mechanics and Heat Transfer", McGraw Hill, 1984

Baldwin, B. S. & Lomax, H., "Thin-layer approximation and algebraic model for separated turbulent flows", *AIAA-78-257*, 1978

Bansod, P. & Bradshaw, P., "The Flow in S-shaped Ducts", *Aeronautical Quarterly*, Vol. 23, pp. 131-140, May 1972

Bell, J. H. & Metha, R. D., "Effects of Imposed Spanwise Perturbations on Plane Mixing-Layer Structure", *Journal of Fluid Mechanics*, Vol. 257, pp. 33-63, 1993

Berger, M. & Jameson, A., "An Adaptive Multigrid Method for the Euler Equations", 9th International Conference on Numerical Methods in Fluid Dynamics, Lecture Notes in Physics, Vol. 218, pp. 92-97, Springer Verlag Berlin, 1984

Berger, S. A., Talbot, L. & Yao, L. S., "Flow in curved pipes", Ann. Rev. Fluid Mech., Vol. 15, pp. 461-512, 1983

Bradshaw, P., "The Analogy between Stream-Line Curvature and Buoyancy in Turbulent Shear Layer", *Journal of Fluid Mechanics*, Vol. 36, pp. 177-191, 1969

Bradshaw, P., Cebici, T. & Whitelaw, J. H., "Engineering Calculation Methods for Turbulent Flow", Academic Press, 1981

Bradshaw, P., Ferriss, D. H. & Atwell, N. P., "Calculation of boundary-layer development using the turbulent energy equation", *Journal of Fluid Mechanics*, Vol. 28, Part 3, pp. 593-616, 1967

Bray, T. P., "A Parametric Study of Vane and Air-jet Vortex Generators", Engineering Doctorate (EngD) Thesis, Cranfield University, 1999

Bridgeman, J. O., Steger, J. L. & Caradona, F. X., "A Conservative Finite Difference Algorithm for the Unsteady Transonic Potential Equation in Generalised Coordinates, *AIAA Paper 82-1388*, 1982

Briley, W. R. & McDonald, H., "Three-Dimensional Viscous Flows with Large Secondary Velocities", *Journal of Fluid Mechanics*, Vol. 144, pp. 47-77, March 1984

Brown, A. C., Nawrocki, H. F. & Paley, P. N., "Subsonic Diffusers Designed Integrally with Vortex Generators", *Journal of Aircraft*, Vol. 5, pp. 221-229, 1968

Bushnell, D. M.., "Longitudinal Vortex Control - Techniques and Applications", The 32nd Lanchester Lecture, *Aeronautical Journal*, pp. 293-312, October, 1992

Castro, I. P. & Jones, J. M., "Studies in Numerical Computations of Recirculating Flows", *International Journal for Numerical Methods in Fluids*", Vol. 7, pp. 793-823, 1987

CFX 4 User Manual, "CFX 4 Release 4.1", CFDS, AEA Industrial Technology Harwell Lab., Oxfordshire, U. K., October, 1995

Chou, P. Y., "On velocity correlations and the solution of the equations of turbulent fluctuation", *Quart. J. Appl. Math.*, Vol. 3, pp. 38-54, 1945

Compton, D. A. & Johnston, J. P., " Streamwise Vortex Production by Pitched and Skewed Jets in a Turbulent Boundary Layer" *AIAA Journal*, Vol. 30, No. 3, pp. 640-647, March, 1992

Courant, R., Isaacson, E. & Rees, M., "On the Solution of Non-linear Hyperbolic Differential Equations by Finite Differences, *Comm. on Pure and Appl. Math.*, Vol. 5, pp. 243-255, 1952

Dannehoffer, J. F., "A Comparison of Adaptive-Grid Redistribution and Embedding for Steady Transonic Flows", *Int. J. Numer. Methods Engrg.*, Vol. 32, pp. 653-663, 1991

Davidov, B. L, "On the statistical dynamics of an incompressible turbulent fluid", Dokl. AN SSSR, Vol.136, p. 47, 1961

Davis, R. L. & Dannehoffer, J. F., "Adaptive Grid Embedding Navier-Stokes Technique for Cascade Flows", *J. Propulsion*, Vol. 7, pp. 792-799, 1991

Dvorak, R., "Vortices and Vortical Structures in Internal Aerodynamics", 3rd Intern. Symp. on Aerothermodyn. of Internal Flows", pp. 551-555, 1996

Eiseman, P. R., Levy, R., McDonald, H. and Briley, W. R., "Development of a three-dimensional turbulent duct flow analysis", NASA CR 3029, 1978

Eriksson, L. E., "Generation of Boundary-Conforming Grids Around Wing-Body Configurations Using Transfinite Interpolation, *AIAA Journal*, Vol. 20, No. 10, pp. 1313-1320, 1982

ESDU, "Vortex Generators for Control of Shock-Induced Separation, Part 1: Introduction and Aerodynamics", ESDU Transonic Data Memorandum. No. 93024, February, 1995

ESDU, "Vortex Generators for Control of Shock-Induced Separation, Part 2: Guide to use of Vane Vortex Generators", ESDU Transonic Data Memorandum. No. 93025, February, 1994

Foster, J., Wendt, B. J., Reichert, B. A. & Okiishi, Th. H., "Flow Through a Rectangular-to-Semiannular Diffusing Transition Duct", *Journal of Propulsion and Power*, Vol. 13, No. 2, pp. 312-317, March-April, 1997

Freitas, C. J., "Perspective: Selected Benchmarks From Commercial CFD Codes", Transactions of the ASME, *Journal of Fluids Engineering*, Vol. 117, pp. 208-218, June 1995

Gad-el-Hak, M. & Bushnell, D. M., "Separation Control: Review", *Journal of Fluids Engineering*, Vol. 113, pp. 5-30, 1991

Gentry, R. A., Martin, R. E. & Daly, B. J., "An Eulerian Differencing Method for Unsteady Compressible Flow Problems", *Journal of Computational Physics*, Vol. 1, pp. 87-118, 1966

Gibb, J. & Anderson, B. H., "Vortex Flow Control Applied to Aircraft Intake Ducts", CEAS European Forum on High Lift & Separation Control, March, 1995, Bath, U. K.

Gordon, W. J. & Hall, C. A., "Construction of Curvilinear Co-ordinate Systems and Applications to Mesh Generation", *Int. J. for Num. Methods in Engineering*, Vol. 7, pp. 461-477, 1973

Guo, R. W. & Seddon, J., "The Investigations of Swirl in an S-duct", *Aeronautical Quarterly*, Vol. 33, pp. 25-58, February 1982

Guo, R. W. & Seddon, J., "The Swirl in an S-duct of typical intake proportions", *Aeronautical Quarterly*, Vol. 34, pp. 99-129, February 1983

Henry, F. S. & Pearcey, H. H., "Numerical Model of Boundary-Layer Control using Air-Jet Generated Vortices", *AIAA Journal*, Vol. 32, No. 12, pp. 2415-2425, 1994

Hinze, J. O., "Turbulence", McGraw Hill, 1959

Issa, R. I., "Solution of the implicitly discretised fluid flow equations by operator splitting", *Journal of Computational Physics*, Vol. 61, p. 40, 1985

Johnston, J. P. & Nishi, M., "Vortex Generator Jets-Means for Flow Separation Control", *AIAA Journal*, Vol. 28, No. 6, pp. 989-994, 1990

Jones, J. P., "The Calculation of the Paths of Vortices from a System of Vortex Generators, and a Comparison with Experiment", Aeronautical Research Council, C. P., No. 361, March 1955

Jones, W. P. & Launder, B. E., "The prediction of laminarization with a two-equation model of turbulence", *International Journal of Heat and Mass Transfer*, Vol. 15, pp. 301-314,-1972

Jongen, T., Mompean, G. & Gatski, T. B., " Predicting S-Duct Flow Using a Composite Algebraic Stress Model", *AIAA Journal*, Vol. 36, No. 3, pp. 327-335, March, 1998

Kim, H. J. & Thompson, J. F., "Three-Dimensional Adaptive Grid Generation on a Composite-Block Grid", *AIAA Journal*, Vol. 28, pp. 470-477, 1990

Kolmogorov, A. N., "Equations of turbulent motions of an incompressible fluid", Report ON/6, Imperial College, Dept. of Mech. Eng., 1968

Kunik, W. G., "Application of a Computational Model for Vortex Generators in Subsonic Internal Flows", *AIAA Paper 86-1458*, June, 1986

Launder, B. E. & Spalding, D. B., "The numerical computation of turbulent flow", Comp. Meth. in Appl. Mech., and Eng.", No. 3, p. 269, 1974

Leonard, B. P., "A Stable and Accurate Convective Modelling Procedure based on Quadratic Upstream Interpolation", *Comp. Meth. Appl. Mech. Eng.*, Vol. 19, pp. 59-98, 1979

Liandrat, J., Aupoix, B. & Couseix, J., "Calculation of Longitudinal Vortices Imbedded in a Turbulent Boundary Layer", Turbulent Shear Flows 5, Springer-Verlag Berlin Heidelberg, 1987

Lin, J. C., Robinson, S. K., McGhee, R. J. & Valarezo, W. O., "Separation Control on High-Lift Airfoils via Micro-Vortex Generators", *Journal of Aircraft*, Vol. 31, No. 6, pp. 1317-1323, November-December 1994

Littell, H. S. & Eaton, J. K., "Unsteady Flowfield Behind a Vortex Generator Rapidly Pitched to Angle of Attack", *AIAA Journal*, Vol. 29, No. 4, pp. 577-584, April, 1991

May, N. E., "The Prediction of Intake/S-Bend Diffuser Flow using Various Two-Equation Turbulence Model Variants, Including Non-Linear Eddy Viscosity Formulation", Aircraft Research Association Contractor Report M316/1, March, 1997

Metha, R. D., Shabaka, I. M. M. A., Shibl, A. & Bradshaw, P., "Longitudinal Vortices Imbedded in Turbulent Boundary Layers", *AIAA Paper 83-0378*, January, 1983

Nakamura, S. & Suzuki, M., "Noniterative Three Dimensional Grid Generation Using a Parabolic-Hyperbolic Hybrid Scheme", *AIAA Paper 87-0277*, 25th Aerospace Sciences Meeting, Reno, NV., 1987

Patankar, S. V., "Numerical Heat *Transfer and Fluid Flow*", 1st ed., McGraw Hill, 1980

Patankar, S. V., "A Calculation Procedure for Two-Dimensional Elliptic Situations", *Numerical Heat Transfer*, Vol. 4, pp. 409-425, 1981

Patankar, S. V. & Spalding, D. B., "A calculation procedure for heat, mass and momentum transfer in three dimensional parabolic flows", *International Journal Heat Mass Transfer*, Vol. 15, pp. 1787-1806, 1972

Pauley, W. R. & Eaton, J. K., "Experimental Study of the Development of Longitudinal Vortex Pairs Embedded in a Turbulent Boundary Layer", *AIAA Journal*, Vol. 26, No. 7, pp. 816-823, July, 1988

Pearcey, H. H., "Shock Induced Separation and its Prevention", Boundary Layer & Flow Control, Vol. 2, Pergamon, New York, pp. 1170-1344, 1961

Pearcey, H. H., Rao, K. & Sykes, D. M., "Inclined Air-Jets used as Vortex Generators to Suppress Shock-Induced Separation", AGARD Fluid Dynamics Symposium Computational and Experimental Assessment of Jets in Cross Flow, Winchester, U. K., Nov., 1993

Piomelli, U., "Introduction to the Modelling of Turbulence", Lecture Series 1997-03, von Karman Institute for Fluid Dynamics, March, 1997

Pratap, V. S. and Spalding, D. B., "Numerical computations of the flow in curved ducts", *The Aeronautical Quarterly*, Vol. 26, Part 3, August 1975

Quirk, J. J., "An Alternative to Unstructured Grids for Computing Gas Dynamic Flows around Arbitrarily Complex Two-Dimensional Bodies", *Computers and Fluids*, Vol. 23, pp. 125-142, 1994

Raj, P. & Iversen, J. D., "Computational Studies of Turbulent Merger of Co-Rotational Vortices", *AIAA Paper 78-108*, January, 1978

Reichert, B. A. & Wendt, B. J., "Improving S-Duct Performance by Secondary Flow Control", *AIAA Paper 94-0365*, January, 1994

Reichert, B. A. & Wendt, B. J., "Improving Curved Subsonic Diffuser Performance with Vortex Generators", *AIAA Journal*, Vol. 34, No. 1, pp. 65-72, January, 1996

Rhie, C. M. & Chow, W. L. A., "Numerical Study of the Turbulent Flow Past an Airfoil with Trailing Edge Separation", *AIAA Journal*, Vol. 21, pp. 1525-1532, 1983

Roache, P. J., "Computational Fluid Dynamics", Hermosa Publishers, Albuquerque, New Mexico, 1972

Rodi, W., "Turbulence Models and Their Application in Hydraulics", Institut für Hydromechanik, Uni Karlsruhe, 1980

Rotta, J. C., "Statistische Theorie nichthomogener Turbulenz", Reports TWF/TN/38, Vol. 39, Imperial College, Dept. of Mech. Eng., 1968

Runchal, A. K. & Wolfstein, M., "Numerical Integration Procedure for the Steady State Navier-Stokes Equations", *Journal of Mechanical Engineering and Science*, Vol. 11, No. 5, pp. 445-453, 1969

Saffman, P. G., "A model for inhomogeneous turbulent flow", Proc. Roy. Soc., Series A, Vol. 317, pp. 417-433, 1970

Schlichting, H., "Boundary Layer Theory", 7th ed., McGraw Hill, 1979

Schoenung, B. E., "Numerische Stroemungsmechanik", *Springer-Verlag*, 1990

Seddon, J., "Understanding and Countering the Swirl in S-Ducts, Tests on the Sensitivity 9 of Swirl to Fences", *Aeronautical Journal*, Vol. 88, No. 874, pp. 117-127, April, 1984

Selby, G. V., Lin, J. C. & Howard, F. G., "Control of Low-Speed Turbulent Separated Flow using Jet Vortex Generators", *Experiments in Fluids*, Vol. 12, No. 6, pp. 394-400, 1992

Senseney, M. B., Buter, T. A. & Bowersox, R. D. W., "Performance Characterisation of a Highly Offset Diffuser with Vortex Generator Jets", *Journal of Propulsion and Power*, Vol. 12, No. 2, pp. 237-244, March-April, 1996

Shabaka, I. M. M. A., Metha, R. D. & Bradshaw, P., "Longitudinal Vortices Imbedded in Turbulent Boundary Layers, Part I, Single Vortex, *Journal of Fluid Mechanics*, Vol. 155, pp. 37-57, 1985

Shieh, C. F., "Three-Dimensional Grid Generation Using Elliptic Equations with Direct Grid Distribution Control", *AIAA Journal*, Vol. 22, No. 3, pp. 361-364, 1984

Smith, C. F., Bruns, J. E., Harloff, G. J. & Debonis, J. R., "Three-Dimensional Compressible Turb. *Computations for a Diffusing* S-Duct", Sverdrup Technology, Inc. NASA CR 4392, 1991

Sorenson, R. L., "A Computer Program to Generate Two-Dimensional Grids about Airfoils and Other Shapes by the Use of Poisson's Equation", NASA Technical Memorandum 81198, 1980

Spalding, D. B., "The kW model of turbulence", Report (TM/TN/A/16), Imperial College, Dept. of Mech. Eng., 1971

Spalding, D. B., "A Novel Finite-Difference Formulation for Differential Expressions Involving Both First and Second Derivatives", *International Journal of Numerical Methods Engineering*, Vol. 4, p. 551, 1972

Spalding, D. B., "Mathematical Methods in Nuclear-Reactor Thermal Hydraulics", American Nuclear Society, Meeting on Nuclear-Reactor Thermal Hydraulics, Saratoga, NY, USA, 1980

Spardling, M. L., Nakamura, S. & Kuwahara, K., "Application of Elliptic Grid Generation Equations Blended with Hyperbolic Method to Three-Dimensional Grids for Vehicle Aerodynamic Analysis", Proc. 3rd International Conference on Numerical Grid Generation in CFD and Related Fields (Arcilla, A. S., Hauser, J., Eiseman, P. R. & Thompson, J. F.), pp. 237-245, North Holland, New York, 1991

Sparis, P. D., "A Method for Generating Boundary-Orthogonal Curvilinear Coordinate Systems Using the Biharmonic Equation", *Journal of Computational Physics*, Vol. 61, pp. 445-462, 1985

Speziale, C. G., "Analytical Methods For The Development Of Reynolds-Stress Closures In Turbulence", Annual Review of Fluid Mechanics, Vol. 23, pp. 107-157, 1991

Steger, J. L. & Chausee, D. S., "Generation of *Body-Fitted Coordinates* Using Hyperbolic Partial Differential Equations", *SIAM J. of Scientific and Statistical Computing*, Vol. 1, No. 4, pp. 431-437, 1980

Taylor, H. D., "Application of Vortex Generator Mixing Principles to Diffusers", Concluding Report R-15064-5, United Aircraft Corp. Research Department, December, 1948

Taylor, A. M. K. P., Whitelaw, J. H. & Yianneskis, M., "Developing Flow in S-Shaped Ducts II - Circular Cross-Section Duct", Imperial College of Science and Technology NASA Contractor Report 3759, Feb. 1984

Tennekes, H. & Lumley, J. L., "A First Course in Turbulence", MIT-Press, Cambridge, Mass., 1972

Thompson, J. F., Warsi, Z. U. A. & Mastin, C. W., "Numerical Grid Generation Foundations and Applications, North Holland, New York, 1985

Tobak, M. & Peake, D. J., "Topology of Three-Dimensional Separated Flows", Ann. Review of Fluid Mechanics, Vol. 14, pp. 61-85, 1982

Towne, C. E., "Computation of Viscous Flow in Curved Ducts and Comparison with Experimental Data", *AIAA Paper 84-0531*, 1984

Van Doormal, J. P. & Raithby, G. D., "Enhancements of the SIMPLE method for predicting incompressible fluid flows", *Numerical Heat Transfer*, Vol. 7, pp. 147-163, 1984

Vakili, A., Wu, P. Hingst, W. R. & Towne, C. E., "Comparison of Experimental and Computational Compressible Flow in an S-Duct", *AIAA Paper 84-0033*, Jan. 1984

Vakili, A., Wu, J. M., Liver, P. & Bhat, M. K., "Flow Control in a Diffusing S-Duct", *AIAA Paper 85-0524*, March 1985

Vakili, A., Wu, J. M., Liver, P. & Bhat, M. K., "Compressible Flow in a Diffusing S-duct with Flow Separation ", W. J. Yang, ed., Hemisphere Publishing 1987, pp. 201-211

Wallis, R. A., "The Use of Air-Jets for Boundary Layer Control", Aeronautical Research Council, Australia, Aero Note 110, 1952

Wallis, R. A., "A Preliminary Note on a Modified Type of Air-Jet for Boundary Layer Control", Aeronautical Research Council, Australia, Current-Paper CP 513, 1960

Warsi, Z. U. A., "Numerical Grid Generation in Arbitrary Surface Through a Second-Order Differential-Geometrical Model, *J. Comput. Physics*, Vol. 64, pp. 82-96, 1986

Warsi, Z. U. A. & Thompson, J. L., "Application of Variational Methods in the Fixed and Adaptive Grid Generation", *Comput. Math. Appl.*, Vol. 19, pp. 31-41, 1990

Wellhorn, S. R., Reichert, S. A. & Okiishi, T. H., "An Experimental Investigation of the Flow in a Diffusing S-Duct", *AIAA Paper 92-3622*, July, 1992; also NASA TM 105809, August, 1992

Wendt, B. J. , Greber, I. & Hingst, W. R., "The Structure and Development of Streamwise Vortex Arrays Embedded in a Turbulent Boundary Layer", *AIAA Journal*, Vol. 31, No. 2, pp. 319-325, 1993

Wendt, B. J. & Hingst, W. R., "Flow Structure in the Wake of a Wishbone Vortex Generator", *AIAA Journal*, Vol. 32, No. 11, pp. 2234-2240, November, 1994

Wendt, B. J. & Reichert, B. A., "Vortex Ingestion in a Diffusing S-Duct Inlet", *Journal of Aircraft*, Vol. 33, No. 1, pp. 149-154, January-February, 1996

Weng, P. F. & Guo, R. W., "New Method of Swirl Control in a Diffusing S-Duct", *AIAA Journal*, Vol. 30, No. 7, pp. 1918-1919, 1992

Westphal, R. V., Eaton, J. K. & Pauley, W. R., "Interaction Between a Vortex and a Turbulent Boundary Layer in a Streamwise Pressure Gradient", Turbulent Shear Flows, edited by F. Durst, B. E. Launder, F. W. Schmidt, and J. W. Whitelaw, Springer Verlag, New York, pp. 266-277, 1987

Whitelaw, J. H. & Yu, S. C. M., "Turbulent-Flow Characteristics in an S-shaped Diffusing Duct", *Flow Measurement and Instrumentation*, Vol. 4, No. 3, pp. 171-179, 1993

Wilcox, D. C., "Reassessment of the scale-determining equation for advanced turbulence models", *AIAA Journal*, Vol. 26, pp. 1299-1310, 1988

Zhang, X., "Computational Analysis of Co- and Contra- Rotating Streamwise Vortices in a Turbulent Boundary Layer", *AIAA Paper No. 93-3035*, July, 1993a

Zhang, X., "Interaction between a Turbulent Boundary Layer and Elliptic and Rectangular Jets", 2nd International Symposium on Engineering Turbulence Modelling and Measurements, pp. 251-260, Florence, Italy, May 31-June, 1993b

Appendix A

Governing Equations

Continuity Equation

The following derivation applies to a finite control volume fixed in space and the resulting integral equation will be rearranged into a partial differential equation with conservative character. Conservation of mass can be described as (Anderson, 1995: pp. 53-66):

The net amount of mass which passes through the boundary surface S of the control volume	=	The time depending decrease of the mass within the control volume.

$$B = C$$

According to the sign convention: Outflow ≡ positive (+)

Inflow ≡ negative (-)

The two terms in integral form are: $B = \iint_S \rho V dS$ and $C = -\frac{\partial}{\partial t} \iiint_V \rho dV$

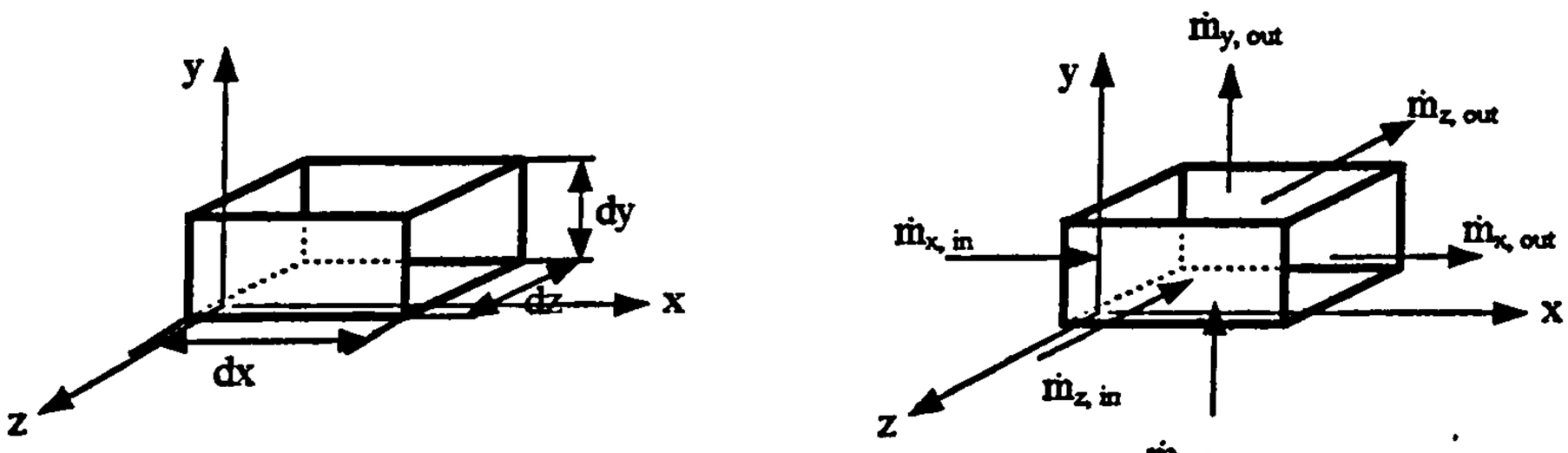

Figure 1: Infinitesimal control volume fixed in space

In Cartesian coordinates, Figure 1, and using the definition of

$$\boxed{\text{Net out flow} = \text{outflow} - \text{inflow}} \quad (1)$$

yields:

Net outflow in x-direction: $$\left[\rho u + \frac{\partial(\rho u)}{\partial x} dx\right] dydz - (\rho u) dydz = \frac{\partial(\rho u)}{\partial x} dxdydz$$

Net outflow in y-direction: $$\left[\rho v + \frac{\partial(\rho v)}{\partial y} dy\right] dxdz - (\rho v) dxdz = \frac{\partial(\rho v)}{\partial y} dxdydz$$

Net outflow in z-direction: $$\left[\rho w + \frac{\partial(\rho w)}{\partial z} dz\right] dxdy - (\rho w) dxdy = \frac{\partial(\rho w)}{\partial z} dxdydz$$

Therefore the net flow out of the control volume has to be:

$$B = \left[\frac{\partial(\rho u)}{\partial x} + \frac{\partial(\rho v)}{\partial y} + \frac{\partial(\rho w)}{\partial z}\right] dxdydz$$

and the time depending decrease of mass is:

$$C = -\frac{\partial \rho}{\partial t}(dxdydz)$$

Continuity requires B to equal C so that:

$$\Rightarrow \quad \left[\frac{\partial(\rho u)}{\partial x} + \frac{\partial(\rho v)}{\partial y} + \frac{\partial(\rho w)}{\partial z}\right] dxdydz + \frac{\partial \rho}{\partial t}(dxdydz) = 0$$

$$\Rightarrow \quad \frac{\partial \rho}{\partial t} + \left[\frac{\partial(\rho u)}{\partial x} + \frac{\partial(\rho v)}{\partial y} + \frac{\partial(\rho w)}{\partial z}\right] \cdot = 0$$

with the divergence of the velocity: $\nabla \cdot (\rho \vec{v}) = \frac{\partial(\rho u)}{\partial x} + \frac{\partial(\rho v)}{\partial y} + \frac{\partial(\rho w)}{\partial z}$

The continuity equation in conservative form yields:

$$\boxed{\frac{\partial \rho}{\partial t} + \nabla \cdot (\rho \vec{v}) = 0} \quad (2)$$

Momentum Equation

The momentum equation is based on Newton's second law which states that a change of momentum per time causes a force, thus: $F = \frac{d}{dt}(mv)$. The total force on the moving fluid element is equal to the change in linear momentum and is divided in a body force F_B and a net surface force F_S. In x-direction the momentum equation yields:

$$\boxed{F_{total\,x} = F_{Sx} + F_{Bx} = ma_x = \rho dxdydza_x = \rho dxdydz\frac{Du}{Dt}} \quad (3)$$

left hand side — right hand side

Where *Du/Dt* is the substantial derivative on the right hand side of equation (3) shows that the derivation of the momentum equations results in a nonconservative form. The surface forces in x-direction are demonstrated in Figure 2.

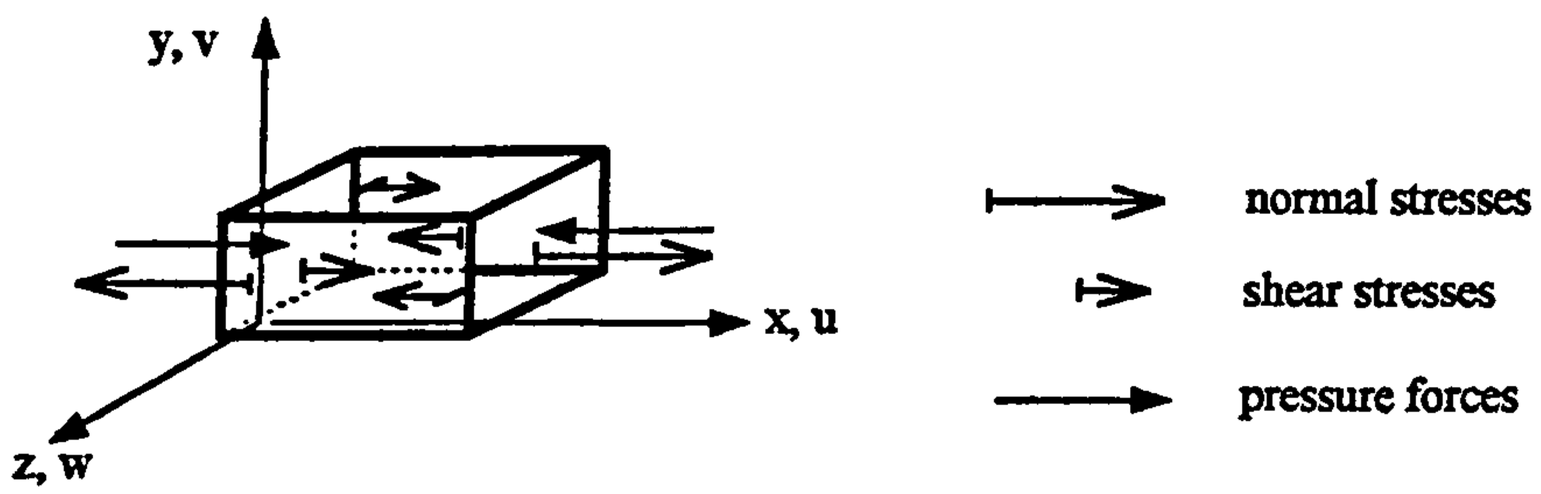

Figure 2: Surface forces acting onto the infinitesimal small fluid element moving with the main flow

The net surface force F_{Sx} in the x-direction according to definition (1) mentioned above yields:

$$\boxed{\begin{aligned} F_{Sx} &= \underbrace{\left[p - \left(p + \frac{\partial p}{\partial x}dx\right)\right]dydz}_{\text{Pressure forces}} + \underbrace{\left[\left(\tau_{xx} + \frac{\partial \tau_{xx}}{\partial x}dx\right) - \tau_{xx}\right]dydz}_{\text{Normal stresses}} \\ &+ \underbrace{\left[\left(\tau_{yx} + \frac{\partial \tau_{yx}}{\partial y}dy\right) - \tau_{yx}\right]dxdz + \left[\left(\tau_{zx} + \frac{\partial \tau_{zx}}{\partial z}dz\right) - \tau_{zx}\right]dxdy}_{\text{Shear stresses}} \end{aligned}} \quad (4)$$

The body force in x-direction acting on the fluid element is: $\boxed{F_{Bx} = \rho f_x (dxdydz)}$ (5)

where f_x is the body force acting in x-direction per unit mass.

Hence the total force in x-direction has to be: $F_{total\,x} = F_{Sx} + F_{Bx}$

$$\Rightarrow \qquad \boxed{F_x = \left[-\frac{\partial p}{\partial x} + \frac{\partial \tau_{xx}}{\partial x} + \frac{\partial \tau_{yx}}{\partial y} + \frac{\partial \tau_{zx}}{\partial z} \right] dxdydz + \rho f_x \, dxdyd = \rho dxdydz \frac{Du}{Dt}} \quad (6)$$

Thus dividing through by dxdydz, the momentum equation in the x-direction, in nonconservative form, becomes:

$$\Rightarrow \qquad \boxed{\rho \frac{Du}{Dt} = \left[-\frac{\partial p}{\partial x} + \frac{\partial \tau_{xx}}{\partial x} + \frac{\partial \tau_{yx}}{\partial y} + \frac{\partial \tau_{zx}}{\partial z} \right] + \rho f_x} \quad (7)$$

Using similar arguments the momentum equation in y-direction can be written:

$$\Rightarrow \qquad \boxed{\rho \frac{Du}{Dt} = \left[-\frac{\partial p}{\partial x} + \frac{\partial \tau_{xy}}{\partial x} + \frac{\partial \tau_{yy}}{\partial y} + \frac{\partial \tau_{zy}}{\partial z} \right] + \rho f_y} \quad (8)$$

and the momentum equation in z-direction can be written:

$$\Rightarrow \qquad \boxed{\rho \frac{Du}{Dt} = \left[-\frac{\partial p}{\partial x} + \frac{\partial \tau_{xz}}{\partial x} + \frac{\partial \tau_{yz}}{\partial y} + \frac{\partial \tau_{zz}}{\partial z} \right] + \rho f_z} \quad (9)$$

To get the Navier-Stokes equations in conservative form one has to expand the substantial derivative on the left-hand side of the momentum equation.

The substantial derivative of the velocity component u is: $\rho \frac{Du}{Dt} = \rho \frac{\partial u}{\partial t} + \rho \vec{v} \cdot \nabla u$

Using: $\frac{\partial (\rho u)}{\partial t} = \rho \frac{\partial u}{\partial t} + u \frac{\partial \rho}{\partial t}$

and: $\nabla \cdot (\rho u \vec{v}) = u \nabla \cdot (\rho \vec{v}) + (\rho \vec{v}) \cdot \nabla u$

The substantial derivative equation of the velocity component u can be written:

$$\Rightarrow \qquad \rho \frac{Du}{Dt} = \rho \frac{\partial u}{\partial t} + \rho \vec{v} \cdot \nabla u = \frac{\partial (\rho u)}{\partial t} - u \left[\frac{\partial \rho}{\partial t} + \nabla \cdot (\rho \vec{v}) \right] + \nabla \cdot (\rho u \vec{v})$$

From continuity $\left[\frac{\partial \rho}{\partial t} + \nabla \cdot (\rho \vec{v}) \right] = 0$ so that the Navier-Stokes equations in conservative form are:

In x-direction:
$$\boxed{\frac{\partial (\rho u)}{\partial t} + \nabla \cdot (\rho u \vec{v}) = \left[-\frac{\partial p}{\partial x} + \frac{\partial \tau_{xx}}{\partial x} + \frac{\partial \tau_{yx}}{\partial y} + \frac{\partial \tau_{zx}}{\partial z} \right] + \rho f_x} \quad (10)$$

In y-direction:
$$\boxed{\frac{\partial (\rho v)}{\partial t} + \nabla \cdot (\rho v \vec{v}) = \left[-\frac{\partial p}{\partial x} + \frac{\partial \tau_{xy}}{\partial x} + \frac{\partial \tau_{yy}}{\partial y} + \frac{\partial \tau_{zy}}{\partial z} \right] + \rho f_y} \quad (11)$$

In z-direction:

$$\boxed{\frac{\partial(\rho w)}{\partial t}+\nabla\cdot(\rho w\vec{v})=\left[-\frac{\partial p}{\partial x}+\frac{\partial \tau_{xz}}{\partial x}+\frac{\partial \tau_{yz}}{\partial y}+\frac{\partial \tau_{zz}}{\partial z}\right]+\rho f_z} \quad (12)$$

For Newtonian fluids the shear stress is proportional to the time rate of strain, Figure 3:

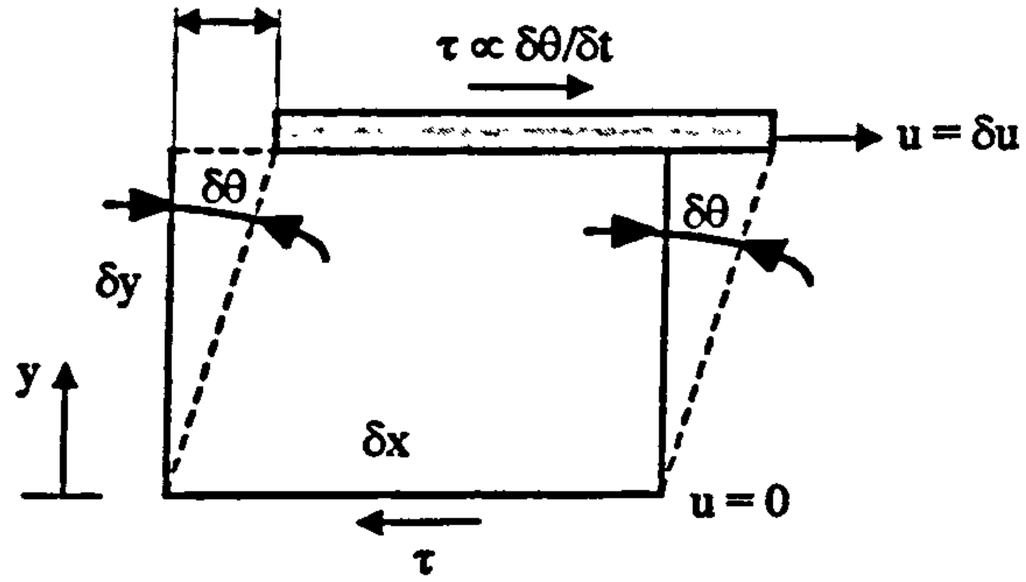

Figure 3: Fluid deformation

$\delta\theta$ = *shear stress angle = angle of deformation*

$$\tau \propto \frac{\delta\theta}{\delta t} \equiv \textit{time rate of strain}$$

$$\tan\delta\theta=\frac{\delta u\delta t}{\delta y} \qquad \text{with} \quad \delta\theta<<1\Rightarrow\delta\theta=\tan\delta\theta \qquad \text{hence} \quad \delta\theta=\frac{\delta u\delta t}{\delta y}$$

and in the limits of infinitesimal changes

$$\frac{d\theta}{dt}=\frac{du}{dy}$$

Thus the shear stress is proportional to the time rate of strain which is equal to the velocity gradient $\frac{du}{dy}$:

$$\tau\propto\frac{d\theta}{dt}\Rightarrow\tau\propto\frac{du}{dy}\Rightarrow\tau=\mu\frac{du}{dy} \quad (13)$$

Based on equation (13) and a hypotheses of a second viscosity Stokes defined (1845) the following general relations between stress and rate of strain:

$$\left.\begin{aligned}\tau_{xx} &= -\frac{2}{3}\mu(\nabla\cdot\vec{v})+2\mu\frac{\partial u}{\partial x}\\ \tau_{yy} &= -\frac{2}{3}\mu(\nabla\cdot\vec{v})+2\mu\frac{\partial v}{\partial y}\\ \tau_{zz} &= -\frac{2}{3}\mu(\nabla\cdot\vec{v})+2\mu\frac{\partial w}{\partial z}\end{aligned}\right\}\quad\text{normal stresses}$$

$$\left.\begin{aligned}\tau_{xy} &= \tau_{yx} = \mu\left[\frac{\partial v}{\partial x}+\frac{\partial u}{\partial y}\right]\\ \tau_{xz} &= \tau_{zx} = \mu\left[\frac{\partial u}{\partial z}+\frac{\partial w}{\partial x}\right]\\ \tau_{yz} &= \tau_{zy} = \mu\left[\frac{\partial w}{\partial y}+\frac{\partial v}{\partial z}\right]\end{aligned}\right\}\quad\text{shear stresses}$$

Substituting the normal and shear stress expressions into equations (10 to 12)the three Navier-Stokes equations in conservative form are:

In x-direction:

$$\boxed{\begin{aligned}&\frac{\partial(\rho u)}{\partial t}+\frac{\partial(\rho u^2)}{\partial x}+\frac{\partial(\rho uv)}{\partial y}+\frac{\partial(\rho uw)}{\partial z}=-\frac{\partial p}{\partial x}+\frac{\partial}{\partial x}\left(-\frac{2}{3}\mu\nabla\cdot\vec{v}+2\mu\frac{\partial u}{\partial x}\right)\\ &+\frac{\partial}{\partial y}\left[\mu\left(\frac{\partial v}{\partial x}+\frac{\partial u}{\partial y}\right)\right]+\frac{\partial}{\partial z}\left[\mu\left(\frac{\partial u}{\partial z}+\frac{\partial w}{\partial x}\right)\right]+\rho f_x\end{aligned}}\quad(14)$$

In y-direction:

$$\boxed{\begin{aligned}&\frac{\partial(\rho v)}{\partial t}+\frac{\partial(\rho uv)}{\partial x}+\frac{\partial(\rho v^2)}{\partial y}+\frac{\partial(\rho vw)}{\partial z}=-\frac{\partial p}{\partial y}+\frac{\partial}{\partial x}\left[\mu\left(\frac{\partial v}{\partial x}+\frac{\partial u}{\partial y}\right)\right]\\ &+\frac{\partial}{\partial y}\left(-\frac{2}{3}\mu\nabla\cdot\vec{v}+2\mu\frac{\partial v}{\partial y}\right)+\frac{\partial}{\partial z}\left[\mu\left(\frac{\partial w}{\partial y}+\frac{\partial v}{\partial z}\right)\right]+\rho f_y\end{aligned}}\quad(15)$$

In z-direction:

$$\boxed{\begin{aligned}&\frac{\partial(\rho w)}{\partial t}+\frac{\partial(\rho uw)}{\partial x}+\frac{\partial(\rho vw)}{\partial y}+\frac{\partial(\rho w^2)}{\partial z}=-\frac{\partial p}{\partial z}+\frac{\partial}{\partial x}\left[\mu\left(\frac{\partial u}{\partial z}+\frac{\partial w}{\partial x}\right)\right]\\ &+\frac{\partial}{\partial y}\left[\mu\left(\frac{\partial w}{\partial y}+\frac{\partial v}{\partial z}\right)\right]+\frac{\partial}{\partial z}\left(-\frac{2}{3}\mu\nabla\cdot\vec{v}+2\mu\frac{\partial w}{\partial z}\right)+\rho f_z\end{aligned}}\quad(16)$$

Following Patankar (1980) the Navier-Stokes equations can be written in a general form which allows the same discretisation method to be applied to all three velocity components. This will be demonstrated for the x-direction:

$$\nabla\vec{v} = div\,\vec{v} = \frac{\partial u}{\partial x} + \frac{\partial v}{\partial y} + \frac{\partial w}{\partial z}, \quad \nabla^2\vec{v} = div\,grad(\vec{v}) = \frac{\partial^2 u}{\partial x^2} + \frac{\partial^2 v}{\partial y^2} + \frac{\partial^2 w}{\partial z^2}$$

$$\nabla(\rho\vec{v}\,u) = \frac{\partial(\rho u^2)}{\partial x} + \frac{\partial(\rho v u)}{\partial y} + \frac{\partial(\rho w u)}{\partial z}$$

$$\boxed{\frac{\partial(\rho u)}{\partial t} + \nabla(\rho\vec{v}\,u) = \rho f_x - \frac{\partial p}{\partial x} + \frac{\partial}{\partial x}\left(-\frac{2}{3}\mu\nabla\cdot\vec{v}\right) + 2\frac{\partial}{\partial x}\left(\mu\frac{\partial u}{\partial x}\right) + \frac{\partial}{\partial y}\left(\mu\frac{\partial u}{\partial y}\right) + \frac{\partial}{\partial z}\left(\mu\frac{\partial u}{\partial z}\right) + \frac{\partial}{\partial y}\left(\mu\frac{\partial v}{\partial x}\right) + \frac{\partial}{\partial z}\left(\mu\frac{\partial w}{\partial x}\right)}$$

- Noting that:

$$div\,(\mu\,grad\,u) = \nabla(\mu\nabla u) = \frac{\partial}{\partial x}\left(\mu\frac{\partial u}{\partial x}\right) + \frac{\partial}{\partial y}\left(\mu\frac{\partial u}{\partial y}\right) + \frac{\partial}{\partial z}\left(\mu\frac{\partial u}{\partial z}\right)$$

yields:

$$\boxed{\frac{\partial(\rho u)}{\partial t} + \nabla(\rho\vec{v}\,u) = \rho f_x - \frac{\partial p}{\partial x} + \nabla(\mu\nabla u) + \frac{\partial}{\partial x}\left(-\frac{2}{3}\mu\nabla\cdot\vec{v}\right) + \frac{\partial}{\partial x}\left(\mu\frac{\partial u}{\partial x}\right) + \frac{\partial}{\partial y}\left(\mu\frac{\partial v}{\partial x}\right) + \frac{\partial}{\partial z}\left(\mu\frac{\partial w}{\partial x}\right)}$$

Inertia forces

Pressure forces

Viscous forces

Body forces

Defining the terms below:

Additional viscous term:

$$V_x = \frac{\partial}{\partial x}\left(-\frac{2}{3}\mu\nabla\cdot\vec{v}\right) + \frac{\partial}{\partial x}\left(\mu\frac{\partial u}{\partial x}\right) + \frac{\partial}{\partial y}\left(\mu\frac{\partial v}{\partial x}\right) + \frac{\partial}{\partial z}\left(\mu\frac{\partial w}{\partial x}\right)$$

Body force term: $B_x = \rho f_x$

Source term: $S_x = -\frac{\partial p}{\partial x} + B_x + V_x$

The Navier-Stokes equation in x-direction for compressible flow becomes:

$$\boxed{\frac{\partial(\rho u)}{\partial t} + \nabla(\rho \vec{v}\, u) = \nabla(\mu \nabla u) + S_x} \quad (17)$$

In a similar way derived the momentum equations in y- and z-direction are:

$$\boxed{\frac{\partial(\rho v)}{\partial t} + \nabla(\rho \vec{v}\, v) = \nabla(\mu \nabla v) + S_y} \quad (18)$$

$$\boxed{\frac{\partial(\rho w)}{\partial t} + \nabla(\rho \vec{v}\, w) = \nabla(\mu \nabla w) + S_z} \quad (19)$$

Introducing a general variable ϕ (= u, v, w) and a general diffusion coefficient Γ the general differential equation is:

$$\boxed{\frac{\partial(\rho \phi)}{\partial t} + \nabla(\rho \vec{v}\, \phi) = \nabla(\Gamma\, \nabla \phi) + S_\phi} \quad (20)$$

Appendix B

Calculation of the Peak Vorticity and Peak Vorticity Position from the Vorticity Field

The position of the peak vorticity location was determined employing a fortran code which estimates the position of the maximum vorticity in a limited, predefined, area. The vortices in all cells and the cell with the maximum vorticity are dumped to a file at the end of the numerical calculations. The vorticity dump file is read in to the fortran code. The cell with the maximum vorticity determines the approximate position of the peak vorticity location. This nodal location is selected to be the origin of a local coordinate system, in computational space, spanning the eight neighbouring nodes (see Figure B-2). A biquadratic function is fitted to the nine points and the location of the maximum of this function is determined.

The biquadratic function may be written as:

$$\boxed{\phi(\xi,\eta)=a_1+a_2\xi+a_3\eta+a_4\xi\eta+a_5\xi^2.+a_6\eta^2+a_7\xi^2\eta+a_8\xi\eta^2 a_9\xi^2\eta^2} \quad (1)$$

where, $\xi=\xi(x,y)$

$\eta=\eta(x,y)$

are coordinates in computational space (see Figure B-1).

The coefficients a_1, a_2 ....a_9 are found from the point values of vorticity.

The location, in computational space, of the peak vorticity is achieved by differentiating equation (1) by ξ and η separately and setting the resultant equations to zero. Thus,

$$\boxed{\frac{\partial\phi}{\partial\xi}=a_2+a_4\eta+a_5\xi+2a_7\xi\eta+a_8\eta^2+2a_9\xi\eta^2=0} \quad (2)$$

$$\boxed{\frac{\partial\phi}{\partial\eta}=a_3+a_4\xi+a_6\eta+a_7\xi^2+2a_8\eta\xi+2a_9\xi^2\eta=0} \quad (3)$$

Rearranging equations (2) and (3) to the coordinates of the computational space yields,

$$\xi_P = \frac{-a_2 - a_4\eta_P - a_8\eta_P^2}{a_5 + 2a_7\eta_P + 2a_9\eta_P^2} \quad (4)$$

$$\eta_P = \frac{-a_3 - a_4\xi_P - a_7\xi_P^2}{a_6 + 2a_8\xi_P + 2a_9\xi_P^2} \quad (5)$$

The peak vorticity is determined using equations (1), (4) and (5) in an iterative manner.

The position in physical space (x, y) to the central grid node (the maximum vorticity cell) is determined by calculating the distances Δx and Δy, as;

$$\Delta x = \frac{\overline{\partial x}}{\partial \xi}\xi_P + \frac{\overline{\partial x}}{\partial \eta}\eta_P \quad (6)$$

$$\Delta y = \frac{\overline{\partial y}}{\partial \xi}\xi_P + \frac{\overline{\partial y}}{\partial \eta}\eta_P \quad (7)$$

where the overbar denotes an average value over ξ and η.

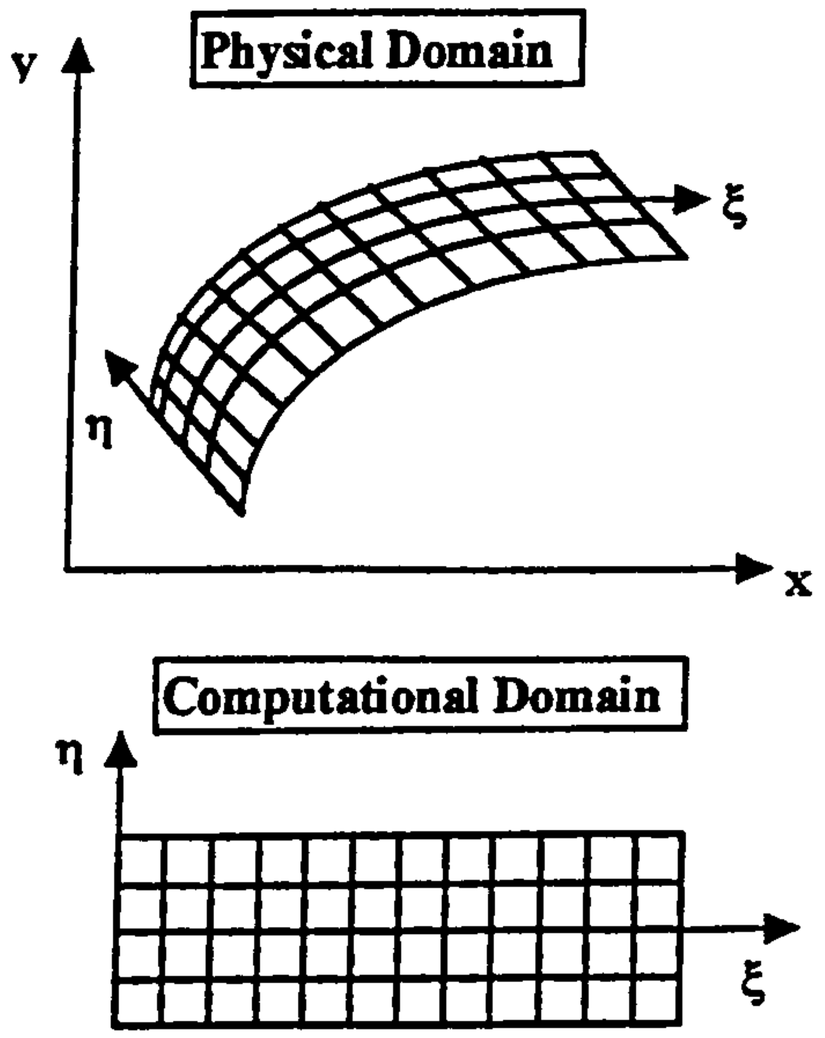

Figure B-1: Computational domain in the physical space, computational domain in the computational space

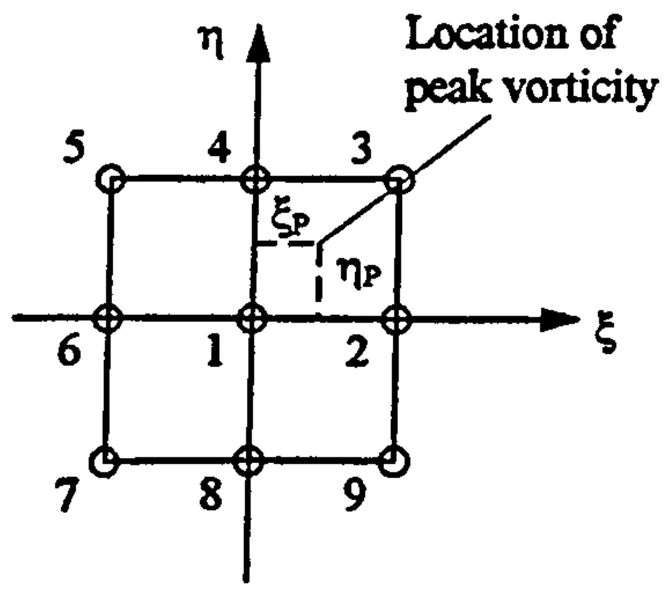

Figure B-2: Location of the peak vorticity point (ξ_P, η_P) in the computational domain

Appendix C

Input Data for RNS3D

The cross-stream locations of the peak vorticities for the investigated pitch and skew configurations are listed in the table below.

	counter-rotating configuration			co-rotating configuration		
pitch/skew angle	$\omega_S/(\delta_0/U_0)$	y/δ_0	z/δ_0	$\omega_S/(\delta_0/U_0)$	y/δ_0	z/δ_0
45°/30°	0.9121	0.1738	-0.2990	0.9085	0.1738	-0.2990
45°/45°	1.0251	0.1738	-0.5620	1.0260	0.1738	-0.5620
45°/60°	1.0083	0.1738	-0.6877	1.0067	0.1306	-0.8220
45°/75°	0.9071	0.1306	-0.8220	0.9115	0.1306	-0.8220
30°/30°	0.9976	0.1738	-0.4328	0.9858	0.1738	-0.4328
30°/45°	1.1759	0.1738	-0.6818	1.1653	0.1738	-0.8166
30°/60°	1.2172	0.1738	-0.9515	1.2195	0.1738	-0.9515
30°/75°	1.1264	0.1738	-1.0863	1.1366	0.1738	-1.0863

The inlet boundary layer height was: $\delta_0 = 0.004$m

The free stream velocity was: $U_0 = 254$m/s

The downstream location X1 was: $X1 = 4.2\delta_0$

The spacing angle α_{VG} was: $\alpha_{VG} = 15°$